BEILSTEIN JOURNAL OF NANOTECHNOLOGY

Exploring synchrotron radiation and free-electron laser tools for nanostructured materials

Edited by Carla Bittencourt, Benedetta Casu and Carlo Mariani

Imprint

Beilstein Journal of Nanotechnology
www.bjnano.org
ISSN 2190-4286
Email: journals-support@beilstein-institut.de

The *Beilstein Journal of Nanotechnology* is published by the Beilstein-Institut zur Förderung der Chemischen Wissenschaften.

Beilstein-Institut zur Förderung der Chemischen Wissenschaften
Trakehner Straße 7–9
60487 Frankfurt am Main
Germany
www.beilstein-institut.de

BEILSTEIN JOURNAL OF NANOTECHNOLOGY

Retrieval of B1 phase from high-pressure B2 phase for CdO nanoparticles by electronic excitations in $Cd_xZn_{1-x}O$ composite thin films

Arkaprava Das*[1], Marcin Zając[2] and Carla Bittencourt[1]

Full Research Paper

Open Access

Address:
[1]Chimie des Interaction Plasma surface, Research Institute for Materials Science and Engineering, Université of Mons, 7000 Mons, Belgium and [2]SOLARIS National Synchrotron Radiation Centre, Jagiellonian University, 30-392 Krakow, Poland

Email:
Arkaprava Das* - arkaprava.das@umons.ac.be

* Corresponding author

Keywords:
irradiation; phase transformation; thermal spike; track diameter; X-ray absorption near edge spectroscopy; X-ray photoelectron spectroscopy

Beilstein J. Nanotechnol. **2025,** *16,* 551–560.
https://doi.org/10.3762/bjnano.16.43

Received: 15 October 2024
Accepted: 04 April 2025
Published: 17 April 2025

This article is part of the thematic issue "Exploring synchrotron radiation and free-electron laser tools for nanostructured materials".

Associate Editor: X. Song

Abstract

This study investigates the recovery of the B1 phase from the high-pressure B2 phase, at atmospheric pressure, in cadmium oxide (CdO) nanoparticles incorporated within sol–gel synthesized $Cd_xZn_{1-x}O$ (x = 0.40) composite thin films. The recovery process is investigated using electronic excitations as an effective tool. Exposure to 120 MeV silver ion irradiation results in the complete amorphization of the B2 phase in CdO nanoparticles, while the crystalline hexagonal wurtzite phase of zinc oxide (ZnO) remains intact. In contrast, 80 MeV oxygen ion irradiation preserves the B2 phase and facilitates the reemergence of the B1 phase. The partial damage caused by electronic energy loss during oxygen ion irradiation in the willemite Zn_2SiO_4 phase is identified as a trigger for the B1 to B2 phase transformation in CdO nanoparticles, enabling the recovery of the B1 phase. The diminishing local pressure exerted by the Zn_2SiO_4 phase on CdO nanoparticles during oxygen ion irradiation leads to the coexistence of both B1 and B2 phases. X-ray absorption near-edge spectra (XANES) reveal minimal changes in the intensity of the spike-like Zn $L_{3,2}$ pre-edge feature associated with the Zn_2SiO_4 phase under oxygen ion irradiation, while it entirely disappears with silver ion irradiation, confirming the amorphization of the Zn_2SiO_4 phase. Complementary observations from X-ray photoelectron spectroscopy (XPS), specifically O 1s and Si 2p peaks in XPS spectra, support these findings. Additionally, the track diameter in CdO subjected to 120 MeV silver ion irradiation is calculated to be approximately 8 nm using an inelastic thermal spike simulation code. This study elucidates the intriguing reappearance of the B1 phase under oxygen ion irradiation and highlights the radiation stability of the B2 phase through diverse characterization techniques, demonstrating the potential reversibility of the B1 to B2 phase transformation induced by ion irradiation.

Introduction

Zinc oxide (ZnO)-based thin films are of significant interest due to their wide bandgap value (3.37 eV at room temperature), transparent electrical conduction, and large excitonic binding energy (60 meV) [1]. In contrast, cadmium oxide (CdO) exhibits a lower bandgap of 2.2 eV, along with high electron mobility (>100 cm^2/V/s) and high electrical conductivity (>10^{14} S/cm), demonstrating its potential for optoelectronic applications [2-4]. The incorporation of cadmium into ZnO effectively reduces the bandgap, rendering the thin films suitable for applications in the visible region of the electromagnetic spectrum [5]. Composite semiconducting thin films have garnered significant attention as their bandgap can be lowered without compromising mobility and conductivity. Beyond optoelectronic applications, CdO–ZnO-based alloys are also employed in gas-sensing technologies [6]. In prior investigations, we reported a local pressure-driven structural phase transformation (PT) from B1 (NaCl) to B2 (CsCl) in $Cd_xZn_{1-x}O$ (x = 0.4) composite binary oxide thin films [1]. The radiation stability of these phases is crucial for optoelectronic applications in space, where the exposure to high-energy particles and gamma radiation can induce lattice defects and lower the device efficiency [7]. Swift heavy ion (SHI) irradiation experiments provide valuable insights into the radiation stability of the transformed B2 phase, which is essential for the future utilization of these composite materials in space-based optoelectronic applications [7]. High-energy ion irradiation can lead to latent track formation or phase transitions, either from crystalline to crystalline or crystalline to amorphous, depending on the threshold electronic energy loss (S_{eth}) [8,9]. The formation of latent tracks has been described through two primary models: the Coulomb explosion model, which relies on electrostatic repulsive forces [10,11], and the thermal spike model, where energy is transferred to lattice atoms, resulting in melting and subsequent quenching to form tracks [12,13]. The latter model has been more widely supported in the literature. Upon penetration in a solid, energetic ions lose energy through two mechanisms: direct energy transfer to target nuclei via elastic collisions (nuclear energy loss (S_n)) and ionization of the target atoms through inelastic collisions (electronic energy loss (S_e)). In the present investigation, we primarily focus on S_e, given the high energy of the irradiation ions (several MeV), while S_n becomes more significant in the keV range [7].

Here, we report on the radiation stability of the transformed B2 phase under 120 MeV Ag and 80 MeV O ion irradiation. Notably, such an investigation has not been previously conducted, as the B2 phase has only been reported through hydrostatic pressure techniques using the in situ diamond anvil cell (DAC) technique [14]. Our study is facilitated by the successful achievement of the B2 phase at atmospheric pressure for $Cd_xZn_{1-x}O$ (x = 0.40) composite thin films [1]. Das et al. reported that S_{eth} for the formation of an amorphous latent track in rock salt CdO is 14.56 keV/nm [7]. Thus, we selected 120 MeV Ag ions, where electronic energy loss (S_e) in CdO is 25.10 keV/nm, and 80 MeV O ions, with S_e at 1.9 keV/nm, to examine the effects on both sides of S_{eth} (i.e., higher and lower sides). Notably, the reappearance of the B1 phase was observed with O ion irradiation, while no such retrieval occurred with Ag ion irradiation. This intriguing finding is explored in detail in this investigation. Crystallographic characterization of both pristine and irradiated thin films was performed with X-ray diffraction and Raman spectroscopy. Additionally, X-ray absorption near-edge structure (XANES) spectroscopy was conducted at the Zn $L_{3,2}$ and O K edges for all the thin films. X-ray photoelectron spectroscopy (XPS) on Si 2p and O 1s core levels provided direct evidence of changes in surface chemical states due to irradiation. In summary, we elucidate the underlying mechanism responsible for the retrieval of the B1 phase from the transformed B2 phase following O ion irradiation using core-level spectroscopy. While the B1 to B2 phase transformation is reported to be irreversible, our findings suggest that with the appropriate choice of irradiating ions and energies, the recovery of the B1 phase is possible. Complementary to this experimental investigation, we conducted thermal spike calculations with 120 MeV Ag ions in rock salt CdO.

Experimental

Thin films with 40% cadmium concentration in zinc oxide (ZnO) were synthesized using the sol–gel chemical route method, as detailed in our previous publication [1]. The irradiation experiments were performed using the 15 UD tandem Pelletron accelerators at the Inter-University Accelerator Centre (IUAC), New Delhi. The irradiation was performed with 120 MeV Ag and 80 MeV O ions. Two different fluences were used for each ion type (i.e., 1×10^{13} ions/cm^2 and 3×10^{13} ions/cm^2). The focus of this study is on a film that underwent a complete transformation to the B2 phase, which is designated as a pristine thin film prior to further irradiation.

The characterization of the thin films was performed using X-ray diffraction (XRD) on a Bruker high-resolution X-ray diffractometer, employing a Cu Kα beam over a 2θ range of 30–50°. Raman spectroscopic measurements were conducted at room temperature with a SENTERRA spectrometer (Bruker), equipped with an Ar ion laser (532 nm) with 0.2 mW laser operating power. Scanning electron microscopy (SEM) analysis was carried out with a HITACHI SU8020 model, using an electron beam energy of 3.0 keV. X-ray photoelectron spectroscopy (XPS) was performed using an ESCA-5000 Versa Probe system (Physical Electronics) with an Al Kα (1486.7 eV) beam

and a 124 mm hemispherical electron analyzer. X-ray absorption near-edge structure experiments were performed at PIRX beamline [15] in the SOLARIS synchrotron facility in Poland [16], focusing on Zn $L_{2,3}$ and O K edges in total electron yield mode. Table 1 summarizes the irradiation ion energies and fluences for each thin film, along with their corresponding labels.

Results and Discussion

Influence of Ag and O ion irradiation on crystallographic phase by X-ray diffraction and Raman spectroscopy

Figure 1a shows the XRD patterns illustrating the B1 to B2 PT in $Cd_xZn_{1-x}O$ (x = 0.4) binary oxide thin films subjected to various annealing temperatures of 700, 800, 850, and 900 °C [1]. The data reveals the emergence of the B2 phase characterized by the (100) Bragg reflection in CdO nanoparticles as the annealing temperature increases. In contrast, the ZnO nanoparticles consistently exhibit the hexagonal wurtzite phase. Figure 1b portrays the effect of 80 MeV O and 120 MeV Ag ion irradiation on the CZ900_Pris sample, wherein the complete transition from B1 to B2 PT has already occurred. The reflections corresponding to the hexagonal wurtzite phase (space group $P6_3mc$) are situated at 31.6° (100), 34.3° (002), 36.1° (101), and 47.4° (102) for the CZ900_Pris sample. The (100) and (110) Bragg reflections associated with the transformed B2 phase (space group $Pm_{-3}m$) are located at 32.2° and 37.8°, respectively. Additionally, a low-intensity peak corresponding to willemite Zn_2SiO_4 (space group R_{-3}) is observed at 38.8°, pre-

Table 1: Sample name with irradiating ion and fluence.

Sample acronym[a]	Post-synthesis annealing temperature (°C)	Irradiating ion and energy (MeV)	Irradiation fluence (ions/cm^2)
Z700	700	no irradiation	0
Z900	900	no irradiation	0
CZ900_Pris	900	no irradiation	0
CZ900_113O	900	80 MeV O ion	1×10^{13}
CZ900_313O	900	80 MeV O ion	3×10^{13}
CZ900_113Ag	900	120 MeV Ag ion	1×10^{13}
CZ900_313Ag	700	120 MeV Ag ion	3×10^{13}

[a]$Cd_xZn_{1-x}O$ (x = 0.40) labelled CZ and ZnO labelled Z.

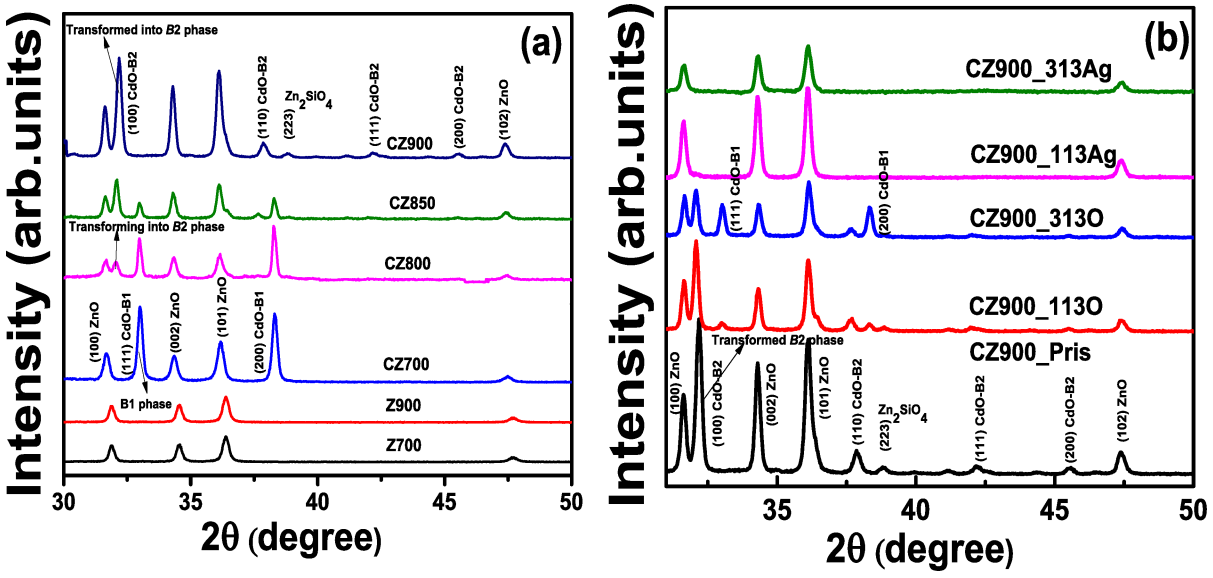

Figure 1: (a) Figure 1a was reprinted from [1], Acta Materialia, vol. 267, by A. Das; C. Latouche; S. Jobic; E. Gautron; A. Merabet; M. Zajac; A. Shibui; P. Krüger; W.-H. Huang; C.-L. Chen; A. Kandasami and C. Bittencourt, "Stabilization of the high-pressure phase of CdO by nanoparticle formation in $Cd_xZn_{1-x}O$ thin films", article no. 119744, Copyright (2024), with permission from Elsevier. This content is not subject to CC BY 4.0 (b) XRD pattern for CZ900_Pris, CZ900_113O, CZ900_313O, CZ900_113Ag, and CZ900_313Ag thin films.

viously identified as a contributing factor to the B2 phase transition [1]. In the case of the CZ900_113O sample, a reduction in the intensity of the B2 phase reflections is noted, accompanied by a subtle emergence of the B1 phase (space group $Fm_{-3}m$) at 32.9° and 38.3°, corresponding to the (111) and (200) reflections, respectively. The presence of the willemite Zn_2SiO_4 phase persists in the CZ900_113O sample. Upon applying an O ion irradiation fluence of 3×10^{13} ions/cm^2 in the CZ900_313O sample, a further decrease in the intensity of the B2 phase is observed, which is attributed to enhanced electronic energy loss and the phenomenon of multiple ion impacts. The B1 phase is fully reestablished in this thin film, while the signature of the Zn_2SiO_4 phase is no longer detectable. This amorphization of the Zn_2SiO_4 phase facilitates the re-emergence of the B1 phase under higher fluence. For the CZ900_113Ag sample subjected to Ag irradiation, both the B2 phase and the Zn_2SiO_4 phase exhibit complete amorphization due to irradiation-induced damage, precluding any observable evolution of the B1 phase. Consequently, the wurtzite ZnO phase remains intact in both the CZ900_113Ag and CZ900_313Ag thin films. Notably, the absence of a distinct phase for CdO nanoparticles indicates that the radiation stability of the wurtzite ZnO structure significantly surpasses that of the B1/B2 CdO phase.

In Figure 2, the Raman spectra for both pristine and irradiated thin films are shown. The spectra for the undoped ZnO thin film annealed at 900 °C (Z900) are included to facilitate a comparative analysis concerning the presence of the B2 phase. These measurements were conducted in backscattering geometry without accounting for any polarization effects of the incident laser light. The optically active phonon modes at the center of the Brillouin zone have the following point symmetries:

$$\Gamma_{opt} = 1A_1 + 2B_1 + 1E_1 + 2E_2. \quad (1)$$

In this equation, the A_1 and E_1 modes correspond to Raman and infrared (IR) active branches, characterized by polar symmetries that further degenerate doubly longitudinal optical (LO) and transverse optical (TO) components with different frequencies. The E_2 mode represents the only Raman-active nonpolar branch, which comprises two sub-branches, E_2(H) and E_2(L). This branch is both Raman and IR active [17]. The peaks observed in the Raman spectra are predominantly attributed to the silicon substrate, with notable peaks at 303, 520, 620, and 671 cm^{-1}. The peak at 435.9 cm^{-1} corresponds to the E_2(H) mode characteristic of the wurtzite ZnO phase [17]. The persistence of the E_2(high) mode across all O and Ag ion irradiated thin films, indicates the stability of the wurtzite phase under the used irradiation conditions.

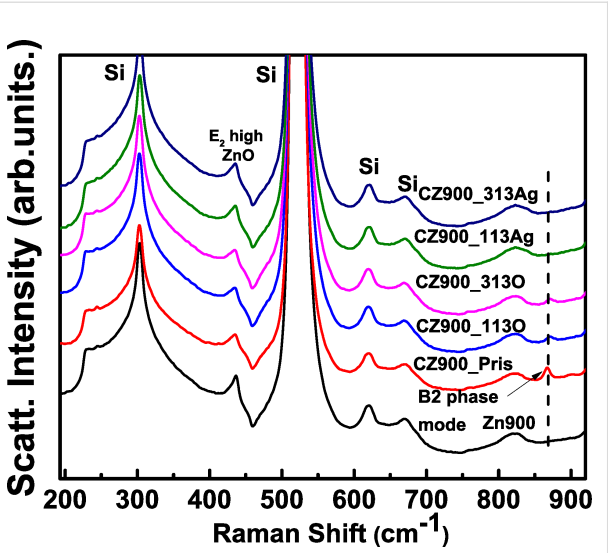

Figure 2: Raman spectra for undoped ZnO (Zn900), CZ900_Pris, CZ900_113O, CZ900_313O, CZ900_113Ag, and CZ900_313Ag thin films.

In Figure 2, the Raman spectra for CZ900_Pris and Z900 thin film are reproduced from our previous publication [1]. The presence of the B2 phase at 868.5 cm^{-1} is indicated by an arrow for the CZ900_Pris sample, which is absent in the Z900 sample. The intensity of this peak diminishes in the CZ900_113O and CZ900_313O samples, while it completely vanishes in the CZ900_113Ag and CZ900_313Ag samples. Thus, the Raman spectroscopic results, in conjunction with the XRD patterns, corroborate the observations regarding the presence of the B2 phase of CdO nanoparticles.

Microscopic modifications observed from SEM micrographs

Figure 3a–c illustrates the SEM micrographs for the CZ900_Pris, CZ900_313O, and CZ900_313Ag thin films, respectively. In the CZ900_Pris sample, an interconnected homogenous distribution of grains is not evident; rather, distinct void regions are observed. Given that CdO has a melting temperature of ≈1000 °C, a portion of CdO may have melted during the annealing process at 900 °C, subsequently condensing in energetically favorable sites at the film surface. The whitish regions in the CZ900_Pris thin film may indicate areas enriched in cadmium. Our earlier investigation into CdO thin film noted similar Cd-rich whitish regions and the formation of nanosheets [18]. In the CZ900_313O thin film, no significant surface alterations were detected. However, the CZ900_313Ag thin film exhibits visible damage on the surface resulting from Ag ion irradiation. The previously distinct void regions are no longer present, suggesting that material may have been sputtered from the film surface due to Ag ion irradiation, poten-

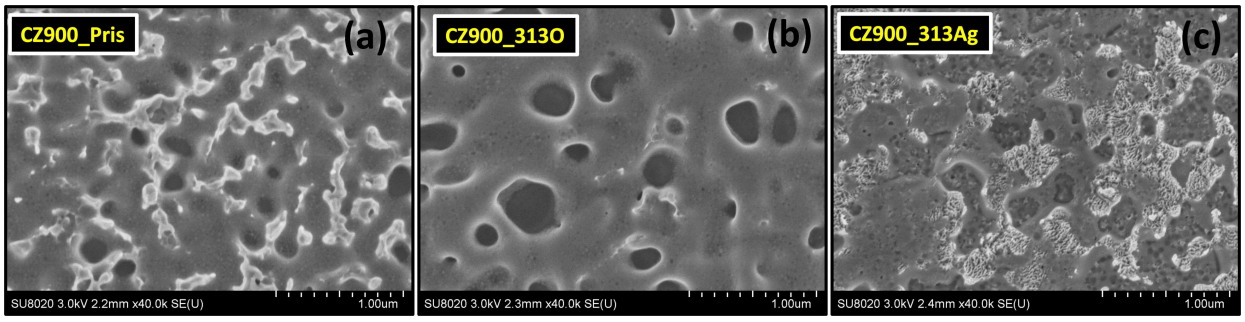

Figure 3: Plane view scanning electron microscopic images for CZ900_Pris (a), CZ900_313O (b), and CZ900_313Ag (c) thin films.

tially leading to the amorphization of the crystallographic B2 phase associated with CdO.

Influence of ion irradiation on electronic structure from XANES spectra

Figure 4a,b presents the XANES spectra at the O *K* and Zn $L_{3,2}$ edges for the CZ900_Pris, CZ900_313O, and CZ900_313Ag thin films. The spectra for the O *K* and Zn $L_{3,2}$ edge for the CZ900_Pris sample are reproduced from our previous publication [1]. The prominent features a1 and a2 observed at 535 eV and 537 eV, respectively, in the O *K* edge spectrum of the CZ900_Pris sample correspond to electronic transitions from O 1s to hybridized Zn 4s and O 2p orbitals. In the CZ900_313O thin film, there is a significant reduction in the intensity of the O *K* edge spectrum. This attenuation suggests that O ion irradiation diminishes the likelihood of core-level electronic transitions from O 1s to the hybridized Zn 4s–O 2p orbitals. It is plausible that O ion irradiation generates oxygen vacancies (V_O) at lattice sites and introduces defects such as interstitial oxygen (O_i). The formation of V_O may hinder the hybridization between Zn 4s–O 2p orbitals, further decreasing the probability of electronic transitions, which is reflected in the diminished a1 and a2 features. In contrast, the spectral characteristics of the CZ900_313Ag sample exhibit a complete transformation compared to those of the CZ900_Pris sample. The introduction of a substantial number of defects may have relaxed the dipole selection rule, resulting in a destructive interference pattern within the multiple scattering signal. Such out-of-phase oscillations can lead to flat pre- and post-absorption edge features, lacking the typical wavy nature. However, direct evidence for the degradation of the Zn_2SiO_4 phase cannot be conclusively determined from the O *K* edge spectrum; this information is more clearly discernible from the Zn $L_{3,2}$ edge, as illustrated in Figure 4b.

The main absorption edge in the Zn $L_{3,2}$ edge begins at 1023 eV, and is associated with electronic transitions from the Zn 2p level to unoccupied Zn 4s states. Additionally, transitions from the Zn $2p_{1/2} \rightarrow 3d$ antibonding orbitals significantly contribute to the formation of this main absorption edge. The

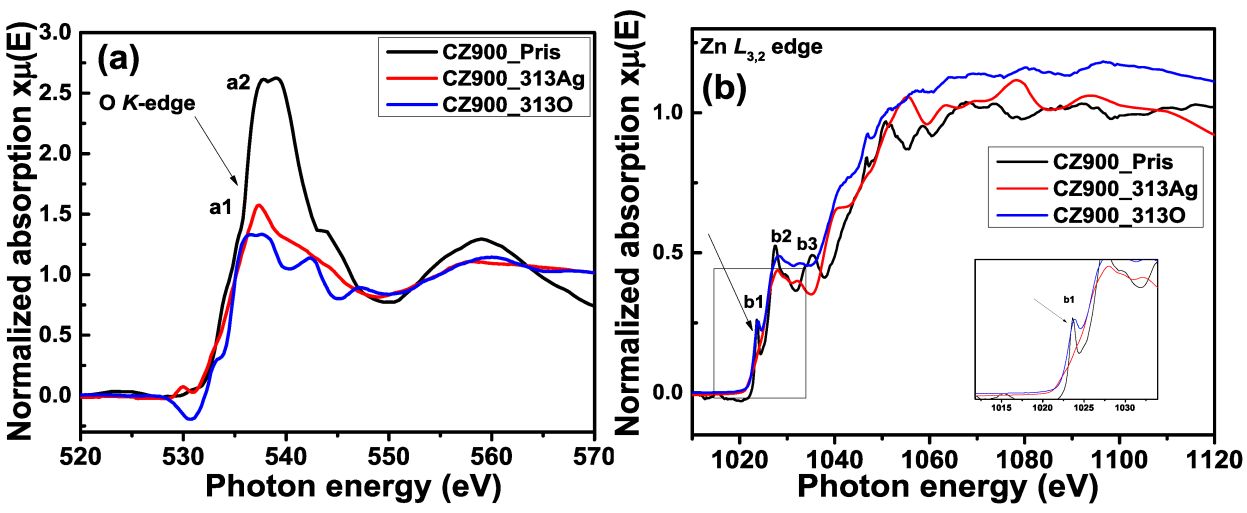

Figure 4: O *K* (a) and Zn $L_{3,2}$ (b) XANES spectra for CZ900_Pris, CZ900_313O, and Z900_313Ag thin films.

spike-like feature designated as B1 arises from the formation of the willemite Zn_2SiO_4 phase [1]. Notable differences are observed in the b2 and b3 features of the CZ900_313Ag sample compared to the CZ900_Pris sample. Specifically, the B1 feature is absent in the CZ900_313Ag sample, providing clear evidence of the amorphization of the Zn_2SiO_4 phase due to Ag ion irradiation. In contrast, in CZ900_313O, the thin film exhibits a broader B1 feature with a larger full width at half maximum (FWHM) and reduced sharpness, although it does not completely disappear as seen in the CZ900_313Ag thin film. This observation further supports the presence of the Zn_2SiO_4 phase in the CZ900_313O thin film, which has not been detected in the XRD pattern due to limitations in detection sensitivity. Thus, X-ray absorption spectroscopy (XAS) has effectively addressed this limitation, providing evidence for the existence of the Zn_2SiO_4 phase. Furthermore, the presence of the Zn_2SiO_4 phase in the CZ900_313O thin film suggests local pressure conditions that may contribute to the formation of the B2 phase in CdO nanoparticles. Consequently, both XRD and XANES analyses yield complementary evidence regarding the presence of the B2 phase. In the Zn $L_{3,2}$ edge (inset of Figure 4b), the B1 feature is magnified, clearly illustrating the changes in the B1 feature corresponding to the willemite Zn_2SiO_4 phase across all three thin films.

Influence of irradiation on Zn_2SiO_4 phase from Si 2p XPS spectra

Figure 5a–d illustrates the Cd $3d_{5/2}$, Zn $2p_{3/2}$, O 1s, and Si $2p_{3/2}$ peaks in XPS spectra for both pristine and irradiated thin films. The calibration of all peaks was conducted using the C 1s peak, situated at 284.6 eV. The peak deconvolution was performed using Gaussian (70%) and Lorentzian (30%) (GL) functions within the CASA software, with Shirley background removal applied during the fitting process. The Cd $3d_{5/2}$ peak in Figure 5a appears at 404.5 eV for CZ900_Pris, CZ900_313O, and CZ900_313Ag thin films, indicative of Cd–O bonding

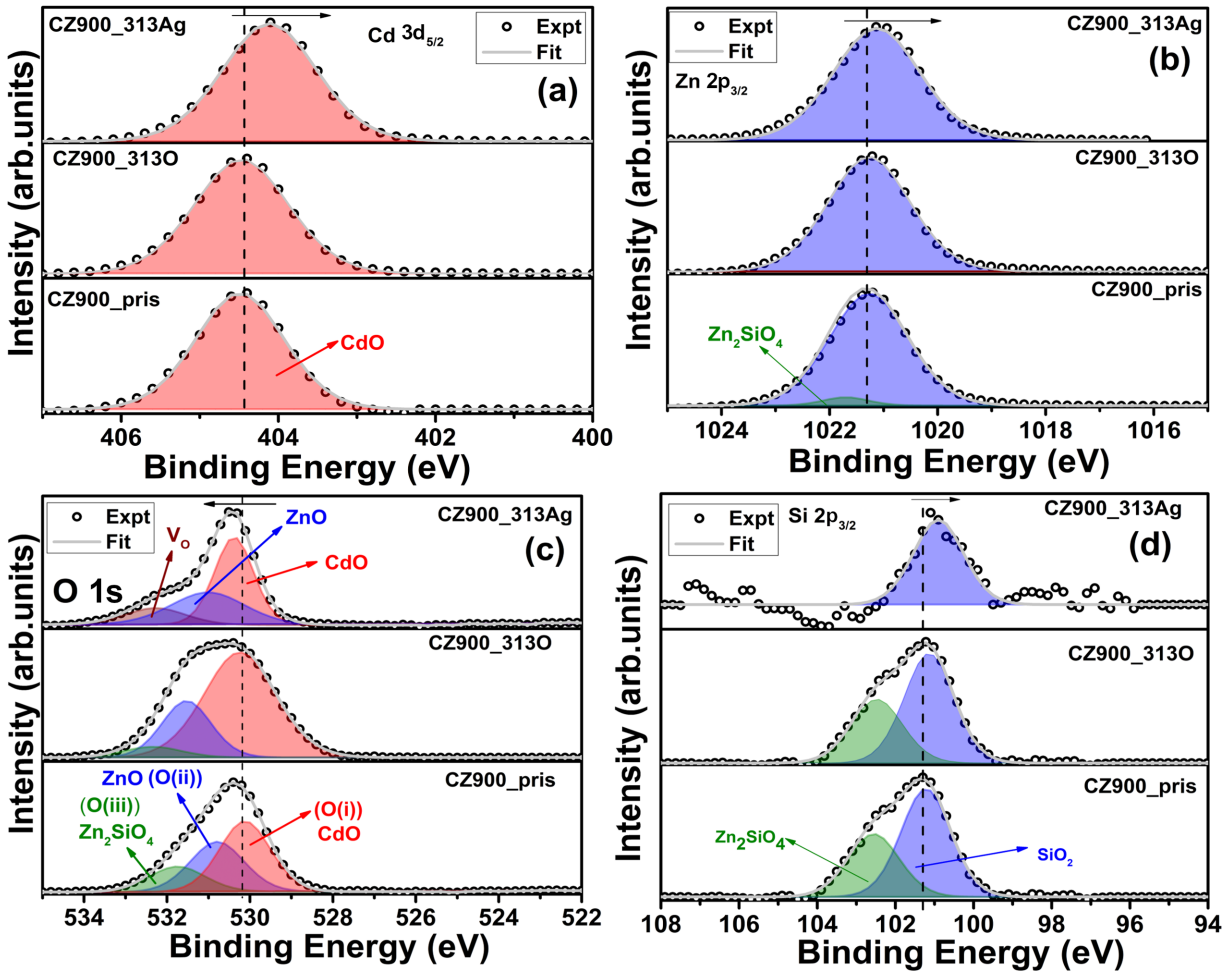

Figure 5: X-ray photoelectron spectra for Cd $3d_{5/2}$ (a), Zn $2p_{3/2}$ (b), O 1s (c), and Si $2p_{3/2}$ (d) edges for CZ900_Pris, CZ900_313O, and CZ900_313Ag thin films.

[18,19]. Notably, the Cd $3d_{5/2}$ peak position for the CZ900_313Ag thin film has shifted toward lower binding energy. This shift can be attributed to the formation of V_O defects, resulting in reduced oxidation of the Cd atom, as reflected in the observed binding energy change. Figure 5b presents Zn $2p_{3/2}$ peaks for the three thin films. The Zn $2p_{3/2}$ peak is located at 1021.2 eV, corresponding to Zn–O bonds. Additionally, a low-intensity peak at 1021.7 eV in the CZ900_Pris thin film is associated with the willemite Zn_2SiO_4 phase. This peak is absent in the CZ900_313O and CZ900_313Ag thin films, likely due to lattice damage induced by Ag and O ion irradiation at the film surface. Furthermore, the Zn $2p_{3/2}$ peak in the CZ900_313Ag thin film exhibits a shift toward lower binding energy, consistent with the formation of V_O defects. The presence of the Zn_2SiO_4 phase is further supported by the O 1s and Si $2p_{3/2}$ peaks, as shown in Figure 5c,d, respectively. The O 1s peak for the CZ900_Pris thin film is deconvoluted into three components: O(i), O(ii), and O(iii), corresponding to the CdO, ZnO, and Zn_2SiO_4 phases, located at 530.0, 530.8, and 531.7 eV, respectively. In the CZ900_313O thin film, the peak area for the O(iii) component has diminished, indicating that the electronic energy loss from O ion irradiation affects the Zn_2SiO_4 phase. However, it is important to note that the peak cannot be solely attributed to the Zn_2SiO_4 phase, as the presence of defects such as V_O is also possible. The small shift in binding energy for V_O defects and Zn_2SiO_4 phases makes it difficult to distinguish them. For the CZ900_Pris thin film, the O(iii) component can be confidently assigned to the Zn_2SiO_4 phase, given that this film was annealed in a flowing oxygen atmosphere, which minimizes the potential for V_O defects at the surface. In contrast, the area corresponding to the V_O peak has increased in the CZ900_313Ag thin film. The generation of V_O in semiconducting oxides due to energetic ion irradiation is well-documented, as the formation energy for V_O is lower than that for defects such as cation interstitials [7]. The peak at 532.2 eV is thus solely attributed to V_O, with no contribution from the Zn_2SiO_4, as indicated by the single peak fitting of the Si $2p_{3/2}$ peak in Figure 5d. The presence of the Zn_2SiO_4 phase is evident in the Si $2p_{3/2}$ peak for CZ900_Pris and CZ900_313O thin films. Therefore, the data from the O 1s and Si $2p_{3/2}$ peaks indicate that the Zn_2SiO_4 phase is not significantly affected by O ion irradiation. In contrast, Ag ion irradiation results in complete amorphization of the Zn_2SiO_4 phase at the film surface. The XPS spectra for the CZ900_Pris sample are reproduced from previous research [1].

Track diameter calculation from inelastic thermal spike model

The phenomena of "Coulomb explosion" and "Thermal spike" represent two established models used to explain the high electronic-energy-loss-induced latent track and the subsequent amorphization effects resulting from SHI irradiation. In the first model, the formation of an ion track is attributed to the electrostatic repulsion among charged ions, which exceeds the chemical bond energy of the host lattice, ultimately leading to amorphization. The second model incorporates the concept of radial energy distribution to account for track formation. Within the framework of the inelastic thermal spike model, energy transfer to the electronic system occurs through electron–electron interactions, followed by transference to the lattice atomic system via electron–phonon correlation [20,21]. Along the ion trajectory, a cylindrical region is generated, characterized by temperature exceeding the melting point of the material, which facilitates the amorphization process. The confined of molten material within this narrow cylindrical volume promotes rapid cooling, thereby enhancing the quenching process and resulting in solidification and ion track formation. We have calculated the track diameter for CdO subjected to 120 MeV silver ion irradiation. The subsequent two coupled differential equations describe the energy distribution within the electronic and lattice subsystems, framed within cylindrical geometry, and represent the transient thermal process involved:

$$C_e \frac{\partial T_e}{\partial t} = \nabla\left(K_e \nabla T_e\right) - g\left(T_e - T_a\right) + B\left(r,t\right), \tag{2}$$

$$\rho C\left(T_a\right)\frac{\partial T_a}{\partial t} = \nabla\left(K_a\left(T_a\right)\nabla T\right) + g\left(T_e - T_a\right). \tag{3}$$

Equation 2 corresponds to the energy transfer to the electronic sub-system, and Equation 3 describes the same for the lattice subsystem. Here C_e and $C(T_a)$ are the specific heat; T_e and T_a are the temperatures; K_e, and K_a are the specific heat values of the electronic and atomic subsystem, respectively. g is the electron–phonon coupling constant, and ρ is the specific mass of the lattice. In Equation 2, $B(r,t)$ indicates the energy density provided to the electron subsystem by the SHI [22,23].

The numerical solutions of the coupled differential equation, obtained through simulation codes, yield a graph depicting the temperature of the ion core as a function of time relative to the difference from the ion core, as shown in Figure 6. This analysis focuses on the calculated track diameter for cadmium oxide (CdO) subjected to 120 MeV silver ion irradiation. Figure 6 clearly indicates that the measured track diameter is 8 nm, corresponding to the melting temperature derived from multiple impact processes. Given that CdO has significantly high electrical conductivity (>10^{14} S/cm) and high mobility (>100 cm^2/V/s), the simulation was conducted under the assumption that CdO behaves as a metallic system [2-4].

Furthermore, due to the minimal variation in lattice temperature (≈300 K) and Debye temperature (≈255 K) for CdO, the electron–phonon coupling constant can be expressed using the following equations:

$$g = \frac{\pi^4 \left(k_B n_e v\right)^2}{18 k_e \left(T_e\right)}, \tag{4}$$

where v is the velocity of sound in CdO, n_e is the electron number density, K_e and T_e are the specific heat and temperature of the electronic system, and

$$v = \frac{k_B T_D}{\hbar\left(6\pi^2 n_a\right)^{1/3}}, \tag{5}$$

where T_D is the Debye temperature and n_a is the atomic number density. All the calculated values used in the simulation code are mentioned in Table 2.

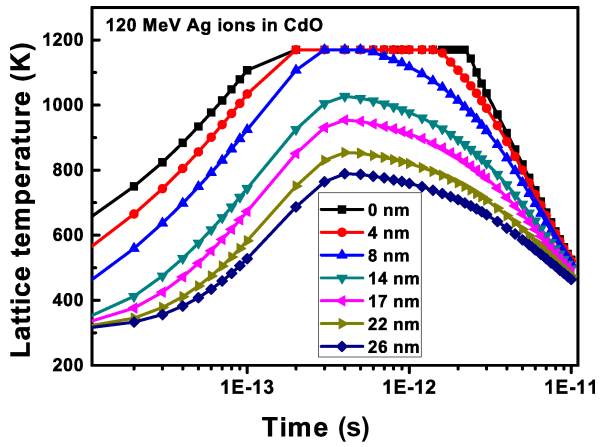

Figure 6: Plot showing lattice temperature as a function of time using thermal spike code to track diameter calculation.

Table 2: The calculated values used in the simulation code.

Bandgap (eV)	2.2
Solid density (g/cc)	8.15
Liquid density (g/cc)	6.95
Velocity of sound in CdO (m/sec)	2541.57
Electron–phonon coupling constant (W/cc-K)	1.38×10^{13}
Se (keV/nm), SRIM 2013	25.1
Melting temperature (K)	1170
Lattice heat of fusion (Joule/g)	1896.27

Discussion for retrieval of the B1 phase with O ion irradiation

The thermal annealing at temperatures exceeding 800 °C induces atomic interdiffusion at the interface between the $Cd_xZn_{1-x}O$ (x = 0.4) alloy film and the Si wafer substrate [24]. This process initiates significant diffusion of Si atoms, starting at the film–substrate interface and extending into the thin film layer, leading to the formation of Si–O bonds. At an annealing temperature of 900 °C, Si diffusion intensifies, resulting in an increased thickness of the amorphous silicon oxide layer at the film–substrate interface [24]. The interdiffusion of Si, O, Cd, and Zn atoms near the SiO_x layer (i.e., at the substrate–film interface) facilitates the formation of willemite Zn_2SiO_4 nanoparticles [24]. Previous investigations have elucidated that the out-diffusion of Zn_2SiO_4 nanoparticles from the film–substrate interface to the surface occurs with a larger unit cell volume (1569.22 Å^3) compared to CdO (105.29 Å^3) and ZnO (47.40 Å^3) generating localized pressure [1]. This localized pressure triggers the phase transition from B1 to B2 in CdO nanoparticles. Notably, 80 MeV oxygen ion irradiation results in the reappearance of the B1 phase, while 120 MeV silver ion irradiation completely amorphizes the B2 phase due to a higher S_e (25.1 keV/nm). In contrast, the S_e value for 120 MeV silver ions in ZnO is 1.62 keV/nm, indicating minimal impact on the wurtzite ZnO phase under silver ion irradiation. For Zn_2SiO_4, the S_e values for 80 MeV oxygen and 120 MeV silver ions are 8.2 keV/nm and 11.2 keV/nm, respectively, while the S_e value for 80 MeV oxygen ions in CdO is 1.9 keV/nm. All the energy loss values were calculated using the SRIM 2013 code. Consequently, the influence of oxygen ion irradiation is more pronounced in Zn_2SiO_4 than in CdO. This is attributable to the higher S_e value, which inflicts greater damage on the Zn_2SiO_4 lattice at the surface. The observed decrease in the intensity of the B2 phase peak and the reappearance of the B1 phase peak in the XRD patterns for the CZ900_113O and CZ900_313O films, as shown in Figure 1b, aligns with similar findings in Zn_2SiO_4. This phenomenon is attributed to a decrease in the local pressure exerted by Zn_2SiO_4 nanoparticles on CdO nanoparticles following oxygen ion irradiation at increasing ion fluences (3×10^{13} ions/cm^2). The Zn $L_{3,2}$ edge spectrum for CZ900_313O thin film in Figure 4b and the Si $2p_{3/2}$ peak in the XPS spectra in Figure 5d further corroborate this observation, indicating the presence of the Zn_2SiO_4 phase in oxygen-ion-irradiated thin films, while this phase is absent in those subjected to silver ion irradiation. The presence of the Zn_2SiO_4 nanoparticles in the oxygen-ion-irradiated films reaffirms the localized pressure exerted by these nanoparticles on CdO nanoparticles, causing the phase transition from B1 to B2. In the cases of the CZ900_113Ag and CZ900_313Ag thin films, both the willemite Zn_2SiO_4 nanoparticles and the B2 phase of CdO nanoparticles are entirely amorphized, leaving no possibility for

the recovery of the B1 phase in these films. Thus, the primary reason for the reappearance of the B1 phase is the reduction of localized pressure exerted by Zn_2SiO_4 nanoparticles due to oxygen ion irradiation. This phase transition from B1 to B2 is reported to be irreversible under hydrostatic pressure [14] or localized pressure [1]. However, ion irradiation has emerged as an effective method to render this phase transition reversible, allowing for the subsequent recovery of the B1 phase at atmospheric pressure. From a thermodynamic perspective, the enthalpy difference (ΔH) in the phase transition process can be subdivided into two contributions: the pressure (ΔPV) and the change in internal energy (ΔU). The ΔU value is positive and independent of the pressure, serving as a barrier that stabilizes the B1 phase during the transition to the B2 phase. Transition to the B2 occurs when ΔPV surpasses this barrier. The increasing chemical pressure resulting from the diffusion of Zn_2SiO_4 nanoparticles renders ΔPV more negative than positive ΔU, thereby triggering the phase transition [25]. Consequently, for the pristine CZ900 thin film, ΔPV is more negative than positive ΔU. Following oxygen ion irradiation, the reduction of localized pressure on CdO nanoparticles results in ΔPV becoming less negative than positive ΔU, which further promotes the resurgence of the B1 phase.

Conclusion

The presence of the willemite Zn_2SiO_4 phase was identified as a primary factor in generating localized pressure on CdO nanoparticles, facilitating the B1 to the B2 phase transition. This study investigated the irradiation stability of the B2 phase through SHI with 120 MeV silver and 80 MeV oxygen ions, revealing distinct behaviors in response to each ion type. Silver ion irradiation was shown to induce amorphization in the B2 phase, while oxygen ion irradiation led to the notable recovery of the B1 phase. This suggests that the electronic energy loss associated with oxygen ion irradiation partially damages the Zn_2SiO_4 lattice, resulting in the deterioration of local pressure on CdO nanoparticles and promoting the recovery of the B1 phase. The absence of the spike-like pre-edge feature in the Zn $L_{3,2}$ edge with silver ion irradiation indicates the complete amorphization of the Zn_2SiO_4 phase. However, the intensity of this feature remains relatively unchanged with oxygen ion irradiation. The fitting analysis of the Si 2p XPS peak, showing the absence of the component related to Zn_2SiO_4 after Ag ion irradiation, further supports these findings. The correlation between core-level spectroscopic techniques and X-ray diffraction patterns reinforces the conclusion that electronic energy loss from oxygen ions leads to partial degradation of the Zn_2SiO_4 crystalline structure, diminishing local pressure on the CdO nanoparticles with the B2 phase and facilitating the retrieval of the B1 phase. Furthermore, the calculated track diameter for 120 MeV silver ions within the CdO rock salt phase was determined to be 8 nm. Collectively, these findings enrich the understanding of the B1 to B2 phase transition phenomenon and substantiate the hypothesis regarding local pressure-induced phase transitions mediated by the willemite Zn_2SiO_4 phase.

Acknowledgements

One of the authors, A. Das, acknowledges Prof. M. Toulemonde for providing the simulation code to perform thermal spike calculation. The authors acknowledge Dr. A. Kaur and Dr. K. Asokan for their support during the irradiation experiment. A. Das acknowledges Dr. Xavier Noirfalise for his support during XPS measurements and Dr. Damien Cossement for his support during Raman spectroscopic measurements. C.B. is a Research Associate of the FRS-FNRS, Belgium. This publication was partly developed under the provision of the Polish Ministry and Higher Education project “Support for research and development with the use of research infrastructure of the National Synchrotron Radiation Centre SOLARIS" under contract No. 1/SOL/2021/2. We acknowledge the SOLARIS Centre for providing access to the PIRX Beamline.

Funding

A. Das acknowledges a Wallonie Bruxelles International's postdoctoral scholarship. There is no separate grant/funding received for conducting this research work.

Conflict of Interest

The Authors declare no conflict of interest.

Author Contributions

Arkaprava Das: conceptualization; data curation; formal analysis; funding acquisition; investigation; methodology; project administration; software; validation; visualization; writing – original draft; writing – review & editing. Marcin Zając: investigation. Carla Bittencourt: funding acquisition; resources; supervision; validation; writing – review & editing.

ORCID® iDs

Arkaprava Das - https://orcid.org/0000-0002-2624-1676
Marcin Zając - https://orcid.org/0000-0001-6980-5315
Carla Bittencourt - https://orcid.org/0000-0002-3330-6693

Data Availability Statement

All data that supports the findings of this study is available in the published article and/or the supporting information of this article.

References

1. Das, A.; Latouche, C.; Jobic, S.; Gautron, E.; Merabet, A.; Zajac, M.; Shibui, A.; Krüger, P.; Huang, W.-H.; Chen, C.-L.; Kandasami, A.; Bittencourt, C. *Acta Mater.* **2024,** *267,* 119744. doi:10.1016/j.actamat.2024.119744

2. Yu, K. M.; Mayer, M. A.; Speaks, D. T.; He, H.; Zhao, R.; Hsu, L.; Mao, S. S.; Haller, E. E.; Walukiewicz, W. *J. Appl. Phys.* **2012,** *111,* 123505. doi:10.1063/1.4729563
3. Yang, Y.; Jin, S.; Medvedeva, J. E.; Ireland, J. R.; Metz, A. W.; Ni, J.; Hersam, M. C.; Freeman, A. J.; Marks, T. J. *J. Am. Chem. Soc.* **2005,** *127,* 8796–8804. doi:10.1021/ja051272a
4. Yan, M.; Lane, M.; Kannewurf, C. R.; Chang, R. P. H. *Appl. Phys. Lett.* **2001,** *78,* 2342–2344. doi:10.1063/1.1365410
5. Schleife, A.; Rödl, C.; Furthmüller, J.; Bechstedt, F. *New J. Phys.* **2011,** *13,* 085012. doi:10.1088/1367-2630/13/8/085012
6. Bharath, S. P.; Bangera, K. V.; Shivakumar, G. K. *J. Alloys Compd.* **2017,** *720,* 39–46. doi:10.1016/j.jallcom.2017.05.240
7. Das, A.; Singh, F. *Vacuum* **2017,** *146,* 287–296. doi:10.1016/j.vacuum.2017.10.007
8. Lian, J.; Wang, L. M.; Wang, S. X.; Chen, J.; Boatner, L. A.; Ewing, R. C. *Phys. Rev. Lett.* **2001,** *87,* 145901. doi:10.1103/physrevlett.87.145901
9. Wang, L.; Gong, W.; Wang, S.; Ewing, R. C. *J. Am. Ceram. Soc.* **1999,** *82,* 3321–3329. doi:10.1111/j.1151-2916.1999.tb02246.x
10. Barbu, A.; Dunlop, A.; Lesueur, D.; Averback, R. S. *Europhys. Lett.* **1991,** *15,* 37–42. doi:10.1209/0295-5075/15/1/007
11. Liu, L.; Huang, Y.; Li, Y.; Fang, L.; Dammak, H.; Fan, H.; Thi, M. P. *Mater. Lett.* **2012,** *68,* 300–302. doi:10.1016/j.matlet.2011.10.103
12. Szenes, G. *Phys. Rev. B* **1995,** *51,* 8026–8029. doi:10.1103/physrevb.51.8026
13. Audouard, A.; Balanzat, E.; Bouffard, S.; Jousset, J. C.; Chamberod, A.; Dunlop, A.; Lesueur, D.; Fuchs, G.; Spohr, R.; Vetter, J.; Thomé, L. *Phys. Rev. Lett.* **1990,** *65,* 875–878. doi:10.1103/physrevlett.65.875
14. Liu, H.; Mao, H.-k.; Somayazulu, M.; Ding, Y.; Meng, Y.; Häusermann, D. *Phys. Rev. B* **2004,** *70,* 094114. doi:10.1103/physrevb.70.094114
15. Zając, M.; Giela, T.; Freindl, K.; Kollbek, K.; Korecki, J.; Madej, E.; Pitala, K.; Kozioł-Rachwał, A.; Sikora, M.; Spiridis, N.; Stępień, J.; Szkudlarek, A.; Ślęzak, M.; Ślęzak, T.; Wilgocka-Ślęzak, D. *Nucl. Instrum. Methods Phys. Res., Sect. B* **2021,** *492,* 43–48. doi:10.1016/j.nimb.2020.12.024
16. Szlachetko, J.; Szade, J.; Beyer, E.; Błachucki, W.; Ciochoń, P.; Dumas, P.; Freindl, K.; Gazdowicz, G.; Glatt, S.; Guła, K.; Hormes, J.; Indyka, P.; Klonecka, A.; Kołodziej, J.; Kołodziej, T.; Korecki, J.; Korecki, P.; Kosiorowski, F.; Kosowska, K.; Kowalski, G.; Kozak, M.; Kozioł, P.; Kwiatek, W. M.; Liberda, D.; Lichtenberg, H.; Madej, E.; Mandziak, A.; Marendziak, A.; Matlak, K.; Maximenko, A.; Nita, P.; Olszowska, N.; Panaś, R.; Partyka-Jankowska, E.; Piszak, M.; Prange, A.; Rawski, M.; Roman, M.; Rosmus, M.; Sikora, M.; Sławek, J.; Sobol, T.; Sowa, K.; Spiridis, N.; Stępień, J.; Szczepanik, M.; Ślęzak, M.; Ślęzak, T.; Tyliszczak, T.; Ważny, G.; Wiechecki, J.; Wilgocka-Ślęzak, D.; Wolanin, B.; Wróbel, P.; Wróbel, T.; Zając, M.; Wawrzyniak, A.; Stankiewicz, M. *Eur. Phys. J. Plus* **2023,** *138,* 1. doi:10.1140/epjp/s13360-022-03592-9
17. Gayen, R. N.; Sarkar, K.; Hussain, S.; Bhar, R.; Pal, A. K. *Indian J. Pure Appl. Phys.* **2011,** *49,* 470–477.
18. Das, A.; Saini, C. P.; Singh, D.; Ahuja, R.; Kaur, A.; Aliukov, S.; Shukla, D.; Singh, F. *Nanoscale* **2019,** *11,* 14802–14819. doi:10.1039/c9nr01832h
19. Das, A.; Singh, D.; Saini, C. P.; Ahuja, R.; Kaur, A.; Aliukov, S. *Nanoscale* **2020,** *12,* 669–686. doi:10.1039/c9nr05184h
20. Valdez, J. A.; Chi, Z.; Sickafus, K. E. *J. Nucl. Mater.* **2008,** *381,* 259–266. doi:10.1016/j.jnucmat.2008.07.045
21. Benyagoub, A. *Nucl. Instrum. Methods Phys. Res., Sect. B* **2010,** *268,* 2968–2971. doi:10.1016/j.nimb.2010.05.019
22. Wang, Z. G.; Dufour, C.; Paumier, E.; Toulemonde, M. *J. Phys.: Condens. Matter* **1995,** *7,* 2525–2526. doi:10.1088/0953-8984/7/12/015
23. Toulemonde, M.; Dufour, C.; Wang, Z.; Paumier, E. *Nucl. Instrum. Methods Phys. Res., Sect. B* **1996,** *112,* 26–29. doi:10.1016/0168-583x(95)01129-3
24. Yuk, J. M.; Lee, J. Y.; Jung, J. H.; Lee, D. U.; Kim, T. W.; Son, D. I.; Choi, W. K. *J. Appl. Phys.* **2008,** *103,* 083520. doi:10.1063/1.2902477
25. Chen, Y.; Zhang, S.; Gao, W.; Ke, F.; Yan, J.; Saha, B.; Ko, C.; Suh, J.; Chen, B.; Ager, J. W., III; Walukiewicz, W.; Jeanloz, R.; Wu, J. *Appl. Phys. Lett.* **2016,** *108,* 152105. doi:10.1063/1.4947022

License and Terms

BEILSTEIN JOURNAL OF NANOTECHNOLOGY

Nanostructured materials characterized by scanning photoelectron spectromicroscopy

Matteo Amati[1], Alexey S. Shkvarin[‡2], Alexander I. Merentsov[2], Alexander N. Titov[2], María Taeño[‡3,4], David Maestre[3], Sarah R. McKibbin[‡5], Zygmunt Milosz[1], Ana Cremades[3], Rainer Timm[5] and Luca Gregoratti[*1]

Review

Open Access

Address:
[1]Elettra – Sincrotrone Trieste S.C.p.A., SS14-Km163.5 in Area Science Park, 34149 Trieste, Italy, [2]M.N. Miheev Institute of Metal Physics of Ural Branch of Russian Academy of Sciences, 620990, Ekaterinburg, Russia, [3]Department of Materials Physics, Universidad Complutense de Madrid, Plaza Ciencias 1, 28040 Madrid, Spain, [4]Center for Cooperative Research on Alternative Energies (CIC energiGUNE), Basque Research and Technology Alliance (BRTA), Alava Technology Park, Albert Einstein 48, 01510 Vitoria-Gasteiz, Spain and [5]Department of Physics, Lund University, 221 00 Lund, Sweden

Email:
Luca Gregoratti[*] - luca.gregoratti@elettra.eu

* Corresponding author ‡ Equal contributors

Keywords:
nanostructured materials; operando; oxides; scanning photoelectron spectromicroscopy; semiconductor nanowires; transition metal dichalcogenides; XPS

Beilstein J. Nanotechnol. **2025,** *16,* 700–710.
https://doi.org/10.3762/bjnano.16.54

Received: 19 December 2024
Accepted: 25 April 2025
Published: 23 May 2025

This article is part of the thematic issue "Exploring synchrotron radiation and free-electron laser tools for nanostructured materials".

Guest Editor: C. Bittencourt

Abstract

Nanostructured materials play a key role in modern technologies adding new functionalities and improving the performance of current and future applications. Due to their nature resulting in diffused heterogeneous structures (chemical and electronic composition typically organized in phases or building blocks) characterizing these materials needs state of the art technologies which combine nanometer spatial resolution, environmental reliability, and operando capabilities. Scanning photoelectron spectromicroscopy (SPEM) is one of the characterization tools that combine high spectral resolution X-ray photoelectron spectroscopy with submicron spatial resolution. In particular, the SPEM equipment hosted at the ESCA microscopy beamline at Elettra is capable of in situ and operando analysis regardless of sample morphology. The review presents three different case studies illustrating the capabilities of SPEM in the investigation of catalytic materials in different conditions and processes.

Introduction

Nanometer or micrometer-sized materials play a key role in modern technologies in the search of new routes for unforeseen performances generating breakthroughs in societal challenges [1]. When composed of different elements, molecules, or compounds, these materials often show a regular and/or diffused heterogeneous structure based on elementary building blocks

(e.g., crystallites or atomic/molecular groups) forming the entire solid or, in other cases, just their surfaces. The characterization of the building blocks is of paramount importance to deeply understand their functionalities and mutual interactions when they are part of a nanostructured body. The building blocks may differ in their atomic structure, crystallographic orientation, chemical composition, and charge distribution, to list the most important features. If the building blocks are crystallites, any change in the structure or chemical composition may lead to the formation of incoherent or coherent interfaces among them which may influence the final properties of the material. Often the volumes of the materials formed by similar building blocks, then having similar properties, are called phases from which another possible definition of these heterogeneous materials such as multi-phase materials comes [2-4].

Nanostructured materials are the playground for the advancement of some key technologies associated with electronics, energy conversion and storage, and many other fields due to their unique physical properties which may open unforeseen doors for technical and performance advances [5-8]. The full chain of steps necessary for the implementation of nanostructured materials in devices, which include the synthesis, characterization, and processing, are part of an emerging and rapidly growing field referred to as nanotechnology. However, despite the large efforts of the scientific and industrial communities in the development of new nanostructured materials and related technologies, the main obstacle in the application still resides in having a full control of their parameters in the production step. This is important to guarantee the availability of bulk materials with reproducible and fully reliable engineered properties and technological functionalities.

In the last decades, many characterization tools used to investigate chemical, electronic, or structural properties of materials have been developed or upgraded to match the requirements imposed by nanotechnology. Imaging capabilities covering from meso- to atomic scales, spatially resolved spectroscopies with enhanced sensitivities are examples of capabilities that modern techniques of characterization in nanotechnology must possess. X-ray photoelectron spectroscopy (XPS) is still one of the fundamental tools for chemical and electronic characterization of surfaces and subsurface layers. In the last three to four decades, several important upgrades have spread the original ability of XPS of chemical analysis to include, for instance, band mapping through angle resolved measurements (ARPES), spin detection, and imaging or spectromicroscopy at a nanoscale spatial resolution [9,10]. It is worth noting that several improvements have been developed at synchrotron light facilities where unique properties of X-ray radiation can be found. Scanning photoelectron microscopy (SPEM) combines XPS analysis with lateral resolution; chemical imaging as well as XPS spectroscopy at nanoscale sized areas can be performed providing fine chemical and electronic analysis of samples regardless of their morphology, which often limits the capabilities of other microscopy techniques [11]. This work reports three examples of SPEM experiments focused on the characterization of nanostructured materials. Measurements were performed at the SPEM microscope hosted at the ESCA microscopy beamline at the Elettra synchrotron research center. In the first example, chemical heterogeneous layered transition metal dichalcogenides were analyzed, showing the importance of spatial resolution in their characterization. In the second example, an operando chemical and electronic characterization of an InP nanowire heterostructure device under applied bias is reported. In the last example, the results of a SPEM investigation of self-organized NiO microcavity arrays exhibiting dimensions in the micrometric range concludes this overview of nanostructured materials characterized by SPEM.

Results and Discussion

Chemical heterogeneities in layered transition metal dichalcogenides

The heterogeneous chemical composition of the $Cr_xTi_{1-x}Se_2$ system was for the first time observed and described in [12]. The observed heterogeneity led to the splitting of the Se 3d core level lines. One of the components was found to correspond to Se in $TiSe_2$; the second component, which had no known analogues, was attributed to structural fragments of $CrSe_2$. This confirmation was obtained directly by SPEM [13]. In the cleaved surface of the $Cr_{0.78}Ti_{0.36}Se_2$ single crystal, regions displaying differential contrast in the Se 3d line were observed (Figure 1a–c).

In the regions of image a) delineated by the red rectangle, the shape and binding energy of the Se 3d line approximated those observed in $TiSe_2$ (Figure 1b). In the region defined by the blue rectangle, values exhibited correspondence with those observed in $Cr_{0.83}Ti_{0.26}Se_2$, but not with the data for $TiSe_2$. This approach enabled the demonstration that selenium atoms with different chemical bonding characteristics are spatially distinct [12], and form separate structural fragments.

The question thus arises as to why these structural fragments form a single crystal and not independent phases. An analysis of the binding energy of the core levels of Cr 3p, Ti 3p, Ti 2p, and Cr $2p_{3/2}$ (Figure 1d–f) in the different fragments reveals a shift of about 0.5 eV in the binding energy, indicating that the fragments are charged relative to each other. It is evident that this is the mechanism by which the individual fragments are linked into a single crystal.

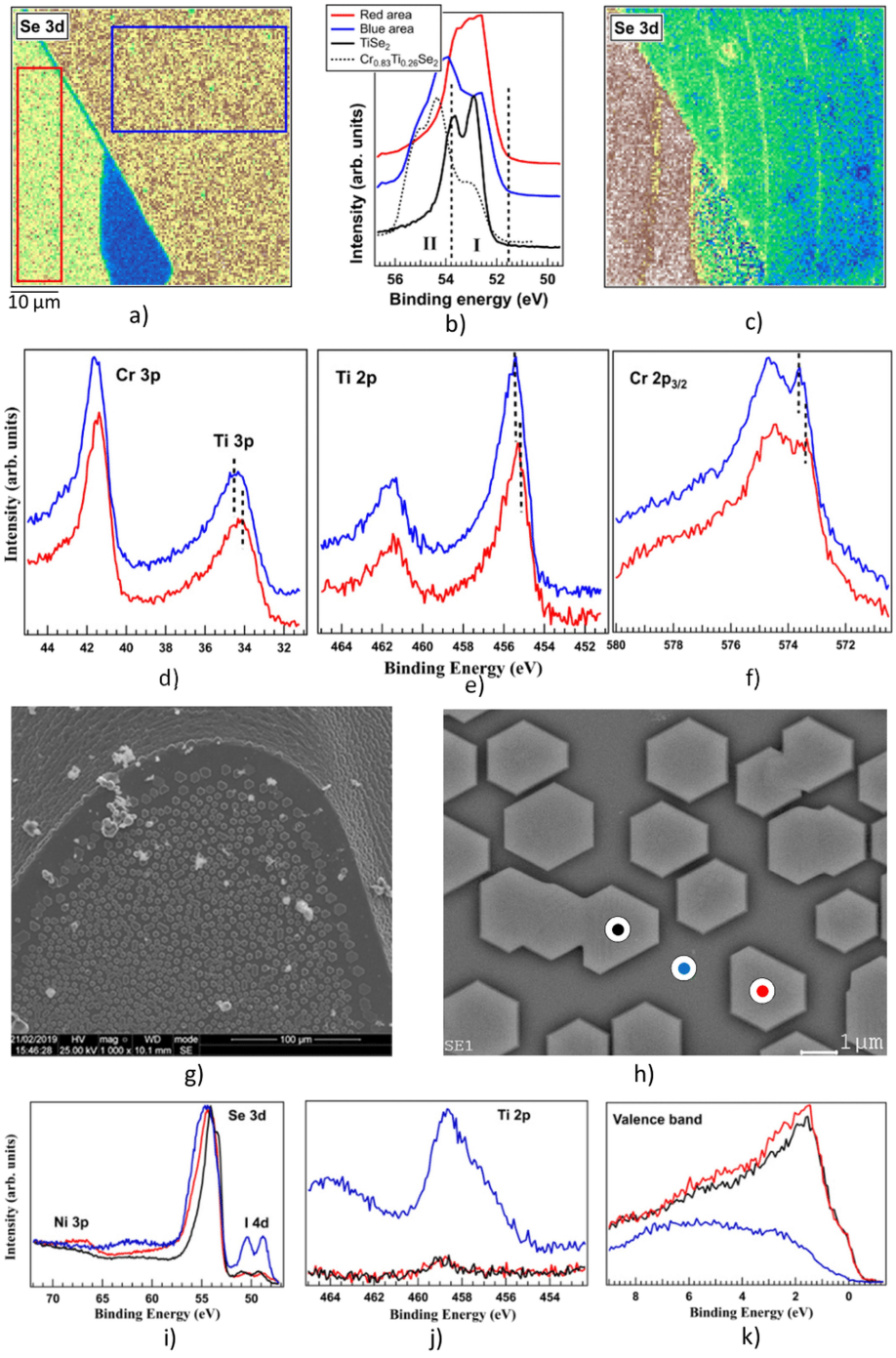

Figure 1: a) SPEM image of the $Cr_{0.78}Ti_{0.36}Se_2$ single crystal obtained at the area corresponding to the Se 3d core-level spectrum (Se 3d contrast). b) Se 3d core level spectra for $Cr_{0.78}Ti_{0.36}Se_2$ collected from areas marked as coloured rectangles in panel a) along with Se 3d spectra for previously investigated $Cr_{0.83}Ti_{0.26}Se_2$ (black dashed line) and $TiSe_2$ (black line) [12]; energy regions I and II correspond to different Se $3d_{5/2}$ states. c) Map in the Se 3d contrast plotted as II/III intensity ratio in each point, where II and III are the intensities of the Se $3d_{5/2}$ peak in the energy regions I and II (panel b)), respectively. Ti 3p and Cr 3p (d), Ti 2p (e) and Cr $2p_{3/2}$ (f) core-level spectra for $Cr_{0.78}Ti_{0.36}Se_2$ collected from the "red" and "blue" regions (panel a)). SEM images (g), h)) of the as-grown $(Fe,Ni)_{0.25}TiSe_2$ single crystal. Se 3d and Ni 3p (i)), Ti 2p (j)) core level and valence band (k)) spectra for $(Fe,Ni)_{0.25}TiSe_2$ in red, blue and black points (panel h)). Figure 1a–f were reprinted from [13], *J. Phys. Chem. Solids*, vol. 160, by A. I. Merentsov; A. S. Shkvarin; M. S. Postnikov; L. Gregoratti; M. Amati; P. Zeller; P. Moras; A. N. Titov, "Studying the heterogeneity of the $Cr_xTi_{1-x}Ch_2$ (Ch = S, Se) single crystals using X-ray scanning photoemission microscopy", article no. 110309, Copyright (2022), with permission from Elsevier. This content is not subject to CC BY 4.0. Figure 1g–k were reprinted from [14], *Materials Science and Engineering: B*, vol. 283, by A. S. Shkvarin; A. I. Merentsov; M. S. Postnikov; E. I. Patrakov; E. Betz-Guttner; L. Gregoratti; M. Amati; P. Zeller; A. N. Titov, "Morphology and composition of nanoinclusions in $(Fe,Ni)_{0.25}TiSe_2$", article no. 115821, Copyright (2022), with permission from Elsevier. This content is not subject to CC BY 4.0.

The SPEM technique is fundamental for the detection of such inhomogeneities, given that the photoelectron yield depth in this instance does not exceed 12 angstroms. This is significantly smaller than the yield depth in a scanning electron microscope (≈4 µm) or transmission electron microscope (≈1000 Å).

Another advantageous aspect of the SPEM is its capacity to achieve high lateral resolution, which enables the investigation of inhomogeneities which are relatively small in lateral dimensions. The $Fe_{0.25}Ni_{0.25}TiSe_2$ system provides an illustrative example of such a system [14]. The single-crystal growth of a mixture of $Fe_{0.25}TiSe_2$ and $Ni_{0.25}TiSe_2$ results in the formation of a $(Fe,Ni)_{0.25}TiSe_2$ single crystal, which is covered with faceted single-crystal inclusions of $(Ni,Fe)_4Se_5$ (Figure 1g,h). The identical orientation of the $(Ni,Fe)_4Se_5$ crystals indicates that they have undergone coherent coupling with the lattice of the main crystal. The SPEM technique enables the determination of both the composition of inclusions and the shape of the valence band (Figure 1i–k).

Operando characterization of InP nanowire p–n junctions

Semiconductor nanowires offer unprecedented possibilities in utilizing, combining, and modifying material properties for application in electronic, photonic, energy harvesting, or quantum information devices [15,16]. Their small footprint allows for the combination of different materials with dislocation-free interfaces and to form axial or radial heterostructures of varying material, doping, or crystal phase [17-19]. Nanowire heterostructures based on III–V semiconductors are especially promising for electronic, optoelectronic, or photovoltaic devices, as they combine a direct bandgap of tunable size with high charge carrier mobility [20]. Furthermore, they can be grown on Si substrates [21,22], which enables integration with a well-established technology platform and constrains the use of high performance, but expensive III–V materials to the active device area. The flexible geometry of nanowires standing upright on their growth substrate directly leads to gate-all-around metal-oxide-semiconductor stacks [23,24], and advanced electronic device designs such as nanowire tunneling field-effect transistors [24] or one-transistor-one-resistor cells with minimal footprint [25] can be realized. Optimizing nanowire diameter and distance further enhances the strong light adsorption of III–V materials, resulting in nanowire-based solar cells of high efficiency [26].

While such nanowire-based devices are highly promising, their performance is often limited by surface properties of the III–V semiconductor material, which furthermore can vary for individual nanowires. This includes native oxides on semiconductor surfaces and their possible removal, surface passivation, and interface defects [27]. Therefore, in-depth surface characterization of individual nanowires is urgently needed. This task is difficult for many conventional surface characterization techniques due to the nanowire geometry, and it becomes even more challenging in the case of nanowire heterostructure devices, where operando characterization of a working nanowire device under applied bias is desired. SPEM is an ideal tool for this task, as it provides topographic, chemical, and electronic information at the submicrometer scale with intrinsic surface sensitivity, even under electrical operando conditions [18]. While already conventional XPS can be used to obtain detailed information about nanowire surface, interface composition, and chemical reactions averaging over thousands or millions of nanowires in ensemble measurements [28], SPEM allows to investigate individual semiconductor nanostructures [29].

We investigated the surface chemical composition and the surface potential across InP nanowire p–n junctions for individual nanowire devices. InP nanowires were grown on InP(111) substrates by vapor–liquid–solid growth using nanoimprint lithography for generating catalytic Au nanoparticles in a metal–organic vapor phase epitaxy (MOVPE) reactor with trimethylindium and phosphine precursors. Axial p–n junctions were created by switching from diethylzinc to hydrogen sulfide as dopant precursors halfway during nanowire growth. More growth details can be found in references [18,30]. After growth, nanowires were mechanically transferred onto suitable substrates for characterization by scanning probe microscopy and SPEM. An atomic force microscopy (AFM) image of a typical InP p–n junction nanowire is shown in Figure 2a, confirming a homogeneous shape with a nanowire length of about 2.5 µm and a diameter of about 200 nm, fluctuating only by a few nanometers along the entire nanowire.

For operando SPEM measurements, nanowires were transferred onto a prepatterned device template with flat, individually contacted Au/Ti electrodes deposited onto a SiO_2/Si substrate, separated by a 1.5 µm wide insulating gap. Optical microscopy images of the samples including marker structures were used to directly navigate to suitable nanowires in the SPEM measurements. Figure 2b shows elemental-sensitive In 4d and P 2p SPEM images, highlighting the nanowire shape and position, which can even be noticed as a shadow in the Au 4f image, where the signal from the electrodes is attenuated. The apparently larger length of the nanowire in the In and P maps as compared to the Au map is due to the finite width of the X-ray beam, and demonstrates the convolution of nanowire shape and beam shape in the resulting image. The binding energies of the In 4d and P 2p maps were centered at 17.5 and 129 eV, respectively, and therewith below and above the binding energy of Au 4f, imaged here at 83.5 eV. This explains why inelastically scat-

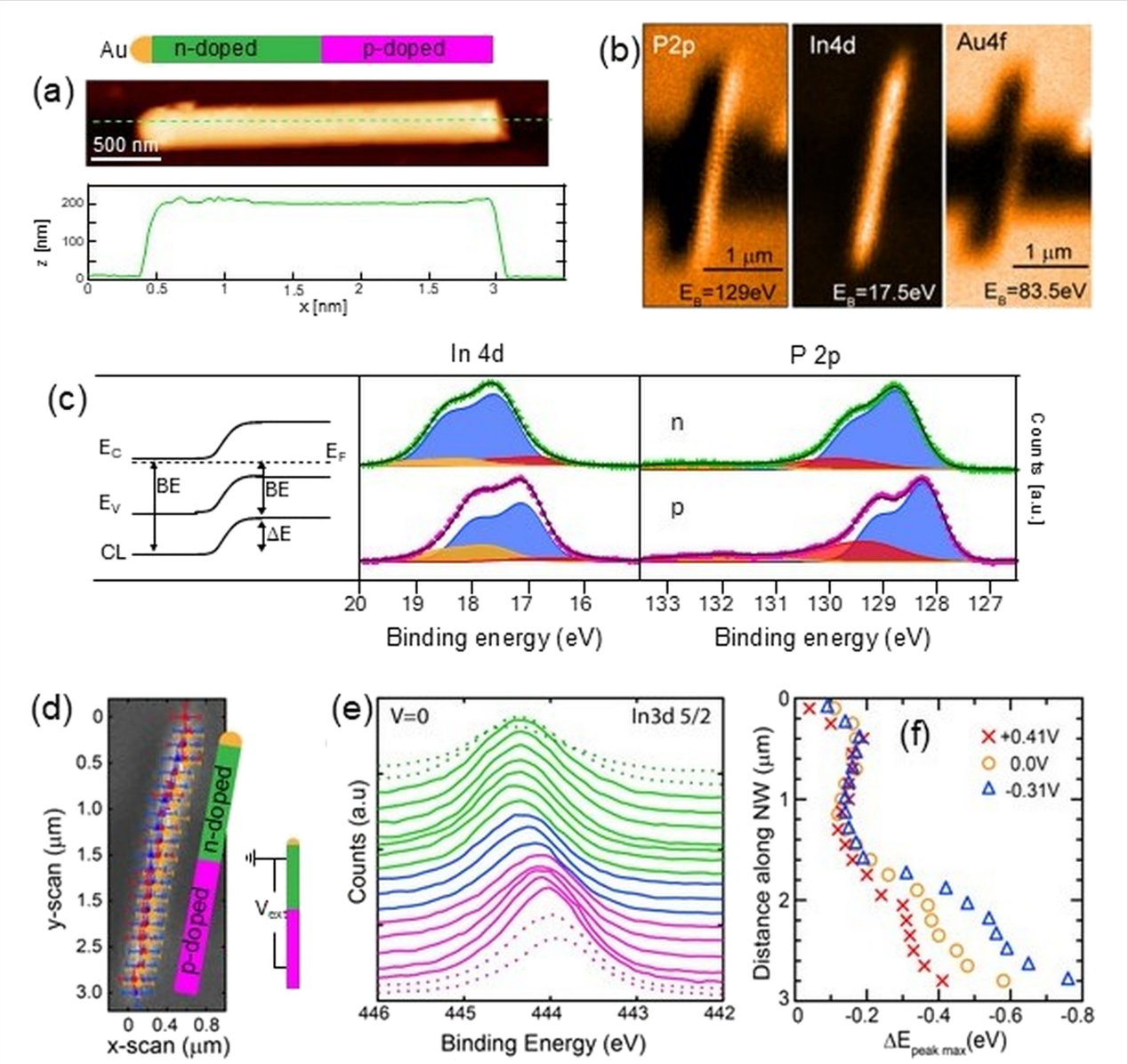

Figure 2: Surface characterization of InP p–n junction nanowires: a) sketched structure (top), AFM image (middle), and resulting height profile (bottom) of a nanowire with its catalytic Au particle at the top. b) SPEM images of a nanowire deposited with both ends on separately contacted Au/Ti electrodes with a trench in between, obtained around binding energies of 129 eV (P 2p, left), 17.5 eV (In 4d, middle), and 83.5 eV (Au 4f, right). c) High-resolution In 4d (middle) and P 2p (right) core-level spectra obtained at n-doped (top) and p-doped (bottom) segments of the nanowire shown in b). The band structure across the p–n junction is indicated (left). d) In 3d SPEM image of the same nanowire, positions of the spectra shown in e,f) are indicated. e) In $3d_{5/2}$ core-level spectra obtained along the nanowire, color-coded for n-doped segment (green), depletion region (blue), and p-doped segment (pink). f) Relative shift of fitted In $3d_{5/2}$ peak positions along the nanowire obtained at forward (red) and backward (blue) bias conditions and without applied bias (yellow), as indicated. Figure 2 was adapted from [18], S. R. McKibbin et al., "Operando Surface Characterization of InP Nanowire p–n Junctions", *Nano Letters*, © 2019 American Chemical Society, distributed under the Standard ACS AuthorChoice/Editors' Choice Usage Agreement, https://pubs.acs.org/page/policy/authorchoice_termsofuse.html. This content is not subject to CC BY 4.0.

tered electrons from the Au electrodes contribute to a strong contrast in the P 2p map but cannot be seen in the In 4d map.

In addition to SPEM images, we also acquired high-resolution XP spectra from specific positions along the nanowire, as shown in Figure 2c for In 4d and P 2p core levels. A significant shift in binding energy is obvious between spectra obtained on the p-doped and on the n-doped segment of the nanowire. Since the local binding energy position of the core level directly follows the energy of the valence and conduction band and thus the band-bending at the interface between the p- and n-doped segments, the observed shift in binding energy directly reflects the in-built potential of the p–n junction at the nanowire surface. The measured binding energy shift amounts to 0.48 eV in

the In 4d spectra and 0.47 eV in the P 2p spectra. Even though this is a significant and well-resolved shift, its value is surprisingly low compared with the InP band gap of 1.34 eV at room temperature. Similarly grown InP p–n junction nanowires have been reported to show an open circuit voltage between 0.6 and 0.9 eV in photovoltaic measurements [31,32]. While those open circuit voltages can be considered as the built-in potential in the nanowire bulk, the values measured by XPS result from the nanowire surface, demonstrating a weaker in-built potential at the surface. This effect can be expected from surface band bending due to defects or native oxides at the surface. This demonstrates the necessity for both bulk- and surface-sensitive measurements in order to fully understand the local potential distribution in such technologically relevant nanostructure devices.

The type and amount of surface oxide and defects can be obtained from XPS peak fitting, as presented in Figure 2c, assuming a Shirley background and Voigt doublet components (more fitting components can be found in [18]). Both the In 4d and P 2p spectra were fitted by a dominating component, attributed to the InP bulk signal, and two smaller doublets each. For P 2p, these smaller components have a 0.95 and a 3.5 eV higher binding energy than that of the bulk component, respectively. According to the literature, the high binding energy component can be attributed to P in a +5 oxidation state, as in $InPO_4$, and the other one as P^0, probably due to metallic P defects at the nanowire surface [18,33,34]. A small oxide component is also found in the In 4d spectra, at a binding energy which is 0.6 eV higher than that of the bulk component. In addition, a small In 4d component with 0.75 lower binding energy as compared to that of the bulk peak is also observed. This component might be due to metallic In or to In alloying with Au, either from the catalytic Au particle at the top of the nanowire, or from the Au electrodes.

After analyzing the chemical composition and electrical potential distribution of the nanowire surface across the p–n junction in the unbiased case, we were ready to proceed to operando measurements during forward and backward applied bias. These can be realized by biasing the two electrodes on which the nanowire is resting with its p- and n-doped ends. In practice, the electrode with the n-doped segment was grounded, while a bias of +0.4, 0, or −0.3 V was applied to the electrode with the p-doped segment, resulting in forward-biased, unbiased, and backward-biased conditions of the p–n junction. High-resolution In 3d core-level spectra were obtained along the nanowire with a step width of about 130 nm, roughly equaling the size of the X-ray beam, as indicated in Figure 2d. The resulting In $3d_{5/2}$ spectra are shown in Figure 2e for the unbiased case, highlighting the p-doped and n-doped nanowire segments with the depletion zone in between, while the energy shift of fitted peak positions along the nanowire is plotted in Figure 2f for both unbiased, forward biased, and backward biased conditions. The energy shift between p- and n-doped segments decreases to about 0.2 eV upon forward bias and increases to about 0.6 eV upon backward bias. While most of the bias drops across the depletion region, as expected for a sharp p–n junction, an additional voltage drop is observed along the p-doped segment.

Our results provide an important step in understanding the electrical behavior of a nanowire p–n junction under device operation with high spatial resolution. We correlate that to the chemical surface composition, distinguishing between surface and bulk effects on the path towards improved surface properties of nanowire solar cells with further enhanced efficiency. Furthermore, they demonstrate the large suitability of SPEM for operando studies of technologically relevant nanoscale heterostructure devices.

Self-organized NiO microcavity arrays fabricated by thermal treatments

In the class of the very few p-type oxides, NiO stands out as one of the most versatile and promising materials in diverse applications including supercapacitors [35,36] fast spintronics [37], electrochromic devices [38,39], catalysts, and gas sensors [40,41], [42,43]. The characteristic p-type conductivity of this transition metal oxide is related to the presence of oxygen interstitials and the inherent nickel deficiency which leads to the formation Ni^{3+} to reach charge neutrality. Additionally, NiO exhibits a wide bandgap, which also prompts considerable research interest. The properties of NiO are highly dependent on the synthesis method, owing to the variable dimensionality, morphology, crystalline orientation, and defect structure [44]. Therefore, it is important to increase research efforts to improve the knowledge and understanding of the properties of this multifaceted material in order to better predict and tailor its role in diverse applications.

XPS has been extensively employed in the study of NiO, leading to relevant insights regarding its electronic structure, where emphasis is common for the study of the Ni 2p signal up to now. However, some discrepancies are still reported on the correct assignment of XPS features [45]. Additionally, less research has been done so far in the analysis of the Ni 3p signal, the study of which can be occasionally necessary in order to avoid overlapping of Ni 2p signal with other XPS contributions in doped NiO or Ni-based compounds.

Taeño et al. [46] recently reported the study of NiO microcrystals with self-organized microcavities synthesized by a vapor–solid process at temperatures ranging from 800 to

1500 °C under a controlled Ar atmosphere. In that study, XPS analysis was performed in combination with complementary microscopy and spectroscopy techniques. The analyzed NiO microstructures exhibit dimensions in the micrometric range, with preferential {100} surface texturing, where self-ordered cavities were formed at temperatures between 1000–1200 °C. The lateral surfaces of those small cavities or pinholes correspond to the {111} family of planes, which tend to be more reactive owing to the higher concentration of Ni^{3+}. Diverse phenomena, including Ni diffusion and inhomogeneous strain, were considered to occur during the growth process, leading to NiO samples with variable properties. Raman spectroscopy indicated changes between the relative intensity of first order modes and the 2M mode due to the variable lattice disorder induced in the samples during the growth process. Cathodoluminescence measurements demonstrated the presence of a visible emission at 2.5 eV associated with Ni deficiency, whose relative intensity varies as a function of the thermal treatment and the consequent structure of defects. The NiO samples showed additional luminescence due to Ni interstitial and d–d transitions. In that work, XPS measurements carried out in the ESCA microscopy beamline at Elettra Synchrotron facilities contributed with significant knowledge to the study of the surface properties of the NiO samples. Particularly, advantage was taken from the SPEM which can work both in spectroscopy and imaging modes. Figure 3 shows Ni 3p, O 1s, and valence band XPS spectra from samples annealed at diverse temperatures, which exhibit variable morphological, crystallographic, and optical properties. Regarding the Ni 3p signal, less-explored so far, four main bands were observed after signal deconvolution (Figure 3a). Bands at lower binding energy, 68.6 and 70.1 eV, were related to Ni^{2+} in the NiO lattice, while doublet at 72.0 and 74.9 eV was associated with Ni^{3+}. An increase in the Ni^{3+}/Ni^{2+} ratio was observed for the samples treated at higher temperature. The O 1s core levels from all the probed samples were dominated by a band at 531.5 eV related to O^{2-} in NiO, while a lower intensity band was observed at 533.2 eV associated with adsorbed oxygen species (Figure 3b). Preferential oxygen absorption is expected for {111} surfaces which were observed in the cavities formed at the surface of some samples. Regarding the

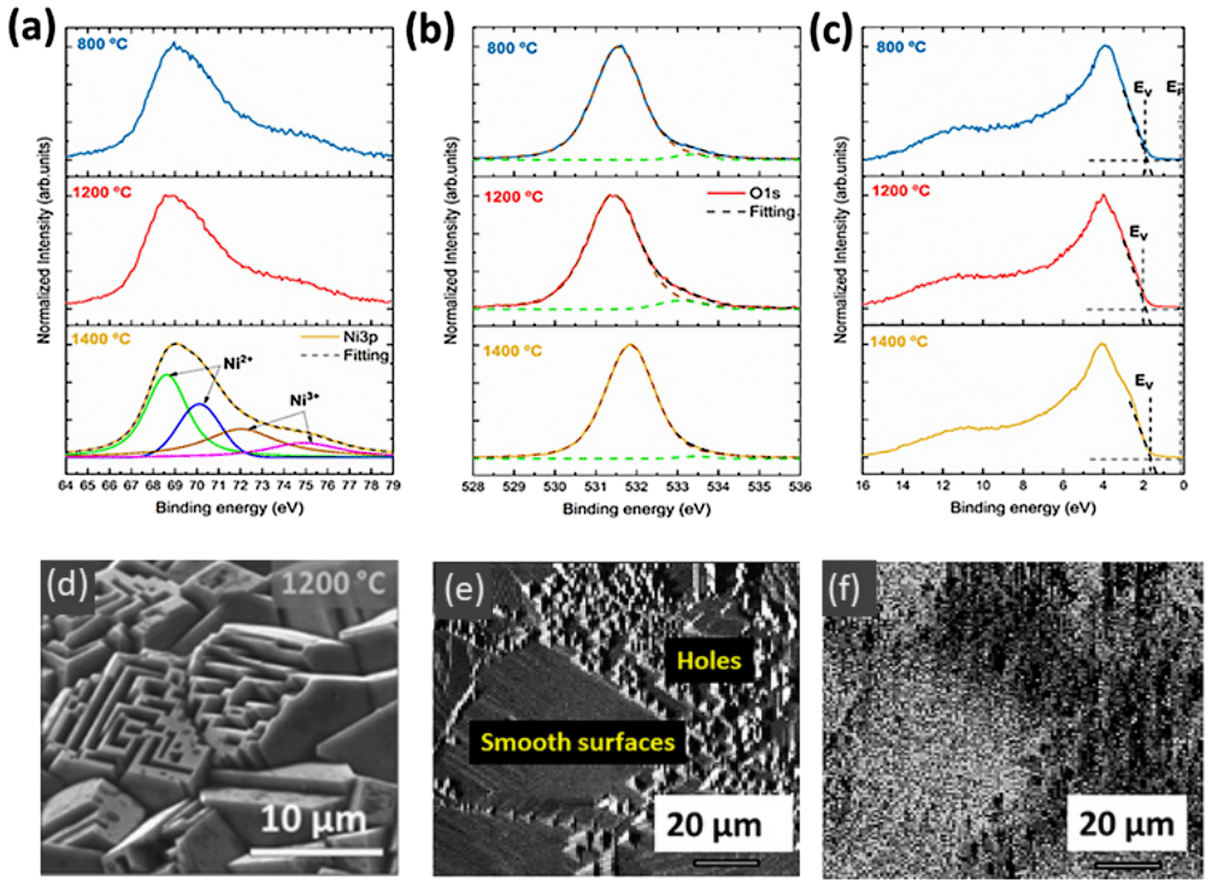

Figure 3: XPS spectra from a) Ni 3p, b) O 1s core levels, and c) valence band region from NiO samples sintered at 800, 1200, and 1400 °C. d) SEM image and e) XPS image acquired with the Ni 3p signal, from the sample treated at 1200 °C. f) XPS energy filtered image from e) corresponding to the Ni^{2+}/Ni^{3+} ratio. Adapted with permission from *Cryst. Growth Des.* 2020, 20, 4082–4091. Copyright 2020 American Chemical Society. Figure 3 was reprinted with permission from [46], Copyright 2020 American Chemical Society. This content is not subject to CC BY 4.0.

valence band photoelectron spectra, mainly formed by O 2p and Ni 3d contributions, a higher p-type character was observed for the samples annealed at 1400 °C, based on the position of the Fermi level relative to the VB maximum (Figure 3c). Special attention was paid to the study of the sample grown at 1200 °C with a high concentration of cavities (Figure 3d). XPS image acquired with the Ni 3p signal (Figure 3e) and the corresponding energy-filtered image (Figure 3f) indicated variable Ni^{3+}/Ni^{2+} ratio at the surface of the probed sample, where either flat regions or areas with cavities were formed. In particular, a higher concentration of Ni^{3+} observed in the regions with surface cavities is also associated to a lower presence of absorbed oxygen. This can be correlated with surface defects responsible for the increase in the relative intensity of the near-infrared emission observed in the corresponding CL spectrum.

XPS measurements provide valuable information on the electronic structure and properties of the NiO samples, which strongly support the development of potential applications including gas sensors and optical resonators [43,47].

Conclusion

SPEM is a synchrotron-based technique combining XPS, submicron spatial resolution, and chemical imaging capabilities. The instrument hosted at the Elettra synchrotron research center, in operation since 1993, has been recently upgraded to fulfil the increasingly demanding needs of in situ and operando experiments. The examples of materials characterization shown in the review demonstrate its usefulness in the investigation on nanostructured materials regardless of their morphology. This feature is of particular interest when device prototypes, such as sensors and batteries, must be analyzed in real conditions. The combination of imaging and spectroscopy can provide an elemental, chemical, and electronic mapping of sample surfaces in the pristine form or after/during their response to external stimuli such as temperature changes, electric and magnetic fields, and light and gas exposure.

In the first example chemical heterogeneous layered transition metal dichalcogenides were analyzed showing the importance of spatial resolution in their characterization. In the second example, the electronic behavior of InP nanowire p–n junctions heterostructures has been investigated under applied bias correlating it to the chemical surface composition and surface/bulk effects. In the last example, the results of a SPEM investigation of self-organized NiO microcavity arrays exhibiting dimensions in the micrometric range concludes this overview of nanostructured materials characterized by SPEM.

After describing the current state of the art of SPEM capabilities in the characterization of nanostructured materials, it is worth spending a few sentences about the future of this technique in the light of the very fast evolution of synchrotron sources towards diffraction-limited performance. Two main parameters that characterize the SPEM technique are its energy and spatial resolution. The first one, which defines the chemical sensitivity of the instrument, is notably higher than what is generally available at spectroscopy stations. The new generations of light sources will dramatically improve the optical transmission of X-rays allowing more photons at the samples. Those may be spent to increase energy resolutions at values lower than 80–100 meV and also at higher energies. Similar improvements may also be reached in the spatial resolution; however, any increase in photon density goes with an enhancement of undesired beam-induced effects, such as surface chemical changes, local charging, and space-charge effects. To partially mitigate this effects, strong efforts must be spent in the development of new photoelectron detection systems capable of collecting the majority of electrons, currently wasted due to the limited acceptance angles of hemispherical analyzers, while guaranteeing adequate energy resolutions.

Experimental

The SPEM hosted at the ESCA microscopy beamline at Elettra uses diffraction optics to focus the incoming X-ray beam shaped by the photon transport optics to a 130 nm Gaussian-shaped spot. As shown with a sketch in Figure 4, focusing optics are composed by a zone plate (ZP) and an order sorting aperture which selects one of the diffracted spots generated by the ZP. The focal distance depends on the geometrical parameters of the ZP and on the photon energy. At the experimental conditions of the experiments reported in this article, the focal distance was ≈10 mm. The narrow X-ray spot normally impinges the sample surface generating a cloud of photoelec-

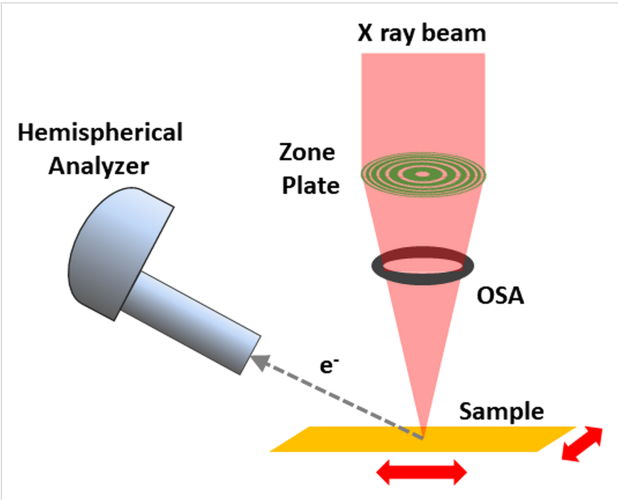

Figure 4: Geometrical displacement of the SPEM focusing optical elements, sample, and electron analyzer.

trons, part of which are collected by a hemispherical electron analyzer pointing at the sample at a 30° take off angle. The choice of such angle is strongly constrained by the crowded area around the sample where the sample and optics holders and analyzer nose must be located within a space of a few millimeters. The further displacement of the electron analyzer increases the natural surface sensitivity of XPS; depending on the kinetic energy of the detected photoelectrons, the probing depth typically stays in the range of 3–10 monolayers. It is straightforward to understand that such feature may uniquely enhance the results of some characterization parameters, but may represent a limit for others.

As shown in Figure 4, the SPEM at Elettra uses a fixed incoming focused X-ray beam, (i.e., the sample is raster scanned with respect to it to create chemical maps). At each step/pixel of the scan/image the number of photoelectrons with a specific kinetic energy corresponding to a particular atomic element chemical state is recorded. The contrast in the final map is then showing the spatial concentration of such state in the analyzed area.

At the photon energy used for the experiments described above (650 eV), the SPEM system guarantees an overall energy resolution in the range of 200–350 meV.

Acknowledgements

Gaute Otnes and Magnus T. Borgström are acknowledged for providing nanowire samples.

Funding

María Taeño, David Maestre, Ana Cremades acknowledge project PID2021-122562NB-I00 from the Spanish Ministry of Science and Innovation.

This work was supported by the Swedish Research Council (Vetenskapsrådet), grant nos. 2017-4108 and 2021-05627.

The work was carried out within the framework of the state assignment of the Ministry of Science and Higher Education of the Russian Federation for the IMP UB RAS. The reported study was funded by RFBR, project number 19-33-60031. This project has received funding from the EU-H2020 research and innovation program under the grant agreement No 654360 having benefitted from the Access provided by IOM-CNR in Trieste (Italy) within the framework of the NFFA-Europe Transnational Access Activity.

Author Contributions

Matteo Amati: conceptualization; supervision; writing – review & editing. Alexey S. Shkvarin: data curation; funding acquisition; writing – original draft. Alexander I. Merentsov: data curation; formal analysis; funding acquisition; writing – original draft. Alexander N. Titov: conceptualization; funding acquisition; writing – original draft. María Taeño: conceptualization; data curation; formal analysis; investigation; writing – original draft. David Maestre: conceptualization; data curation; formal analysis; investigation; writing – original draft. Sarah R. McKibbin: conceptualization; formal analysis; investigation; writing – original draft. Zygmunt Milosz: project administration; supervision; writing – review & editing. Ana Cremades: data curation; investigation; writing – original draft. Rainer Timm: conceptualization; formal analysis; funding acquisition; investigation; writing – original draft. Luca Gregoratti: conceptualization; validation; writing – review & editing.

ORCID® iDs

Alexey S. Shkvarin - https://orcid.org/0000-0002-3774-5669
Zygmunt Milosz - https://orcid.org/0000-0002-4938-9331
Luca Gregoratti - https://orcid.org/0000-0002-4947-2370

Data Availability Statement

Data sharing is not applicable as no new data was generated or analyzed in this study.

References

1. Keller, A. A.; Ehrens, A.; Zheng, Y.; Nowack, B. *Nat. Nanotechnol.* **2023,** *18,* 834–837. doi:10.1038/s41565-023-01409-z
2. Gleiter, H. *Acta Mater.* **2000,** *48,* 1–29. doi:10.1016/s1359-6454(99)00285-2
3. Liu, L.; Mandler, D. *Electrochem. Commun.* **2020,** *120,* 106830. doi:10.1016/j.elecom.2020.106830
4. Liang, R.; Xue, Y.; Fu, X.; Le, A. N.; Song, Q.; Qiang, Y.; Xie, Q.; Dong, R.; Sun, Z.; Osuji, C. O.; Johnson, J. A.; Li, W.; Zhong, M. *Nat. Mater.* **2022,** *21,* 1434–1440. doi:10.1038/s41563-022-01393-0
5. P. M., V.; Semkin, A.; Balakrishnan, R.; Lazovič, S., Eds. *Nanotechnology in Electronics;* Wiley-VCH: Weinheim, Germany, 2023. doi:10.1002/9783527824229
6. Rupprechter, G. Application of XPS in Studies of Model Catalysts: From Single Crystals to Supported Nanoparticles. *Applications of X-ray Photoelectron Spectroscopy to Catalytic Studies;* Catalytic Science Series, Vol. 21; World Scientific, 2023; pp 155–192. doi:10.1142/9781800613294_0007
7. Wiederrecht, G. P.; Bachelot, R.; Xiong, H.; Termentzidis, K.; Nominé, A.; Huang, J.; Kamat, P. V.; Rozhkova, E. A.; Sumant, A.; Ostraat, M.; Jain, P. K.; Heckle, C.; Li, J.; Pupek, K. Z. *ACS Energy Lett.* **2023,** *8,* 3443–3449. doi:10.1021/acsenergylett.3c01303
8. Zhao, X.; Jin, H.; Liu, J.; Chao, J.; Liu, T.; Zhang, H.; Wang, G.; Lyu, W.; Wageh, S.; Al-Hartomy, O. A.; Al-Sehemi, A. G.; Fu, B.; Zhang, H. *Laser Photonics Rev.* **2022,** *16,* 2200386. doi:10.1002/lpor.202200386
9. Shen, K. M. Ultraviolet Photoemission Spectroscopy (UPS) for in Situ Characterization of Thin Film Growth. *In Situ Characterization of Thin Film Growth;* Woodhead Publishing: Cambridge, UK, 2011; pp 55–74. doi:10.1533/9780857094957.2.55

10. Günther, S.; Kaulich, B.; Gregoratti, L.; Kiskinova, M. *Prog. Surf. Sci.* **2002,** *70,* 187–260. doi:10.1016/s0079-6816(02)00007-2
11. Amati, M.; Susi, T.; Jovičević-Klug, P.; Jovičević-Klug, M.; Kosmala, T.; Granozzi, G.; Agnoli, S.; Yang, P.; Zhang, Y.; Scardamaglia, M.; Gregoratti, L. *J. Electron Spectrosc. Relat. Phenom.* **2023,** *265,* 147336. doi:10.1016/j.elspec.2023.147336
12. Merentsov, A. I.; Yarmoshenko, Y. M.; Skorikov, A. N.; Titov, A. N.; Buling, A.; Räkers, M.; Neumann, M.; Galieva, E. G.; Slepuhin, P. A. *J. Electron Spectrosc. Relat. Phenom.* **2010,** *182,* 70–75. doi:10.1016/j.elspec.2010.07.005
13. Merentsov, A. I.; Shkvarin, A. S.; Postnikov, M. S.; Gregoratti, L.; Amati, M.; Zeller, P.; Moras, P.; Titov, A. N. *J. Phys. Chem. Solids* **2022,** *160,* 110309. doi:10.1016/j.jpcs.2021.110309
14. Shkvarin, A. S.; Merentsov, A. I.; Postnikov, M. S.; Patrakov, E. I.; Betz-Guttner, E.; Gregoratti, L.; Amati, M.; Zeller, P.; Titov, A. N. *Mater. Sci. Eng., B* **2022,** *283,* 115821. doi:10.1016/j.mseb.2022.115821
15. Riel, H.; Wernersson, L.-E.; Hong, M.; del Alamo, J. A. *MRS Bull.* **2014,** *39,* 668–677. doi:10.1557/mrs.2014.137
16. Barrigón, E.; Heurlin, M.; Bi, Z.; Monemar, B.; Samuelson, L. *Chem. Rev.* **2019,** *119,* 9170–9220. doi:10.1021/acs.chemrev.9b00075
17. Memisevic, E.; Svensson, J.; Hellenbrand, M.; Lind, E.; Wernersson, L.-E. *IEEE Electron Device Lett.* **2016,** *37,* 549–552. doi:10.1109/led.2016.2545861
18. McKibbin, S. R.; Colvin, J.; Troian, A.; Knutsson, J. V.; Webb, J. L.; Otnes, G.; Dirscherl, K.; Sezen, H.; Amati, M.; Gregoratti, L.; Borgström, M. T.; Mikkelsen, A.; Timm, R. *Nano Lett.* **2020,** *20,* 887–895. doi:10.1021/acs.nanolett.9b03529
19. Knutsson, J. V.; Lehmann, S.; Hjort, M.; Lundgren, E.; Dick, K. A.; Timm, R.; Mikkelsen, A. *ACS Nano* **2017,** *11,* 10519–10528. doi:10.1021/acsnano.7b05873
20. Ning, C.-Z.; Dou, L.; Yang, P. *Nat. Rev. Mater.* **2017,** *2,* 17070. doi:10.1038/natrevmats.2017.70
21. Kilpi, O.-P.; Hellenbrand, M.; Svensson, J.; Persson, A. R.; Wallenberg, R.; Lind, E.; Wernersson, L.-E. *IEEE Electron Device Lett.* **2020,** *41,* 1161–1164. doi:10.1109/led.2020.3004716
22. Borgstrom, M. T.; Magnusson, M. H.; Dimroth, F.; Siefer, G.; Hohn, O.; Riel, H.; Schmid, H.; Wirths, S.; Bjork, M.; Aberg, I.; Peijnenburg, W.; Vijver, M.; Tchernycheva, M.; Piazza, V.; Samuelson, L. *IEEE J. Photovoltaics* **2018,** *8,* 733–740. doi:10.1109/jphotov.2018.2816264
23. Wernersson, L.-E. *J. Appl. Phys.* **2015,** *117,* 112810. doi:10.1063/1.4913836
24. Vasen, T.; Ramvall, P.; Afzalian, A.; Doornbos, G.; Holland, M.; Thelander, C.; Dick, K. A.; Wernersson, L.- E.; Passlack, M. *Sci. Rep.* **2019,** *9,* 202. doi:10.1038/s41598-018-36549-z
25. Ram, M. S.; Persson, K.-M.; Irish, A.; Jönsson, A.; Timm, R.; Wernersson, L.-E. *Nat. Electron.* **2021,** *4,* 914–920. doi:10.1038/s41928-021-00688-5
26. Krogstrup, P.; Jørgensen, H. I.; Heiss, M.; Demichel, O.; Holm, J. V.; Aagesen, M.; Nygard, J.; Fontcuberta i Morral, A. *Nat. Photonics* **2013,** *7,* 306–310. doi:10.1038/nphoton.2013.32
27. Holm, J. V.; Jørgensen, H. I.; Krogstrup, P.; Nygård, J.; Liu, H.; Aagesen, M. *Nat. Commun.* **2013,** *4,* 1498. doi:10.1038/ncomms2510
28. Timm, R.; Hjort, M.; Fian, A.; Borg, B. M.; Thelander, C.; Andersen, J. N.; Wernersson, L.-E.; Mikkelsen, A. *Appl. Phys. Lett.* **2011,** *99,* 222907. doi:10.1063/1.3664399
29. Fanetti, M.; Ambrosini, S.; Amati, M.; Gregoratti, L.; Abyaneh, M. K.; Franciosi, A.; Chia, A. C. E.; LaPierre, R. R.; Rubini, S. *J. Appl. Phys.* **2013,** *114,* 154308. doi:10.1063/1.4826198
30. Otnes, G.; Heurlin, M.; Graczyk, M.; Wallentin, J.; Jacobsson, D.; Berg, A.; Maximov, I.; Borgström, M. T. *Nano Res.* **2016,** *9,* 2852–2861. doi:10.1007/s12274-016-1165-z
31. Wallentin, J.; Anttu, N.; Asoli, D.; Huffman, M.; Åberg, I.; Magnusson, M. H.; Siefer, G.; Fuss-Kailuweit, P.; Dimroth, F.; Witzigmann, B.; Xu, H. Q.; Samuelson, L.; Deppert, K.; Borgström, M. T. *Science* **2013,** *339,* 1057–1060. doi:10.1126/science.1230969
32. Otnes, G.; Barrigón, E.; Sundvall, C.; Svensson, K. E.; Heurlin, M.; Siefer, G.; Samuelson, L.; Åberg, I.; Borgström, M. T. *Nano Lett.* **2018,** *18,* 3038–3046. doi:10.1021/acs.nanolett.8b00494
33. Sun, Y.; Liu, Z.; Machuca, F.; Pianetta, P.; Spicer, W. E. *J. Vac. Sci. Technol., A* **2003,** *21,* 219–225. doi:10.1116/1.1532738
34. Galatage, R. V.; Dong, H.; Zhernokletov, D. M.; Brennan, B.; Hinkle, C. L.; Wallace, R. M.; Vogel, E. M. *Appl. Phys. Lett.* **2011,** *99,* 172901. doi:10.1063/1.3656001
35. Meng, T.; Ma, P.-P.; Chang, J.-L.; Wang, Z.-H.; Ren, T.-Z. *Electrochim. Acta* **2014,** *125,* 586–592. doi:10.1016/j.electacta.2014.01.144
36. Brisse, A.-L.; Stevens, P.; Toussaint, G.; Crosnier, O.; Brousse, T. *Materials* **2018,** *11,* 1178. doi:10.3390/ma11071178
37. Napari, M.; Huq, T. N.; Maity, T.; Gomersall, D.; Niang, K. M.; Barthel, A.; Thompson, J. E.; Kinnunen, S.; Arstila, K.; Sajavaara, T.; Hoye, R. L. Z.; Flewitt, A. J.; MacManus-Driscoll, J. L. *InfoMat* **2020,** *2,* 769–774. doi:10.1002/inf2.12076
38. Diao, C.-C.; Huang, C.-Y.; Yang, C.-F.; Wu, C.-C. *Nanomaterials* **2020,** *10,* 636. doi:10.3390/nano10040636
39. Park, C.; Kim, J.; Lee, K.; Oh, S. K.; Kang, H. J.; Park, N. S. *Appl. Sci. Convergence Technol.* **2015,** *24,* 72–76. doi:10.5757/asct.2015.24.3.72
40. Zhao, C.; Fu, J.; Zhang, Z.; Xie, E. *RSC Adv.* **2013,** *3,* 4018. doi:10.1039/c3ra23182h
41. Kim, H.-J.; Lee, J.-H. *Sens. Actuators, B* **2014,** *192,* 607–627. doi:10.1016/j.snb.2013.11.005
42. Pai, S. H. S.; Pandey, S. K.; Samuel, E. J. J.; Jang, J. U.; Nayak, A. K.; Han, H. *J. Energy Storage* **2024,** *76,* 109731. doi:10.1016/j.est.2023.109731
43. Taeño, M.; Maestre, D.; Cremades, A. *Nanophotonics* **2021,** *10,* 1785–1799. doi:10.1515/nanoph-2021-0041
44. Sandana, V. E.; Rogers, D. J.; Hosseini Teherani, F.; Bove, P.; Ben Sedrine, N.; Correia, M. R.; Monteiro, T.; McClintock, R.; Razeghi, M. *Proc. SPIE* **2015,** *9364,* 93641O. doi:10.1117/12.2177427
45. Bagus, P. S.; Nelin, C. J.; Brundle, C. R.; Crist, B. V.; Ilton, E. S.; Lahiri, N.; Rosso, K. M. *Inorg. Chem.* **2022,** *61,* 18077–18094. doi:10.1021/acs.inorgchem.2c02549
46. Taeño, M.; Bartolomé, J.; Gregoratti, L.; Modrzynski, P.; Maestre, D.; Cremades, A. *Cryst. Growth Des.* **2020,** *20,* 4082–4091. doi:10.1021/acs.cgd.0c00365
47. Bartolomé, J.; Taeño, M.; Martínez-Casado, R.; Maestre, D.; Cremades, A. *Appl. Surf. Sci.* **2022,** *579,* 152134. doi:10.1016/j.apsusc.2021.152134

BEILSTEIN JOURNAL OF NANOTECHNOLOGY

Thickness dependent oxidation in $CrCl_3$: a scanning X-ray photoemission and Kelvin probe microscopies study

Shafaq Kazim*[1], Rahul Parmar[2], Maryam Azizinia[1], Matteo Amati[2], Muhammad Rauf[1], Andrea Di Cicco[1], Seyed Javid Rezvani[1], Dario Mastrippolito[3], Luca Ottaviano[3,4], Tomasz Klimczuk[5], Luca Gregoratti[2] and Roberto Gunnella*[1]

Full Research Paper

Open Access

Address:
[1]Physics Division, School of Science and Technology, University of Camerino, 62032 Camerino (MC), Italy, [2]Elettra-Sincrotrone Trieste, Strada Statale 14, AREA Science Park, 34149 Trieste, Italy, [3]Dipartimento di Scienze Fisiche e Chimiche (DSFC) Università degli Studi dell'Aquila, Via Vetoio 10 67100 L'Aquila, Italy, [4]CNR-SPIN UoS L'Aquila. Via Vetoio 10 67100 L'Aquila, Italy and [5]Gdansk University of Technology, Faculty of Applied Physics and Mathematics, 80-233 Gdansk, Poland

Email:
Shafaq Kazim* - shafaq.kazim@unicam.it; Roberto Gunnella* - roberto.gunnella@unicam.it

* Corresponding author

Keywords:
chemical mapping; CrX_3; Kelvin probe force microscopy; mechanical exfoliation; scanning photoelectron microscopy (SPEM); two-dimensional material; work function

Beilstein J. Nanotechnol. **2025,** *16,* 749–761.
https://doi.org/10.3762/bjnano.16.58

Received: 01 February 2025
Accepted: 29 April 2025
Published: 02 June 2025

This article is part of the thematic issue "Exploring synchrotron radiation and free-electron laser tools for nanostructured materials".

Guest Editor: C. Bittencourt

Abstract

The modifications in the electronic properties induced by the thickness and size of an individual flake of transition-metal halides on different substrates (silicon oxide or In-doped tin oxide) are of particular technological interest, even more in the case of chromium trihalides (CrX_3, X = Cl, Br, and I), whose longer lifetime under ambient conditions is particularly intriguing. By using synchrotron-based scanning photoelectron microscopy with a resolution of 0.1 μm and Kelvin probe force microscopy, we evaluated the surface modification reaction and the surface potential. Our results established the correlations of the two latter properties with the thickness of flakes, observing a natural tendency to preserve their characteristic when the flakes have significantly less thickness. This is in contrast to thicker flakes, which show alteration patterns similar to those observed in bulk-cleaved samples (Kazim, S.; Mastrippolito, D.; Moras, P.; Jugovac, M.; Klimczuk, T.; Ali, M.; Ottaviano, L.; Gunnella, R. *Phys. Chem. Chem. Phys.***2023**, *25*, 3806–3814. doi:10.1039/D2CP04586A). This preliminary study investigates interfaces made by dry transfer of $CrCl_3$ flakes in an atmospheric environment. Cl vacancies and the formation of $O/CrCl_3$ are induced, serving as dissociation centers that facilitate the migration of Cl vacancies between the top and bottom surfaces. By manipulating 2D atomic layers via surface oxidation or the introduction of surface vacancies, a novel and versatile approach is unveiled for the development of low-dimensional multifunctional nanodevices.

Introduction

The family of chromium-based trihalides has garnered significant interest in recent years, particularly after the remarkable discovery of long-lasting magnetism in a single layer of CrI_3 [1]. In our previous reports, we dealt with the environmental stability of $CrCl_3$ [2], which can be easily exfoliated and exhibits a slower degradation rate compared to CrI_3 or $CrBr_3$[3]. To fully exploit the potential of any material, a detailed understanding of its electronic and structural changes arising from intrinsic and extrinsic defects is crucial [4]. Despite this importance, limited experimental research has been conducted on the electronic structure of CrX_3 [5,6]. According to previously published photoelectron spectroscopy results, CrX_3 belongs to metal compounds in which the 3d states are very close to the Fermi level, significantly above the 3p/4p/5p states of the halides. This has been supported by self-consistent band structure calculations by Antoci and Mihich [7], which introduced spin degeneracy, demonstrating that $CrCl_3$ and $CrBr_3$ behave as metallic system because of the prominent role of the 3d states near Fermi level. In our previous publications [8-10], we have found the formation of a stable and partially ordered Cr–O–Cl surface on vacuum- or air-cleaved $CrCl_3$ samples. Building upon these findings, we now extend our chemical and structural investigations using electronically and optically characterized, mechanically cleaved $CrCl_3$ samples [2,8,10,11], focusing on thin layered flakes and the role of the layer thicknesses obtained by spectro- and scanning microscopy with a lateral resolution of a few tens of nanometers. The interaction with the supporting substrate is a crucial factor [3,12] regarding the properties of the flakes, which can be significantly different from those of the bulk [1,13]. A central question remains whether modified structures and compositions arise from stress during cleaving, affecting surface terminations [10], or from the exfoliation process itself, which differs from cleaving. Regarding the bulk, we showed that oxygen adsorption on cleaved surfaces facilitates the formation of a stable structure with charge transfer signatures, as identified by high-resolution photoemission spectroscopy [8]. It remains unclear whether similar effects occur in exfoliated thin flakes. Like in other materials, the content of defects such as adatoms, the length of grain boundaries, vacancies, and substitution impurities influence the electrical, magnetic, and electronic properties of the final device [4,14,15]. To name one, the formation of chalcogenide vacancies is often related to the enhanced dissociation of molecular oxygen [16] at the metal species. These defects do not only change the electronic behavior of the sample by modifying the band structure [17]; they are also responsible for Curie temperature deviations, work function modifications [18], and induced long-range magnetic orders (i.e., magnetic band effect) [19-21]. A well-known and suitable technique to investigate the electronic structure of surfaces is X-ray photoemission spectromicroscopy [6,22]; in order to obtain the necessary spatial resolution, the beam size must be reduced to tens of nanometers. The Electron Spectroscopy for Chemical Analysis (ESCA) Microscopy beamline [23] enables this by means of a zone plate arrangement that can reduce the beam size to 130 nm in diameter, and its grazing collection angle can provide a highly surface-sensitive probing depth of approximately 1 nm [23,24]. Such a short mean free path condition could be suitable for increasing the sensitivity to a number of defects per unit volume forming at the surface, which can be recorded by the significant photoemission core level binding energy shift [25,26]. The significance of these studies lies in the exploration of novel materials with improved properties for 2D magnets by manipulating factors such as layer thickness, applied strain, and induced defect sites. Numerous theoretical studies predict that magnetic order in monolayers occurs at temperatures significantly higher than the bulk Curie temperature (i.e., 17 K). In their work, Liu et al. employed Monte Carlo methods to observe ferromagnetic behavior in monolayers below 66 K and proposed that hole doping could further enhance the Curie temperature [21]. Similarly, another Monte Carlo study found that the transition temperature for monolayer $CrCl_3$ is 49 K, proposing that the Curie temperature could be further increased by applying uniaxial strain [17,27].

In the present study, we examined the surface modifications that occur in thin layers of exfoliated $CrCl_3$ (approximately 1 to 20 ML) by using scanning photoelectron microscopy (SPEM). We collected the chemical maps and spectra of the Cl and Cr core levels at room temperature (RT). By monitoring the core levels and valence band spectra at various spatial resolutions (≥0.13 μm), we obtained quantitative maps of the chemical composition to correlate these maps with the thicknesses measured by AFM. Additionally, we investigated the correlation between the microscopic results and the surface potential of $CrCl_3$ flakes at the nanoscale level using Kelvin probe force microscopy (KPFM) [28]. KPFM is mainly employed to measure the local contact potential difference between the conductive AFM tip and the sample, allowing for high-resolution mapping of the work function and surface atomic states [29]. This technique establishes a correlation between the valence band photoemission data and the morphological information, offering insights into the position of the conduction band [30].

Results and Discussion

Optical contrast and AFM

It is well known that 270 nm SiO_2/Si substrates provide the highest optical contrast (O.C.) value for a single layer or few layers of $CrCl_3$ [2,11]. Because of the insulating behavior of

270 nm SiO_2 and to avoid surface charging, we utilized Si(001) wafers with a 1 nm layer of SiO_2 and ITO films (190 nm) on glass substrates for SPEM investigations. In contrast, 285 nm SiO_2/Si and ITO (190 nm) on glass substrates were used for surface potential studies. On native Si substrates, the optical contrast was insufficient to visualize thin flakes. We were unable to observe flakes with thicknesses smaller than 10 nm using the optical microscope. Therefore, we opted for an alternative substrate, indium tin oxide (ITO), to conduct the SPEM measurements on thinner layers. Figure 1 gives a direct comparison of AFM images and O.C. on the 1 nm SiO_2/Si substrate. Optical contrast, AFM image, and a complete series of profiles showing layer thicknesses are given. To overcome the visibility barrier, systematic optical and AFM studies were performed for $CrCl_3$ flakes on an ITO substrate and are reported for comparison in Figure 2a,b. Based on the colors of the flakes seen in the optical microscope images, an interval of thickness values for each flake could be determined. Since we have already mentioned that flakes thinner than 10 nm on 1 nm SiO_2/Si substrates are hardly visible, we have defined the color range starting from 10 nm or higher.

In Figure 1, light olive indicates a thickness range of 10 to 20 nm, brown represents thicknesses from above 20 to 40 nm, and blue denotes thicknesses from 40 up to 80 nm. The tentative scale bar is presented in Figure 1a. Similar results, but with higher sensitivity, were obtained for the sample on the ITO substrate. The colors of the scale are given in Figure S1, Supporting Information File 1. For the latter sample, we distinguished lean (L) and thick (T) flakes by optical and AFM inspection (Figure 2). The Olympus B×60 system with objective lenses of magnifications of 5×, 10×, 20×, 50×, and 100× was used to find a color scale to interpolate the AFM thickness measurement results.

In Figure 1a and Figure 2a, we report a series of $CrCl_3$ flakes of different thicknesses based on optical determination, and in Figure 1b and Figure 2c,d, we present the related AFM images to evaluate the thickness. Profile 3 in Figure 1b shows the minimum observable flake thickness of $CrCl_3$, which yields a very fade contrast in the optical image in Figure 1a. In contrast, in Figure 2a, clear microscopy images of a few layers of flakes are shown. Based on the optical contrast value, L and T denote lean and thick steps, respectively, and the thickness variation has been confirmed through AFM images in Figure 2c–f. The negative value of optical contrast shows that the surface of $CrCl_3$ looks brighter than the substrate. We show the thickness variation with AFM micrographs in the specific zoomed regions in Figure 2e,f, where the heights of the T and L profiles were measured and presented in inset of the Figure 2e.

Spatially resolved photoemission

In our quest to understand exfoliated materials under varying photon flux conditions, we have extensively investigated the material while varying the incident photon energies [8]. As we aim for more ambitious goals, delving into variations of the material's layers, ESCA microscopy emerges as a prime choice for making these groundbreaking experiments. We studied the layer-dependent surface modification of $CrCl_3$ by SPEM, one of the optimal experimental techniques (Figure 3) for this kind of study. The use of zone plate and order selection aperture (OSA) provides an ideal spot size for the study of 2D materials, focusing on the character of the material in relation to its shape. Sample flakes in the range of 1–10 μm^2, obtained by the exfoliation technique, can be analyzed by SPEM on such characteristic lengths by the precise control of the relative position between the beam and the sample. Thus, a determination of predominant phases without the influence of inhomogeneities or spurious effects (e.g., from the boundary of the flakes or differ-

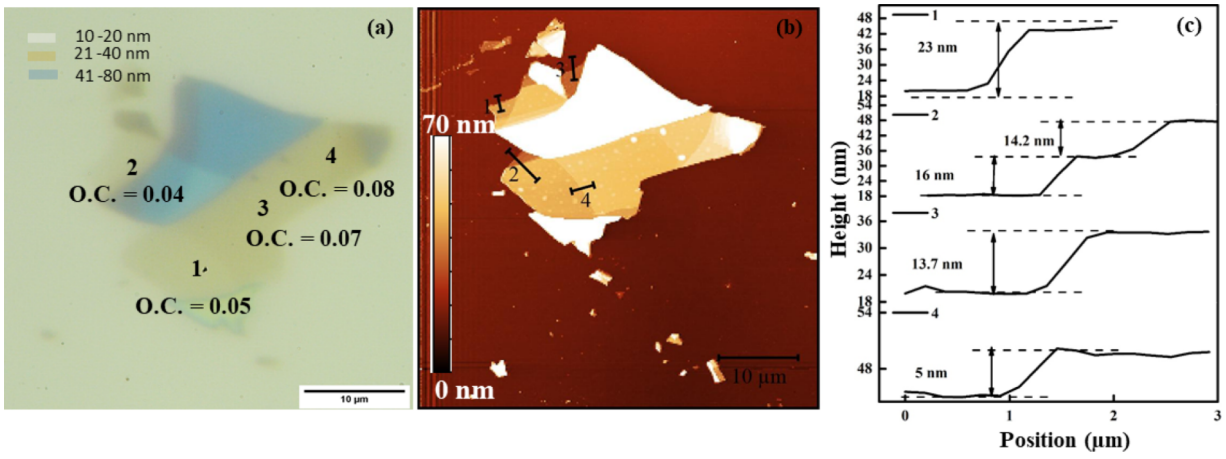

Figure 1: (a) Optical contrast and (b) AFM images of mechanically exfoliated $CrCl_3$ flakes on the native Si (1 nm SiO_2) substrate. (c) AFM thickness profile scans along the various flakes as denoted in Figure 1b.

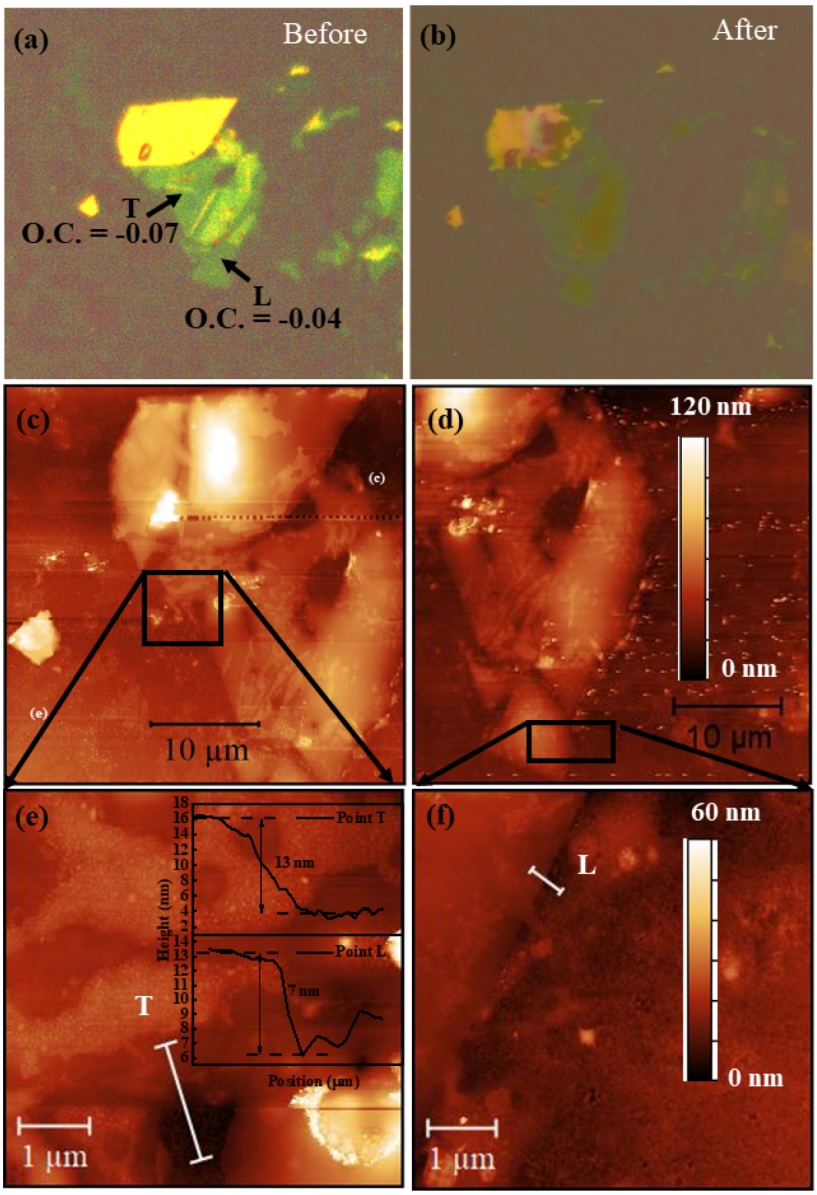

Figure 2: Optical contrast on ITO substrates (a) before and (b) after the SPEM measurements. (c, d) AFM topography images of $CrCl_3$ on the ITO substrate for the points T and L in (a, b), respectively, together with zoomed details in (e) and (f). The inset displays the thickness profiles of T and L, respectively.

ent thicknesses) is possible. Furthermore, the very high background signal from the substrate can be minimized by the special design of the detection system [23].

In SPEM, the spectra can be recorded in three modes, namely, (1) "focused" (beam size of ≈130 nm), (2) "unfocused" (beam size of ≈2 µm), and (3) the so-called OSA mode with a beam size of ≈75 µm. Figure 4 presents XPS survey spectra obtained with all three aforementioned modes on thin $CrCl_3$ flakes at RT on a native Si oxide substrate. The survey spectra indicate beam damage resulting from the focused beam, as evidenced by the high intensity of the Si 2p core level photoemission, which was not observed in the other cases involving defocused beams. In contrast, the OSA measurement spectrum showed a Si component due to the wider beam diameter. This is further supported by the evaluation of the $CrCl_3$ stoichiometry in the latter two cases.

Table 1 displays the area under the peaks for Cl 2p and Cr 2p. The stoichiometry was determined after applying the sensitivity correction factors. Under OSA beam conditions, the stoichiometry of $CrCl_3$ exhibits the nominal value. However, there are

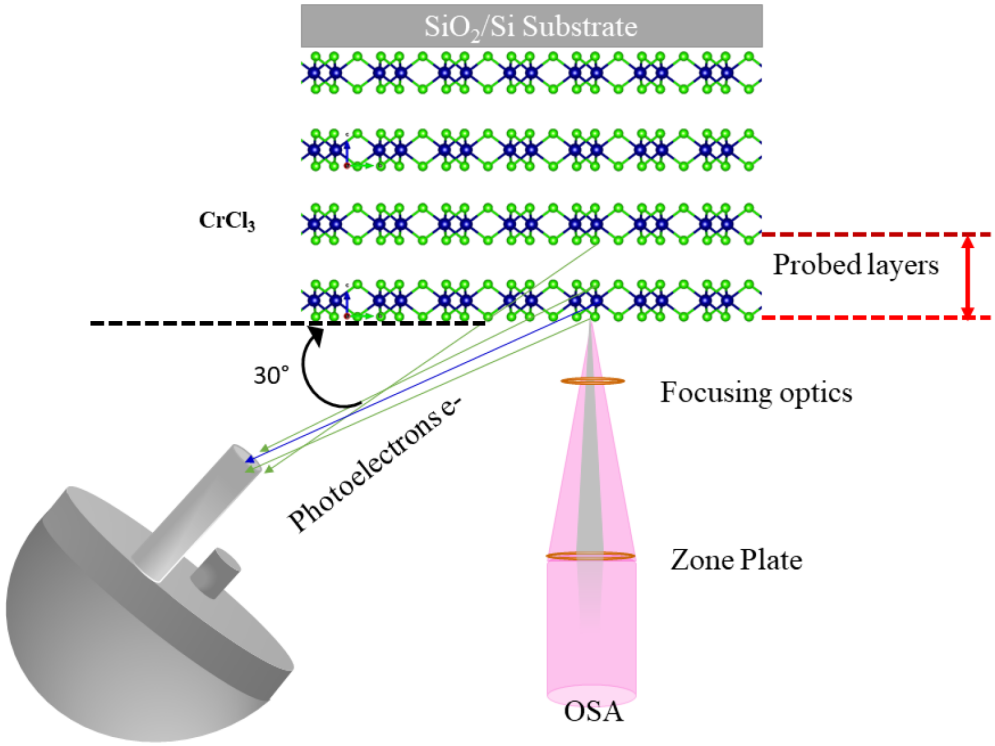

Figure 3: A schematic of experimental SPEM setup in the case of a few layer $CrCl_3$ flake [27]. The lower part of the figure Figure 3 was redrawn from [31].

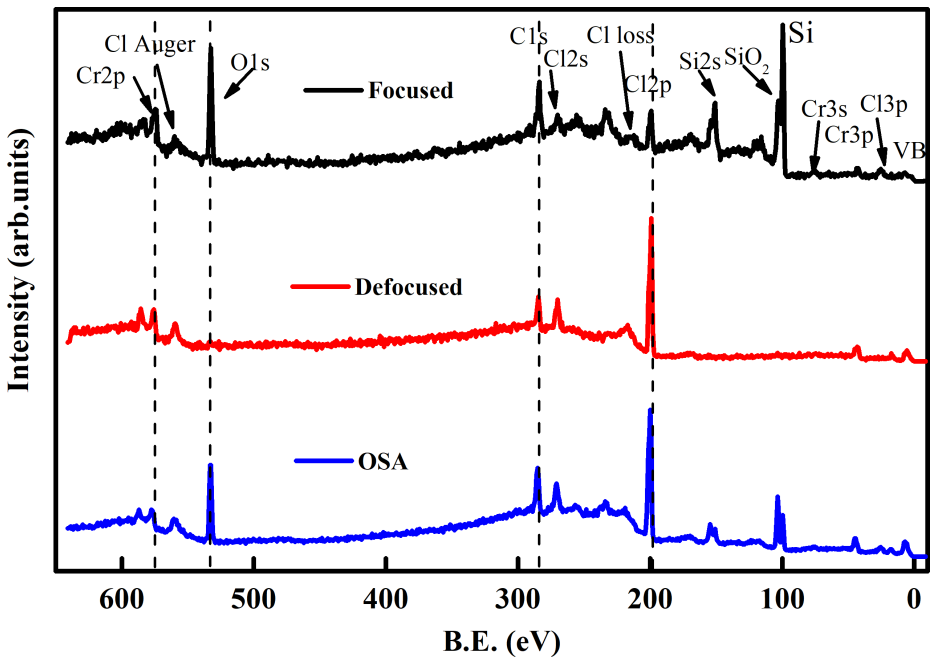

Figure 4: Survey spectra of exfoliated $CrCl_3$ flakes on native Si oxide substrate with different beam modes at RT. From top to bottom: focused beam, defocused beam, and OSA mode of operation.

Table 1: Stoichiometry determined from survey spectra using different photon beam sizes.

Beam mode	Cl 2p area	Cr 2p area	Cl/Cr ratio
focused beam	2190	4430	0.69
defocused beam	7500	5050	2.1
OSA beam	24900	11500	3.0

significant deviations when measuring with a smaller beam size or for thin specimens exposed to high photon doses for several minutes. This behavior is corroborated by the signal from the Si 2p core level of the underlying substrate. When using the OSA mode, a contribution from the substrate is also anticipated because of the larger beam size.

During the mapping process, the sample was continuously scanned and data points were recorded within a few milliseconds. This method significantly reduced the incident photon dose compared to the survey spectra; however, it led to a lower statistical quality of the spectra. For further studies, we preferred to collect the core level spectra from maps using a defocused beam. In Figure 5, we have selected one particular flake consisting of two different main regions on the SiO_2 (1 nm)/Si substrate. Figure 5a shows the Cl 2p map after background correction at a binding energy of about 200 ± 4 eV. We know from a previous work that at this energy the Cl 2p core level only shows the main component at 199.5 eV [8]. In contrast, in Figure 5c the Cr $2p_{3/2}$ spectrum shows also a second component at 576 eV in addition to the main component at 577.5 eV. Both maps display an increased intensity of Cl emission from the parts on the right side of the flake. On the left side, the density of Cl vacancies is supposedly higher (see inset of Figure 5a). In some recent works, the formation of a Cr–O–Cl surface phase [8,10] was characterized by the presence of a low-binding-energy component for Cl 2p at 198 eV (Figure 5b), albeit for a high degree of oxidation at high temperature in air, which we do not observe here, and a low-binding-energy component for Cr $2p_{3/2}$ at 576 eV (Figure 5d) from the presence of oxygen also in UHV. Such a deviation and component appearance is clearly visible in the thicker region of the sample (left region) for the Cr 2p core level. This component is also enhanced in the portion of the surface where beam effects were strong (light blue square in Figure 5c), but it is almost absent anywhere else.

We also performed the core level analysis on the ITO substrate. Figure 6a shows the Cl 2p map around 199.5 eV binding energy. Leaner and thicker regions are designated with L and T, respectively. Figure 6b shows the Cl 2p spectra taken from the correspondingly colored regions after background correction. The upper spectrum was taken at point L, and the lower spectrum was taken at point T. The Cr $2p_{3/2}$ map is given in Figure 6c, and the corresponding Cr $2p_{3/2}$ core level data are shown in Figure 6d. The data were shifted vertically for better visualization. In the Cr 2p spectrum, one can clearly see the fingerprint of the low-binding-energy component for the thicker region (T), which is clearly absent in the leaner part (L). From our previous report, we know that the low-binding-energy component emerges after the formation of the O–$CrCl_3$ phase [8]. To confirm our analysis, we have continued the investigation of the Cr $2p_{3/2}$ and O 1s core level spectra in Figure 7 at different thicknesses on the ITO substrate as reported in Figure 2 with defocused beam and observed the appearance of the peak at the lower binding energy of Cr 2p for the thick region, while the O 1s spectra appear to be enhanced for the same region.

These results can complement the study on cleaved samples [8], where the formation of a stable phase through oxygen in interstitial positions of the surface, which provided a redox source for Cr atoms, was shown by the formation of a low-binding-energy component at the Cr 2p core level. Here, this process occurs only in the presence of Cl vacancies and in the case of the thicker flakes. This lets us conclude that one of the reason of the resilience of the $CrCl_3$ flakes is the fact that the formation of the Cr–O–Cl phase requires a sufficient volume of material, that is, that oxygen-driven phase formation is hindered if there are no specific diffusion processes in the sample. All three SPEM figures (Figure 5, Figure 6, and Figure 7) confirm that the lower-binding-energy component at 576 eV appeared because of the presence of Cl vacancies and the subsequent formation of reactive sites for the dissociation [16] of molecular oxygen to induce a stable phase of Cr–O–Cl [8]. We realized that the low-binding-energy component in Cr $2p_{3/2}$ is arising because of charge transfer effects. This turns the system from a surface Mott–Hubbard insulator to a charge-transfer [8] one in spite of Cr being an early transition metal [32].

What can be presumed from the present study is that Cl–O exchange following Cl vacancy formation is limited in very thin layers because of the limited diffusion processes and the lower number of defects present per unit volume that can be exploited in the process. These numbers are increased under beam irradia-

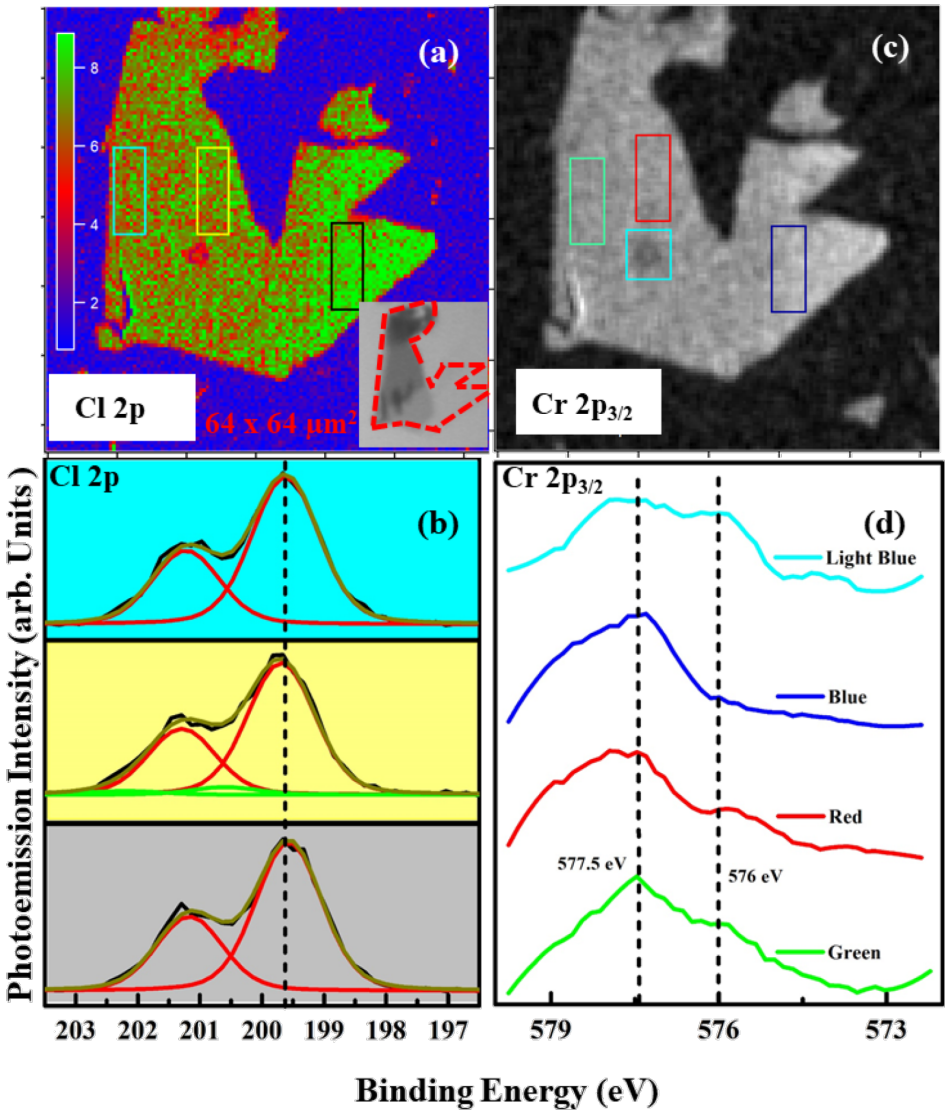

Figure 5: Cl 2p and Cr $2p_{3/2}$ core level SPEM maps with focused beam at RT on 1 nm SiO_2/Si substrate. (a) Cl 2p map at 199.5 eV binding energy; (b) spectra with light blue, yellow, and dark gray backgrounds taken from the correspondingly colored rectangle areas in (a); (c) Cr $2p_{3/2}$ map at 577.5 eV binding energy; (d) binding energy spectra acquired from the correspondingly colored areas in (c).

tion, when damages occurs as shown by the light blue area in Figure 5. These results are consistent with previous studies on bulk samples cleaved in vacuum, where such a formation was very much hindered compared to thick flakes prepared in air [8].

It is nevertheless important to stress that here the modification is mostly driven by Cl vacancies alone. A strong evidence from this study and previous studies [8] is that only in case of bulk samples cleaved in air we observed the huge Cl vacancy signature in Cl 2p core levels (i.e., a low-energy component at 198 eV). Our conclusion is that the thin $CrCl_3$ layers are more difficult to be modified because of the high energy of defect formation and the rapid quenching of them by mobile free atoms; this is confirmed by the high energy of Cl vacancies found by total energy calculations [9].

Kelvin probe force microscopy (KPFM) measurements

One look at the surface potential of the samples could complement our analysis. Figure 8a,c shows topographic maps and the corresponding thickness profiles of $CrCl_3$ flakes on the SiO_2 substrate. The average thicknesses of L and T $CrCl_3$ flakes on the SiO_2 substrate are about 5.3 and 76.5 nm, respectively. Figure 8b,d shows the Kelvin potential maps and the corresponding potential profiles. An obvious variation in the Kelvin

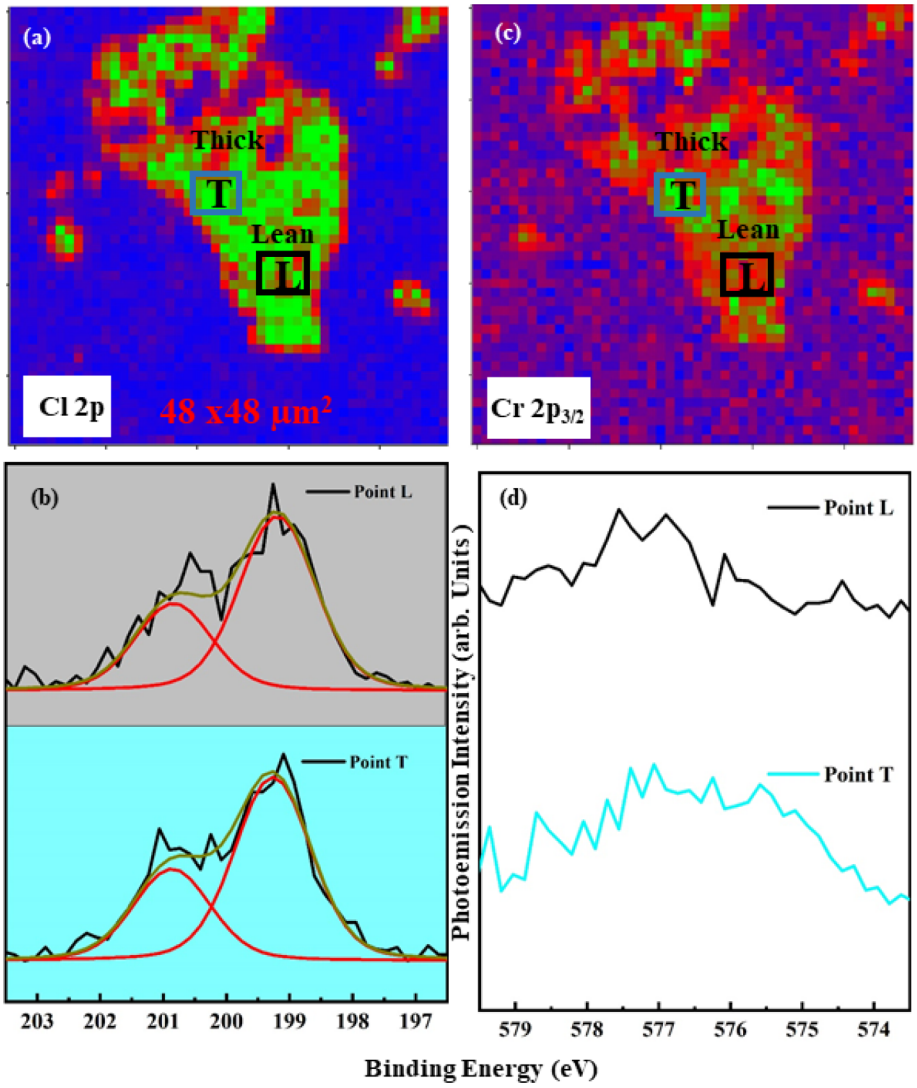

Figure 6: Cl 2p (a, b) (map and spectrum) and Cr $2p_{3/2}$ (c, d) (map and spectrum) core level maps at binding energies of about 200 and 576 eV, respectively.

potential of the flakes (V_{KP}), that is, the difference between the surface potentials of tip and sample, could be observed, which is associated with the work function difference. In the V_{KP} line profiles, the flat region (at high potential) corresponds to the substrate, while the downward curved region (at low potential) is related to flakes. The V_{KP} values of L and T flakes are 0.10 and 0.04 V, respectively. Based on these values, the work functions of L and T flakes are about 5.40 and 5.46 eV, respectively, given the work function of the Pt tip of 5.50 eV. As a control, the work function of SiO_2 was measured correctly as 5.00 eV.

To complete the work begun with the spatially resolved photoemission measurements on the ITO substrate, for the obvious reasons related to the higher conductivity and a better contrast to individuate the flakes, we analyzed flakes in Figure 9, in which the thickness is plotted as a function of the position on the analyzed line. The work functions are 5.39 eV for flake L (thickness 6.6 nm) and 5.43 eV for flake T (thickness 14.0 nm), while 5.34 eV is the value for the ITO substrate. From the analysis of the surface potential on $CrCl_3$ flakes presented in Figure 9, it can be seen that also in this case the areas with larger thickness have a higher surface potential, which is closer to the tip surface potential.

On both substrates, the KPFM results are similar, that is, the flake T has a higher work function than the flake L. This variation in the work functions of flakes is attributed to the chlorine vacancies in the thick region, which promote the chemisorption of oxygen and act as charge acceptor [33], but in a less efficient way with respect to Cl, as we observed by the low-binding-

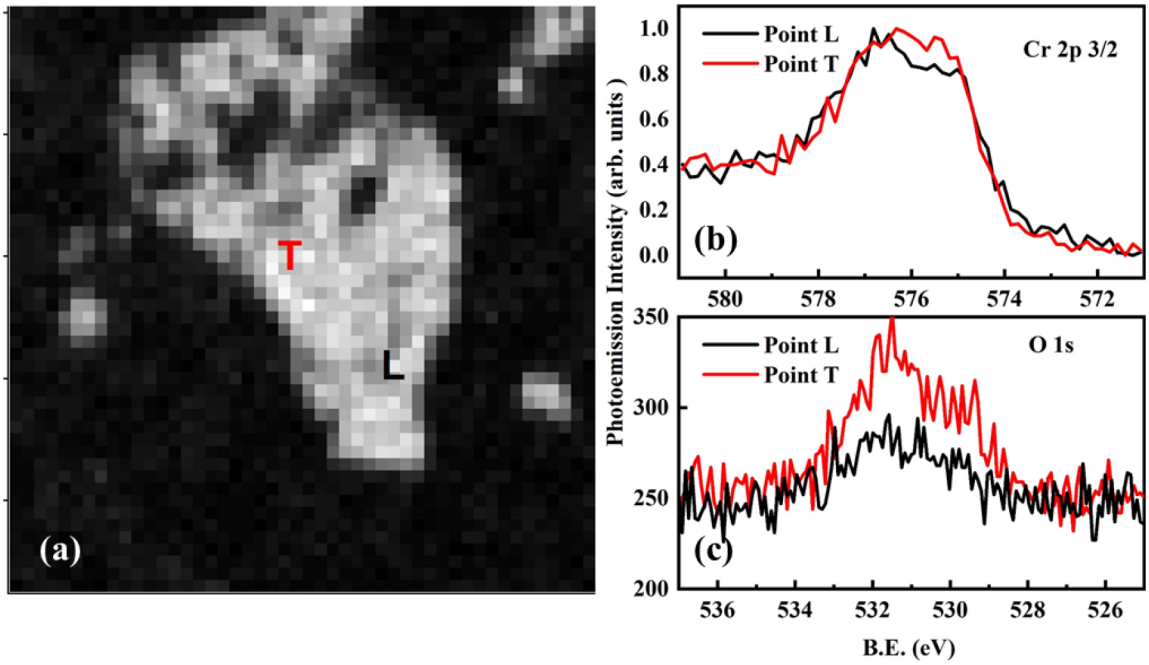

Figure 7: SPEM spectra from thick (T) and lean (L) areas on ITO. (a) SPEM image to verify the area of interest. (b) Cr $2p_{3/2}$ core level spectra. (c) O 1s core level spectra.

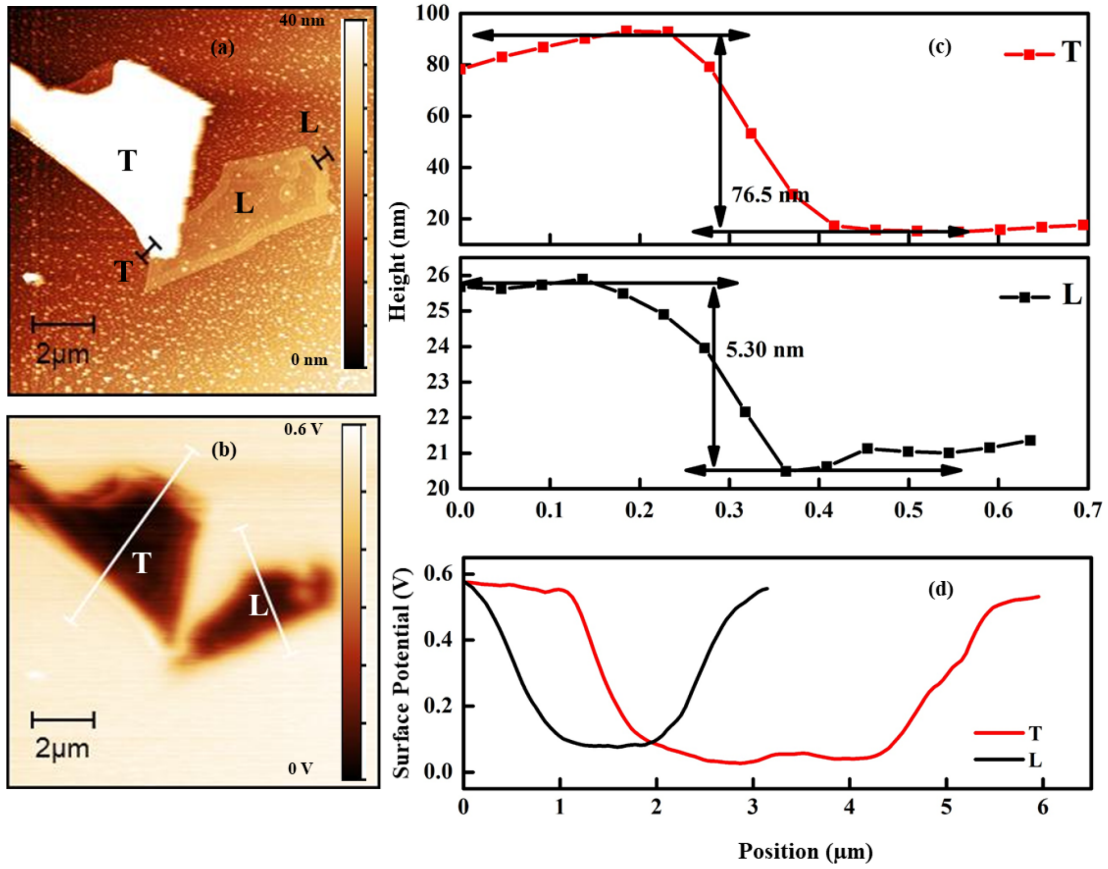

Figure 8: $CrCl_3$ on SiO_2/Si substrate. (a) Topography from non-contact mode AFM of two flakes with different thicknesses; (b) Kelvin surface potential of the samples on SiO_2; (c) z-profiles of the two flakes; (d) Kelvin surface potential scans along the profiles of (a). A Pt-coated tip was used.

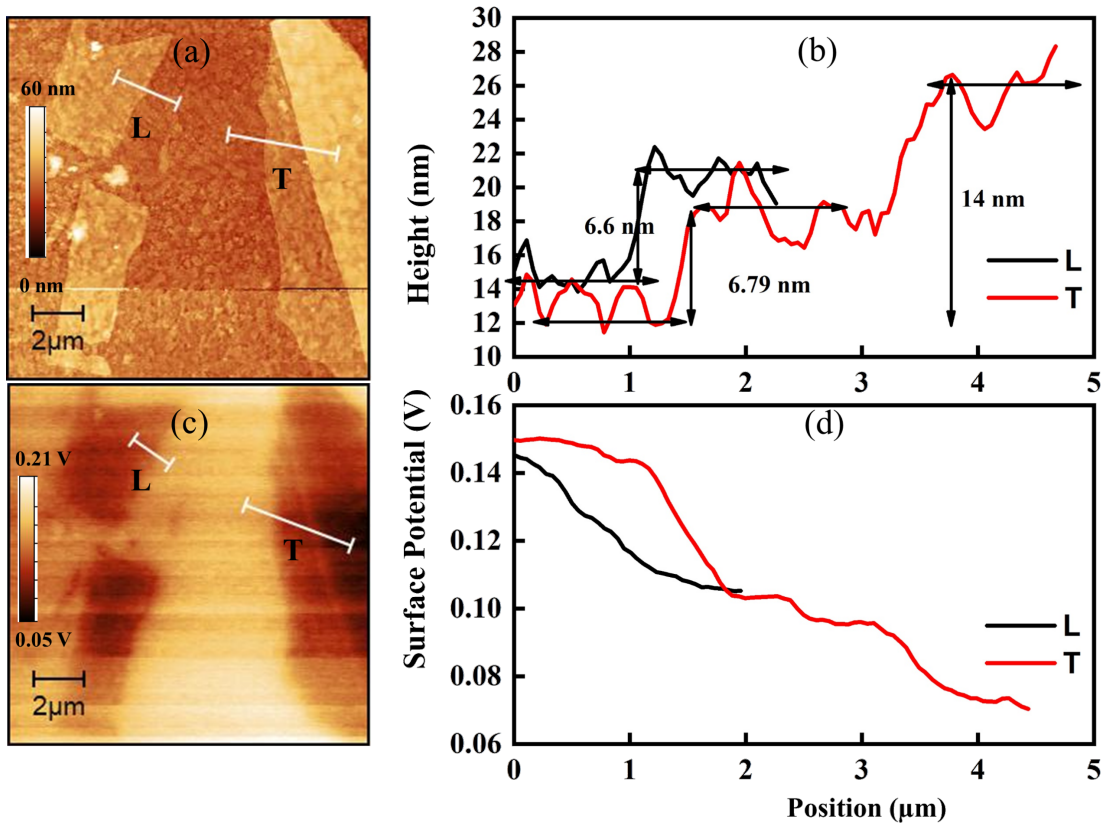

Figure 9: (a)Topography from non-contact mode AFM of flakes with two different thickness deposited on ITO; (b) Kelvin net surface potential of the samples in (a); (c) z-profiles of the two flakes; (d) Kelvin surface potential scans along the profiles of (a). A Pt-coated tip was used.

energy peak in the Cr 2p SPEM spectra. In contrast to physisorption, the chemisorption of oxygen has a significant impact on the electronic properties of a material. Neal et al. [34] reported the effect of chemisorption of oxygen as a kind of p-type doping, which shows consistency with our results. We expect the surface potential to show the same behavior depending on the chemical composition found by spatially resolved photoemission [35].

Valence band results

The valence band spectra of $CrCl_3$ flakes were recorded at the two different regions T and L. Figure 10 shows the valence band maxima (VBMs) for both regions. The VBM of point L is about 1.82 V, while for point T, it is about 1.74 V; the difference of 0.08 V is significantly above the limit of the experimental resolution. These VBM results reveal that point T is closer to the Fermi level than point L. This modulation of the Fermi level is primarily attributed to the existence of the Cr–O–Cl phase in the thick region. As reported in the KPFM results, the work function of point T is higher than that of point L. The difference between the work functions of these points in the KPFM results is about 0.06 V, which is consistent with the VBM results.

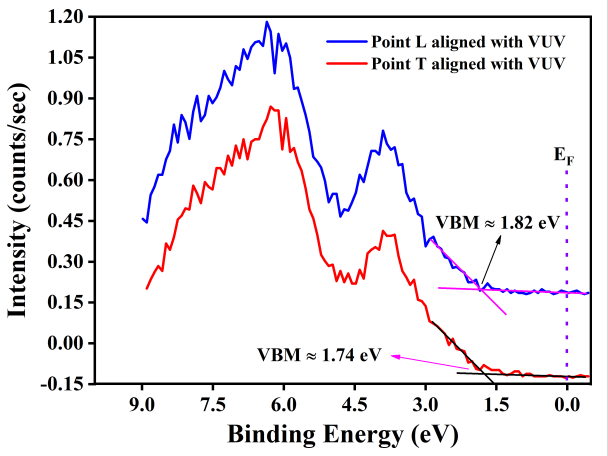

Figure 10: Valence band spectra acquired at point L (lean) and point T (thick). The spectra were aligned with respect to our previously published high-resolution photoemission spectra at 150 eV photon energy [8]. The alignment is shown in Supporting Information File 1, Figure S3.

Conclusion

Our work aimed at providing control of the surface evolution of thin specimens of $CrCl_3$, contributing to establishing a method to engineer the material. In this specific case, it is difficult to

find the reason of the composition modulation we have observed through the spatial resolved techniques. However, it could be the result of the combined effect of vacancies and a possibly induced dissociation of molecular oxygen. KPFM can be an interesting tool to describe the variation of chemical character of the 2D flakes with sizeable details. In Figure 11 we report the $CrCl_3$ values of surface potential measured under different conditions on flakes of various thicknesses on SiO_2 and ITO substrates. A steep increase of the surface potential represents the most evident variation on the $CrCl_3$ surface, where a higher surface potential is related to a higher level of oxidation of the thicker flakes, probably related to an increased density of Cl vacancies acting as dissociation centers and the formation of a Cl-defective or O/$CrCl_3$ surface structure [10,36]. Similarly to what was highlighted by the SPEM measurements, both measurements being surface-sensitive, the counter-intuitive finding of a lower degree of oxygen contamination is corroborating the conclusion that this behavior is a general trend for this material. This is an aspect of particular relevance because of the possible applications of the material to monolayer-thin devices.

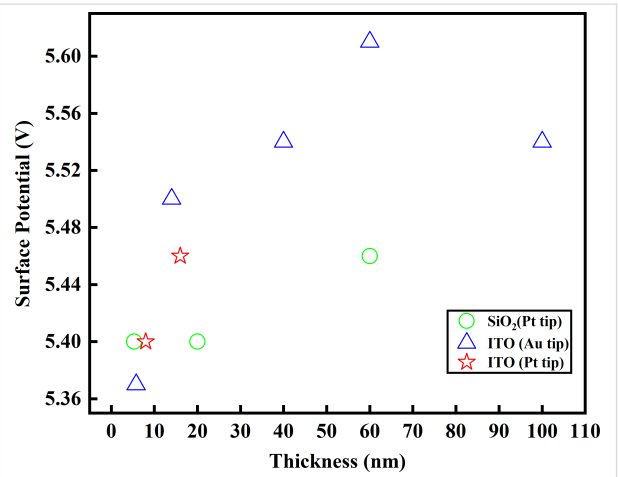

Figure 11: The surface potential values of $CrCl_3$ flakes after several experiments as function of the flake thicknesses determined by AFM. Green: 285 nm SiO_2 on Si substrate measured with Pt-coated tip (Kelvin potential 5.5 eV), red: ITO substrate (190 nm) on glass measured with a Pt-coated tip, and blue: ITO substrate (190 nm) on glass measured with a Au-coated tip (Kelvin potential 5.1 V).

Experimental

The preparation of exfoliated $CrCl_3$ flakes from the single crystal bulk material was reported in our previous papers [2,11]. Though preferentially a 270 nm silicon oxide substrate would help the determination of flakes thickness, we used also a more conductive substrate to measure photoemission under X-ray irradiation, that is, 1 nm thick native oxide Si substrates. Another convenient substrate for SPEM was 190 nm thick indium-doped tin oxide on glass, guaranteeing the necessary conductivity during the photoemission process. The 190 nm thickness was also important during the process of optical selection by showing significant contrast in an optical microscope (×50 magnification), helping a better localization of thin flakes. The SPEM measurements were performed at the ESCA Microscopy beamline 2.2L of Elettra Synchrotron Trieste facility, Italy. The incident photon energy of ≈740 eV was calibrated by means of Au $f_{7/2}$ at 84.0 eV from a clean gold foil sample. To reduce the beam-induced effects on the samples, we recorded the high-energy-resolution spectra with an unfocused beam (≈2.0 μm diameter), while the high-resolution SPEM maps of 128 × 128 μm^2 size using a piezoelectric driven stage were obtained with a focused beam (pixel size of 130 nm) by means of a Fresnel zone and a relatively broad energy resolution mode [23]. The SPEM maps were captured through a 48-channel delay line detector.

To analyze the photoelectron intensity of an individual atomic element on the captured SPEM maps, the image underwent background correction by eliminating the topographic features. We also applied the (3 × 3) filter to reduce the noise before extracting the photoemission spectra from the particular SPEM map. Figure 3 shows the schematic setup of the focusing optics and the hemispherical photoelectrons detector arrangement of the SPEM system.

Atomic force microscopy images were acquired with the NanoObserver (CSI) AFM system in resonant mode using an n-type Si cantilever coated with Pt at the resonance frequency of 68 kHz with an elastic constant of 1–5 N/m (AppNano) and doped diamond tips with 120 kHz and 8 N/m elastic constant (ADAMA). Kelvin probe force microscopy images were taken via double passage before and after applying an electric field by elevating the tip about 50–150 nm to measure the surface potential and avoid the influence of morphological features. The applied voltage was varied from 0.2 to 1 V without significant changes in the measured surface potential value. All micrographs were recorded at room temperature.

Supporting Information

Supporting Information File 1

Technical details.
[https://www.beilstein-journals.org/bjnano/content/supplementary/2190-4286-16-58-S1.pdf]

Acknowledgements

The authors acknowledge that the results presented in this paper were initially discussed at the Società Italiana Luce di Sincro-

trone meetings 2021 and at the IEEE Nanotechnology Materials and Devices Conference (NMDC) in 2023 through poster and oral presentations, respectively. Furthermore, we refer to the abstract published as part of the conference proceedings (doi:10.1109/NMDC57951.2023.10344256).

Funding

This work has been funded by the European Union - NextGenerationEU under the Italian Ministry of University and Research (MUR) National Innovation Ecosystem grant ECS00000041 - VITALITY - Spoke 9 and the PNNR MUR Project PE0000023 NQSTI.

Author Contributions

Shafaq Kazim: conceptualization; data curation; formal analysis; investigation; methodology; project administration; validation; visualization; writing – original draft; writing – review & editing. Rahul Parmar: conceptualization; data curation; investigation; methodology; resources; validation; writing – review & editing. Maryam Azizinia: writing – review & editing. Matteo Amati: conceptualization; formal analysis; investigation; methodology; project administration; resources; software; supervision; validation; writing – review & editing. Muhammad Rauf: formal analysis; validation; writing – review & editing. Andrea Di Cicco: resources; writing – review & editing. Seyed Javid Rezvani: conceptualization; methodology; writing – review & editing. Dario Mastrippolito: methodology; writing – review & editing. Luca Ottaviano: conceptualization; methodology; resources; supervision; writing – review & editing. Tomasz Klimczuk: resources; writing – review & editing. Luca Gregoratti: conceptualization; formal analysis; investigation; methodology; project administration; resources; software; supervision; writing – review & editing. Roberto Gunnella: conceptualization; data curation; investigation; methodology; project administration; resources; supervision; validation; visualization; writing – original draft; writing – review & editing.

ORCID® iDs

Shafaq Kazim - https://orcid.org/0000-0001-6288-7354
Maryam Azizinia - https://orcid.org/0000-0003-2483-5806
Dario Mastrippolito - https://orcid.org/0000-0001-6360-7254
Roberto Gunnella - https://orcid.org/0000-0003-4739-6375

Data Availability Statement

Data generated and analyzed during this study is available from the corresponding author upon reasonable request.

Preprint

A non-peer-reviewed version of this article has been previously published as a preprint: https://doi.org/10.3762/bxiv.2025.5.v1

References

1. Huang, B.; Clark, G.; Navarro-Moratalla, E.; Klein, D. R.; Cheng, R.; Seyler, K. L.; Zhong, D.; Schmidgall, E.; McGuire, M. A.; Cobden, D. H.; Yao, W.; Xiao, D.; Jarillo-Herrero, P.; Xu, X. *Nature* **2017,** *546,* 270–273. doi:10.1038/nature22391
2. Kazim, S.; Alì, M.; Palleschi, S.; D'Olimpio, G.; Mastrippolito, D.; Politano, A.; Gunnella, R.; Di Cicco, A.; Renzelli, M.; Moccia, G.; Cacioppo, O. A.; Alfonsetti, R.; Strychalska-Nowak, J.; Klimczuk, T.; J Cava, R.; Ottaviano, L. *Nanotechnology* **2020,** *31,* 395706. doi:10.1088/1361-6528/ab7de6
3. Wang, J.; Ahmadi, Z.; Lujan, D.; Choe, J.; Taniguchi, T.; Watanabe, K.; Li, X.; Shield, J. E.; Hong, X. *Adv. Sci.* **2023,** *10,* 2203548. doi:10.1002/advs.202203548
4. Rhodes, D.; Chae, S. H.; Ribeiro-Palau, R.; Hone, J. *Nat. Mater.* **2019,** *18,* 541–549. doi:10.1038/s41563-019-0366-8
5. Kundu, A. K.; Liu, Y.; Petrovic, C.; Valla, T. *Sci. Rep.* **2020,** *10,* 15602. doi:10.1038/s41598-020-72487-5
6. Biesinger, M. C.; Brown, C.; Mycroft, J. R.; Davidson, R. D.; McIntyre, N. S. *Surf. Interface Anal.* **2004,** *36,* 1550–1563. doi:10.1002/sia.1983
7. Antoci, S.; Mihich, L. *Phys. Rev. B* **1978,** *18,* 5768–5774. doi:10.1103/physrevb.18.5768
8. Kazim, S.; Mastrippolito, D.; Moras, P.; Jugovac, M.; Klimczuk, T.; Ali, M.; Ottaviano, L.; Gunnella, R. *Phys. Chem. Chem. Phys.* **2023,** *25,* 3806–3814. doi:10.1039/d2cp04586a
9. Mastrippolito, D.; Wang, J.; Profeta, G.; Ottaviano, L. *JPhys Mater.* **2022,** *5,* 014004. doi:10.1088/2515-7639/ac5dcd
10. Mastrippolito, D.; Ottaviano, L.; Wang, J.; Yang, J.; Gao, F.; Ali, M.; D'Olimpio, G.; Politano, A.; Palleschi, S.; Kazim, S.; Gunnella, R.; Di Cicco, A.; Sgarlata, A.; Strychalska-Nowak, J.; Klimczuk, T.; Cava, R. J.; Lozzi, L.; Profeta, G. *Nanoscale Adv.* **2021,** *3,* 4756–4766. doi:10.1039/d1na00401h
11. Kazim, S.; Gunnella, R.; Zannotti, M.; Giovannetti, R.; Klimczuk, T.; Ottaviano, L. *J. Microsc. (Oxford, U. K.)* **2021,** *283,* 145–150. doi:10.1111/jmi.13015
12. Liu, L.; Zhai, K.; Nie, A.; Lv, W.; Yang, B.; Mu, C.; Xiang, J.; Wen, F.; Zhao, Z.; Zeng, Z.; Gong, Y.; Tian, Y.; Liu, Z. *ACS Appl. Nano Mater.* **2019,** *2,* 1597–1603. doi:10.1021/acsanm.9b00058
13. Kazim, S.; Sharma, A.; Yadav, S.; Gajar, B.; Joshi, L. M.; Mishra, M.; Gupta, G.; Husale, S.; Gupta, A.; Sahoo, S.; Ojha, V. N. *Sci. Rep.* **2017,** *7,* 881. doi:10.1038/s41598-017-00976-1
14. Banhart, F.; Kotakoski, J.; Krasheninnikov, A. V. *ACS Nano* **2011,** *5,* 26–41. doi:10.1021/nn102598m
15. Gao, Y.; Wang, J.; Li, Y.; Xia, M.; Li, Z.; Gao, F. *Phys. Status Solidi RRL* **2018,** *12,* 1800105. doi:10.1002/pssr.201800105
16. Zheng, Y. J.; Chen, Y.; Huang, Y. L.; Gogoi, P. K.; Li, M.-Y.; Li, L.-J.; Trevisanutto, P. E.; Wang, Q.; Pennycook, S. J.; Wee, A. T. S.; Quek, S. Y. *ACS Nano* **2019,** *13,* 6050–6059. doi:10.1021/acsnano.9b02316
17. Zhang, W.-B.; Qu, Q.; Zhu, P.; Lam, C.-H. *J. Mater. Chem. C* **2015,** *3,* 12457–12468. doi:10.1039/c5tc02840j
18. Xie, D.; Yang, F.; Qiu, X.; Hu, Y.; Sun, Y.; He, S.; Wang, X. *J. Appl. Phys.* **2024,** *135,* 235105. doi:10.1063/5.0206006
19. Haffad, S.; Benchallal, L.; Lamiri, L.; Boubenider, F.; Zitoune, H.; Kahouadji, B.; Samah, M. *Acta Phys. Pol., A* **2018,** *133,* 1307–1313. doi:10.12693/aphyspola.133.1307

20. Avsar, A.; Ciarrocchi, A.; Pizzochero, M.; Unuchek, D.; Yazyev, O. V.; Kis, A. *Nat. Nanotechnol.* **2019,** *14,* 674–678. doi:10.1038/s41565-019-0467-1
21. Liu, J.; Sun, Q.; Kawazoe, Y.; Jena, P. *Phys. Chem. Chem. Phys.* **2016,** *18,* 8777–8784. doi:10.1039/c5cp04835d
22. Pramanik, A.; Pandeya, R. P.; Ali, K.; Joshi, B.; Sarkar, I.; Moras, P.; Sheverdyaeva, P. M.; Kundu, A. K.; Carbone, C.; Thamizhavel, A.; Ramakrishnan, S.; Maiti, K. *Phys. Rev. B* **2020,** *101,* 035426. doi:10.1103/physrevb.101.035426
23. Zeller, P.; Amati, M.; Sezen, H.; Scardamaglia, M.; Struzzi, C.; Bittencourt, C.; Lantz, G.; Hajlaoui, M.; Papalazarou, E.; Marino, M.; Fanetti, M.; Ambrosini, S.; Rubini, S.; Gregoratti, L. *Phys. Status Solidi A* **2018,** *215,* 1800308. doi:10.1002/pssa.201800308
24. Parmar, R.; de Freitas Neto, D. B.; Kazim, S.; Rezvani, S. J.; Rosolen, J. M.; Gunnella, R.; Amati, M.; Gregoratti, L. *J. Alloys Compd.* **2021,** *888,* 161483. doi:10.1016/j.jallcom.2021.161483
25. Azizinia, M.; Salvato, M.; Castrucci, P.; Amati, M.; Gregoratti, L.; Parmar, R.; Rauf, M.; Gunnella, R. *Appl. Surf. Sci.* **2024,** *675,* 160899. doi:10.1016/j.apsusc.2024.160899
26. Rezvani, S. J.; Abdi, Y.; Parmar, R.; Paparoni, F.; Antonini, S.; Gunnella, R.; Di Cicco, A.; Amati, M.; Gregoratti, L.; Mazaheri, A.; Hajibaba, S. *ACS Appl. Nano Mater.* **2024,** *7,* 13712–13719. doi:10.1021/acsanm.4c02290
27. Kazim, S.; Gunnella, R.; Ottaviano, L.; Parmar, R.; Amati, M.; Gregoratti, L. Cl vacancy evaluation on the surface of $CrCl_3$ through ESCA microscopy. In *Società Italiana Luce di Sincrotrone Meeting 2021,* Società Italiana di Luce di Sincrotrone (SILS), 2021; pp 96–97.
28. Rohwerder, M.; Turcu, F. *Electrochim. Acta* **2007,** *53,* 290–299. doi:10.1016/j.electacta.2007.03.016
29. Nonnenmacher, M.; O'Boyle, M. P.; Wickramasinghe, H. K. *Appl. Phys. Lett.* **1991,** *58,* 2921–2923. doi:10.1063/1.105227
30. Gunnella, R.; Rezvani, S. J.; Kazim, S.; Azizinia, M.; Ottaviano, L.; Mastrippolito, D.; Parmar, R.; Gregoratti, L.; Amati, M. A Detailed examination of layer-dependent photoemission spectra and surface potential of $CrCl_3$. In *2023 IEEE Nanotechnology Materials and Devices Conference (NMDC),* 2023; p 173. doi:10.1109/nmdc57951.2023.10344256
31. Gregoratti, L.; Al-Hada, M.; Amati, M.; Brescia, R.; Roccella, D.; Sezen, H.; Zeller, P. *Top. Catal.* **2018,** *61,* 1274–1282. doi:10.1007/s11244-018-0982-6
32. Poteryaev, A. I.; Ferrero, M.; Georges, A.; Parcollet, O. *Phys. Rev. B* **2008,** *78,* 045115. doi:10.1103/physrevb.78.045115
33. Kim, J. H.; Lee, J.; Kim, J. H.; Hwang, C. C.; Lee, C.; Park, J. Y. *Appl. Phys. Lett.* **2015,** *106,* 251606. doi:10.1063/1.4923202
34. Neal, A. T.; Pachter, R.; Mou, S. *Appl. Phys. Lett.* **2017,** *110,* 193103. doi:10.1063/1.4983092
35. Kaushik, V.; Varandani, D.; Mehta, B. R. *J. Phys. Chem. C* **2015,** *119,* 20136–20142. doi:10.1021/acs.jpcc.5b05818
36. DeJarld, M.; Campbell, P. M.; Friedman, A. L.; Currie, M.; Myers-Ward, R. L.; Boyd, A. K.; Rosenberg, S. G.; Pavunny, S. P.; Daniels, K. M.; Gaskill, D. K. *Sci. Rep.* **2018,** *8,* 16487. doi:10.1038/s41598-018-34595-1

License and Terms

BEILSTEIN JOURNAL OF NANOTECHNOLOGY

Synchrotron X-ray photoelectron spectroscopy study of sodium adsorption on vertically arranged MoS_2 layers coated with pyrolytic carbon

Alexander V. Okotrub[1], Anastasiya D. Fedorenko[1], Anna A. Makarova[2,3], Veronica S. Sulyaeva[1], Yuliya V. Fedoseeva[1] and Lyubov G. Bulusheva[*1]

Full Research Paper

Open Access

Address:
[1]Nikolaev Institute of Inorganic Chemistry, SB RAS, 630090 Novosibirsk, Russia, [2]Physical Chemistry, Institute of Chemistry and Biochemistry, Free University of Berlin, 14195 Berlin, Germany and [3]Helmholtz-Zentrum Berlin für Materialien und Energie, 14109 Berlin, Germany

Email:
Lyubov G. Bulusheva[*] - bul@niic.nsc.ru

* Corresponding author

Keywords:
graphitic coating; molybdenum disulfide film; Na adsorption/desorption; sodium vapor; XPS

Beilstein J. Nanotechnol. **2025,** *16,* 847–859.
https://doi.org/10.3762/bjnano.16.64

Received: 31 March 2025
Accepted: 22 May 2025
Published: 10 June 2025

This article is part of the thematic issue "Exploring synchrotron radiation and free-electron laser tools for nanostructured materials".

Guest Editor: C. Bittencourt

Abstract

Hybrid materials consisting of molybdenum disulfide (MoS_2) and graphitic-like carbon have great potential for practical application as anodes in high-performance sodium-ion batteries. In this work, to reveal the effect of carbon coating on the interaction of sodium with the MoS_2 layers located vertically relative to the substrate, model experiments were carried out using synchrotron-radiation-induced X-ray photoelectron spectroscopy (XPS). Sodium vapor obtained by heating a sodium source was simultaneously deposited in vacuum on the surfaces of MoS_2, pyrolytic carbon, and a hybrid sample obtained by transferring a pyrolytic carbon film onto the MoS_2 film. According to XPS data, sodium easily penetrates into the space between the vertical layers of the uncoated film, and its interaction with MoS_2 leads to the transformation of the original hexagonal structure into a distorted tetragonal one. Under the experimental conditions, sodium is unable to diffuse through the carbon film consisting of horizontally oriented graphene domains and is almost completely removed by annealing the sample at 773 K in ultrahigh vacuum. The presence of the underlying MoS_2 film facilitates the diffusion of sodium through the graphitic coating, but not all of the deposited sodium reaches MoS_2. As a result, the sodium-induced rearrangement of the carbon-coated MoS_2 is less than that of the free MoS_2 film, and annealing of the sodiated sample restores its structure. The obtained results demonstrate the important role of the graphitic coating in the development of viable MoS_2-based electrodes for energy storage systems.

Introduction

Sodium-ion batteries (SIBs) attract increasing interest as a low-cost alternative to lithium-ion batteries due to the abundance and wide availability of sodium. Research in this field is currently focused on developing new electrode materials to increase the capacity and cycle life of SIBs. Molybdenum disulfide (MoS_2) has a layered structure and a high theoretical capacity of 669 $mAh \cdot g^{-1}$, so it is considered as a promising anode material for SIBs [1,2]. The large sodium ion can diffuse with a low energy barrier between the S−Mo−S layers due to the interlayer spacing of 0.62 nm and weak van der Waals interactions between them. At a sodium ion intercalation potential of about 1.4 V vs Na/Na^+, the thermodynamically preferred 2H-MoS_2 phase transforms into the metastable 1T-MoS_2 phase [3,4]. With further increase in the intercalated sodium concentration (according to calculations above 1.75 Na per unit MoS_2), the intercalate decomposes into amorphous Na_2S and Mo; this reaction occurs at potentials below 0.8 V vs Na/Na^+ [3]. The reaction products cannot be converted back to MoS_2 due to the strong Na–S bonding [5]. The irreversible conversion reaction resulting in low electrical conductivity and huge volume expansion of the anode material limits the application of MoS_2 anodes in high-energy SIBs. Thus, the main issues that need to be addressed for SIBs with MoS_2 anodes are long-term stability and high rate performance.

Conducting graphitic-like carbon additives have been proposed as an effective way to solve the problem of electrical conductivity and stability of MoS_2 anodes [6]. To date, several hybrid MoS_2–carbon anode materials have been developed, which have demonstrated excellent cycling stability and rate performance in SIBs, as well as high reversible specific capacity [7-16]. Moreover, it has been reported that the electrochemical reaction of MoS_2 with sodium ions could be reversible in the presence of graphitic components [17]. Wang et al. showed that in an anode material in which graphitic layers were sandwiched between MoS_2 layers, the MoS_2 component was not converted to Mo and Na_2S even at a high degree of sodiation [18]. An ex situ study of a fully sodiated anode composed of MoS_2 nanosheets coupled with few-layered graphene revealed a partial transformation of 2H-MoS_2 into a distorted tetragonal structure without significant formation of Mo and Na_2S [19]. The carbon coating improved the electrical contact between the MoS_2 agglomerates, while the sandwich-like structure of MoS_2-graphene facilitated the diffusion of sodium ions [20,21].

There are various possibilities to improve the properties of hybrid anodes based on MoS_2. The diffusion of sodium ions in layered MoS_2 is highly anisotropic. It is fast along the basal planes and is not possible through defect-free layers [3]. Thus, when the interlayer channels coincide with the Na^+ movement paths, the diffusion distance is shortened, resulting in fast intercalation reaction kinetics. Flower-like MoS_2–carbon hybrids have demonstrated superior alkali metal storage capability and high rate performance due to the fast Na^+ diffusion in radially orientated ultrathin MoS_2 and graphene layers; the latter component ensured high electron transfer and structural stability of the material [22-24].

The orientation of the carbon component in the hybrid can also affect the electrochemical processes. For example, interlayer-expanded MoS_2 nanosheets vertically anchored on graphene film and carbon fibers showed a good rate performance in SIBs [25,26]. It was shown that carbon coating on MoS_2 particles prevents their aggregation, increases conductivity and reduces structural expansion during electrochemical cycling [21,27]. Hybrid materials consisting of vertically oriented MoS_2 layers and graphitic carbon coating with horizontal layer orientation remain poorly understood with respect to sodium-ion storage behavior. Comprehensive studies in this direction are needed.

In this work, a thin MoS_2 film with vertically aligned layers was coated by a thin film of pyrolytic carbon (PyC) with predominantly horizontal orientation of graphitic domains. The resulting hybrid and individual films of MoS_2 and PyC were placed on the same sample holder to study the interaction with sodium vapor in the ultrahigh vacuum (UHV) chamber of the experimental station of the Russian–German beamline at the BESSY-II synchrotron radiation facility. Such model experiments make it possible to differentiate the diffusion rate of sodium in the hybrid and to identify the possible synergistic effect of the components in their interaction with sodium. Previously reported similar model experiments on lithiation of graphene [28], MoS_2 crystals [29-31], and MoS_2–graphene heterostructures [32] demonstrated an advantage in studying the interaction of lithium with carbon and other elements of the materials. It should be noted that anode materials with alkali ions introduced during electrochemical reactions in SIBs are difficult to study because of the presence of electrolyte decomposition residues.

Results and Discussion

Figure 1a shows the schematic diagram of the synthesis route of a hybrid film consisting of MoS_2 coated with PyC. A molybdenum layer is deposited on a SiO_2/Si substrate by magnetron sputtering for a short time of 10 s. This layer interacts with sulfur vapor at a temperature of 873 K for 30 min. Heating the raw film in a hydrogen atmosphere at 1073 K removes excess sulfur and other contaminations from the film surface. In the final step, a thin PyC film synthesized by chemical vapor deposition (CVD) technique is placed on the surface of the cleaned MoS_2 film using the wet transfer method (see the Experimental

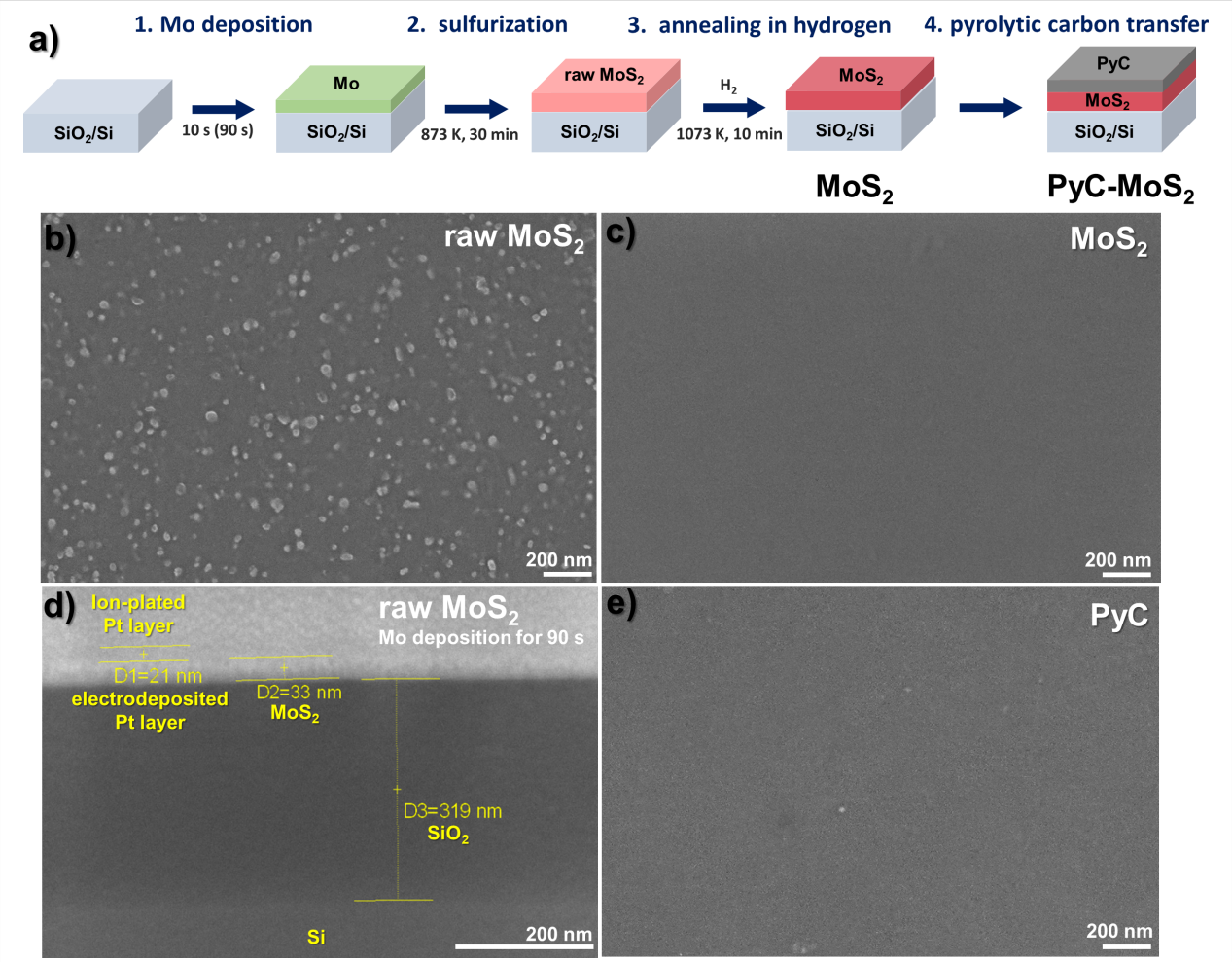

Figure 1: (a) Schematic diagram of the synthesis of MoS_2 and PyC-MoS_2 films. SEM images of the top view of (b) the raw MoS_2 film obtained using a Mo layer sputtered for 10 s and (c) the film after heating in hydrogen. (d) Cross-sectional view of the MoS_2 film obtained using a Mo layer sputtered for 90 s and (e) the top view of the PyC film on a SiO_2/Si substrate.

section for details). The resulting hybrid, designated PyC-MoS_2, together with a surface-cleaned MoS_2/SiO_2/Si sample and a PyC film transferred onto a SiO_2/Si substrate, were used to comparatively study the ability to adsorb and accumulate evaporated sodium.

The scanning electron microscopy (SEM) images of the surface of raw MoS_2 film, hydrogen-annealed film, and PyC film are compared in Figure 1b,c,e. The raw MoS_2 film covers the entire area of the substrate and contains polysulfide nanoparticles on the surface (Figure 1b). These nanoparticles are absent on the surface of the MoS_2 film annealed in a hydrogen atmosphere (Figure 1c). An attempt to measure the cross section of this film did not yield a contrast image because of the charging effect. Therefore, to estimate the thickness of the studied film, we used a thicker MoS_2 film synthesized with a molybdenum layer sputtered for 90 s. Part of the film surface was covered with a protective Pt layer and a lamella was cut using a focused ion beam (FIB) system (see the Experimental section for details). Figure 1d shows the SEM image of the cross section of the lamella. The bright round spots on the film surface correspond to Pt nanoparticles, the presence of which is confirmed by energy-dispersive X-ray (EDX) spectroscopy (Supporting Information File 1, Figure S1). These nanoparticles have a uniform size and are densely distributed on the sample surface, in contrast to the polysulfide particles of different sizes formed during CVD synthesis (Figure 1b). The thickness of the MoS_2 film estimated from the cross-sectional SEM image is about 33 nm (Figure 1d). Therefore, it can be estimated that the MoS_2 film obtained using a molybdenum layer sputtered for 10 s has a thickness of no more than 4 nm. The SEM image of PyC transferred onto the SiO_2/Si substrate also shows a uniform film surface (Figure 1e).

The Raman spectrum of the MoS_2 film contains two strong peaks at 382.6 and 408.9 cm^{-1} (Figure 2a) corresponding to the

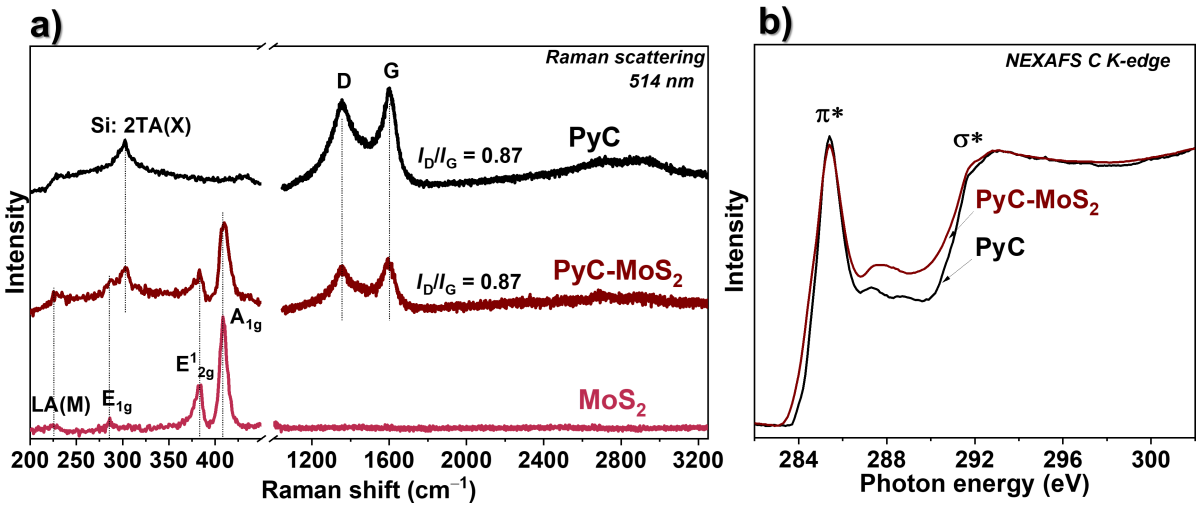

Figure 2: (a) Raman spectra of MoS_2, PyC-MoS_2, and PyC films. (b) NEXAFS C K-edge spectra of PyC and PyC-MoS_2 films.

E^1_{2g} mode and the A_{1g} mode, respectively, of 2H-MoS_2 [33]. The difference between the positions of these peaks is often used to determine the number of layers in MoS_2 particles [34]. The distance between the peaks of ≈26.3 cm^{-1} for the MoS_2 film is similar to that for bulk MoS_2 [35]. Because of the small thickness of the MoS_2 film, such a large number of the layers can be realized only when they are oriented vertically to the substrate surface. The weak peak at about 280 cm^{-1} observed in the Raman spectrum corresponds to the E_{1g} mode, which is forbidden when the laser beam is incident perpendicularly on the *c* axis of MoS_2 [36]. The activation of this mode in our case confirms the vertical orientation of the MoS_2 layers relative to the substrate surface [37]. The weak defect-induced mode LA(M) at 227 cm^{-1} and the asymmetric shape of the E^1_{2g} and A_{1g} modes indicate the nanometer size of the MoS_2 crystallites in the plane [38,39]. All the above modes are visible in the Raman spectrum of the PyC-MoS_2 sample, so the coating with PyC film does not destroy the structure of the MoS_2 film. The Raman spectra of PyC and PyC-MoS_2 show a peak at 1600 cm^{-1} corresponding to the in-plane stretching of C=C bonds (G mode) and a peak at 1355 cm^{-1} caused by the disorder in the graphite lattice (D mode) [40]. The position of the G mode is higher than the position of the G peak at 1582 cm^{-1} for crystalline graphite and graphene [41], indicating the disorder in the layers and their functionalization. In fact, the intensity ratio of the D to G peaks (I_D/I_G) of 0.87 is relatively high. The weak second-order band between 2700 and 2900 cm^{-1} is due to the three-dimensional ordering along the *c* axes of the graphitic film.

The NEXAFS spectra measured at the C K-edge of PyC and PyC-MoS_2 films pre-annealed in UHV at 673 K for 10 min exhibit two main resonances located at 285.4 and 291.8 eV (Figure 2b), which are attributed to the electron transitions from the C 1s core levels to the π* and σ* C=C states in the graphitic structure, respectively [42]. The rather sharp shape of the π* resonance indicates the graphitic-like structure of the PyC film. Weak features appearing between the π* and σ* resonances suggest that the PyC film is slightly functionalized with oxygen- and/or hydrogen-containing groups. The spectrum of the PyC-MoS_2 film almost repeats the shape of the spectrum of the PyC film. A slight decrease in the intensity of the π* resonance and an increase in the intensity in the regions before and after the π* resonance at 284–285 eV and 286–289 eV can be associated with the interaction between PyC and MoS_2 components [43]. The shift of the C K-edge spectrum of the PyC-MoS_2 film toward lower photon energies corresponds to the electron density transfer from the carbon component to MoS_2, as shown by density functional theory (DFT) calculations for the MoS_2/graphene heterostructure [44,45]. According to the DFT calculations, the changes observed in the PyC-MoS_2 spectrum between the π* and σ* resonances may result from the interaction of the π electrons of carbon with the p orbitals of sulfur [44].

Figure 3 shows the sequence of a three-step sodiation/desodiation experiment performed with samples in the UHV chamber of the spectrometer. Sodium vapor was deposited simultaneously on three studied samples for 10 min. The second step included additional deposition of sodium for 20 min. The thickness of the sodium layer was measured using a quartz microbalance; it was 2.5 Å after the 10 min experiment and 7.6 Å after the 30 min experiment. In the third step, the samples with deposited sodium were annealed at 773 K for 30 min. The XPS spectra were measured before the three-step experiment and after each modification.

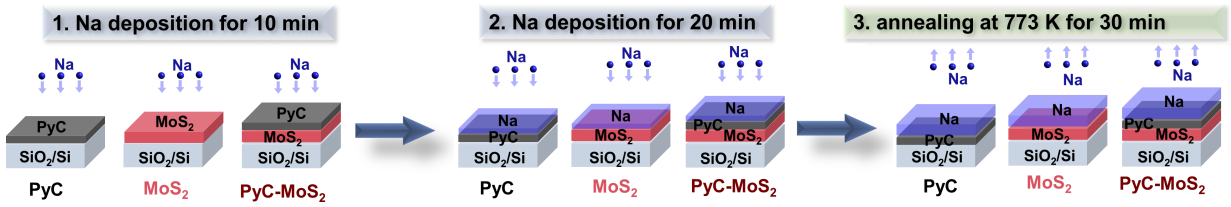

Figure 3: Schematic diagram of sequential processing of PyC, MoS_2, and PyC-MoS_2 films, comprising three steps: (1) sodium deposition for 10 min, (2) sodium deposition next 20 min, (3) vacuum annealing at 773 K for 30 min.

Survey XPS spectra of the samples revealed the presence of molybdenum, sulfur, carbon, sodium, and oxygen (Supporting Information File 1, Figure S2). The intense lines of silicon and oxygen detected in the spectrum of the PyC film are associated with the substrate. The absence of the Si 2p line in the spectra of MoS_2 and PyC-MoS_2 films indicates the formation of a continuous MoS_2 film with a thickness of more than 3 nm [46]. The atomic concentrations of Mo and S in the MoS_2 film are about 9 and 28 atom %, respectively, and decrease to about 2 and 7 atom % after coating the film with PyC.

Figure 4 compares the S/Mo, Na/Mo, and Na/C ratios in the samples determined from the XPS survey spectra measured at excitation photon energies of 470 and 830 eV. The former energy provides a probing depth of about 1 nm and therefore allows for the determination of the surface composition of the films. At 830 eV, the probing depth is about 3 nm, which corresponds to almost the entire volume of the thin films under study. The S/Mo ratio in the MoS_2 film is 6 on the surface and 3.1 in the bulk (Figure 4a,b). Excess sulfur in the MoS_2 film is associated with the formation of polysulfide groups on the surface due to the synthesis conditions, including the increased content of sulfur vapor. An additional factor for the high S/Mo surface ratio is the vertical orientation of the MoS_2 layers. The S/Mo values determined for the PyC-MoS_2 sample and after deposition/removal of sodium deviate from the corresponding values for the initial MoS_2 film by no more than 16% for the surface and 9% for the bulk. The deviations may be due to the fact that it is practically impossible to record spectra from the same place on the sample, which is repeatedly moved between the preparation and measurement chambers.

The Na/Mo ratio on the surface of the MoS_2 film is 2.0 after Na deposition for 10 min, 5.5 after additional Na deposition for

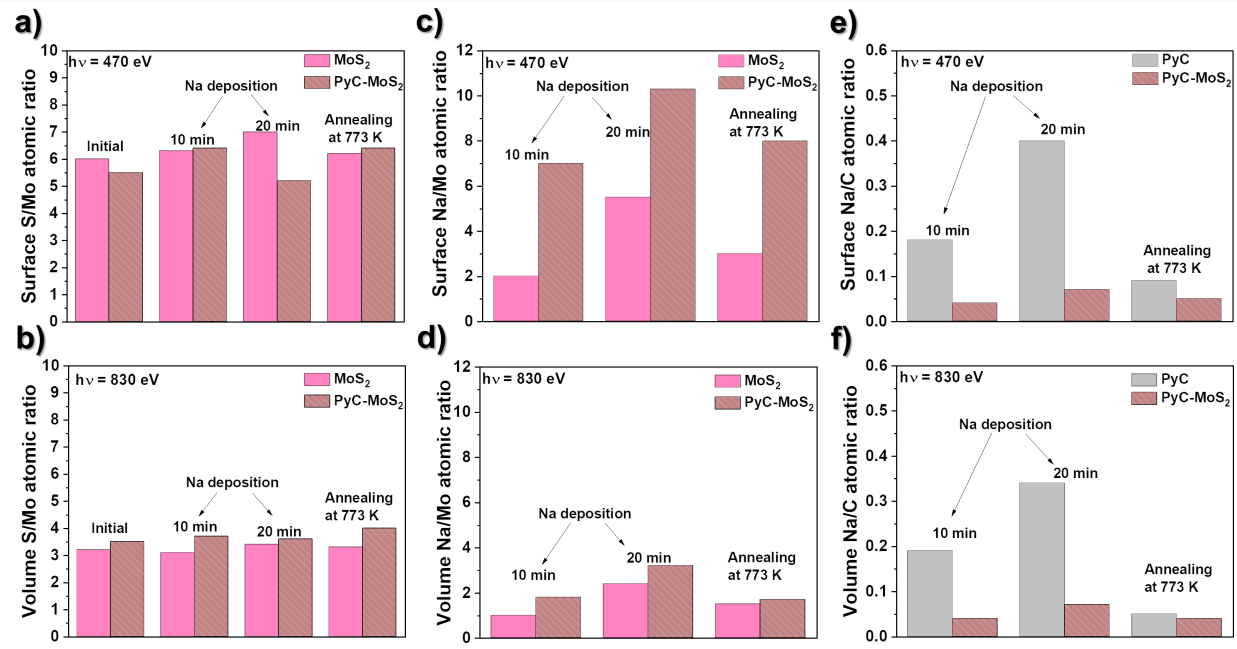

Figure 4: (a, b) XPS-derived atomic concentration ratios of sulfur to molybdenum (S/Mo), (c, d) sodium to molybdenum (Na/Mo), and (e, f) sodium to carbon (Na/C) directly on the surface (470 eV excitation, top line) and deeper from the surface (830 eV excitation, bottom line) of PyC, MoS_2, and PyC-MoS_2 films.

20 min, and 3.0 after annealing (Figure 4c). The corresponding Na/Mo ratios in the bulk of the MoS_2 film are 1.0, 2.4, and 1.5 (Figure 4d). The Na content in the bulk is approximately two times smaller than that on the surface because of the slower Na diffusion rate as compared to the deposition rate. However, the increase in the sodiation time leads to an increase in the sodium content not only on the surface but also in the interior of the film. After annealing, the Na/Mo ratio decreased both on the surface and in the bulk of the MoS_2 film. The results show that sodium can easily penetrate into the film consisting of vertically aligned MoS_2 layers and be partially released during annealing.

The concentration of Na in the PyC-MoS_2 film determined from the XPS survey spectra measured at 830 eV is about 6 atom % after sodium vapor deposition for 10 min, and this value does not change after an additional deposition of 20 min (Supporting Information File 1, Figure S2). This suggests that in the hybrid film, Na was not trapped in the upper PyC layer, but penetrated deeper into MoS_2. The similar Na/C ratios for the surface (Figure 4e) and bulk (Figure 4f) of the PyC film and the PyC-MoS_2 film indicate that sodium is fairly uniformly distributed within the carbon component. Thus, the sodiation of the PyC-MoS_2 film results in Na/C ratios of 0.05 and 0.07 after Na deposition for 10 min and additional 20 min, respectively. These values are about five times lower than those in sodiated PyC, indicating that sodium preferentially passes through the PyC film to be stored on the surface of MoS_2 rather than within its volume. The Na/C ratio in the annealed sodiated PyC-MoS_2 is similar to that of PyC. The PyC-MoS_2 hybrid film exhibits high recovery because a significant portion of Na is removed from the film surface after annealing, similar to what occurs with the pure PyC film.

A comparison of the XPS Mo 3d spectra of MoS_2 and PyC-MoS_2 films is shown in Figure 5. The low-energy peak at 226.1–226.3 eV corresponds to the S 2s line. The Mo 3d spectra of the initial MoS_2 and PyC-MoS_2 consist of an intense spin–orbit doublet with the binding energy of the Mo $3d_{5/2}$ component of 228.9 eV (Figure 5a,b). This energy corresponds to the Mo^{4+} state in 2H-MoS_2 [47]. In addition to the main peak, there are two weak doublets with Mo $3d_{5/2}$ binding energies of 230.1–230.3 eV and 231.6–231.9 eV, which belong to the oxidized forms of molybdenum in the Mo^{5+} and Mo^{6+} sates, respectively [48].

The XPS S 2p spectra of the initial MoS_2 and PyC-MoS_2 films exhibit an intense doublet with the S $2p_{3/2}$ component located at 161.7–161.8 eV (Figure 6a,b), corresponding to the S^{2-} sate [49]. In addition, the spectra contain two weak doublets, with the S $2p_{3/2}$ component at a binding energy of 163.4 eV, characteristic of S_2^{2-} and polysulfide groups [50], and at 160.5 eV, associated with under-coordinated sulfur atoms formed at the MoS_2 edges [51] as a result of preliminary sample annealing in H_2 at 1073 K.

The Mo 3d (Figure 5) and S 2p spectra (Figure 6) of MoS_2 and PyC-MoS_2 films after sodium deposition exhibit additional low-energy doublets with the Mo $3d_{5/2}$ component at ≈228.5 eV and the S $2p_{3/2}$ component at ≈162.0 eV. These energies are characteristic for the distorted tetragonal 1T′-MoS_2 [52]. Similar spectral changes were observed earlier after lithiation and sodiation of MoS_2 and were associated with the transfer of electron density from alkali metals to MoS_2, which led to the 2H–1T′ transition [19,32,53,54]. Such structural transformations are accompanied by the formation of Mo–Mo and Na–S bonds and the weakening of S–Mo bonds [3]. In the spectra of sodiated films, the Mo 3d and S 2p doublets related to sodium-free 2H-MoS_2 are retained, but their positions shift toward higher energies as compared to the spectra of the initial samples. The shift value of the Mo 3d and S 2p components of 2H-MoS_2 increases with the deposited sodium concentration because of increased charge doping. The intensity of Mo 3d and S 2p components attributed to sodiated 1T′-MoS_2 increases with sodium deposition time because more sulfur is bound to sodium. The areas of the 1T′-MoS_2 doublet are similar in the Mo 3d spectra of MoS_2 and PyC-MoS_2 after sodium deposition for 10 min and constitute 7–8% of the total spectrum area (Figure 5). After additional sodium deposition for 20 min, the relative area of this doublet increases to 31% for the MoS_2 film and to 25% for the PyC-MoS_2 film. The smaller 1T′-MoS_2 contribution in the latter case implies that the portion of sodium accumulated in the MoS_2 structure of the carbon-containing PyC-MoS_2 film is less than that in the bare MoS_2 film. Annealing of the sodiated MoS_2 and PyC-MoS_2 in vacuum at 773 K leads to a decrease in the intensity of the 1T′-MoS_2 doublet, which is more pronounced for the latter sample. Sodium is more easily released from the hybrid film because it is predominantly located on its surface and interacts more weakly with PyC than with MoS_2.

The analysis of XPS C 1s spectra of PyC and PyC-MoS_2 films before and after sodium deposition followed by annealing is used to reveal the contribution of the PyC component to the interaction of PyC-MoS_2 with sodium (Figure 7). The XPS C 1s spectrum of the PyC film shows an asymmetric peak at 284.4 eV (Figure 7a), which is typical for graphite-like carbon. In addition, there is a low-intensity component with a binding energy of 286.2 eV, corresponding to C–O bonds [55]. The C 1s spectrum of PyC-MoS_2 has a similar shape (Figure 7b), indicating that the PyC films transferred onto the surface of the SiO_2/Si substrate and the MoS_2 film have the same structure.

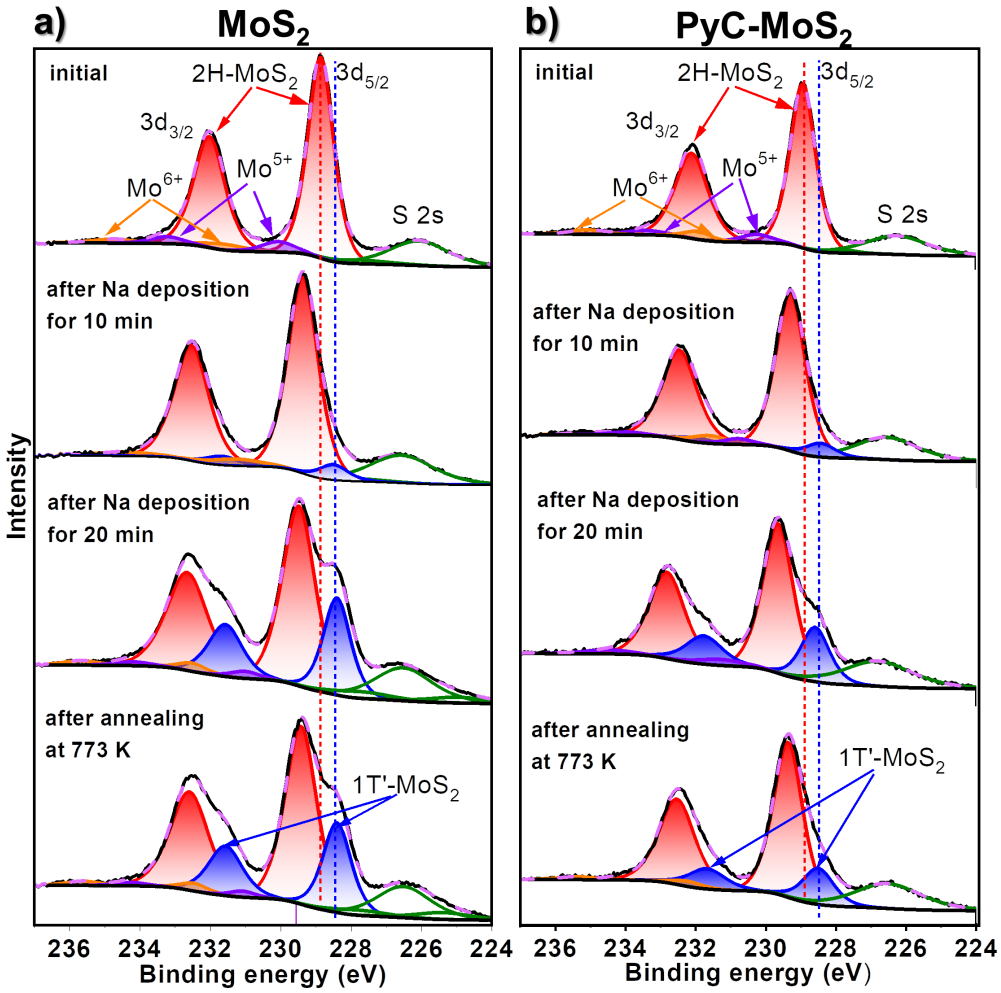

Figure 5: XPS Mo 3d spectra of (a) MoS_2 and (b) PyC-MoS_2 before and after sodium deposition for 10 min and additional 20 min and then after vacuum annealing at 773 K. The spectra were measured at 830 eV.

After sodium deposition on the PyC film for 10 min and then 20 min, the sp^2 peak shifts by 0.5 and 0.6 eV, respectively, towards higher binding energies. This shift is due to the charge transfer from sodium to the carbon layers. For PyC-MoS_2, the shifts of the C 1s line caused by sodium deposition are smaller. A new high-energy component (Na-sp^2) appearing at 286 and 285 eV in the spectra of sodiated PyC and PyC-MoS_2 films, respectively, is due to carbon bonding with sodium. The intensity of this component is lower in the PyC-MoS_2 spectrum measured after the total 30 min sodiation process. This is due to the lower charge transfer from sodium to the PyC component in the hybrid film as compared to the free PyC film, caused by its diffusion into the MoS_2 component. According to the XPS data, sodium is redistributed between the components of PyC-MoS_2.

After annealing, most of the sodium was removed from the PyC film, since the C 1s spectrum measured after this treatment completely returned to the spectrum of initial PyC (Figure 7a). In contrast to the PyC film, a significant portion of sodium remained in the PyC-MoS_2 film after annealing. The shift of the sp^2 component by 0.1 eV and the presence of a weak Na-sp^2 component in the spectrum (Figure 7b) confirm that residual sodium interacts with carbon component.

The XPS Na 2s spectra of sodiated samples before and after annealing are presented as a single symmetric peak located at a binding energy of ≈65 eV for the PyC film and at ≈64 eV for the MoS_2 film (Supporting Information File 1, Figure S3). The Na 2s spectrum of PyC-MoS_2 film exhibits one peak at an intermediate position of 64.4 eV, confirming that Na binds with both PyC and MoS_2 components.

Figure 8 schematically illustrates the difference in the sodium adsorption and desorption on the samples under study. Sodium

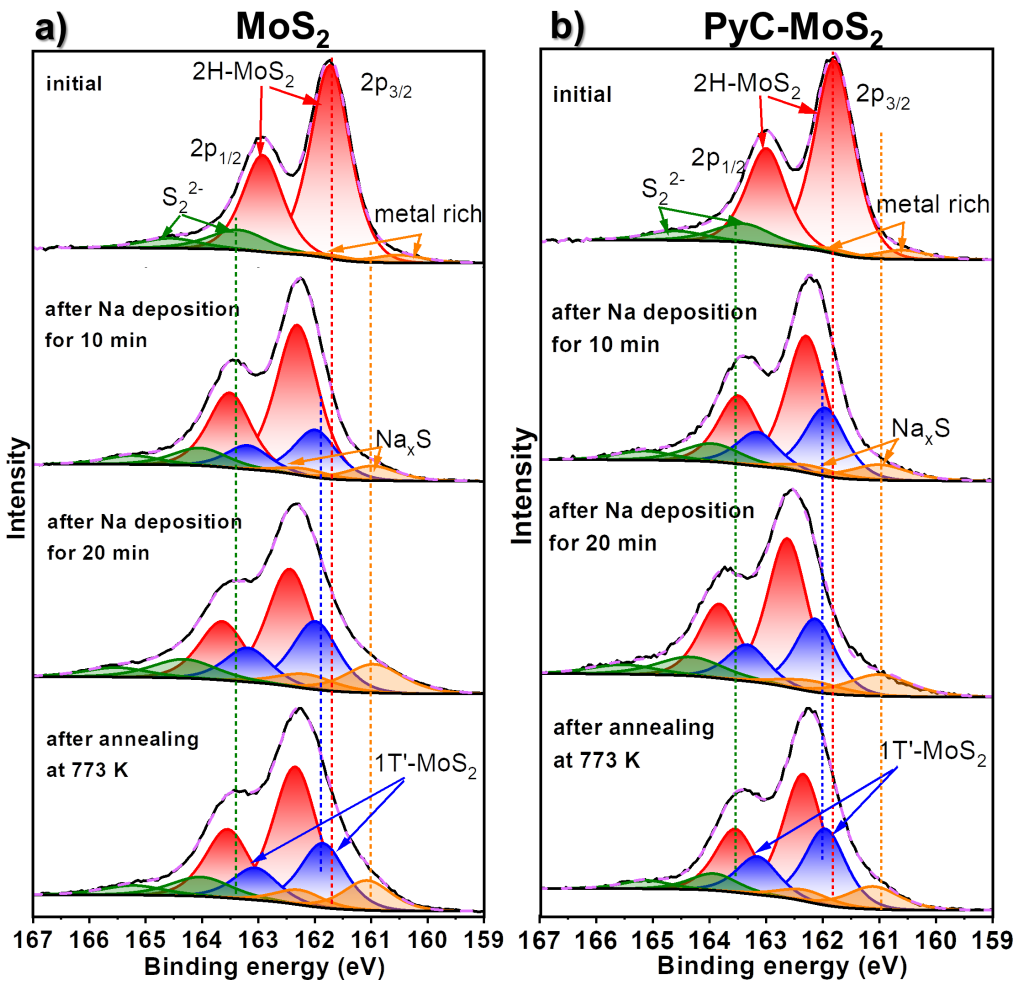

Figure 6: XPS S 2p spectra of (a) MoS_2 and (b) PyC-MoS_2 before and after sodium deposition for 10 min and additional 20 min and then after vacuum annealing at 773 K. The spectra were measured at 830 eV.

deposition for 30 min on the PyC film results in a high Na/C ratio of 0.34 at a depth of 3 nm. Sodium is not only adsorbed on the film surface but also accumulates in the film volume, most likely between the graphitic layers. According to the XPS C 1s spectra, an electron density transfer from sodium to carbon occurs. Vacuum annealing of the sodiated PyC film at 773 K removes most of the sodium. The Na/C ratio in the sample is 0.05.

Deposition of the same amount of sodium on the MoS_2 film gives a Na/Mo ratio of 2.4. Half of the sodium is located on the film surface. The high Na/Mo ratio can be explained by the easy penetration of sodium into the vertically oriented layers of the MoS_2 film. The XPS Mo 3d spectra reveal that the intercalation of sodium between the MoS_2 layers leads to a 2H–1T′ transition and electron charge doping from sodium. The Na/Mo ratio decreases after annealing of the sodiated MoS_2 film because of the partial removal of sodium, primarily from the film surface. After annealing, the sodiated MoS_2 film still contains a high concentration of sodium in its bulk, since the Na/Mo ratio is 1.5. The annealing conditions used are insufficient to remove all the sodium from the MoS_2 film and restore its initial 2H structure.

In the case of the PyC-MoS_2 hybrid, the top PyC layer traps some of the sodium, so the amount of sodium that penetrates into MoS_2 and accumulates there is less than for the bare MoS_2 film. It should be noted that the Na/C ratio in the sodiated PyC-MoS_2 film is approximately five times smaller than in the sodiated PyC film. Sodium atoms prefer to diffuse through PyC to the more attractive MoS_2, but some of them are retained in the carbon layers. The horizontally oriented graphitic layers act as a barrier and prevent sodium from penetrating into the underlaying MoS_2 film. In the PyC-MoS_2 hybrid, sodium accumula-

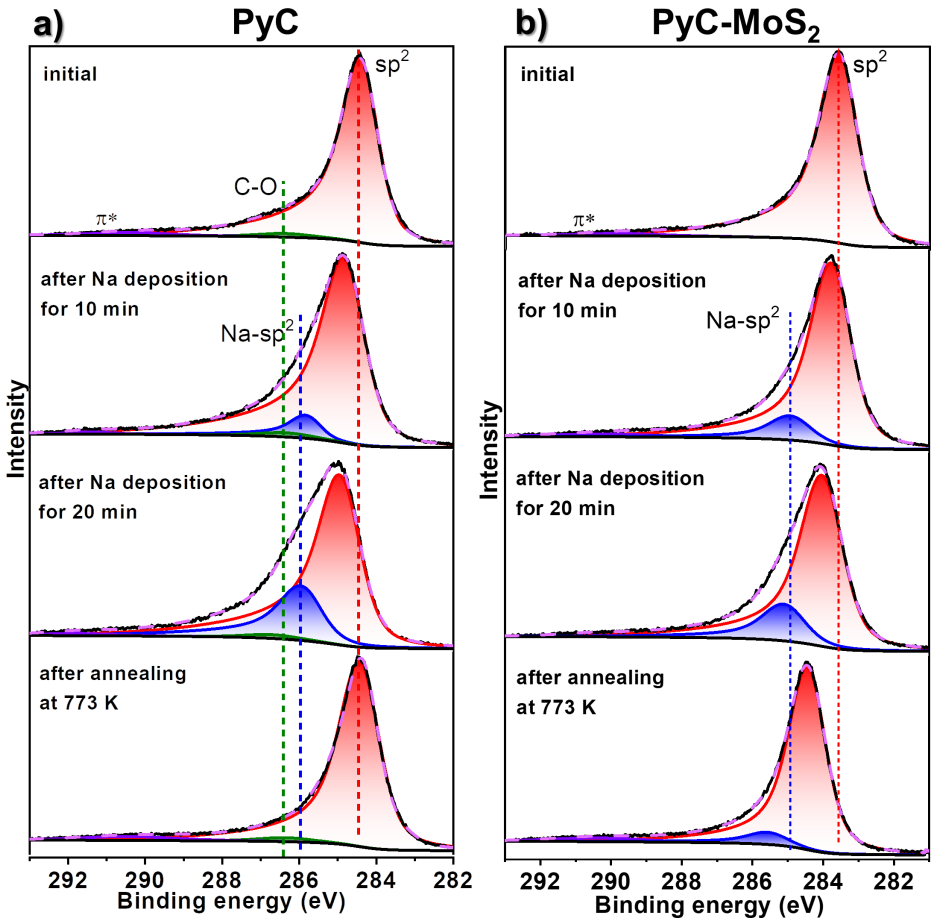

Figure 7: XPS C 1s spectra of (a) MoS_2 and (b) PyC-MoS_2 before and after sodium deposition for 10 min and additional 20 min and then after vacuum annealing at 773 K. The spectra were measured at 830 eV.

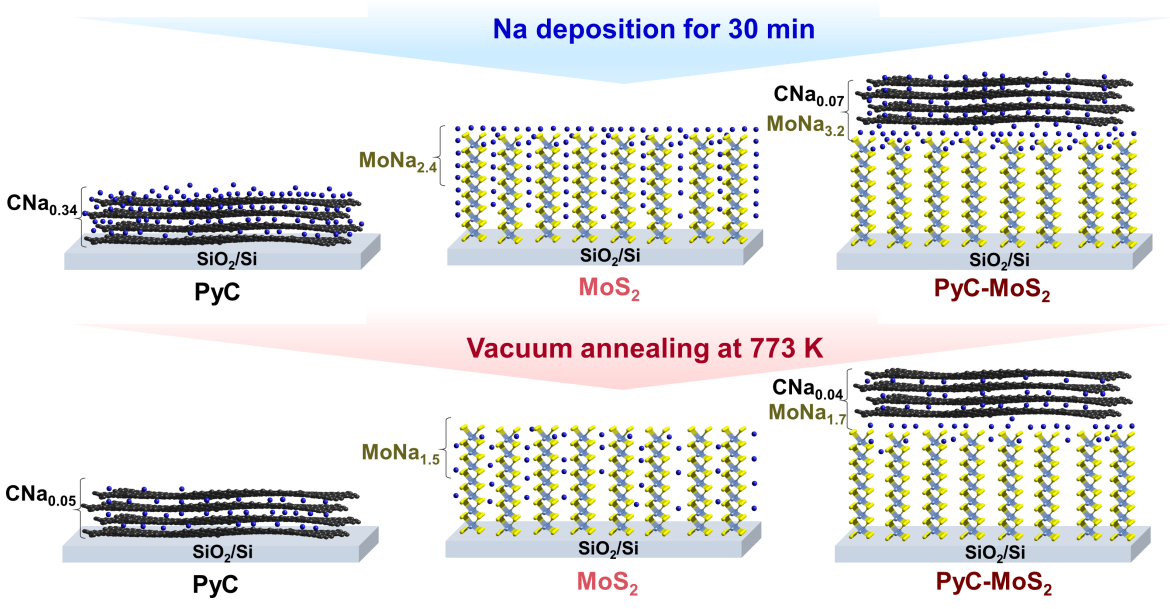

Figure 8: Scheme of the sodium deposition on PyC, MoS_2, and PyC-MoS_2 films and subsequent vacuum annealing.

tion occurs more on the MoS_2 surface or at the interface between MoS_2 and PyC, than in the bulk of MoS_2. Annealing causes sodium to leave the PyC coating to a lesser extent than in PyC alone, but it is released from the MoS_2 component more readily than from uncoated MoS_2. It can be concluded that the graphite layers introduced into the MoS_2 anode material will play a key role in the diffusion and storage of sodium during the charge–discharge of SIBs.

Conclusion

Synchrotron XPS tool is invoked to study sodium adsorption/desorption in thin films of graphitic PyC, vertically aligned MoS_2 layers, and PyC-MoS_2. The MoS_2 film with a thickness of about 4 nm was synthesized by sulfurization of a molybdenum layer deposited on a SiO_2/Si substrate using magnetron sputtering. Raman spectroscopy and SEM revealed the vertical orientation of the MoS_2 layers relative to the substrate surface. According to XPS data, the surface of the MoS_2 film is enriched with sulfur even after its annealing at 1073 K in hydrogen. PyC films were synthesized by CVD and transferred onto the surfaces of SiO_2/Si and MoS_2. PyC, MoS_2 film, and PyC-MoS_2 hybrid were used to deposit equal amounts of sodium via evaporation in UHV. Analysis of XPS data revealed a higher sodium concentration on the PyC-MoS_2 surface than on the MoS_2 surface since the PyC top layer and the hybrid interface accumulate sodium. Sodium deeply penetrated into the bare MoS_2 film, causing a transition from the 2H structure to the 1T´ structure due to the transfer of electron density to MoS_2. Annealing of sodiated samples at 773 K in ultrahigh vacuum resulted in almost complete removal of sodium from PyC and its retention on the surface and in the bulk of the MoS_2 film. Comparison of MoS_2 films with and without the PyC coating showed that sodium is released more poorly from the latter. Our findings help explain the electrochemical properties of hybrid anode materials consisting of MoS_2 and graphite thin layers in SIBs. The presence of PyC protects the surface of MoS_2 from excess sodium concentration and, consequently, from the destruction of the original MoS_2 structure.

Experimental

The substrates cut from a single-crystal silicon wafer were annealed in air at 1323 K for 16 h to form a 250–300 nm thick surface oxidized layer. The substrates were thoroughly cleaned using hot mineral acids and placed in a magnetron sputtering system (OJSC Vacuum Systems). The substrates were annealed at 573 K for 30 min in a vacuum at a pressure of 2×10^{-2} Pa. Immediately after this, molybdenum was sputtered from a Mo target with a purity of 99.9% for 10 s at a magnetron power of 100 W and an argon partial pressure of 5.4×10^{-1} Pa. The output pressure in the chamber was controlled by the argon flow.

The MoS_2 films were synthesized by sulfurization of molybdenum layers deposited on SiO_2/Si substrates in a two-zone quartz reactor. The substrate was placed in the high-temperature zone and annealed there at 423 K for 30 min in an argon flow of 250 sccm. Then, this zone was heated to 873 K. 200 mg of sulfur powder (99.9% purity) were placed in a quartz crucible in the low-temperature reactor zone heated to 473 K. A flow of 24 sccm argon was passed through both reactor zones for 30 min at atmospheric pressure. After this time, sulfurization of the Mo layer was complete. Both zones were cooled to room temperature in a flow of 250 sccm argon. To remove polysulfide impurities and form a more crystallized structure, the MoS_2 film was annealed in H_2 atmosphere at 1073 K for 10 min.

PyC films were grown on copper foil at 1273 K for 20 min using low-pressure CVD of methane mixed with hydrogen. The CH_4 pressure was 800 Pa, and the H_2 pressure was 2000 Pa. The resulting sample was placed in an aqueous solution of iron chloride (30 wt %) for 2 h to dissolve the copper foil. The remaining free PyC film was washed twice in dilute HCl (10 wt %) and then in deionized water until neutral pH was reached. The floating PyC film was trapped either on bare or MoS_2-covered SiO_2/Si substrates and then dried under ambient conditions.

Morphology of sample surfaces was examined by SEM with a CIQTEK SEM5000 (CIQTEK Ltd., Hefei, Anhui, PRC) microscope at an accelerating voltage of 15 kV. The cross section of MoS_2 film was prepared using a gallium-ion column FIB system and a two-stage protective cap deposition. Initially, a Pt layer of 21 nm was electrodeposited at 5 keV and 1 nA. After that, a thick Pt cap layer was ion-plated at 30 keV and 250 pA. Then, the FIB was operated at an ion accelerating voltage of 30 keV and ion current of 20 nA to cut the sample. Finally, the section was finely polished at an ion current of 250 pA to obtain a smooth surface. The image was acquired using a TESCAN AMBER (TESCAN Ltd., Brno, Czech Republic) microscope at an accelerating voltage of 5 kV in secondary electron mode.

Raman spectra were recorded using a LabRAM HR Evolution spectrometer (Horiba, Kyoto, Japan) using an Ar^+ laser at a wavelength of 514 nm.

XPS and NEXAFS experiments and sodium deposition were carried out at the RGL-PES end-station of the Russian–German dipole beamline (RGBL dipole) of the Berliner Elektronenspeicherring für Synchrotronstrahlung (BESSY II) operated by Helmholtz-Zentrum Berlin für Materialien und Energie (Berlin, Germany) [56]. Three samples, namely, MoS_2, PyC, and PyC-

MoS_2 films on SiO_2/Si substrates were fixed to a holder and placed into UHV (10^{-7} Pa) at the end-station and annealed at 673 K for 10 min to remove the contaminations. NEXAFS C K-edge spectra were acquired by measuring leakage current in total electron yield mode. The experimental data were normalized to the ring current and a photon flux measured using a clean gold crystal.

The XPS spectra were measured at synchrotron radiation of 830 and 470 eV. After the XPS and NEXAFS measurements were completed, the samples were simultaneously exposed to Na vapor from a well-outgassed sodium source (SAES Getters) for 10 min and then again for 20 min (30 min in total) at a current of 7.5 A. XPS measurements of the sodiated samples were performed immediately after each step of Na deposition. To desorb sodium, the samples, after a total of 30 min of Na deposition, were annealed at 773 K for 30 min in UHV. After the annealing procedure, XPS spectra were recorded again. The samples after each step of Na deposition and annealing did not come into contact with air, their transfer between the analytical and preparation chambers was carried out without breaking the vacuum. The energy scale was calibrated using the binding energy of the Au $4f_{7/2}$ component at 84.0 eV measured from a clean gold foil. The surface concentration of the elements was determined from the XPS survey spectra taking into account the photoelectron cross sections. Shirley background subtraction was used in analysis of fine lines. For the Mo 3d, S 2p, and Na 2s spectra, curve fitting was performed using a Gaussian (40%)/Lorentzian (60%) product function. For the C 1s spectra, the main peak at ≈284.4 eV was fitted using a Lorentzian asymmetric line shape with tail damping, convoluted with a Gaussian function, which closely approximates a Gaussian/Lorentzian product function. Energy position, full width at half maximum, and area for fitted components of the XPS spectra of initial samples are collected in Table S1, Supporting Information File 1.

Supporting Information

Supporting Information File 1

EDX spectroscopy study of Pt layers protecting MoS_2 surface, XPS survey spectra of the studied samples, and XPS Na 2s spectra of the sodiated samples.
[https://www.beilstein-journals.org/bjnano/content/supplementary/2190-4286-16-64-S1.pdf]

Acknowledgements

We are grateful to E. V. Shlyakhova for the Raman spectra. We thank the Helmholtz-Zentrum Berlin für Materialien und Energie for the allocation of synchrotron radiation beamtime at RGBL Dipole.

Funding

This research was funded by the Russian Science Foundation, grant No. 23-73-00048.

Author Contributions

Alexander V. Okotrub: conceptualization; supervision; validation; writing – review & editing. Anastasiya D. Fedorenko: data curation; investigation; writing – original draft. Anna A. Makarova: data curation; formal analysis; resources. Veronica S. Sulyaeva: data curation; formal analysis; investigation. Yuliya V. Fedoseeva: formal analysis; validation; visualization; writing – original draft. Lyubov G. Bulusheva: funding acquisition; methodology; validation; writing – review & editing.

ORCID® iDs

Alexander V. Okotrub - https://orcid.org/0000-0001-9607-911X
Veronica S. Sulyaeva - https://orcid.org/0000-0001-6940-057X
Yuliya V. Fedoseeva - https://orcid.org/0000-0003-1681-1708
Lyubov G. Bulusheva - https://orcid.org/0000-0003-0039-2422

Data Availability Statement

All data that supports the findings of this study is available in the published article and/or the supporting information of this article.

References

1. Zhang, Y.; Zhang, R.; Guo, Y.; Li, Y.; Li, K. *J. Alloys Compd.* **2024,** *998,* 174916. doi:10.1016/j.jallcom.2024.174916
2. Bulusheva, L. G.; Semushkina, G. I.; Fedorenko, A. D. *Nanomaterials* **2023,** *13,* 2182. doi:10.3390/nano13152182
3. Li, Q.; Yao, Z.; Wu, J.; Mitra, S.; Hao, S.; Sahu, T. S.; Li, Y.; Wolverton, C.; Dravid, V. P. *Nano Energy* **2017,** *38,* 342–349. doi:10.1016/j.nanoen.2017.05.055
4. Ren, W.; Zhang, H.; Guan, C.; Cheng, C. *Adv. Funct. Mater.* **2017,** *27,* 1702116. doi:10.1002/adfm.201702116
5. Kang, W.; Wang, Y.; Xu, J. *J. Mater. Chem. A* **2017,** *5,* 7667–7690. doi:10.1039/c7ta00003k
6. Lee, J. M.; Singh, G.; Cha, W.; Kim, S.; Yi, J.; Hwang, S.-J.; Vinu, A. *ACS Energy Lett.* **2020,** *5,* 1939–1966. doi:10.1021/acsenergylett.0c00973
7. Liu, M.; Zhang, P.; Qu, Z.; Yan, Y.; Lai, C.; Liu, T.; Zhang, S. *Nat. Commun.* **2019,** *10,* 3917. doi:10.1038/s41467-019-11925-z
8. Xie, X.; Ao, Z.; Su, D.; Zhang, J.; Wang, G. *Adv. Funct. Mater.* **2015,** *25,* 1393–1403. doi:10.1002/adfm.201404078
9. Zhang, X.; Vermeulen, N. A.; Huang, Z.; Cui, Y.; Liu, J.; Krzyaniak, M. D.; Li, Z.; Noh, H.; Wasielewski, M. R.; Delferro, M.; Farha, O. K. *ACS Appl. Mater. Interfaces* **2018,** *10,* 635–641. doi:10.1021/acsami.7b15326
10. Hao, L.; Meyers, D.; Dean, M. P. M.; Liu, J. *J. Phys. Chem. Solids* **2019,** *128,* 39–53. doi:10.1016/j.jpcs.2017.11.018
11. Zhang, X.; Li, X.; Liang, J.; Zhu, Y.; Qian, Y. *Small* **2016,** *12,* 2484–2491. doi:10.1002/smll.201600043

12. Shi, Z.-T.; Kang, W.; Xu, J.; Sun, Y.-W.; Jiang, M.; Ng, T.-W.; Xue, H.-T.; Yu, D. Y. W.; Zhang, W.; Lee, C.-S. *Nano Energy* **2016,** *22,* 27–37. doi:10.1016/j.nanoen.2016.02.009
13. Xiong, F.; Cai, Z.; Qu, L.; Zhang, P.; Yuan, Z.; Asare, O. K.; Xu, W.; Lin, C.; Mai, L. *ACS Appl. Mater. Interfaces* **2015,** *7,* 12625–12630. doi:10.1021/acsami.5b02978
14. Liu, Y.; He, X.; Hanlon, D.; Harvey, A.; Coleman, J. N.; Li, Y. *ACS Nano* **2016,** *10,* 8821–8828. doi:10.1021/acsnano.6b04577
15. Fei, L.; Xu, Y.; Wu, X.; Chen, G.; Li, Y.; Li, B.; Deng, S.; Smirnov, S.; Fan, H.; Luo, H. *Nanoscale* **2014,** *6,* 3664–3669. doi:10.1039/c3nr05815h
16. Li, M.; Wu, Z.; Wang, Z.; Yu, S.; Zhu, Y.; Nan, B.; Shi, Y.; Gu, Y.; Liu, H.; Tang, Y.; Lu, Z. *RSC Adv.* **2017,** *7,* 285–289. doi:10.1039/c6ra24800d
17. Hao, S.; Shen, X.; Tian, M.; Yu, R.; Wang, Z.; Chen, L. *Nano Energy* **2017,** *41,* 217–224. doi:10.1016/j.nanoen.2017.09.039
18. Wang, K.; Hua, W.; Li, Z.; Wang, Q.; Kübel, C.; Mu, X. *ACS Appl. Mater. Interfaces* **2021,** *13,* 40481–40488. doi:10.1021/acsami.1c07743
19. Bulusheva, L. G.; Zaguzina, A. A.; Fedorenko, A. D.; Semushkina, G. I.; Gusel'nikov, A. V.; Shubin, Y. V.; Nikolenko, A. D.; Okotrub, A. V. *Phys. Status Solidi B* **2025,** *262,* 2400272. doi:10.1002/pssb.202400272
20. Feng, M.; Zhang, M.; Zhang, H.; Liu, X.; Feng, H. *Carbon* **2019,** *153,* 217–224. doi:10.1016/j.carbon.2019.07.021
21. Chen, N.; Han, C.; Shi, R.; Xu, L.; Li, H.; Liu, Y.; Li, J.; Li, B. *Electrochim. Acta* **2018,** *283,* 36–44. doi:10.1016/j.electacta.2018.06.082
22. Yu, X.; Li, R.; Hu, X.; He, R.; Xue, K.; Sun, R.; Yang, T.; Wang, W.; Fang, X. *J. Solid State Chem.* **2021,** *297,* 122027. doi:10.1016/j.jssc.2021.122027
23. Zheng, F.; Zhong, W.; Deng, Q.; Pan, Q.; Ou, X.; Liu, Y.; Xiong, X.; Yang, C.; Chen, Y.; Liu, M. *Chem. Eng. J.* **2019,** *357,* 226–236. doi:10.1016/j.cej.2018.09.105
24. Anwer, S.; Huang, Y.; Li, B.; Govindan, B.; Liao, K.; Cantwell, W. J.; Wu, F.; Chen, R.; Zheng, L. *ACS Appl. Mater. Interfaces* **2019,** *11,* 22323–22331. doi:10.1021/acsami.9b04260
25. Li, H.; Wen, X.; Shao, F.; Xu, S.; Zhou, C.; Zhang, Y.; Wei, H.; Hu, N. *J. Alloys Compd.* **2021,** *877,* 160280. doi:10.1016/j.jallcom.2021.160280
26. Zhang, Y.; Tao, H.; Li, T.; Du, S.; Li, J.; Zhang, Y.; Yang, X. *ACS Appl. Mater. Interfaces* **2018,** *10,* 35206–35215. doi:10.1021/acsami.8b12079
27. Yu, X.; Guan, S.; Zhang, G.; Li, H.; Wang, J.; Liu, Z.; Xu, B.; Li, K.; Guan, T. *Composites, Part B* **2025,** *292,* 112101. doi:10.1016/j.compositesb.2024.112101
28. Bulusheva, L. G.; Kanygin, M. A.; Arkhipov, V. E.; Popov, K. M.; Fedoseeva, Y. V.; Smirnov, D. A.; Okotrub, A. V. *J. Phys. Chem. C* **2017,** *121,* 5108–5114. doi:10.1021/acs.jpcc.6b12687
29. Papageorgopoulos, C. A.; Jaegermann, W. *Surf. Sci.* **1995,** *338,* 83–93. doi:10.1016/0039-6028(95)00544-7
30. Kondekar, N. P.; Boebinger, M. G.; Woods, E. V.; McDowell, M. T. *ACS Appl. Mater. Interfaces* **2017,** *9,* 32394–32404. doi:10.1021/acsami.7b10230
31. Park, K. T.; Kong, J.; Klier, K. *J. Phys. Chem. B* **2000,** *104,* 3145–3154. doi:10.1021/jp993298s
32. Fedoseeva, Y. V.; Makarova, A. A.; Stolyarova, S. G.; Arkhipov, V. E.; Rühl, E.; Okotrub, A. V.; Bulusheva, L. G. *Appl. Surf. Sci.* **2022,** *598,* 153846. doi:10.1016/j.apsusc.2022.153846
33. Li, H.; Zhang, Q.; Yap, C. C. R.; Tay, B. K.; Edwin, T. H. T.; Olivier, A.; Baillargeat, D. *Adv. Funct. Mater.* **2012,** *22,* 1385–1390. doi:10.1002/adfm.201102111
34. Carvalho, B. R.; Pimenta, M. A. *2D Mater.* **2020,** *7,* 042001. doi:10.1088/2053-1583/ab98ef
35. Robinson, B. J.; Giusca, C. E.; Gonzalez, Y. T.; Kay, N. D.; Kazakova, O.; Kolosov, O. V. *2D Mater.* **2015,** *2,* 015005. doi:10.1088/2053-1583/2/1/015005
36. Frey, G. L.; Tenne, R.; Matthews, M. J.; Dresselhaus, M. S.; Dresselhaus, G. *Phys. Rev. B* **1999,** *60,* 2883–2892. doi:10.1103/physrevb.60.2883
37. Bolhuis, M.; Hernandez-Rueda, J.; van Heijst, S. E.; Tinoco Rivas, M.; Kuipers, L.; Conesa-Boj, S. *Nanoscale* **2020,** *12,* 10491–10497. doi:10.1039/d0nr00755b
38. Mignuzzi, S.; Pollard, A. J.; Bonini, N.; Brennan, B.; Gilmore, I. S.; Pimenta, M. A.; Richards, D.; Roy, D. *Phys. Rev. B* **2015,** *91,* 195411. doi:10.1103/physrevb.91.195411
39. Blanco, É.; Afanasiev, P.; Berhault, G.; Uzio, D.; Loridant, S. *C. R. Chim.* **2016,** *19,* 1310–1314. doi:10.1016/j.crci.2015.08.014
40. Thomsen, C.; Reich, S. *Phys. Rev. Lett.* **2000,** *85,* 5214–5217. doi:10.1103/physrevlett.85.5214
41. Schuepfer, D. B.; Badaczewski, F.; Guerra-Castro, J. M.; Hofmann, D. M.; Heiliger, C.; Smarsly, B.; Klar, P. J. *Carbon* **2020,** *161,* 359–372. doi:10.1016/j.carbon.2019.12.094
42. Ehlert, C.; Unger, W. E. S.; Saalfrank, P. *Phys. Chem. Chem. Phys.* **2014,** *16,* 14083–14095. doi:10.1039/c4cp01106f
43. Koroteev, V. O.; Bulusheva, L. G.; Okotrub, A. V.; Yudanov, N. F.; Vyalikh, D. V. *Phys. Status Solidi B* **2011,** *248,* 2740–2743. doi:10.1002/pssb.201100123
44. Wang, Q.; Song, Z.; Tao, J.; Jin, H.; Li, S.; Wang, Y.; Liu, X.; Zhang, L. *RSC Adv.* **2023,** *13,* 2903–2911. doi:10.1039/d2ra07949f
45. Qiu, B.; Zhao, X.; Hu, G.; Yue, W.; Ren, J.; Yuan, X. *Nanomaterials* **2018,** *8,* 962. doi:10.3390/nano8110962
46. Krawczyk, M.; Pisarek, M.; Szoszkiewicz, R.; Jablonski, A. *Materials* **2020,** *13,* 3595. doi:10.3390/ma13163595
47. Stolyarova, S. G.; Kotsun, A. A.; Shubin, Y. V.; Koroteev, V. O.; Plyusnin, P. E.; Mikhlin, Y. L.; Mel'gunov, M. S.; Okotrub, A. V.; Bulusheva, L. G. *ACS Appl. Energy Mater.* **2020,** *3,* 10802–10813. doi:10.1021/acsaem.0c01837
48. Amin, R.; Hossain, M. A.; Zakaria, Y. *ACS Appl. Mater. Interfaces* **2018,** *10,* 13509–13518. doi:10.1021/acsami.8b01104
49. Mosconi, D.; Till, P.; Calvillo, L.; Kosmala, T.; Garoli, D.; Debellis, D.; Martucci, A.; Agnoli, S.; Granozzi, G. *Surfaces (Basel, Switz.)* **2019,** *2,* 531–545. doi:10.3390/surfaces2040039
50. Shirota, G.; Nasu, A.; Deguchi, M.; Sakuda, A.; Tatsumisago, M.; Hayashi, A. *Solid State Ionics* **2022,** *376,* 115848. doi:10.1016/j.ssi.2021.115848
51. Bulusheva, L. G.; Fedoseeva, Y. V.; Lavrukhina, S. A.; Sysoev, V. I.; Maksimovskii, E. A.; Makarova, A. A.; Okotrub, A. V. *Appl. Surf. Sci.* **2025,** *679,* 161104. doi:10.1016/j.apsusc.2024.161104
52. Liu, L.; Wu, J.; Wu, L.; Ye, M.; Liu, X.; Wang, Q.; Hou, S.; Lu, P.; Sun, L.; Zheng, J.; Xing, L.; Gu, L.; Jiang, X.; Xie, L.; Jiao, L. *Nat. Mater.* **2018,** *17,* 1108–1114. doi:10.1038/s41563-018-0187-1
53. Shu, H.; Li, F.; Hu, C.; Liang, P.; Cao, D.; Chen, X. *Nanoscale* **2016,** *8,* 2918–2926. doi:10.1039/c5nr07909h
54. Huang, Q.; Li, X.; Sun, M.; Zhang, L.; Song, C.; Zhu, L.; Chen, P.; Xu, Z.; Wang, W.; Bai, X. *Adv. Mater. Interfaces* **2017,** *4,* 1700171. doi:10.1002/admi.201700171

55. Bulusheva, L. G.; Arkhipov, V. E.; Popov, K. M.; Sysoev, V. I.; Makarova, A. A.; Okotrub, A. V. *Materials* **2020,** *13,* 1173. doi:10.3390/ma13051173
56. Bulusheva, L. G.; Okotrub, A. V.; Yashina, L. V.; Velasco-Velez, J. J.; Usachov, D. Y.; Vyalikh, D. V. *Phys. Sci. Rev.* **2018,** *3,* 20180042. doi:10.1515/psr-2018-0042

License and Terms

BEILSTEIN JOURNAL OF NANOTECHNOLOGY

Insights into the electronic and atomic structures of cerium oxide-based ultrathin films and nanostructures using high-brilliance light sources

Paola Luches*[1] and Federico Boscherini[2]

Review

Open Access

Address:
[1]Istituto Nanoscienze – Consiglio Nazionale delle Ricerche, Via G. Campi 213/a, 41125 Modena, Italy and [2]Istituto Officina dei Materiali – Consiglio Nazionale delle Ricerche, Strada Statale 14, km 163.5, 34149 Trieste, Italy

Email:
Paola Luches* - paola.luches@nano.cnr.it

* Corresponding author

Keywords:
cerium oxide; free-electron lasers; thin films; X-ray absorption spectroscopy; X-ray photoelectron spectroscopy

Beilstein J. Nanotechnol. **2025,** *16,* 860–871.
https://doi.org/10.3762/bjnano.16.65

Received: 16 March 2025
Accepted: 26 May 2025
Published: 10 June 2025

This article is part of the thematic issue "Exploring synchrotron radiation and free-electron laser tools for nanostructured materials".

Guest Editor: C. Bittencourt

Abstract

High-brilliance light sources, such as synchrotrons and free-electron lasers, allow researchers to probe the structural, electronic, and dynamic properties of functional materials at an unprecedented level of detail. Techniques like X-ray photoelectron spectroscopy and X-ray absorption spectroscopy, can reveal atomic-scale information about material behavior under different conditions. This thorough understanding can be leveraged to optimize materials for various applications, including energy storage, catalysis, and electronics. This review focuses on cerium oxide, an important material for catalytic and energy applications, examining the application of high-brilliance light sources on model systems such as supported thin films and epitaxial nanostructures. We review selected studies exploiting the high energy resolution and sensitivity of synchrotron radiation-based X-ray photoelectron spectroscopy and X-ray absorption spectroscopy to explain the factors influencing the material's reducibility, with particular focus on dimensionality effects and on metal–oxide interaction, and the interaction with molecules. The potential of studies conducted under ambient pressure conditions is highlighted, and, finally, the perspectives offered by the ultrahigh brilliance and ultrashort free-electron laser pulses for dynamic studies of the processes that take place upon photoexcitation are discussed.

Introduction

Transition metal oxides in the form of thin films or nanostructures find extensive use in sustainable energy technologies [1,2]. They serve as active materials or supports for catalysts for various chemical reactions, essential to energy conversion, sensing, and environmental remediation [3,4]. Additionally, because of their often high efficiency at harnessing solar energy, they find application in photocatalysis and photovoltaics [5,6]. Optimizing these applications requires unravelling the often complex processes that influence functionality through an atomic-level description. To this end, materials are often studied as model systems, such as well-controlled supported thin films or nanostructures with simplified complexity

compared to real systems, allowing the results from advanced experimental methods to be directly compared with theoretical simulations [7,8]. Thanks to their remarkable sensitivity, atomic selectivity, spatial and energy resolution, synchrotron radiation-based techniques, which utilize high-brilliance photon beams, have enabled refined characterization of the electronic, structural, and morphological properties of these materials, as well as the modifications they undergo under operating conditions. Furthermore, free-electron lasers (FELs), with orders-of-magnitude higher peak brilliance than synchrotrons, have made it possible to achieve temporal resolution of the order of a few tens of femtoseconds, facilitating an ultrafast, element-sensitive characterization of the dynamic processes occurring for example upon photoexcitation.

Among transition metal oxides, cerium oxide (or ceria) has unique redox properties, linked to the relative stability of Ce cations in the 4+ and 3+ oxidation states, which make the material highly effective in automotive catalysts and in the field of environmental remediation [9]. The related ability of the material to easily store and release oxygen also plays a key role in energy conversion technologies, including fuel cells and batteries [10,11]. Gas sensing applications of ceria-based materials are based on the modifications of the transport properties in the presence of specific gases, due to the redox reactions that take place on the surface [12,13]. An atomic level understanding of the structure–function relationship in this oxide is essential for guiding the design of efficient materials to optimize the performance of the applications. Studies on cerium oxide nanostructures and powders prepared by chemical synthesis methods are quite numerous, and they are typically carried out on systems with a marked and often unexplored complexity [14-17]. For studies on cerium oxide as model systems, such as low-index surfaces, thin films, and supported nanostructures, investigated using laboratory-based surface science methods, we refer the reader to existing reviews [18-20].

The aim of this work is to provide an overview of recent studies highlighting the advantages of using synchrotron and FEL radiation to achieve a refined understanding of cerium oxide-based materials, particularly when examined in the form of well-controlled thin films and nanostructures prepared by physical synthesis methods.

Review

Studies by X-ray photoelectron spectroscopy and related techniques

Synchrotron radiation-based X-ray photoelectron spectroscopy (XPS) has significantly advanced the characterization of low-dimensional cerium oxide structures by offering much higher sensitivity and energy resolution than conventional XPS [21-24]. In addition, the possibility to select photon energies in a broad range permits to tune the depth sensitivity of the method and to selectively probe the surface and or deeper layers, like buried interfaces.

Since the early studies of epitaxial cerium oxide films by Mullins and coworkers [22], it became clear that synchrotron radiation could provide high-resolution Ce 3d, Ce 4d, and valence band spectra. It is important to emphasize that the significantly higher brilliance of synchrotron radiation beams, compared with laboratory sources, provides much higher sensitivity towards diluted elements, such as low-concentration dopants and low-density metal NPs.

A significant step forward in the understanding of cerium oxide-based systems was introduced by the application of resonant photoemission to selectively probe valence band features related to Ce^{4+} and Ce^{3+} ions. This can be done by tuning the photon energy at specific resonances related to Ce 4d→Ce $4f^0$ (Ce^{4+}) and Ce 4d→Ce $4f^1$ (Ce^{3+}) electronic configurations at 110 and 125 eV, respectively [23,25-28]. Figure 1 reports valence band spectra from an ultrathin cerium oxide film before and after ultrahigh vacuum (UHV) annealing at 600 °C, acquired at the two resonant energies. Using a photon energy at the Ce^{4+}-related resonance (110 eV), the spectrum shows only minor modifications after annealing, while if the Ce^{3+}-related

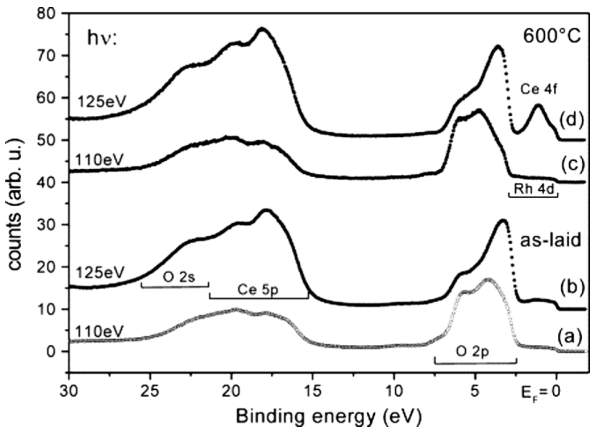

Figure 1: Valence band photoemission spectra of 1.3 MLE cerium oxide/Rh(111) as laid (a, b) and after annealing at 600 °C (c, d). Spectra (b) and (d) have been excited by a photon energy of 125 eV corresponding to the maximum of the Ce 4d→4f giant resonance (on-resonance), while spectra (a) and (c) have been excited with a photon energy of 110 eV (off-resonance). Reprinted from [23], Surface Science, vol. 520, by S. Eck; C. Castellarin-Cudia; S. Surnev; M. G. Ramsey; F. P. Netzer, "Growth and thermal properties of ultrathin cerium oxide layers on Rh(111)", pages 173-185, Copyright (2002), with permission from Elsevier. This content is not subject to CC BY 4.0.

resonant energy is used (125 eV), a marked Ce 4f peak appears around 2 eV binding energy after the annealing. This demonstrates the significantly higher sensitivity to Ce^{3+} that can be achieved by exploiting resonant photoemission, as compared to non-resonant photoemission.

Synchrotron radiation-based resonant photoemission has facilitated an accurate determination of the dependence of Ce^{3+} concentration on dimensionality [23]. The technique has also provided an accurate description of the charge transfer processes and hybridization occurring at the interface between cerium oxide and metals, either as substrates [23], as supported nanoparticles (NPs) [26,27] or as dopants [28]. The insight provided by such studies is highly relevant, since cerium oxide is often combined with metals in various applications. For example, it was possible to identify different types of interactions between Pt NPs and cerium oxide surfaces including electron transfer from Pt NPs to CeO_2 and transport of oxygen atoms from ceria to Pt NPs, the latter occurring only when the ceria support surface is nanostructured [26]. In addition, thanks to its sensitivity, the method, when combined with other techniques, has provided quantitative information on the number of electrons transferred per particle to the support (Figure 2), enabling the optimization of the size of the supported active Pt catalyst [27]. This is a crucial factor in minimizing the concentration of critical and expensive noble metals in applications.

The possibility of tuning the kinetic energy of the photoelectrons by varying the photon energy has also enabled a much higher surface sensitivity than laboratory XPS by selecting a photoelectron kinetic energy close to the minimum of the inelastic mean free path. A study by Simon et al. on porous Pt-doped cerium oxide films prepared by direct liquid injection chemical vapor deposition, comparing conventional and synchrotron-radiation based XPS, has demonstrated that the Pt atoms are uniformly dispersed in the nanoparticles that form the film, while the Pt ions in the 2+ oxidation state are confined at the outermost layers [29].

The interplay of ceria surfaces with adsorbed molecules, a crucial factor in understanding reactivity, has become a significant research focus, also thanks to synchrotron-radiation-based XPS methods [30-32]. Initial studies were performed by exposing the surface of interest to the chosen molecule at UHV-compatible pressures. The interaction between cerium oxide and, for example, CO [21,33], SO_2 [34], methanol [32], ethanol [35], and water [36] have been considered. The higher energy resolution and the tunable surface sensitivity of synchrotron radiation-based XPS, as compared to conventional XPS, permits a more accurate description of the different contributions to the spectra. Figure 2 shows high-resolution synchrotron-radiation-based C 1s spectra, for different ethanol exposures at 150 K, using a photon energy of 410 eV. At low exposure, the most

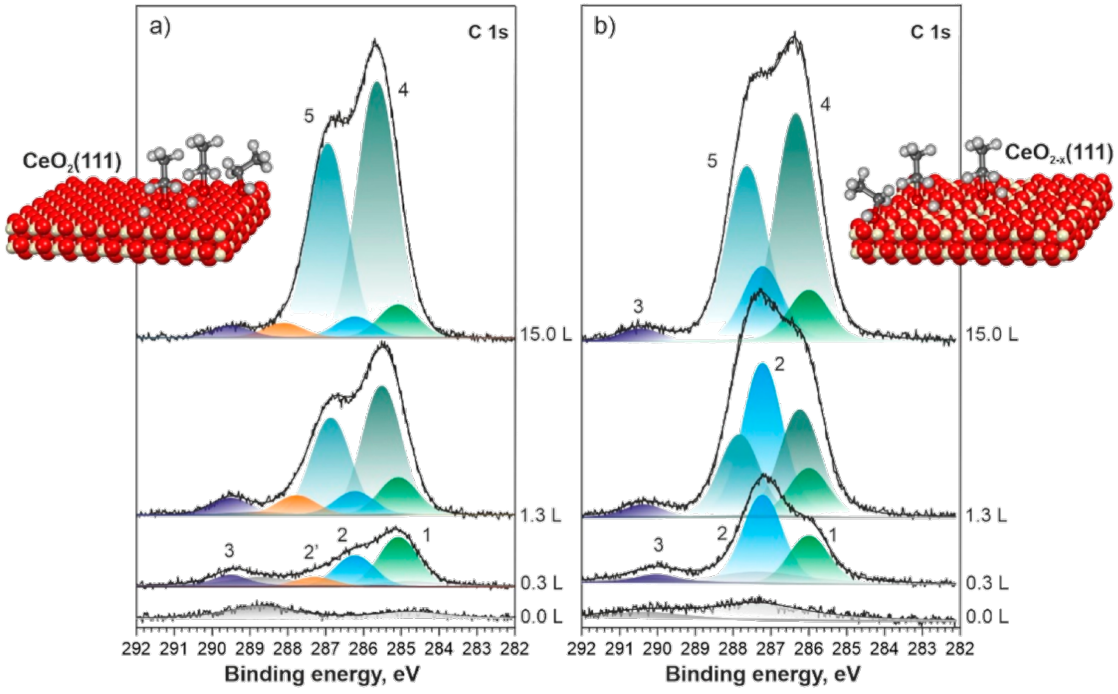

Figure 2: High-resolution synchrotron radiation C 1s XPS spectra on CeO_2(111) (a) and CeO_{2-x} (111) (b) for different ethanol exposures at 150 K. Reprinted from [35] (@ 2022 Y. Lykhach et al., published by IOP Publishing, distributed under the terms of the Creative Commons Attribution 4.0 International License, https://creativecommons.org/licenses/by/4.0).

intense peaks at 285.1 eV (1) and at 286.2 eV (2) on CeO_2(111) and at 286.3 eV (1) and at 287.6 eV (2) on CeO_{2-x}(111) are ascribed to methyl and alkoxy groups of adsorbed ethoxy species, respectively. The slightly different binding energies on the two surfaces are ascribed to the different Ce^{3+} concentrations in the two ceria films. The different intensity ratios between the methyl- and alkoxy-related peaks on the two surfaces are assigned to different adsorption and dissociation pathways for ethanol on a stoichiometric and a non-stoichiometric ceria surface. At higher exposures, the new peaks at 285.6 eV (4) and at 287.0 eV (5) on CeO_2(111) and at 286.3 eV (4) and at 287.6 eV (5) on CeO_{2-x}(111) are ascribed to physisorbed ethanol.

To identify the role of the interaction between ceria and metals, the adsorption and reaction of ethylene on Pt NPs supported on ceria were compared with the ones observed on a Pt(111) surface [31]. The oxide-supported NPs were shown to have an enhanced reactivity and additional reaction pathways [31]. Regarding the same system, the efficient decomposition of methanol and the resistance to poisoning have rationalized the observed high activity of the material in direct methanol fuel cells [37]. Regarding the Ni-CeO_{2-x}(111) system, a study of the methanol reaction revealed that the strong metal–support interactions between Ni and CeO_2 determines the high selectivity for CO_2 production, instead of the formation of surface C or CO [38].

Resonant photoemission detected by a spectroscopic photoemission and low-energy electron microscope (SPLEEM) was also used to acquire local information on the oxidation degree of cerium in mixed zirconia–ceria nanostructures supported on a Rh(111) single crystal [39]. Figure 3a shows a sequence of μ-XPS valence band spectra acquired using a photon at the Ce^{3+}-related Ce 4d→Ce $4f^1$ resonance ($h\nu$ = 120.8 eV) on a $Ce_{0.4}Zr_{0.6}O_{2-x}$ film upon removal and reintroduction of oxygen (P_{O2} = 1 × 10^{-7} mbar) in the experimental chamber. When oxygen is removed (red spectrum in Figure 3b), the intensity of the Ce^{3+}-related feature at ≈2 eV decreases with photon exposure, while when oxygen is reintroduced (red spectrum Figure 3b), its intensity re-increases. The comparison of the time evolution of the Zr^{4+}-related $3d_{5/2}$ μ-XPS intensity acquired on a $Ce_{0.4}Zr_{0.6}O_{2-x}$ and on a ZrO_2 film is reported in Figure 3c. The exposure to the photon beam induces a much

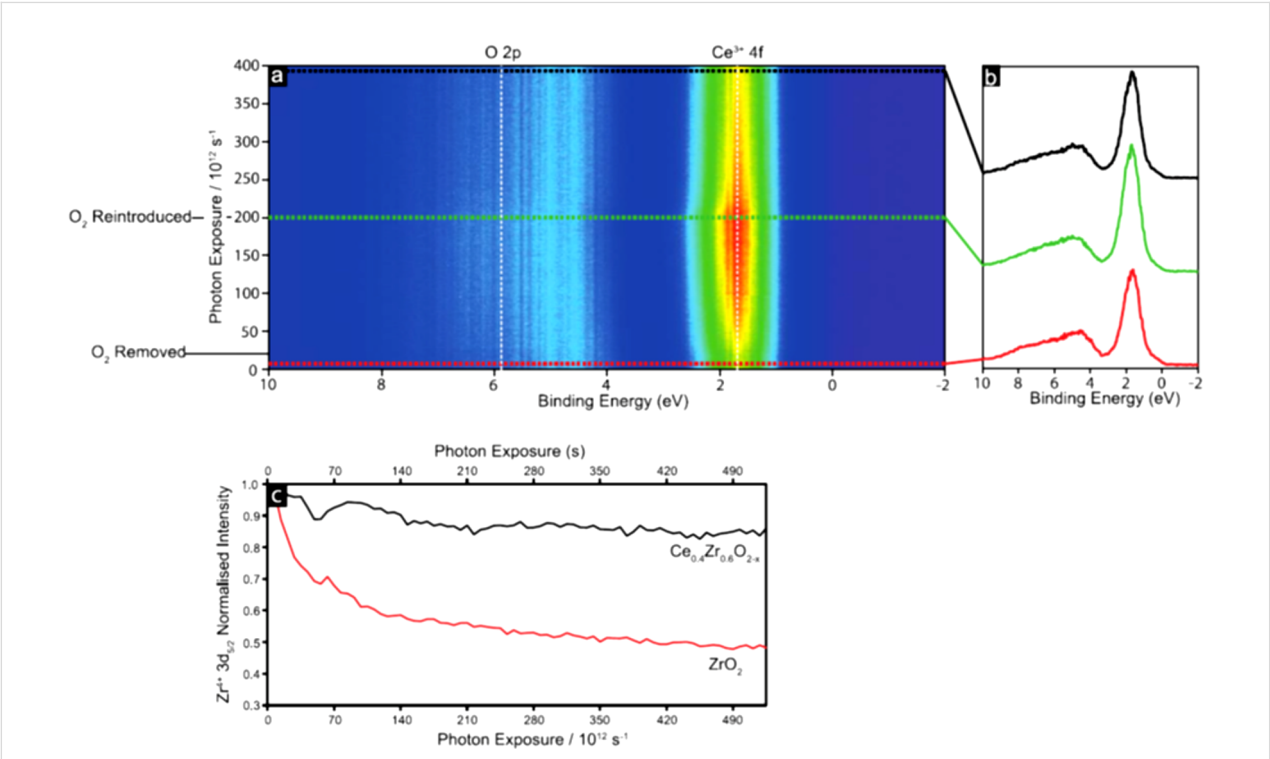

Figure 3: μ-XPS valence band spectra of a $Ce_{0.4}Zr_{0.6}O_{2-x}$ film acquired using a photon at the Ce^{3+}-related Ce 4d→Ce $4f^1$ resonance ($h\nu$ = 120.8 eV), acquired at different photon exposure times after removal and subsequent reintroduction of oxygen (P_{O2} = 1 × 10^{-7} mbar) in the chamber. (b) Selected spectra of oxidized film (red), reduced film (green) and reoxidized film (black). (c) Evolution of the Zr^{4+} $3d_{5/2}$ intensity as a function of photon exposure time for a $Ce_{0.4}Zr_{0.6}O_{2-x}$ and a ZrO_2 film. Adapted from [39], Surface Science, vol. 682, by M. Allan; D. Grinter; S. Dhaliwal; C. Muryn; T. Forrest; F. Maccherozzi; S.S. Dhesi; G. Thornton, "Redox behaviour of a ceria–zirconia inverse model catalyst", pages 8-13, Copyright (2019), with permission from Elsevier. This content is not subject to CC BY 4.0.

more pronounced decrease of Zr^{4+} intensity in the ceria–zirconia mixed oxide film than in pure zirconia. This was ascribed to a synergy between the two oxides inducing an oxygen transfer from ceria to zirconia upon reduction using soft X-ray irradiation. The observed effect was identified as responsible for the enhanced catalytic activity of mixed ceria–zirconia materials in the applications [39].

Photoemission is a technique with a sensitivity limited to the topmost surface layers. In typical resonant photoemission experiments on ceria, performed with photon energies close to the Ce N_{45} adsorption edge, the probed valence band photoelectrons have a kinetic energy close to the minimum of their inelastic mean free path, and the information comes from the topmost one or two atomic layers. If photons in the hard X-ray range are used in hard X-ray photoelectron spectroscopy (HAXPES) and photoelectrons with kinetic energies of a few kiloelectronvolts are probed, the depth sensitivity can be extended to the topmost 5–10 nm of the sample. The possibility to select a much higher photon energy than at typical laboratory sources has also permitted to acquire and analyze Ce $2p_{3/2}$ core level spectra using HAXPES at photon energies higher than the core-level binding energy of 5723 eV [24]. The analysis of Ce 2p core level spectra enables an accurate determination of Ce^{3+} and Ce^{4+} concentration due to the absence of spectral overlap between spin–orbit split lines [24]. In contrast, Ce 3d spectra exhibit five partially overlapped spin–orbit split components originating from different final states, which complicate the analysis [40].

Synchrotron radiation-based photoemission has proven to be significantly more versatile than XPS/UPS with laboratory sources. However, the information it provides primarily pertains to the surface atomic layers of the sample, as it relies on detecting electrons that strongly interact with materials.

Studies by X-ray absorption spectroscopy and related techniques

X-ray absorption spectroscopy (XAS) has provided complementary information to that obtained by synchrotron radiation-based photoemission on cerium oxide-based materials. The depth sensitivity of XAS can be tuned on a much wider range than XPS by choosing the desired absorption edge and by selecting a specific detection mode. Moreover, complementary information on the electronic properties and on the local atomic structure can be obtained from the analysis of XAS data. X-ray absorption near-edge spectroscopy (XANES), analyzing the signal within the first few tens of electronvolts above the absorption edge, provides information mainly on the density of empty states of the investigated sample. In contrast, the extended energy range X-ray absorption fine structure (EXAFS), up to a few hundred electronvolts above the absorption edge, is sensitive to the local atomic structure around the absorbers.

A polarization-dependent Ce L_3-edge EXAFS study of ultrathin epitaxial cerium oxide films on Pt(111) demonstrated the influence of the substrate in 2 monolayer (ML) films. Figure 4a shows the Ce–O in-plane and out-of-plane distances obtained from the analysis of EXAFS data acquired on a 2 ML and on a

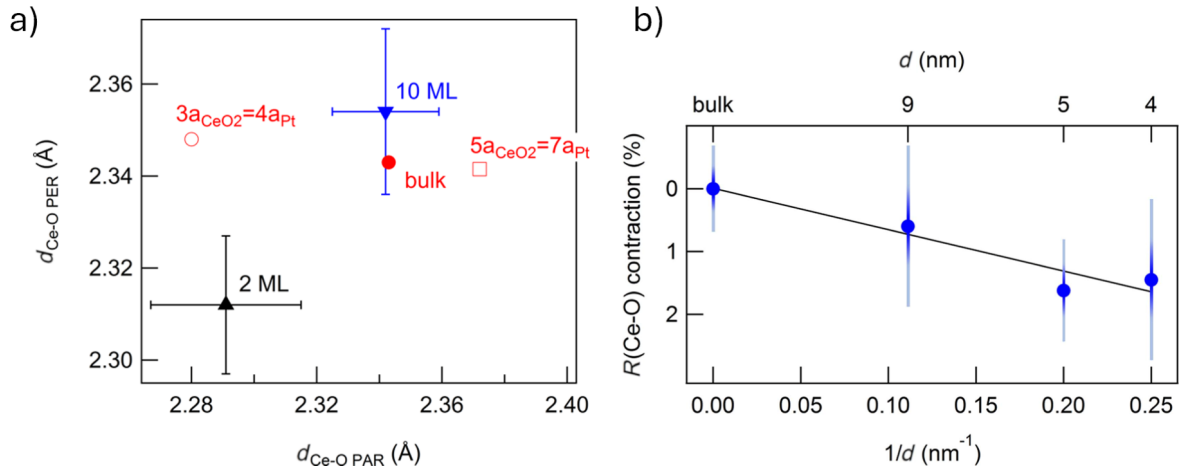

Figure 4: (a) Ce–O interatomic distances for 2 ML and 10 ML CeO_2 films evaluated by fitting Ce L_3-edge EXAFS with the electric field parallel ($d_{Ce-O\ PAR}$) and perpendicular ($d_{Ce-O\ PER}$) to the sample surface. The value expected for a bulk (red dot) and assuming in-plane $3a_{CeO2} = 4a_{Pt}$ and $5a_{CeO2} = 7a_{Pt}$ coincidence are also shown. Reprinted with permission from [41], Copyright 2013 American Chemical Society. This content is not subject to CC BY 4.0. (b) Contraction of the Ce–O interatomic distance in CeO_2 NPs of different diameter as function of the reciprocal average diameter evaluated by fitting Ce L_3-edge EXAFS. The solid line is a linear fit of the data. Used with permission from [42] ("Contraction, cation oxidation state and size effects in cerium oxide nanoparticles", by J. S. P. Cresi et al., Nanotechnology, vol. 28, issue 49, article no. 495702, published on 13 November 2017; https://iopscience.iop.org/article/10.1088/1361-6528/aa926f; © 2017 IOP Publishing Ltd; permission conveyed through Copyright Clearance Center, Inc. All rights reserved. This content is not subject to CC BY 4.0.

10 ML ceria film. Figure 4a also reports the values expected for bulk ceria and for epitaxially distorted ceria, assuming that the film adopts an in-plane $3a_{CeO2} = 4a_{Pt}$ or a $5a_{CeO2} = 7a_{Pt}$ coincidence to compensate from the large lattice mismatch with the Pt support. The values of the expected out-of-plane Ce–O distances in the two cases are calculated assuming the bulk elastic constants. The 2 ML film adopts an epitaxial in-plane compression to match the substrate in a dominant $3a_{CeO2} = 4a_{Pt}$ (Figure 4a). The out-of-plane Ce–O bonds in the ultrathin film appear shorter than expected considering the bulk elastic constants, possibly because of the reduced dimensionality of the system. In contrast, the epitaxial compression is completely relaxed in the 10 ML film, which assumes interatomic distances compatible with the bulk value (Figure 4a) [41].

In analogy, for CeO_2 NPs of different diameters prepared using physical synthesis the analysis of Ce L_3-edge EXAFS data demonstrated a progressive contraction of the Ce–O distance with respect to the bulk value with decreasing diameter (Figure 4b). The contraction showed a linear dependence on the surface-to-volume ratio (Figure 4b), and it was ascribed to a compressive strain arising from reduced dimensionality [42]. This effect was theoretically predicted [43], but it was never experimentally observed on chemically synthesized NPs, where an expansion typically occurs [44-46], possibly due to the higher Ce^{3+} surface concentration compared to physically synthesized NPs.

The short- and long-range structural modifications associated with thermal reduction in CeO_2/Pt(111) films, as well as the influence of the Pt substrate's proximity, were investigated using XANES/EXAFS combined with surface X-ray diffraction (SXRD) [47]. A strong interaction between cerium oxide and platinum was identified and associated to the formation of a Ce–Pt alloyed interfacial phase exhibiting a (2 × 2) periodicity [47]. The influence of the substrate on the stability and reactivity of supported ceria nanoislands has also been investigated by Ce M_5 XANES in the case of Au(111) [48]. A loss of redox activity accompanied by an irreversible amorphization was observed at high reduction temperatures, while a partial decomposition of the ceria nanoislands to metallic cerium was found to occur under milder conditions than on Pt(111) or other metal substrates [48].

High-energy resolution fluorescence detected (HERFD)-XANES was used to achieve a more detailed understanding of the processes accompanying thermal reduction in ultrathin Pt(111) supported cerium oxide nanostructures [49]. In this technique, the incident photon energy is scanned across an absorption edge, while a spectrometer selects the energy of the emitted photons [50]. If a specific fluorescence decay with a sufficiently narrow energy bandwidth is selected, an energy resolution higher than that limited by core–hole lifetime broadening can be achieved. For Ce L_3-edge absorption (5715–5750 eV), the emission spectrometer was tuned to the $L_{\alpha 1}$ channel at 4840 eV to obtain HERFD-XANES, which showed to be sensitive to the electronic configurations of the Ce 4f levels and 5d band [51,52]. This approach, applied to Pt-supported cerium oxide films of 2 and 10 ML thickness, permitted to clearly resolve the fine structure of the two groups of white lines in Figure 2, ascribed to screened (A1) and unscreened (A2) 2p–5d transitions with the additional splitting due to the fine structure of the 5d band due to crystal field effects. As shown in Figure 2a, the intensity and shape of the A1 feature of the 2 ML sample are significantly modified by thermal treatment in vacuum up to 770 K. At 1020 K, a new peak, labeled B1 in Figure 5a, characteristic of Ce^{3+}, appears. The A1 and A2 structures reappear after heating in O_2, and recover a shape close to the initial one after sample cooling to RT in O_2. The spectra of the 10 ML film (Figure 5b) instead show only minimal changes with the same thermal treatments in vacuum [49]. The study allowed the authors to conclude that in 2 ML films vertical confinement and/or charge transfer from the platinum substrate, determine a higher reducibility than in 10 ML films [49]. This is evidenced by the greater Ce^{3+} concentration formed during thermal treatments in high vacuum up to 770 K and by the full reversibility of the process upon thermal treatments in O_2 (Figure 5) [49].

The interaction between cerium oxide and Ag NPs of varying sizes supported on a cerium oxide film were investigated using EXAFS at the Ag K-edge [53]. The NPs exhibited an Ag–Ag interatomic distance contracted by 3–4% compared to the bulk value [53]. The contraction was mainly ascribed to dimensionality effects, with epitaxial effects having a minor role. Additionally, the Ag–O interatomic distance at the interface between the NPs and the supporting oxide was found to decrease with decreasing NP size [53], possibly due to a stronger interaction between Ag and cerium oxide in smaller NPs, resulting from a greater charge transfer per atom [54].

A further possibility offered by synchrotrons is to measure spatially resolved Ce M-edge absorption spectra in photoemission electron microscopy (PEEM) mode, in which the photon energy is scanned across the XAS edge and the intensity of the secondary electrons is detected using a PEEM. This allowed to image the shape and size of ceria nanoislands on Ru(0001) and to probe and compare the oxidation state in selected areas with sub-micrometer spatial resolution [55]. In addition, the morphology of zirconia–ceria mixed oxides supported on Rh(111) and the oxidation states of the two oxides, individually and in the mixed phase, were determined [39].

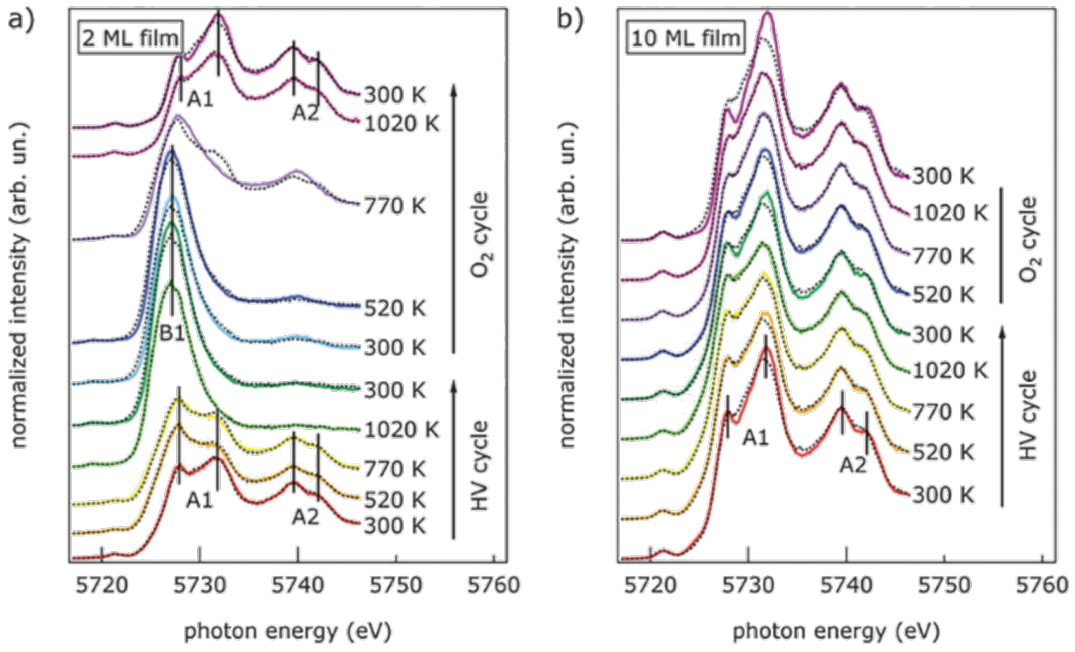

Figure 5: Ce L_3-edge HERFD-XANES spectra of (a) 2 ML and b) 10 ML CeO_2 films acquired during the thermal cycles in high vacuum and in oxygen-rich atmosphere. The characteristic Ce^{4+}-(A1 and A2) and Ce^{3+}-(B1) related peaks are marked. The fits with linear combinations of the Ce^{3+} and Ce^{4+} references are shown as dashed lines. Reprinted from [49] with permission of the Royal Society of Chemistry ("Electronic properties of epitaxial cerium oxide films during controlled reduction and oxidation studied by resonant inelastic X-ray scattering" by G. Gasperi et al., Phys. Chem. Chem. Phys. vol. 18, issue 30, article no. 20511, © 2016); permission conveyed through Copyright Clearance Center, Inc. This content is not subject to CC BY 4.0.

Studies at ambient pressure

The identification of active sites in catalysts is a crucial problem in view of the optimization of catalyst efficiency and selectivity. The possibility of carrying out spectroscopic studies under conditions as close as possible to ambient pressure has largely contributed to this goal. The application of these methods to model systems allowed for a comparison with simulations that were extremely valuable for a reliable interpretation of the results.

Ambient pressure XPS studies can be performed using a differentially pumped analyzer, which collects electrons at ambient pressure while the body of the analyzer remains under UHV conditions. Such instruments, installed at synchrotron radiation facilities and applied to ceria-based model systems have given an important contribution to understanding the surface chemistry of specific reactions. Coexisting Pt and ceria nanoparticles supported on TiO_2(110) were found to exhibit a unique reactivity for the binding and dissociation of CO_2, not observed on the TiO_2(110) surface, on ceria supported on TiO_2(110), or on bulk platinum surfaces [56]. In the same system, the high ability to bind and activate CO_2 was exploited for the hydrogenation of CO_2 to methanol, with the addition of water facilitating the production of ethanol [57].

Given the high penetration depth of hard X-rays in materials, XAS in the hard X-ray range is much easier than XPS to be carried out under ambient pressure conditions; it provided valuable insight into the working principles of ceria-based catalysts. In the soft X-ray range, the relatively high absorption of X-rays by gases or liquids at ambient pressure and the limited inelastic mean free path of secondary electrons, when total electron yield is used as a detection mode, put some constraints on the application of ambient pressure XAS in the soft X-ray range. Reaction cells with an ultrathin membrane that confines the gas in a narrow region extremely close to the sample surface were applied to the study of Cu- and Fe-doped cerium oxide films during thermal treatments in hydrogen at ambient pressure [58]. The combination of ambient pressure XANES and gas chromatography was employed to correlate in real time the changes of the chemical state of Cu, Fe, and Ce cations with oxygen vacancy and water formation during thermal treatments in hydrogen at ambient pressure [58]. The pure ceria film, in the Ce^{4+} oxidation state with a dominant Ce L_3-edge XANES feature at 881 eV, showed a progressively increasing relative intensity of the Ce^{3+}-related features at 878.8 and 879.9 eV with increasing temperature in H_2 pressure (Figure 6a compared with Figure 6d). In Cu-doped films, as the Cu concentration increases, the same treatment leads to a progres-

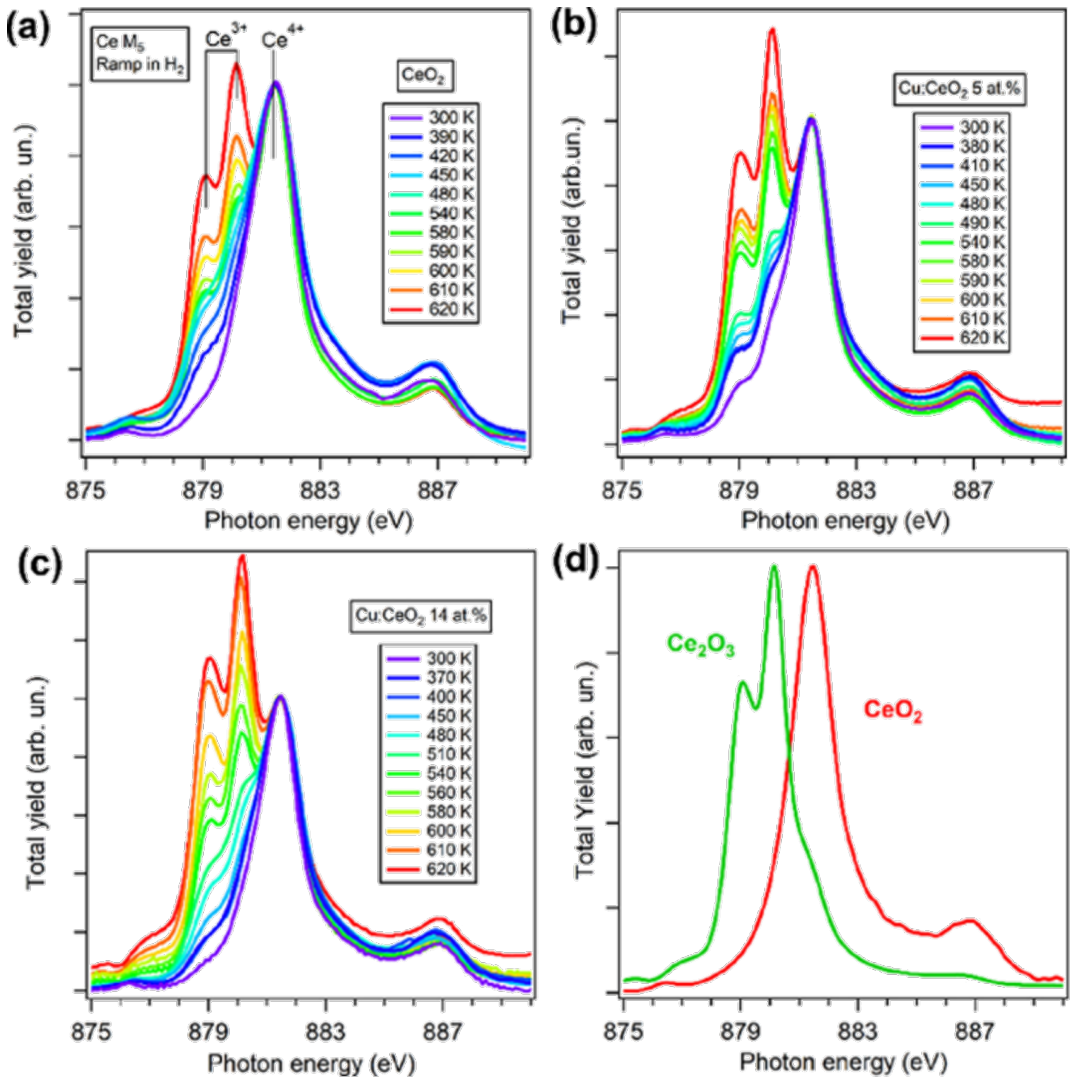

Figure 6: Ce M_5-edge XANES spectra of (a) an undoped CeO_2 film, (b) a Cu:CeO_2 5 atom % doped film and (c) a Cu:CeO_2 14 atom % doped film acquired at different *T* in H_2 at ambient pressure. (d) Reference spectra measured for CeO_2 and Ce_2O_3. Reprinted with permission from [58], Copyright 2024 American Chemical Society. This content is not subject to CC BY 4.0.

sively higher intensity of the Ce^{3+}-related features (Figure 6b,c). This evidence, combined with the evolution of the Cu oxidation state and with gas chromatography, suggested that at moderate temperatures, H_2 dissociation is favored by the presence of Cu^{1+} sites, and at higher temperatures, water is desorbed from the surface with the uptake of oxygen from cerium oxide [58].

The same method was used to investigate the same system also during exposure to water and to laser light at different temperatures [59]. Also in this case the Cu dopant ions were found to be active in modifying the electronic structure of CeO_2 and in enabling a more efficient hydrogen production at lower temperatures, as compared to the pure oxide [59].

Dynamic studies of photoexcited states

The advent of X-ray free electron lasers has opened entirely new research pathways in the field of oxides for energy applications. The ultrashort and ultraintense photon beams with variable energy across a broad range can provide an accurate description of the processes that accompany any perturbation, for example, photoexcitation, in materials. The element sensitivity and the time resolution of the order of tens of femtoseconds and below can be exploited to obtain insight into the processes following photoexcitation in photocatalysts, important for the rational optimization of these materials' efficiency.

In ceria, as well as in other semiconducting oxides, the formation of photoinduced small polarons after bandgap

photoexcitation, was hypothesized based on optical pump–probe spectroscopy experiments [60]. These quasi-particles, which originate from the coupling between photoexcited charge and lattice distortions induced by the extra charges themselves, largely influence the transport properties of the material.

A study by Katoch et al. investigated the dynamics of photoexcited electron and hole polarons in a cerium oxide single crystal and in a nanocrystal using FEL-based pump–probe XANES at the Ce M_5 and O K edges detected in total electron yield mode [61]. The samples contained a non-negligible concentration of Ce^{3+} sites within the probed depth. The authors found evidence for electron polaron formation within 0.7 ps, followed by fast decay within a few picoseconds and remnant effects persisting for longer than 1000 ps. In nanocrystals, the holes were found to have longer lifetimes than in single crystals, and they appeared mainly located close to the surface [61]. A different study performed on clean and stoichiometric cerium oxide films by pump–probe XAS at the Ce L_3 edge in the XANES and EXAFS range, detected in the total fluorescence yield mode, provided proof for photoinduced polaron formation by clearly demonstrating a time correlation between the electronic and structural modifications within 500 fs and by finding a structural distortion quantitatively compatible with the one foreseen for a photoinduced polaron [62]. The photoinduced polarons were found to have a lifetime that exceeded 300 ps. The two studies on samples with different defectivity and using techniques with different probing depths suggest that defects can act as polaron trapping and recombination sites and that the excited charge dynamics can be different on the surface and in the bulk of the investigated oxide.

The chemical sensitivity of FEL was also exploited to investigate the electron transfer process in a composite plasmonic/semiconductor system, based on silver NPs embedded in a CeO_2 film [63]. Pump–probe XANES measurements were performed at the Ce $N_{4,5}$ edge upon photoexcitation of plasmonic resonances in the metal NPs by visible laser pulses at an energy lower than the cerium oxide bandgap. The four panels on the right of Figure 7 show the variation of the transient absorption as a function of the pump–probe delay time at selected FEL photon energies across the Ce $N_{4,5}$ edge. The left panel of Figure 7 shows the steady-state Ce $N_{4,5}$ XANES acquired using synchrotron radiation on the composite film and two reference spectra of Ce^{4+} and Ce^{3+} from literature [64]. Also, it evidences the photon energies used for the pump–probe FEL measurements. The transient XANES intensity after pumping the Ag plasmonic resonance, exhibits an increase by about 10% at 119 and 122 eV and a decrease by about 5% at 130 and 133 eV. The changes in the transient XANES intensity occur within the first few hundred femtoseconds and persist up to 1 ps delay time between the pump and the probe. The observed ultrafast changes across the Ce $N_{4,5}$ absorption edge are compatible with a transient reduction of Ce ions in the film, as shown by the left panel of Figure 7, and they demonstrate that the resonantly

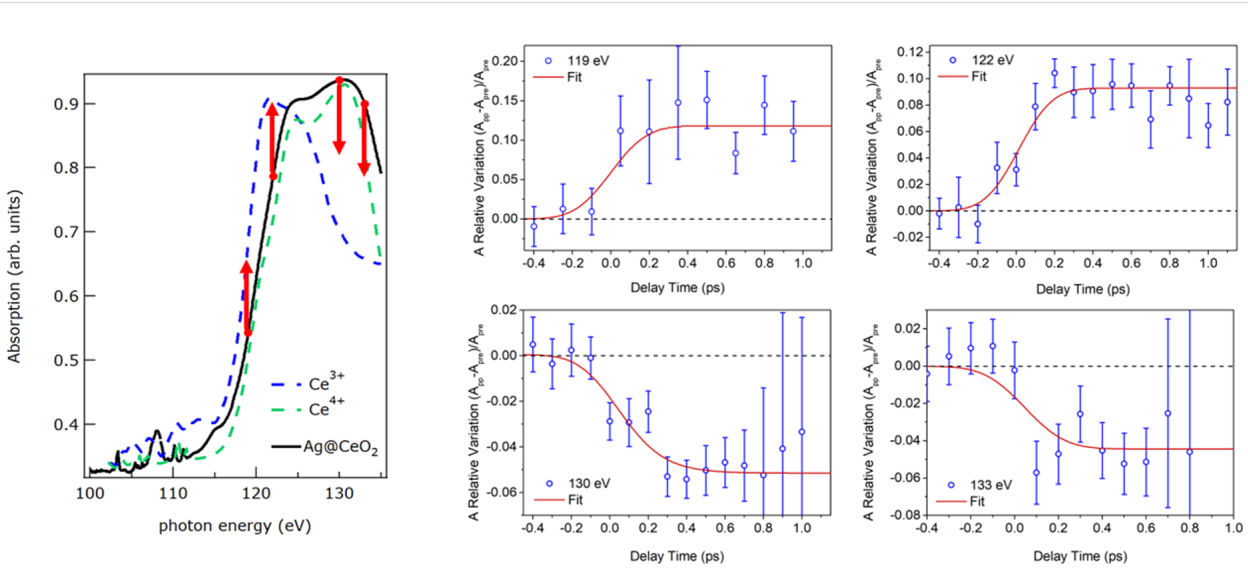

Figure 7: Left: Ce $N_{4,5}$ XAS absorption spectra measured in transmission mode for the CeO_2 film with embedded Ag NPs (solid black line). The spectra of Ce^{4+} (dashed green line) and Ce^{3+} (dashed blue line) reference samples, taken from the literature [64], are also reported. The red arrows indicate the selected FEL energies used to probe the variations of absorption with pump–probe delay time reported in the four right panels, and the direction of the observed variations. Reproduced from [63] (© 2021 J.S. Pelli Cresi et al., published by American Chemical Society, distributed under the terms of the Creative Commons Attribution 4.0 International License, https://creativecommons.org/licenses/by/4.0).

excited plasmonic Ag NPs transfer electrons to the Ce atoms of the CeO_2 film through a highly efficient electron-based mechanism [63]. The importance of this finding is that it provided a direct explanation for the observed sensitization of wide-bandgap oxides, such as cerium oxide, to the visible range through the coupling with suitable plasmonic metal NPs. The NPs convert the resonantly absorbed visible photons into excited charges in the oxide, which have similar properties as the ones induced by direct UV photoexcitation across the bandgap.

Conclusions and Perspectives

The present review reports the advances brought by the use of high-brilliance photon beams generated by synchrotron radiation and FEL sources in the study of cerium oxide-based materials in the form of model systems. Synchrotron radiation-based spectroscopy methods have provided a higher energy resolution and a higher sensitivity to elements with low concentration than laboratory sources, allowing for the study of the properties of ultrathin films, of the effect of low-concentration dopants, and of the interaction with supported NPs. A quantitatively accurate description of the material in its static form has thus been achieved. The possibility to apply ultrashort and ultraintense FEL pulses has opened exciting perspectives for element-sensitive and time-resolved studies of the photoinduced processes in cerium oxide-based and related systems. The first results obtained by pump–probe XAS are very encouraging in view of a more extensive application of other ultrafast FEL-methods, for example, pump–probe photoemission, pump–probe resonant X-ray emission spectroscopy, or pump–probe X-ray diffraction, to more complex systems like highly doped and ternary oxides, or to systems with variable and well-controlled defect densities and architecture, also under operando conditions. Optimizing the lifetime of photoexcited charges, but also understanding the mechanisms and the extent of their spatial propagation, are extremely relevant questions in order to design materials with optimal efficiency.

Acknowledgements

This review was written in the framework of the Italian Ministry of Foreign Affairs and International Cooperation (MAECI) funded project “Ultrafast Dynamics in Materials for Energy Conversion (U-DYNAMEC)” under the program 2023 Italy – Germany Science and Technology Cooperation.

Funding

Financial support from the Italian Ministry of Foreign Affairs and International Cooperation (MAECI) funded project “Ultrafast Dynamics in Materials for Energy Conversion (U-DYNAMEC)” under the program 2023 Italy – Germany Science and Technology Cooperation is acknowledged.

ORCID® iDs

Paola Luches - https://orcid.org/0000-0003-1310-5357
Federico Boscherini - https://orcid.org/0000-0002-9703-3903

Data Availability Statement

Data sharing is not applicable as no new data was generated or analyzed in this study.

References

1. Pacchioni, G.; Valeri, S., Eds. *Oxide ultrathin films;* Wiley-VCH: Weinheim, Germany, 2011. doi:10.1002/9783527640171
2. Pacchioni, G. *Chem. – Eur. J.* **2012,** *18,* 10144–10158. doi:10.1002/chem.201201117
3. Sivaperuman, K.; Thomas, A.; Thangavel, R.; Thirumalaisamy, L.; Palanivel, S.; Pitchaimuthu, S.; Ahsan, N.; Okada, Y. *Prog. Mater. Sci.* **2024,** *142,* 101222. doi:10.1016/j.pmatsci.2023.101222
4. Gao, F.; Goodman, D. W. *Annu. Rev. Phys. Chem.* **2012,** *63,* 265–286. doi:10.1146/annurev-physchem-032511-143722
5. Pedanekar, R. S.; Shaikh, S. K.; Rajpure, K. Y. *Curr. Appl. Phys.* **2020,** *20,* 931–952. doi:10.1016/j.cap.2020.04.006
6. Baby, B. H.; Patel, M.; Lee, K.; Kim, J. *Appl. Sci. Convergence Technol.* **2022,** *31,* 1–8. doi:10.5757/asct.2022.31.1.1
7. Freund, H.-J. *J. Am. Chem. Soc.* **2016,** *138,* 8985–8996. doi:10.1021/jacs.6b05565
8. Surnev, S.; Fortunelli, A.; Netzer, F. P. *Chem. Rev.* **2013,** *113,* 4314–4372. doi:10.1021/cr300307n
9. Montini, T.; Melchionna, M.; Monai, M.; Fornasiero, P. *Chem. Rev.* **2016,** *116,* 5987–6041. doi:10.1021/acs.chemrev.5b00603
10. Fiala, R.; Figueroba, A.; Bruix, A.; Vaclavu, M.; Rednyk, A.; Khalakhan, I.; Vorokhta, M.; Lavkova, J.; Illas, F.; Potin, V.; Matolinova, I.; Neyman, K. M.; Matolin, V. *Appl. Catal., B* **2016,** *197,* 262–270. doi:10.1016/j.apcatb.2016.02.036
11. Liang, F.; Yang, J.; Zhao, Y.; Zhou, Y.; Yan, Z.; He, J.; Yuan, Q.; Wu, J.; Liu, P.; Zhong, Z.; Han, M. *Int. J. Hydrogen Energy* **2022,** *47,* 36926–36952. doi:10.1016/j.ijhydene.2022.08.237
12. Kapuścik, P.; Wojcieszak, D.; Pokora, P.; Mańkowska, E.; Domaradzki, J.; Mazur, M.; Mazur, P.; Kosto, J.; Morales, C.; Kot, M.; Flege, J. I. *Sens. Actuators, B* **2024,** *417,* 136148. doi:10.1016/j.snb.2024.136148
13. Durrani, S. M. A.; Al-Kuhaili, M. F.; Bakhtiari, I. A. *Sens. Actuators, B* **2008,** *134,* 934–939. doi:10.1016/j.snb.2008.06.049
14. Aneggi, E.; Boaro, M.; de Leitenburg, C.; Dolcetti, G.; Trovarelli, A. *J. Alloys Compd.* **2006,** *408–412,* 1096–1102. doi:10.1016/j.jallcom.2004.12.113
15. Boaro, M.; Colussi, S.; Trovarelli, A. *Front. Chem. (Lausanne, Switz.)* **2019,** *7,* 28. doi:10.3389/fchem.2019.00028
16. Gamarra, D.; Munuera, G.; Hungría, A. B.; Fernández-García, M.; Conesa, J. C.; Midgley, P. A.; Wang, X. Q.; Hanson, J. C.; Rodríguez, J. A.; Martínez-Arias, A. *J. Phys. Chem. C* **2007,** *111,* 11026–11038. doi:10.1021/jp072243k
17. Xu, W.; Si, R.; Senanayake, S. D.; Llorca, J.; Idriss, H.; Stacchiola, D.; Hanson, J. C.; Rodriguez, J. A. *J. Catal.* **2012,** *291,* 117–126. doi:10.1016/j.jcat.2012.04.013
18. Grinter, D. C.; Thornton, G. *J. Phys.: Condens. Matter* **2022,** *34,* 253001. doi:10.1088/1361-648x/ac5d89
19. Mullins, D. R. *Surf. Sci. Rep.* **2015,** *70,* 42–85. doi:10.1016/j.surfrep.2014.12.001

20. Luches, P.; Valeri, S. *Materials* **2015,** *8,* 5818–5833. doi:10.3390/ma8095278
21. Škoda, M.; Libra, J.; Šutara, F.; Tsud, N.; Skála, T.; Sedláček, L.; Cháb, V.; Prince, K. C.; Matolín, V. *Surf. Sci.* **2007,** *601,* 4958–4965. doi:10.1016/j.susc.2007.08.010
22. Mullins, D. R.; Radulovic, P. V.; Overbury, S. H. *Surf. Sci.* **1999,** *429,* 186–198. doi:10.1016/s0039-6028(99)00369-6
23. Eck, S.; Castellarin-Cudia, C.; Surnev, S.; Ramsey, M. G.; Netzer, F. P. *Surf. Sci.* **2002,** *520,* 173–185. doi:10.1016/s0039-6028(02)02272-0
24. Allahgholi, A.; Flege, J. I.; Thieß, S.; Drube, W.; Falta, J. *ChemPhysChem* **2015,** *16,* 1083–1091. doi:10.1002/cphc.201402729
25. Matsumoto, M.; Soda, K.; Ichikawa, K.; Tanaka, S.; Taguchi, Y.; Jouda, K.; Aita, O.; Tezuka, Y.; Shin, S. *Phys. Rev. B* **1994,** *50,* 11340–11346. doi:10.1103/physrevb.50.11340
26. Vayssilov, G. N.; Lykhach, Y.; Migani, A.; Staudt, T.; Petrova, G. P.; Tsud, N.; Skála, T.; Bruix, A.; Illas, F.; Prince, K. C.; Matolı´n, V.; Neyman, K. M.; Libuda, J. *Nat. Mater.* **2011,** *10,* 310–315. doi:10.1038/nmat2976
27. Lykhach, Y.; Kozlov, S. M.; Skála, T.; Tovt, A.; Stetsovych, V.; Tsud, N.; Dvořák, F.; Johánek, V.; Neitzel, A.; Mysliveček, J.; Fabris, S.; Matolín, V.; Neyman, K. M.; Libuda, J. *Nat. Mater.* **2016,** *15,* 284–288. doi:10.1038/nmat4500
28. Matolín, V.; Cabala, M.; Cháb, V.; Matolínová, I.; Prince, K. C.; Škoda, M.; Šutara, F.; Skála, T.; Veltruská, K. *Surf. Interface Anal.* **2008,** *40,* 225–230. doi:10.1002/sia.2625
29. Simon, P.; Zanfoni, N.; Avril, L.; Li, Z.; Potin, V.; Domenichini, B.; Bourgeois, S. *Adv. Mater. Interfaces* **2017,** *4,* 1600821. doi:10.1002/admi.201600821
30. Matolín, V.; Matolínová, I.; Sedláček, L.; Prince, K. C.; Skála, T. *Nanotechnology* **2009,** *20,* 215706. doi:10.1088/0957-4484/20/21/215706
31. Lykhach, Y.; Staudt, T.; Tsud, N.; Skála, T.; Prince, K. C.; Matolín, V.; Libuda, J. *Phys. Chem. Chem. Phys.* **2011,** *13,* 253–261. doi:10.1039/c0cp00345j
32. Matolín, V.; Libra, J.; Škoda, M.; Tsud, N.; Prince, K. C.; Skála, T. *Surf. Sci.* **2009,** *603,* 1087–1092. doi:10.1016/j.susc.2009.02.010
33. Eck, S.; Castellarin-Cudia, C.; Surnev, S.; Prince, K. C.; Ramsey, M. G.; Netzer, F. P. *Surf. Sci.* **2003,** *536,* 166–176. doi:10.1016/s0039-6028(03)00594-6
34. Rodriguez, J. A.; Jirsak, T.; Freitag, A.; Hanson, J. C.; Larese, J. Z.; Chaturvedi, S. *Catal. Lett.* **1999,** *62,* 113–119. doi:10.1023/a:1019007308054
35. Lykhach, Y.; Johánek, V.; Neitzel, A.; Skála, T.; Tsud, N.; Beranová, K.; Mysliveček, J.; Brummel, O.; Libuda, J. *J. Phys.: Condens. Matter* **2022,** *34,* 194002. doi:10.1088/1361-648x/ac5138
36. Matolín, V.; Matolínová, I.; Dvořák, F.; Johánek, V.; Mysliveček, J.; Prince, K. C.; Skála, T.; Stetsovych, O.; Tsud, N.; Václavů, M.; Šmíd, B. *Catal. Today* **2012,** *181,* 124–132. doi:10.1016/j.cattod.2011.05.032
37. Brummel, O.; Waidhas, F.; Faisal, F.; Fiala, R.; Vorokhta, M.; Khalakhan, I.; Dubau, M.; Figueroba, A.; Kovács, G.; Aleksandrov, H. A.; Vayssilov, G. N.; Kozlov, S. M.; Neyman, K. M.; Matolín, V.; Libuda, J. *J. Phys. Chem. C* **2016,** *120,* 19723–19736. doi:10.1021/acs.jpcc.6b05962
38. Liu, Z.; Yao, S.; Johnston-Peck, A.; Xu, W.; Rodriguez, J. A.; Senanayake, S. D. *Catal. Today* **2018,** *311,* 74–80. doi:10.1016/j.cattod.2017.08.041
39. Allan, M.; Grinter, D.; Dhaliwal, S.; Muryn, C.; Forrest, T.; Maccherozzi, F.; Dhesi, S. S.; Thornton, G. *Surf. Sci.* **2019,** *682,* 8–13. doi:10.1016/j.susc.2018.12.005
40. Romeo, M.; Bak, K.; El Fallah, J.; Le Normand, F.; Hilaire, L. *Surf. Interface Anal.* **1993,** *20,* 508–512. doi:10.1002/sia.740200604
41. Luches, P.; Pagliuca, F.; Valeri, S.; Boscherini, F. *J. Phys. Chem. C* **2013,** *117,* 1030–1036. doi:10.1021/jp310375t
42. Cresi, J. S. P.; Chiara Spadaro, M.; D'Addato, S.; Valeri, S.; Amidani, L.; Boscherini, F.; Bertoni, G.; Deiana, D.; Luches, P. *Nanotechnology* **2017,** *28,* 495702. doi:10.1088/1361-6528/aa926f
43. Loschen, C.; Bromley, S. T.; Neyman, K. M.; Illas, F. *J. Phys. Chem. C* **2007,** *111,* 10142–10145. doi:10.1021/jp072787m
44. Deshpande, S.; Patil, S.; Kuchibhatla, S. V.; Seal, S. *Appl. Phys. Lett.* **2005,** *87,* 133113. doi:10.1063/1.2061873
45. Baranchikov, A. E.; Polezhaeva, O. S.; Ivanov, V. K.; Tretyakov, Y. D. *CrystEngComm* **2010,** *12,* 3531–3533. doi:10.1039/c0ce00245c
46. Wu, L.; Wiesmann, H. J.; Moodenbaugh, A. R.; Klie, R. F.; Zhu, Y.; Welch, D. O.; Suenaga, M. *Phys. Rev. B* **2004,** *69,* 125415. doi:10.1103/physrevb.69.125415
47. Pelli Cresi, J. S.; Carlà, F.; Znaiguia, R.; Isern, H.; Benedetti, F.; Gasperi, G.; Amidani, L.; Valeri, S.; Boscherini, F.; Luches, P. *Adv. Mater. Interfaces* **2020,** *7,* 2000737. doi:10.1002/admi.202000737
48. Tschammer, R.; Buß, L.; Pożarowska, E.; Morales, C.; Senanayake, S. D.; Prieto, M. J.; Tănase, L. C.; de Souza Caldas, L.; Tiwari, A.; Schmidt, T.; Niño, M. A.; Foerster, M.; Falta, J.; Flege, J. I. *J. Phys. Chem. C* **2025,** *129,* 3583–3594. doi:10.1021/acs.jpcc.4c08072
49. Gasperi, G.; Amidani, L.; Benedetti, F.; Boscherini, F.; Glatzel, P.; Valeri, S.; Luches, P. *Phys. Chem. Chem. Phys.* **2016,** *18,* 20511–20517. doi:10.1039/c6cp04407g
50. Kotani, A.; Shin, S. *Rev. Mod. Phys.* **2001,** *73,* 203–246. doi:10.1103/revmodphys.73.203
51. Kvashnina, K. O.; Butorin, S. M.; Glatzel, P. *J. Anal. At. Spectrom.* **2011,** *26,* 1265–1272. doi:10.1039/c0ja00142b
52. Cafun, J.-D.; Kvashnina, K. O.; Casals, E.; Puntes, V. F.; Glatzel, P. *ACS Nano* **2013,** *7,* 10726–10732. doi:10.1021/nn403542p
53. Benedetti, F.; Luches, P.; Spadaro, M. C.; Gasperi, G.; D'Addato, S.; Valeri, S.; Boscherini, F. *J. Phys. Chem. C* **2015,** *119,* 6024–6032. doi:10.1021/jp5120527
54. Luches, P.; Pagliuca, F.; Valeri, S.; Illas, F.; Preda, G.; Pacchioni, G. *J. Phys. Chem. C* **2012,** *116,* 1122–1132. doi:10.1021/jp210241c
55. Flege, J. I.; Höcker, J.; Kaemena, B.; Menteş, T. O.; Sala, A.; Locatelli, A.; Gangopadhyay, S.; Sadowski, J. T.; Senanayake, S. D.; Falta, J. *Nanoscale* **2016,** *8,* 10849–10856. doi:10.1039/c6nr02393b
56. Grinter, D. C.; Graciani, J.; Palomino, R. M.; Xu, F.; Waluyo, I.; Sanz, J. F.; Senanayake, S. D.; Rodriguez, J. A. *Surf. Sci.* **2021,** *710,* 121852. doi:10.1016/j.susc.2021.121852
57. Graciani, J.; Grinter, D. C.; Ramírez, P. J.; Palomino, R. M.; Xu, F.; Waluyo, I.; Stacchiola, D.; Fdez Sanz, J.; Senanayake, S. D.; Rodriguez, J. A. *ACS Catal.* **2022,** *12,* 15097–15109. doi:10.1021/acscatal.2c03823
58. Vikatakavi, A.; Mauri, S.; Rivera-Salazar, M. L.; Dobovičnik, E.; Pelatti, S.; D'Addato, S.; Torelli, P.; Luches, P.; Benedetti, S. *ACS Appl. Energy Mater.* **2024,** *7,* 2746–2754. doi:10.1021/acsaem.3c03169
59. Spurio, E.; Mauri, S.; Pelatti, S.; Rivera-Salazar, M. L.; D'Addato, S.; Torelli, P.; Luches, P.; Benedetti, S. *in preparation* **2025**.
60. Pelli Cresi, J. S.; Di Mario, L.; Catone, D.; Martelli, F.; Paladini, A.; Turchini, S.; D'Addato, S.; Luches, P.; O'Keeffe, P. *J. Phys. Chem. Lett.* **2020,** *11,* 5686–5691. doi:10.1021/acs.jpclett.0c01590

61. Katoch, A.; Park, S. H.; Jeong, K.; Lazemi, M.; Wang, R.-P.; Ahn, H. S.; Kim, T. K.; de Groot, F. M. F.; Kwon, S. *Adv. Opt. Mater.* **2024,** *12,* 2401386. doi:10.1002/adom.202401386
62. Pelatti, S.; Spurio, E.; Catone, D.; O'Keeffe, P.; Turchini, S.; Ammirati, G.; Paleari, F.; Varsano, D.; Benedetti, S.; di Bona, A.; D'Addato, S.; Jiang, Y.; Zalden, P.; Uemura, Y.; Wang, H.; Vinci, D.; Huang, X.; Lima, F.; Biednov, M.; Khakhulin, D.; Jackson Milne, C.; Boscherini, F.; Luches, P. *in preparation* **2025**.
63. Pelli Cresi, J. S.; Principi, E.; Spurio, E.; Catone, D.; O'Keeffe, P.; Turchini, S.; Benedetti, S.; Vikatakavi, A.; D'Addato, S.; Mincigrucci, R.; Foglia, L.; Kurdi, G.; Nikolov, I. P.; De Ninno, G.; Masciovecchio, C.; Nannarone, S.; Kopula Kesavan, J.; Boscherini, F.; Luches, P. *Nano Lett.* **2021,** *21,* 1729–1734. doi:10.1021/acs.nanolett.0c04547
64. Kucheyev, S. O.; Clapsaddle, B. J.; Wang, Y. M.; van Buuren, T.; Hamza, A. V. *Phys. Rev. B* **2007,** *76,* 235420. doi:10.1103/physrevb.76.235420

License and Terms

BEILSTEIN JOURNAL OF NANOTECHNOLOGY

Heat-induced transformation of nickel-coated polycrystalline diamond film studied in situ by XPS and NEXAFS

Olga V. Sedelnikova[*,‡1], Yuliya V. Fedoseeva[‡1], Dmitriy V. Gorodetskiy[1], Yuri N. Palyanov[2], Elena V. Shlyakhova[1], Eugene A. Maksimovskiy[1], Anna A. Makarova[3,4], Lyubov G. Bulusheva[1] and Aleksandr V. Okotrub[1]

Full Research Paper

Open Access

Address:
[1]Nikolaev Institute of Inorganic Chemistry, SB RAS, 630090 Novosibirsk, Russia, [2]Sobolev Institute of Geology and Mineralogy, SB RAS, 630090 Novosibirsk, Russia, [3]Physical Chemistry, Institute of Chemistry and Biochemistry, Free University of Berlin, 14195 Berlin, Germany and [4]Helmholtz-Zentrum Berlin für Materialien und Energie, 14109 Berlin, Germany

Email:
Olga V. Sedelnikova[*] - o.sedelnikova@gmail.com

* Corresponding author ‡ Equal contributors

Keywords:
graphitization; near-edge X-ray absorption fine structure spectroscopy; nickel coating; polycrystalline diamond film; single-crystal diamond; X-ray photoelectron spectroscopy

Beilstein J. Nanotechnol. **2025,** *16,* 887–898.
https://doi.org/10.3762/bjnano.16.67

Received: 04 March 2025
Accepted: 19 May 2025
Published: 12 June 2025

This article is part of the thematic issue "Exploring synchrotron radiation and free-electron laser tools for nanostructured materials".

Guest Editor: C. Bittencourt

Abstract

Controlling high-temperature graphitization of diamond surfaces is important for many applications, which require the formation of thin conductive electrodes on dielectric substrates. Transition metal catalysts can facilitate the graphitization process, which depends on the diamond face orientation. In the present work, the role of a nickel coating on the electronic structure and chemical state of graphite layers formed on the surface of a polycrystalline diamond (PCD) film with mixed grain orientation was studied. A synthetic single-crystal diamond (SCD) with a polished (110) face was examined for comparison. The samples were coated with a thin nickel film deposited by thermal evaporation. The graphitization of diamond with and without a nickel coating as a result of high-vacuum annealing at a temperature of about 1100 °C was studied in situ using synchrotron-based X-ray photoelectron spectroscopy (XPS) and near-edge X-ray absorption fine structure (NEXAFS) methods. XPS data revealed the formation of a thin graphite-like film with low-ordered atomic structure on the surface of the nickel-coated PCD film. The chemical state of sp^2-hybridized carbon atoms was found to be insensitive to the face orientation of the diamond micro-sized crystallites; however, the layer defectiveness increased in areas with fine-dispersed crystallites. According to NEXAFS and Raman spectroscopy data, the most ordered atomic structure of graphitic layers was obtained by annealing nickel-coated SCD. The angular dependence of NEXAFS C K-edge spectra of nickel-coated (110) face after annealing discovered the vertical orientation of sp^2-hybridized carbon layers relative to the diamond surface. The observed behavior suggests that sp^2 carbon layers were formed on the diamond surface due to its saturation by released carbon atoms as a result of etching by nickel.

Introduction

Diamond and graphite, both composed entirely of carbon atoms, exhibit vastly different properties due to their distinct atomic structures. Diamond is a wide bandgap semiconductor, which makes it resistant to high voltages and ionizing radiation. In contrast, graphitic materials demonstrate excellent electrical conductivity. This divergence in physical properties has encouraged significant interest in producing hybrid materials which combine these two forms of carbon [1-3]. In particular, such graphene-on-diamond heterostructures have been shown to be attractive for power electronics [4,5], microelectronic devices [6,7], and detectors [7,8].

At room temperature and atmospheric pressure, carbon in sp^3 hybridization is a metastable material. A significant activation barrier hampers its relaxation into sp^2 graphitic carbon, and this transformation occurs during vacuum heating in the temperature range of 1500–1800 °C [9]. According to molecular dynamics simulations, graphitization of nonterminated diamond surfaces is initiated at 750 °C. A temperature of about 1500 °C is needed for the formation of extended graphene-like layers, and temperatures higher than 2000 °C are required for the complete conversion of the diamond (111) surface to graphitic layers [10,11]. Thermal stability of diamond crystals depends on the crystallographic orientation of their faces [12,13]. In particular, the (100) face exhibits greater resistance to annealing compared to that of the (111) face [10,13-15], and the (110) face has proven to be the most unstable when exposed to high temperatures [14,16].

The coating of diamond surface with a metal catalyst has been explored to reduce the temperatures required for the initiation of the graphitization process. Nickel [17-24], iron [25-28], copper [29,30], gallium [31], and molybdenum [32] allow the fabrication of graphene-on-diamond heterostructures by annealing. Among those, nickel attracts specific attention since the 1960s [33] because its lattice parameter is close to that of diamond. Single-crystal diamond (SCD) substrates were subjected to nickel-assisted graphitization [17-21]. The transformation of the SCD surface into graphene requires annealing at temperatures above 800 °C [21]. The annealing of nanocrystalline diamond (NCD) films in the presence of a Ni catalyst has been recently explored [22-24]. It was shown that graphitization of Ni-coated NCD films begins at a relatively lower temperature of about 500 °C [23]. Such a significant decrease in the temperature at which graphitization starts compared to that of the Ni-coated SCD is due to the presence of multiple grain boundaries, along which the diffusion of Ni atoms takes place, facilitating the graphitization process [34].

The process occurring at the interface between diamond and Ni nanoparticles was revealed using high-resolution transmission electron microscopy (HRTEM) [19,24]. During annealing, Ni nanoparticles etch the diamond surface, resulting in the formation of a narrow interdiffusion zone. The carbon atoms released from the diamond surface diffuse across the Ni surface. After the Ni particles are saturated with carbon, the excess carbon precipitates to form the sp^2-hybridized graphitic layers parallel to the Ni surface [19,24]. Alternatively, these atoms could diffuse along the etched diamond surface, saturating the dangling bonds and producing the sp^2 carbon on the free diamond surface, or diffuse into the Ni bulk, feeding the graphite formation from the side of the catalytic particle [19]. Comparing the morphology of Ni-coated SCDs annealed under similar conditions revealed the anisotropic nature of both the diamond etching [35,36] and the graphitization of the diamond surface [19]. In particular, the (111) face was found to be resistant to etching, producing a thin layer of disordered graphite that was weakly bonded to the underlying diamond surface but strongly attached to the Ni particles. In contrast, the Ni nanoparticles penetrate beneath the (110) and (100) surfaces, creating pits that were partially filled with graphite covalently bonded to the etched diamond surface.

From prior works, it can be seen that the Ni-assisted graphitization of diamond has been studied on either SCDs, which have better properties but high cost, or on more affordable NCD films, whose properties are notably inferior to their monocrystalline counterparts. In this regard, microcrystalline diamond (MCD) films could serve as a more suitable alternative to SCDs. Therefore, the Ni-assisted graphitization of MCD films requires a detailed study. HRTEM has proven very useful for investigating the graphite–diamond interface [19,24]. However, it provides information about local morphology and ordering of diamond surface and graphite layers. X-ray photoelectron spectroscopy (XPS) and near-edge X-ray absorption fine structure (NEXAFS) methods are noncontact and nondestructive methods to investigate the chemical state of the elements on the surface and in the bulk of solids. The signals collected over a large surface area provide overall insight into the surface state. Moreover, the polarization-dependence of NEXAFS spectra provides information about the spatial orientation of π and σ orbitals relative to the photon incidence.

In the present work, we focused on the changes in the surface state of Ni-coated polycrystalline diamond (PCD) films composed of micron-sized grains with (110) and (111) faces during high-vacuum annealing at a temperature of about 1100 °C. To exclude the influence of impurities from the air, the annealed samples were examined in situ using XPS and

NEXAFS without contact with the air. XPS and NEXAFS spectroscopy investigations of heat-induced transformation of the surface of bare and Ni-coated PCD films were conducted at the experimental station of the Russian–German Beamline using the BESSY II synchrotron radiation facility. To achieve variable depth sensitivity, XPS spectra were collected at two excitation photon energies, and NEXAFS spectra were recorded using two registration modes. Additionally, angle-resolved NEXAFS spectra of annealed Ni-coated SCD were measured to reveal the orientation of the formed graphitic layers. After synchrotron measurements, the samples were exposed to air and further analyzed using Raman spectroscopy and scanning electron microscopy (SEM). The obtained results revealed detailed information about the morphology of the graphitized layer formed on the PCD film surface during annealing in the presence of nickel. We were also able to determine the texture of these graphitized layers relative to the (110) face of SCD.

Results and Discussion

Surface transformation of bare and nickel-coated polycrystalline diamond films under high-vacuum annealing

The PCD film was produced by plasma-enhanced chemical vapor deposition (PE CVD) using acetone $(CH_3)_2CO$, hydrogen, and air as the precursor gases for the plasma [37]. The film consists of crystallites with nonuniform geometry, dimensions, and orientation (Supporting Information File 1, Figure S1a–c). The large diamond micro-sized crystallites, measuring about 100 µm, have a complex cuboctahedron shape with facets that have straight and acute angles. Electron backscatter diffraction (EBSD) analysis detected (110) and (111) crystallographic planes on the surface of the PCD film (Supporting Information File 1, Figure S1b). The mapping did not show regions with the (100) orientation, although cubic faces are visible in the SEM images. The signal from these faces is probably weakened due to the tilt of the crystallites and the rough PCD film. Various growth defects, including pits, cracks, steps, and protrusions are present on the diamond faces. The secondary nucleation of diamond caused the formation of submicron-sized diamond grains and smoothing of the shape of large crystals. Raman spectroscopy revealed high crystalline quality in the PCD film at the micron scale (Supporting Information File 1, Figure S2). Thermal evaporation of nickel and its deposition on the PCD film surface resulted in the formation of a uniform metallic layer with a thickness of about 40 nm (Supporting Information File 1, Figure S1d). The bare PCD film and that with a nickel coating (denoted Ni-PCD) were placed on the same holder and simultaneously annealed in the vacuum chamber of the RGL-PES end-station of BESSY at 1100 °C for 15 min. After annealing, PCD and Ni-PCD films were cooled to room temperature without contact with air and examined in situ using NEXAFS and XPS methods. The changes in the chemical state of the surface of the PCD and Ni-PCD films as a result of annealing were examined.

The NEXAFS C K-edge spectra were simultaneously recorded in total electron yield (TEY) and Auger electron yield (AEY) modes to probe the volume (10 nm) and the surface (3 nm) of the films, respectively (Figure 1). The C K-edge spectra of the annealed samples show a sharp peak at 289.3 eV assigned to the electron transition from 1s to unoccupied σ* states within the sp^3-hybridized carbon atoms in the diamond (σ*(sp^3)) and a wide dip at 302.2 eV corresponding to a second absolute gap in

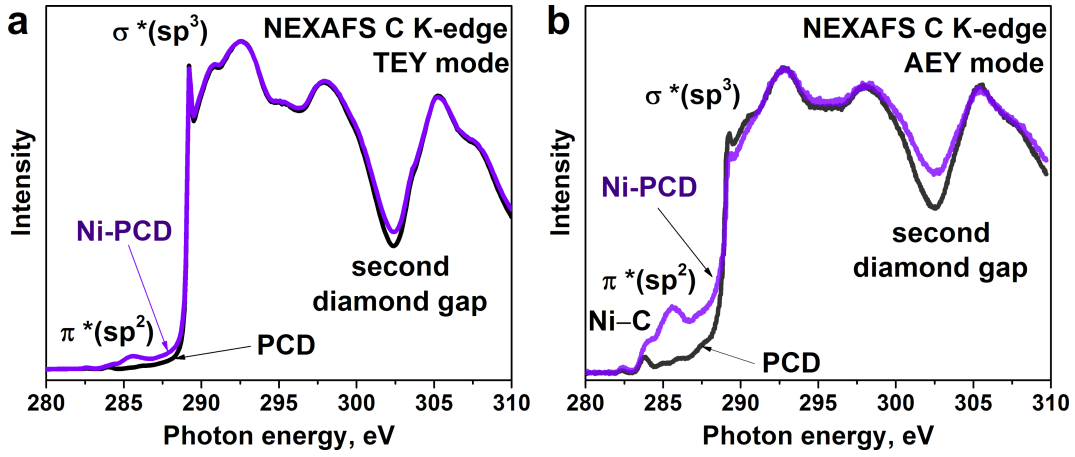

Figure 1: NEXAFS C K-edge spectra of PCD and Ni-PCD films after high-vacuum annealing at 1100 °C, measured in a) TEY mode and b) AEY mode.

the diamond band structure [38]. In the TEY spectra of both PCD and Ni-PCD films, the aforementioned spectral features are well pronounced, indicating the preservation of the ordered crystalline structure of diamond in the bulk of the film after annealing (Figure 1a). In the AEY spectra of both films, the smoother shape of the $\sigma^*(sp^3)$ resonance and the shallower dip suggest to the presence of structural disorders on the surface of diamond films (Figure 1b). The amount of these disorders in Ni-PCD is higher than that in PCD. This result confirms previous findings that the metal catalyst induces the formation of disordered carbon on the diamond surface during annealing [21-23]. All spectra also show a weak feature at 285.5 eV, which corresponds to the electron transitions from C 1s to unoccupied π^* states in sp^2-hybridized carbon species ($\pi^*(sp^2)$). It was found that 1s–$\pi^*(sp^2)$ excitations in the aromatic molecules and graphene also contribute to the spectral region between 286.0 and 288.5 eV, albeit with a low intensity [39,40].

The $\pi^*(sp^2)$ peak is more intense in the AEY spectra than in the TEY spectra, meaning that the film surface consists of carbon atoms in sp^2-hybridized state. The $\pi^*(sp^2)$ peak in the spectra of the annealed Ni-PCD film has a much higher intensity than that in the spectra of the annealed PCD film. Based on this observation, we can conclude that nickel promotes the conversion of the diamond film surface into an sp^2-carbon coating upon annealing. This result confirms previously reported findings, which demonstrated the catalytic role of nickel in the reconstruction of a diamond surface [17-24]. Based on electron microscopy and Raman spectroscopy data, the authors of those studies claimed that graphite or graphene-like layers are products of the diamond annealing process.

The intensity ratio of $\pi^*(sp^2)$- and $\sigma^*(sp^2)$-resonances in NEXAFS C K-edge spectra of the annealed samples can be used for qualitative assessment of structural perfection in a graphitic-like material. Graphite and graphene have a high degree of local crystallinity (i.e., high ordering of carbon atoms in the honeycomb network) and their C K-edge spectra contain a narrow and intense $\pi^*(sp^2)$-resonance [41,42]. However, the rather low intensity of the $\pi^*(sp^2)$-resonance in the spectrum of the annealed Ni-PCD film indicates that annealing of polycrystalline films on average leads to the formation of structurally highly disordered forms of sp^2 carbon layers. The AEY spectra of the annealed PCD and Ni-PCD films exhibit an additional pronounced feature at about 284.0 eV, which can also be assigned to $\pi^*(sp^2)$-resonance and associated with the presence of large aromatic fragments on the surface of both annealed films [43]. Moreover, this peak overlaps with the characteristic C K-edge features of transition metal carbides. Therefore, it can also be attributed to the presence of Ni–C states in the annealed Ni-PCD film [44].

Survey XPS spectra of the annealed samples showed a strong C 1s line at ≈285 eV and a weak Ni 3p peak at ≈67 eV only for the Ni-PCD film (Supporting Information File 1, Figure S3). Oxygen and other elements were not detected on the surface of the samples. The low surface concentration of nickel (0.1 atom %) could be associated with the heat-induced reorganization of the Ni layer into particles, which can penetrate into the diamond substrate due to the counter-diffusion of carbon and nickel [19]. The immersing of metal particles into diamond was discussed in detail in previous works [27,28].

The XPS C 1s spectra were measured upon excitation by photons with energies of 830 and 330 eV to probe different surface depths of the samples after annealing (Figure 2). In these cases, the inelastic mean free path for electrons emitted from the C 1s level in diamond is about 1.0 nm (probing depth of 3 nm) for 830 eV and 0.7 nm (probing depth of 2.1 nm) for 330 eV, respectively [45]. The C 1s spectrum of PCD after high-vacuum annealing was fitted with two components. The dominant peak at 285.2 eV is assigned to sp^3-hybridized carbon atoms in diamond crystals. Additionally, there is a tiny peak at 284.3 eV assigned to sp^2-hybridized carbon atoms. The relative area of this sp^2-peak is 3% in the spectrum measured at 830 eV, and becomes significantly larger (16%) as the photon excitation energy decreases to 330 eV. The rather small amount of sp^2 carbon in the 2 nm thick surface layer indicates that the temperature and duration of the annealing process were not sufficient to achieve significant graphitization of the PCD surface without a nickel layer. In contrast, an intense sp^2-carbon component is observed in the C 1s spectra of Ni-PCD, confirming that the diamond surface in the presence of nickel catalyst more readily transforms to sp^2-hybridized carbon. For excitation at 830 eV, the sp^2 peak is quite broad (1.1 eV) compared to that in the spectrum of a highly ordered graphite crystal (0.6 eV) [42]. The reason for this is the high density of defects in the carbon layer formed on the Ni-PCD surface during annealing. In the spectrum of the annealed Ni-PCD surface, the peak at 285.2 eV can be assigned to diamond sp^3-states similar to that in the initial diamond. However, highly disordered sp^3 carbon states (C_{dis}) can also give rise to this peak. According to a recent XPS study of the graphitization process of Ni-coated NCD films, a disordered carbon was found to form on the nickel surface, which then partially transformed into a graphitic phase at higher temperatures [23]. Moreover, the spectra of the annealed Ni-PCD film demonstrate an additional peak at a low binding energy of 283.3 eV corresponding to carbon bonded with nickel (denoted as C–Ni in Figure 2). The amount of C–Ni states decreases as the probing depth increases. The XPS data are consistent with the AEY NEXAFS spectrum of the annealed Ni-PCD, confirming that the Ni coating facilitates the transformation of the diamond surface upon heating, resulting in the develop-

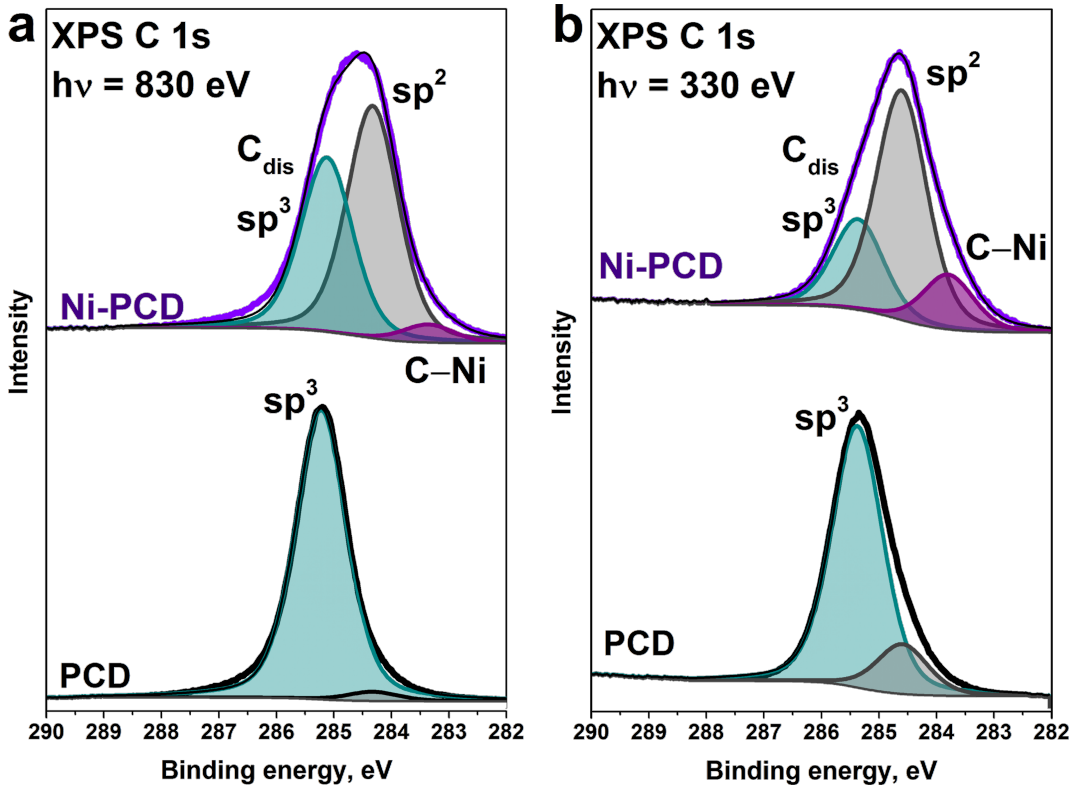

Figure 2: XPS C 1s spectra of PCD and Ni-PCD films after high-vacuum annealing at 1100 °C, measured at excitation photon energies of a) 830 eV and b) 330 eV.

ment of a thin sp² carbon layer over the entire surface of the sample.

The chemical state of nickel in the annealed Ni-PCD film was elucidated using XPS and NEXAFS spectroscopy to probe the local environment of metal atoms on the surface and inside the bulk (Figure 3). The XPS Ni 3p spectrum was fitted by three doublets, related to the spin–orbit splitting into Ni $3p_{3/2}$ and Ni $3p_{1/2}$ components, separated by 1.6 eV (Figure 3a). The most intense doublet with the Ni $3p_{3/2}$ component at 66.1 eV is attributed to metallic nickel [46]. The high-energy doublet with the Ni $3p_{3/2}$ component at 68.1 eV corresponds to the oxidized

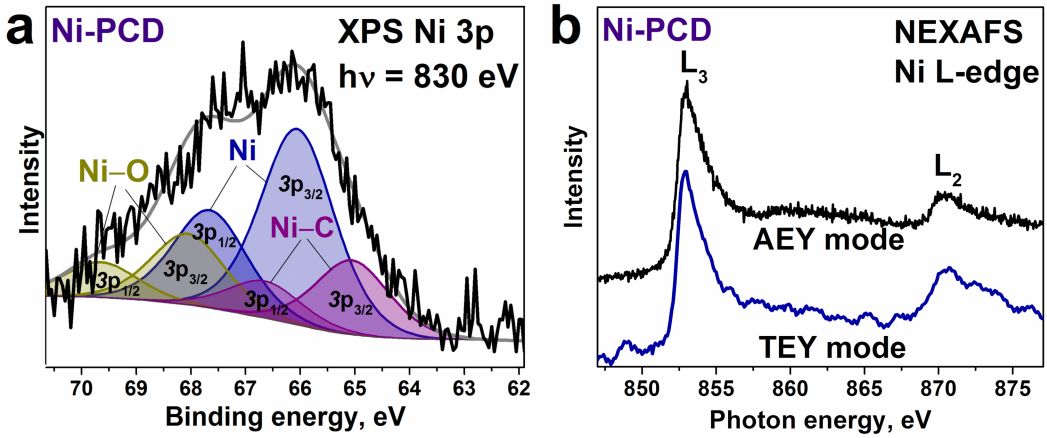

Figure 3: a) XPS Ni 3p spectrum measured at 830 eV and b) NEXAFS Ni L-edge spectra recorded in TEY and AEY modes of Ni-PCD film after high-vacuum annealing at 1100 °C.

states of nickel (Ni–O). The appearance of these states may be due to the interaction of nickel with residual water in the vacuum chamber or with oxygen desorbed from the silicon substrate during annealing [47]. The low-energy doublet with the Ni $3p_{3/2}$ component at 65.0 eV can be referred to nickel bonded with carbon (Ni–C) [48]. The Ni–O and Ni–C doublets contribute no more than 14% to the total spectral area (with a surface content of less than 0.01 atom %). The NEXAFS Ni L-edge spectra measured in TEY and AEY modes show peaks at 852.7 and 870.4 eV, corresponding to L_3 and L_2-edges, respectively (Figure 3b). According to their energy positions, the metallic nature of the nickel appears to dominate both in the bulk and on the surface of Ni-PCD after annealing [49].

After completion of synchrotron investigations, the PCD and Ni-PCD films were removed from the vacuum chamber for further SEM and Raman analysis under ambient conditions. Figure 4 shows SEM images of some large crystallites of about 100 µm in size on the surfaces of the annealed PCD and Ni-PCD. These crystallites have well-defined triangular (111) faces and truncated rectangular faces, which could be assigned to either the (110) or (100) planes. Since the (110) orientation of grains strongly dominates, as shown by the EBSD map, the rectangular faces will be referred to as (110). The bare film almost completely preserved its initial morphology after annealing. A close examination revealed that the diamond faces are sufficiently flat and show no signs of thermal degradation. In the annealed Ni-PCD film, the crystallites have a rougher surface. SEM images do not allow for a definite confirmation of whether sp^2 carbon is present on the surface, even near defective states, partly due to its fine structure.

Comparison of SEM images taken from two different faces of the Ni-coated crystallite reveals that the initially solid nickel layer is rearranged into particles whose shape and distribution depend on the orientation of the diamond face (bright spots in bottom panels in Figure 4). In particular, on the rectangular (110) faces, nickel particles are flatter and more evenly distributed than those on the triangular (111) face. Previous studies showed that the etching of diamond through the reaction with Ni during annealing is an anisotropic process [19,35,36]. In particular, the (100) and (110) faces are etched simply, while the (111) face is flattened during the process. We assume that small nickel nanoparticles formed above the (110) faces are embedded in the diamond, while their agglomerates remain on the (111) faces, appearing as large particles enclosed in carbon shells. Element mapping analysis based on energy-dispersive X-ray (EDX) spectroscopy revealed a uniform distribution of nickel particles in the top layers of all diamond faces after annealing (Supporting Information File 1, Figure S4). The low resolution of the EDX instrument used did not allow the detection of nickel-free areas of diamond surfaces.

Raman spectroscopy was used to compare the different regions of the annealed PCD and Ni-PCD films (Figure 5 and Supporting Information File 1, Figure S5). The spectra recorded for two

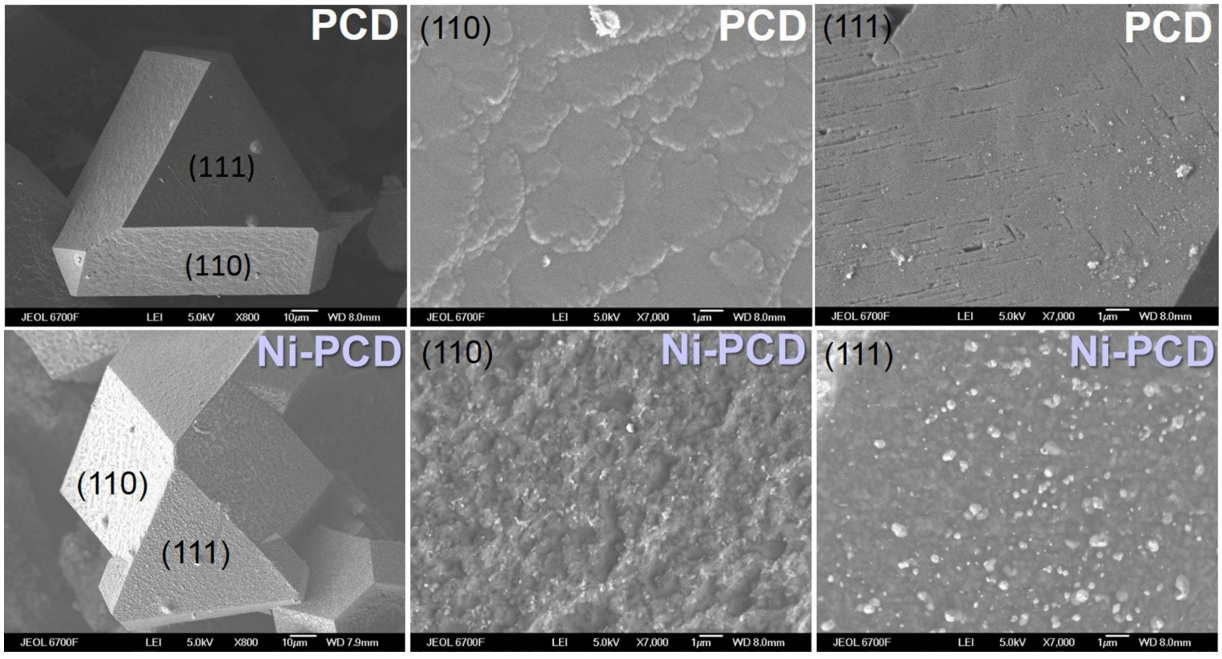

Figure 4: SEM images of crystallites with different faces in annealed PCD and Ni-PCD films.

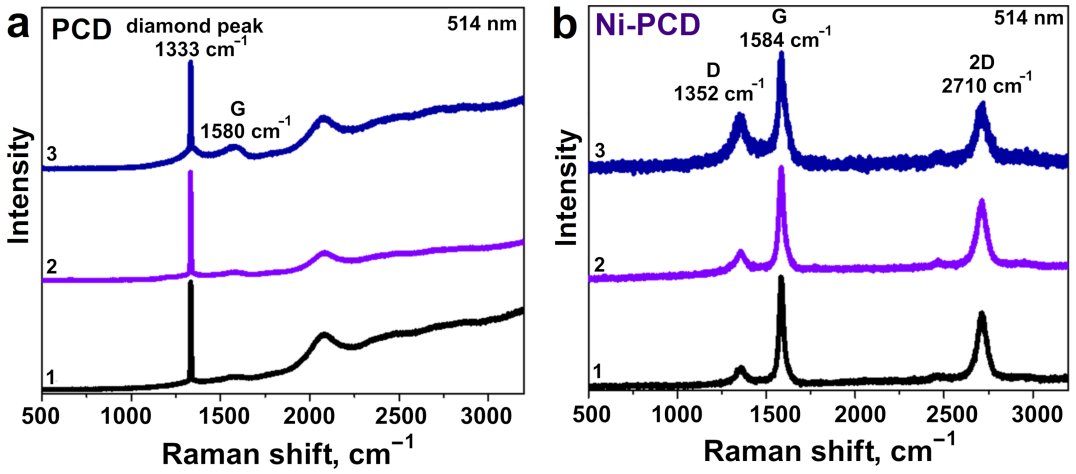

Figure 5: Raman spectra of a) PCD and b) Ni-PCD films after annealing in high vacuum at 1100 °C. The spectra were registered from two different faces of a diamond microcrystal (1 and 2) and from the region between microcrystals (3).

different faces of large microcrystallites in the annealed PCD film look similar (Figure 5a, Supporting Information File 1, Figure S5a,b). They demonstrate the main diamond peak at 1333 cm^{-1} corresponding to the first-order scattering of the F_{2g} symmetry. The high intensity and small full width at half maximum (FWHM) of 4 cm^{-1} of this band and the absence of other Raman features indicate the high crystallinity of the sp^3 lattice and the low concentration of nondiamond phases in the annealed PCD. The spectrum taken from the area between the microcrystallites, in addition to the diamond band, shows a weak Raman signal from the sp^2-hybridized carbon, namely a broad G band at 1580 cm^{-1} from C=C stretching vibrations. This indicates that in our experimental conditions, the partial graphitization of bare PCD film occurs more actively in the areas with small crystallites enriched with boundaries and defects, while large crystallites retain their diamond structure.

The out-of-focus Raman spectrum of the annealed Ni-PCD film taken from a large area demonstrates intense Raman peaks from both diamond and sp^2-carbon (Supporting Information File 1, Figure S6). In contrast, the Raman spectra taken from two different faces of large crystallites and from an area with small crystallites in the annealed Ni-PCD film only demonstrate the Raman peaks from sp^2-carbon and the absence of the diamond peak at 1333 cm^{-1} (Figure 5b, Supporting Information File 1, Figure S5c-e). The probing depth of Raman scattering is estimated to be about 90 nm (Supporting Information File 1, Table S1). This suggests that nondiamond components with a thickness of no less than 90 nm, consisting of sp^2-carbon and Raman-inactive nickel particles, uniformly cover the faces of large diamond crystallites. In addition to the G band at 1584 cm^{-1}, there are two distinct peaks at 1352 and 2710 cm^{-1}, corresponding to the D and 2D bands. The D band represents the disordered vibration modes of graphitic hexagonal layers, and the 2D band originates from the second-order double-resonant scattering process. In general, the quality of graphene layers can be evaluated by the ratio of the intensities of the D and G peaks (I_D/I_G). The spectrum recorded from the area containing small diamond crystallites exhibits the highest I_D/I_G value of 0.43, which is approximately twice as high as the I_D/I_G value of 0.25 for the faces of the large diamond crystallite. This indicates that the sp^2-hybridized carbon layers formed during the catalytic graphitization of small crystallites contain more defects compared to those formed on the continuous surface of micro-sized crystallites. The number of graphitic layers in the carbon coating forming the graphitized surface of the annealed Ni-PCD film can be analyzed by the ratio of the intensity of 2D and G peaks (I_{2D}/I_G) and the FWHM of the 2D peak [50]. A monolayer graphene typically has the I_{2D}/I_G values greater than 2 and the FWHM of the 2D peak of ≈30 cm^{-1}. In all spectra measured from different areas of the annealed Ni-PCD film, the I_{2D}/I_G value is about 0.6 and the FWHM of the 2D peak is ≈90 cm^{-1}. This suggests the formation of multilayer graphitic stacks on different faces of the annealed Ni-PCD film.

To summarize this section, diamond microcrystallites are highly resistant to transformation into sp^2 carbon as a result of vacuum annealing at a temperature of 1100 °C. An exception is smaller diamond crystallites, whose surfaces partially transform into amorphous sp^2-like carbon. The presence of a nickel layer promotes the conversion of the diamond surface into graphitic-like thin films with high concentration of structural defects. Although the morphology of nickel nanoparticles varies depending on the orientation of the diamond face, we did not observe differences in the chemical state of sp^2 carbon located in the same regions. This suggests that the structure of the

graphitic-like coating formed during Ni-assisted graphitization depends to a small extent on the crystallographic orientation of the diamond surface, and is mainly determined by the annealing temperature. On the other hand, the defectiveness of the sp^2 layers is influenced by the crystallite size and the presence of intrinsic structural defects in the diamond.

Orientation of graphitic layers on the (110) face of single-crystal diamond after annealing at 1150 °C

In order to eliminate the role of nickel in the reconstruction of the (110) diamond surface and the orientation of sp^2 carbon layers, we coated the (110) face of SCD with a thin nickel film of the same thickness as that on the PCD. Next, we annealed it and conducted angle-dependent TEY NEXAFS measurements at the C K-edge.

Figure 6 compares the C K-edge spectra of the bare polished (110) face of SCD (Figure 6a) and the Ni-coated (110) face of SCD (Figure 6b) after annealing and subsequent cooling to room temperature. The spectra display the characteristic features of sp^3-hybridized carbon, namely, the $\sigma^*(sp^3)$-resonance at 289.3 eV and the second gap at 302.3 eV, as well as the $\pi^*(sp^2)$- and $\sigma^*(sp^2)$-resonances at 285.3 and 291.4 eV of the sp^2-hybridized carbon. In the spectrum of the Ni-SCD face, the $\pi^*(sp^2)$- and $\sigma^*(sp^2)$-resonances have lower width and significantly higher intensities (Figure 6b) compared to the spectra of the annealed PCD and SCD, as well as to the Ni-PCD film (Figure 1b). This data indicates that nickel-assisted transformation of the (110) face of SCD produced the graphitic-like coating with a much more ordered structure than that formed on the nickel-coated polycrystalline film. The Raman spectrum of the annealed Ni-SCD sample exhibits a weak D-band and a narrow G-band with the I_D/I_G ratio of 0.15 (see inset in Figure 6b). This value is lower than that for the annealed Ni-PCD film. Together with the higher intensity of the $\pi^*(sp^2)$-resonance in the NEXAFS C K-edge spectrum, this suggests that the defectiveness of the formed sp^2-hybridized carbon layers decreases as the size of the annealed diamond face increases.

For the annealed Ni-SCD sample, the spectra were measured at angles of 90° and 50° between the photon beam and the sample surface (Figure 6b). This change in the orientation of the diamond crystal relative to the incident radiation from normal to tilted leads to a decrease in the intensity ratio of the $\pi^*(sp^2)$-resonance to the $\sigma^*(sp^2)$-resonance (I_{π^*}/I_{σ^*}). This is opposite to the dependence for highly oriented pyrolytic graphite [51], and is similar to the dependence for a film of vertically aligned carbon nanotubes [52]. In layered graphite, there is a separation of electron orbitals with respect to symmetry: σ orbitals lie in the basal plane of graphite, while π orbitals are oriented perpendicular to this plane [53]. The difference in the polarization of π- and σ-electrons explains the dependence of NEXAFS spectra of graphitic materials on the angle of incidence of the radiation. Thus, it can be concluded that the orientation of graphitic layers is predominantly vertical relative to the diamond surface.

The intensity ratio I_{π^*}/I_{σ^*} is 0.67 at an angle of incidence of 90° and decreases to 0.44 with decreasing angle to 50°. These values can be used to quantitatively estimate the disordering of graphitic layers in crystallites. An increase in the width of the angular distribution of graphitic layers results in a weakening of the angular dependence of NEXAFS spectra. Comparing the calculated dependences of the intensity ratio I_{π^*}/I_{σ^*} [52] with our experimental results, the width of the angular distribution of

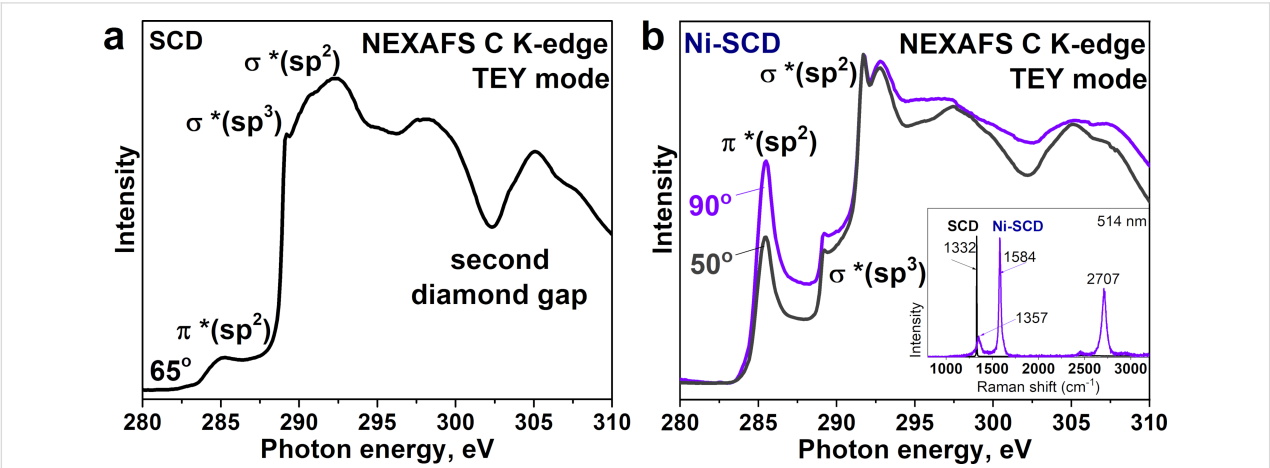

Figure 6: NEXAFS C K-edge spectra measured in TEY mode for a) bare and b) Ni-coated (110) face of SCD after high-vacuum annealing at 1150 °C. The angle of incidence of the synchrotron radiation was a) 65° for SCD and b) 50 and 90° for Ni-SCD. The inset in panel (b) shows Raman spectra of annealed SCD and Ni-SCD samples.

graphitic layers is no more than 5°, meaning a slight deviation of graphitic layers from the vertical position.

According to [19], graphite layers grow both on Ni particles parallel to their surface and on the etched (110) face of Ni-free diamond at a large angle to the diamond surface. The observed angular dependence of NEXAFS resonances from sp^2 carbon indicates that the majority of graphite layers is predominantly located on the outermost surface of Ni-free diamond at a large angle, close to a right angle. A similar angular behavior of the NEXAFS spectrum was previously observed for the iron-coated (100) face of a polished SCD after vacuum annealing at 1150 °C [27] and for the (111) face of SCD annealed at 1250 °C [15].

Conclusion

Polycrystalline diamond films with mixed grain orientations were synthesized by the PE CVD method from hydrogen/acetone/air plasma and coated with a 40 nm thick nickel layer. In situ XPS and NEXAFS data revealed the difference in the chemical state of carbon atoms on the surface of bare and Ni-coated PCD films after annealing in high vacuum at 1100 °C. The temperature used was found to be hardly sufficient to transform the bare surface of the polycrystalline film, while the presence of the nickel catalyst promoted this process, causing the formation of the thin graphitic-like coating. Nickel increases the degree of atomic ordering of the graphite layers formed as a result of the thermal transformation of diamond. The SEM images revealed that nickel particles effectively etch the (110) face, while they mostly stay on the (111) surface, indicating anisotropic diamond etching during heating. Despite these differences, the Raman spectra recorded from the different faces of the annealed microcrystallites were similar, indicating that the carbon coating consisted of graphitic multilayers with a similar structure. The (110) face of SCD was covered with nickel and annealed in high vacuum at 1150 °C. Comparing the NEXAFS C K-edge spectra and Raman spectra of the annealed Ni-SCD and Ni-PCD samples indicates that the amount of defects in the formed graphite layers decreases as the size of the diamond face increases. The best crystallinity of the sp^2 carbon coating was observed in the case of the SCD substrate. Changing the angle between the synchrotron beam and the flat surface of Ni-SCD revealed a significant increase in the $\pi^*(sp^2)$ peak intensity at normal incidence. This behavior indicates an anisotropic texture of sp^2 carbon coating, corresponding to the upright orientation of graphitic layers relative to the (110) face of SCD. Given that the nickel particles coated with sp^2 layers are primarily embedded within the diamond bulk, this suggests that the topmost surface of the annealed (110) face of diamond is mainly formed through the saturation of bonds on the etched diamond surface by free carbon atoms diffusing from the Ni-diamond interface. This implies that the multilayer graphitic layers formed on the surface of micro-sized crystallites in the annealed Ni-coated PCD are also oriented perpendicular to the crystallite surface. Our results can be useful for controlling the growth of graphitic coatings on dielectric diamond surfaces with a polycrystalline structure and grains of different sizes and crystallographic orientations.

Experimental

The growth of PCD films on silicon substrates was performed using PE CVD with a hydrogen/acetone/air mixture. The deposition parameters were typical of those previously employed for an “Astex” system (2.45 GHz, 4.5 kW): a pressure of 115 Torr, hydrogen, acetone, and air flow rates of 500, 18, and 0.3 sccm, respectively, and substrate temperature in the range of 940–980 °C [28,37]. The obtained films were about 500 μm thick. Synthetic SCD were produced using high-pressure high-temperature (HPHT) method on a BARS apparatus [54]. The starting materials included a graphite rod (99.99% purity), a $Ni_{0.7}Fe_{0.3}$ alloy as a solvent catalyst, and a synthetic diamond (≈0.5 mm) as a seed crystal. The SCD crystals were polished along the (110) plane to obtain the (110)-oriented crystal face. The surface of a PCD film and the (110) face of a diamond crystal were coated with a nickel film using thermal evaporation method (HBA Carl Zeiss Jena setup). The parameters of similar metal depositions are described elsewhere [27]. Nickel was deposited onto the surfaces of the samples for 30 s, resulting in the formation of metallic films with a thickness of about 40 nm.

The thermal transformation of the samples and XPS and NEXAFS experiments were carried out at the RGL-PES end station of the Russian–German dipole beamline (RGBL dipole) of the Berliner Elektronenspeicherring für Synchrotronstrahlung (BESSY II) operated by the Helmholtz-Zentrum Berlin für Materialien und Energie (Berlin, Germany) [55]. Light polarization at the RGBL dipole is linearly horizontal. The samples were fixed in pairs to a molybdenum holder using molybdenum foil strips so that spectra could be recorded from bare and Ni-covered PCD films and bare and Ni-coated SDC with the (110) face directed outwardly. Before the measurements, the samples were annealed in ultrahigh vacuum (10^{-9} mbar) in a preparation chamber of the end station. The annealing was performed at 1100 °C for bare and Ni-coated PCD films and at 1150 °C for bare and Ni-coated SCD samples for 15 min to reconstruct the sample surface. After annealing, the samples were cooled naturally and transferred to an analytical chamber without breaking ultrahigh vacuum conditions.

The NEXAFS spectra of the annealed samples were registered using TEY and AEY modes, which provided complementary

information about the chemical state of carbon in the volume and at the surface of the samples. The mean probing depth was estimated to be no more than 10 nm for TEY and 3 nm for AEY. The TEY spectra were recorded by measuring the leakage current with a Keithley ammeter. The experimental data were normalized to the ring current and photon flux measured using a clean gold crystal. In the AEY spectra, emitted Auger electrons were measured using a PHOIBOS 150 analyzer. The polar rotation of the annealed Ni-coated SCD on the manipulator was used to measure the C K-edge spectra at angles of 50° and 90° between a horizontally polarized photon beam and the sample surface. The spectra of bare SCD and PCD samples were measured at angles of 65° and 35°.

The XPS spectra were collected using the PHOIBOS 150 analyzer at photon excitation energies of 330 and 830 eV. Considering the electron inelastic mean free path in solids, the probing depth of the XPS spectra is estimated to be approximately 3 nm for 830 eV and about 2 nm for 330 eV. The energy calibration of the XPS spectra was performed by referring to the Au $4f_{7/2}$ line at 84.0 eV measured from a clean Au foil. XPS data processing was carried out using CASA XPS software version 2.3.15. Fitting of the core-level spectra was performed using the sum of Gauss–Lorenz and Doniach–Sunjic functions after the subtraction of a Shirley's background.

The morphology of the clean and Ni-coated PCD film after annealing in high vacuum at 1100 °C was studied using SEM with a JEOL 6700F microscope (accelerating voltage of 5 kV, JEOL Ltd., Tokyo, Japan). EDX spectroscopy analysis was carried out on a Bruker XFlash 6 spectrometer. EBSD analysis of PCD crystalline orientation was performed using a Hitachi S-3400N microscope (accelerating voltage of 20 kV, Hitachi Ltd., Berkshire, UK) equipped with a HKL Advanced EBSD System Nordlys II S. The diffraction patterns were obtained using Flamenco software and analyzed using Tango software. Raman analysis was conducted using a LabRAM HR Evolution spectrometer (Horiba Ltd., Kyoto, Japan). The spectra were excited with a 514 nm laser at a power of 1.9 mW. The laser beam was focused to a diameter of about 1 μm using an LMPlan FL 50×/0.50 Olympus objective. All measurements were carried out at room temperature.

Supporting Information

Supporting Information File 1

Additional figures and tables.
[https://www.beilstein-journals.org/bjnano/content/supplementary/2190-4286-16-67-S1.pdf]

Funding

This research is supported by the Russian Science Foundation Grant number 22–72–10097. The HPHT growth of diamond single crystals and fabrication of the oriented crystal substrates were carried out as part of the state assignment of the IGM SB RAS (project No. 122041400159-3).

Author Contributions

Olga V. Sedelnikova: conceptualization; data curation; funding acquisition; project administration; validation; writing – original draft; writing – review & editing. Yuliya V. Fedoseeva: data curation; formal analysis; validation; visualization; writing – original draft; writing – review & editing. Dmitriy V. Gorodetskiy: data curation; formal analysis; investigation; writing – review & editing. Yuri N. Palyanov: resources; writing – review & editing. Elena V. Shlyakhova: formal analysis; investigation; writing – review & editing. Eugene A. Maksimovskiy: formal analysis; investigation; writing – review & editing. Anna A. Makarova: methodology; writing – review & editing. Lyubov G. Bulusheva: formal analysis; validation; writing – review & editing. Aleksandr V. Okotrub: conceptualization; data curation; formal analysis; investigation; supervision; validation; writing – review & editing.

ORCID® iDs

Olga V. Sedelnikova - https://orcid.org/0000-0002-0491-3208
Yuliya V. Fedoseeva - https://orcid.org/0000-0003-1681-1708
Dmitriy V. Gorodetskiy - https://orcid.org/0000-0002-3446-7480
Elena V. Shlyakhova - https://orcid.org/0000-0001-8034-7693
Eugene A. Maksimovskiy - https://orcid.org/0000-0002-1555-2719
Anna A. Makarova - https://orcid.org/0000-0002-5603-5566
Lyubov G. Bulusheva - https://orcid.org/0000-0003-0039-2422
Aleksandr V. Okotrub - https://orcid.org/0000-0001-9607-911X

Data Availability Statement

Data generated and analyzed during this study is available from the corresponding author upon reasonable request.

Preprint

A non-peer-reviewed version of this article has been previously published as a preprint: https://doi.org/10.3762/bxiv.2025.15.v1

References

1. Yuan, Q.; Lin, C.-T.; Chee, K. W. A. *APL Mater.* **2019,** *7,* 030901. doi:10.1063/1.5082767
2. Vejpravová, J. *Nanomaterials* **2021,** *11,* 2469. doi:10.3390/nano11102469
3. Aitkulova, A.; Majdi, S.; Suntornwipat, N.; Isberg, J. *Phys. Status Solidi A* **2025,** *222,* 2400567. doi:10.1002/pssa.202400567
4. Yu, J.; Liu, G.; Sumant, A. V.; Goyal, V.; Balandin, A. A. *Nano Lett.* **2012,** *12,* 1603–1608. doi:10.1021/nl204545q

5. Zhao, F.; Vrajitoarea, A.; Jiang, Q.; Han, X.; Chaudhary, A.; Welch, J. O.; Jackman, R. B. *Sci. Rep.* **2015,** *5,* 13771. doi:10.1038/srep13771
6. Wu, Y.; Lin, Y.-m.; Bol, A. A.; Jenkins, K. A.; Xia, F.; Farmer, D. B.; Zhu, Y.; Avouris, P. *Nature* **2011,** *472,* 74–78. doi:10.1038/nature09979
7. Luo, B.; Yuan, A.; Yang, S.; Han, L.; Guan, R.; Duan, J.; Wang, C.; Dong, L.; Zhang, B.; Li, D. *ACS Appl. Nano Mater.* **2021,** *4,* 1385–1393. doi:10.1021/acsanm.0c02930
8. Yuan, Q.; Liu, L.; Dai, D.; Zhou, Y.; Liu, Y.; Yang, M.; Qiu, M.; Jia, Z.; Li, H.; Nishimura, K.; Tian, G.; Chee, K. W. A.; Du, S.; Lin, C.-T.; Jiang, N.; Ouyang, X. *Funct. Diamond* **2022,** *2,* 94–102. doi:10.1080/26941112.2022.2099766
9. Seal, M. *Nature* **1960,** *185,* 522–523. doi:10.1038/185522a0
10. Bai, Q.; Wang, Z.; Guo, Y.; Chen, J.; Shang, Y. *Curr. Nanosci.* **2018,** *14,* 377–383. doi:10.2174/1573413714666180517080721
11. Song, Y.; Larsson, K. *Adv. Nanosci. Nanotechnol.* **2018,** *2,* 1–8. doi:10.33140/ann/02/01/00002
12. Enriquez, J. I. G.; Halim, H. H.; Yamasaki, T.; Michiuchi, M.; Inagaki, K.; Geshi, M.; Hamada, I.; Morikawa, Y. *Carbon* **2024,** *226,* 119223. doi:10.1016/j.carbon.2024.119223
13. Bokhonov, B. B.; Dudina, D. V.; Sharafutdinov, M. R. *Diamond Relat. Mater.* **2021,** *118,* 108563. doi:10.1016/j.diamond.2021.108563
14. Khmelnitsky, R. A.; Gippius, A. A. *Phase Transitions* **2014,** *87,* 175–192. doi:10.1080/01411594.2013.807429
15. Okotrub, A. V.; Sedelnikova, O. V.; Gorodetskiy, D. V.; Gusel'nikov, A. V.; Palyanov, Y. N.; Bulusheva, L. G. *Appl. Surf. Sci.* **2025,** *701,* 163270. doi:10.1016/j.apsusc.2025.163270
16. Davies, G.; Evans, T. *Proc. R. Soc. London, Ser. A* **1972,** *328,* 413–427. doi:10.1098/rspa.1972.0086
17. García, J. M.; He, R.; Jiang, M. P.; Kim, P.; Pfeiffer, L. N.; Pinczuk, A. *Carbon* **2011,** *49,* 1006–1012. doi:10.1016/j.carbon.2010.11.008
18. Kanada, S.; Nagai, M.; Ito, S.; Matsumoto, T.; Ogura, M.; Takeuchi, D.; Yamasaki, S.; Inokuma, T.; Tokuda, N. *Diamond Relat. Mater.* **2017,** *75,* 105–109. doi:10.1016/j.diamond.2017.02.014
19. Tulić, S.; Waitz, T.; Čaplovičová, M.; Habler, G.; Vretenár, V.; Susi, T.; Skákalová, V. *Carbon* **2021,** *185,* 300–313. doi:10.1016/j.carbon.2021.08.082
20. Suntornwipat, N.; Aitkulova, A.; Djurberg, V.; Majdi, S. *Thin Solid Films* **2023,** *770,* 139766. doi:10.1016/j.tsf.2023.139766
21. Wang, S.; Bai, Q.; Chen, S. *Cryst. Res. Technol.* **2023,** *58,* 2300122. doi:10.1002/crat.202300122
22. Berman, D.; Deshmukh, S. A.; Narayanan, B.; Sankaranarayanan, S. K. R. S.; Yan, Z.; Balandin, A. A.; Zinovev, A.; Rosenmann, D.; Sumant, A. V. *Nat. Commun.* **2016,** *7,* 12099. doi:10.1038/ncomms12099
23. Romanyuk, O.; Varga, M.; Tulic, S.; Izak, T.; Jiricek, P.; Kromka, A.; Skakalova, V.; Rezek, B. *J. Phys. Chem. C* **2018,** *122,* 6629–6636. doi:10.1021/acs.jpcc.7b12334
24. Tulić, S.; Waitz, T.; Čaplovičová, M.; Habler, G.; Varga, M.; Kotlár, M.; Vretenár, V.; Romanyuk, O.; Kromka, A.; Rezek, B.; Skákalová, V. *ACS Nano* **2019,** *13,* 4621–4630. doi:10.1021/acsnano.9b00692
25. Cooil, S. P.; Song, F.; Williams, G. T.; Roberts, O. R.; Langstaff, D. P.; Jørgensen, B.; Høydalsvik, K.; Breiby, D. W.; Wahlström, E.; Evans, D. A.; Wells, J. W. *Carbon* **2012,** *50,* 5099–5105. doi:10.1016/j.carbon.2012.06.050
26. Cooil, S. P.; Wells, J. W.; Hu, D.; Niu, Y. R.; Zakharov, A. A.; Bianchi, M.; Evans, D. A. *Appl. Phys. Lett.* **2015,** *107,* 181603. doi:10.1063/1.4935073
27. Okotrub, A. V.; Gorodetskiy, D. V.; Palyanov, Y. N.; Smirnov, D. A.; Bulusheva, L. G. *J. Phys. Chem. C* **2023,** *127,* 3563–3569. doi:10.1021/acs.jpcc.2c08080
28. Sedelnikova, O. V.; Gorodetskiy, D. V.; Lavrov, A. N.; Grebenkina, M. A.; Fedorenko, A. D.; Bulusheva, L. G.; Okotrub, A. V. *Synth. Met.* **2024,** *307,* 117675. doi:10.1016/j.synthmet.2024.117675
29. Ueda, K.; Aichi, S.; Asano, H. *Diamond Relat. Mater.* **2016,** *63,* 148–152. doi:10.1016/j.diamond.2015.10.021
30. Yuan, Q.; Liu, Y.; Ye, C.; Sun, H.; Dai, D.; Wei, Q.; Lai, G.; Wu, T.; Yu, A.; Fu, L.; Chee, K. W. A.; Lin, C.-T. *Biosens. Bioelectron.* **2018,** *111,* 117–123. doi:10.1016/j.bios.2018.04.006
31. Shen, B.; Ji, Z.; Lin, Q.; Gong, P.; Xuan, N.; Chen, S.; Liu, H.; Huang, Z.; Xiao, T.; Sun, Z. *Chem. Mater.* **2022,** *34,* 3941–3947. doi:10.1021/acs.chemmater.1c04322
32. Okotrub, A. V.; Sedelnikova, O. V.; Gorodetskiy, D. V.; Fedorenko, A. D.; Asanov, I. P.; Palyanov, Y. N.; Lapega, A. V.; Gurova, O. A.; Bulusheva, L. G. *Materials* **2023,** *16,* 1650. doi:10.3390/ma16041650
33. Strong, H. M. *J. Chem. Phys.* **1963,** *39,* 2057–2062. doi:10.1063/1.1734582
34. Huang, W.-T.; Lin, C.; Li, X.; Zang, J.; Wan, L.; Zhang, Z.; Cheng, S.; Shan, C. *Acta Mater.* **2024,** *263,* 119527. doi:10.1016/j.actamat.2023.119527
35. Nagai, M.; Nakanishi, K.; Takahashi, H.; Kato, H.; Makino, T.; Yamasaki, S.; Matsumoto, T.; Inokuma, T.; Tokuda, N. *Sci. Rep.* **2018,** *8,* 6687. doi:10.1038/s41598-018-25193-2
36. Chen, S.; Bai, Q.; Wang, H.; Guo, W.; Dou, Y. *J. Phys. Chem. C* **2022,** *126,* 18411–18420. doi:10.1021/acs.jpcc.2c04409
37. Polyakov, O. V.; Gorodetskii, D. V.; Okotrub, A. V. *Tech. Phys. Lett.* **2013,** *39,* 501–504. doi:10.1134/s1063785013060096
38. Morar, J. F.; Himpsel, F. J.; Hollinger, G.; Hughes, G.; Jordan, J. L. *Phys. Rev. Lett.* **1985,** *54,* 1960–1963. doi:10.1103/physrevlett.54.1960
39. Horsley, J. A.; Stöhr, J.; Hitchcock, A. P.; Newbury, D. C.; Johnson, A. L.; Sette, F. *J. Chem. Phys.* **1985,** *83,* 6099–6107. doi:10.1063/1.449601
40. Ehlert, C.; Unger, W. E. S.; Saalfrank, P. *Phys. Chem. Chem. Phys.* **2014,** *16,* 14083–14095. doi:10.1039/c4cp01106f
41. Wahab, H.; Haverkamp, R.; Kim, J. H.; Cadogan, J. M.; Mertins, H.-C.; Choi, S.-H.; Timmers, H. *Carbon* **2016,** *110,* 414–425. doi:10.1016/j.carbon.2016.09.028
42. Lapteva, L. L.; Fedoseeva, Y. V.; Gevko, P. N.; Smirnov, D. A.; Gusel'nikov, A. V.; Bulusheva, L. G.; Okotrub, A. V. *J. Struct. Chem.* **2017,** *58,* 1173–1179. doi:10.1134/s0022476617060154
43. Massimi, L.; Ourdjini, O.; Lafferentz, L.; Koch, M.; Grill, L.; Cavaliere, E.; Gavioli, L.; Cardoso, C.; Prezzi, D.; Molinari, E.; Ferretti, A.; Mariani, C.; Betti, M. G. *J. Phys. Chem. C* **2015,** *119,* 2427–2437. doi:10.1021/jp509415r
44. Hwu, H. H.; Fruhberger, B.; Chen, J. G. *J. Catal.* **2004,** *221,* 170–177. doi:10.1016/j.jcat.2003.08.003
45. Tanuma, S.; Powell, C. J.; Penn, D. R. *Surf. Interface Anal.* **2005,** *37,* 1–14. doi:10.1002/sia.1997
46. Fedoseeva, Y. V.; Okotrub, A. V.; Bulusheva, L. G.; Maksimovskiy, E. A.; Senkovskiy, B. V.; Borzdov, Y. M.; Palyanov, Y. N. *Diamond Relat. Mater.* **2016,** *70,* 46–51. doi:10.1016/j.diamond.2016.09.023
47. Yamashita, T.; Hayes, P. *Appl. Surf. Sci.* **2008,** *254,* 2441–2449. doi:10.1016/j.apsusc.2007.09.063
48. Lv, M.; Zhou, Y.; Rasaki, S. A.; Shen, H.; Wang, C.; Song, W.; Thomas, T.; Yang, M.; Wang, J. *ChemElectroChem* **2019,** *6,* 5744–5749. doi:10.1002/celc.201901439

49. Ufuktepe, Y.; Akgül, G.; Aksoy, F.; Nordlund, D. *X-Ray Spectrom.* **2011,** *40,* 427–431. doi:10.1002/xrs.1362
50. Ferrari, A. C. *Solid State Commun.* **2007,** *143,* 47–57. doi:10.1016/j.ssc.2007.03.052
51. Okotrub, A. V.; Yudanov, N. F.; Asanov, I. P.; Vyalikh, D. V.; Bulusheva, L. G. *ACS Nano* **2013,** *7,* 65–74. doi:10.1021/nn305268b
52. Belavin, V. V.; Okotrub, A. V.; Bulusheva, L. G.; Kotosonov, A. S.; Vyalykh, D. V.; Molodtsov, S. L. *J. Exp. Theor. Phys.* **2006,** *103,* 604–610. doi:10.1134/s1063776106100128
53. Skytt, P.; Glans, P.; Mancini, D. C.; Guo, J.-H.; Wassdahl, N.; Nordgren, J.; Ma, Y. *Phys. Rev. B* **1994,** *50,* 10457–10461. doi:10.1103/physrevb.50.10457
54. Pal'yanov, Yu. N.; Khokhryakov, A. F.; Borzdov, Yu. M.; Sokol, A. G.; Gusev, V. A.; Rylov, G. M.; Sobolev, N. V. *Russ. Geol. Geophys.* **1997,** *38,* 920–945.
55. Fedoseenko, S. I.; Vyalikh, D. V.; Iossifov, I. E.; Follath, R.; Gorovikov, S. A.; Püttner, R.; Schmidt, J.-S.; Molodtsov, S. L.; Adamchuk, V. K.; Gudat, W.; Kaindl, G. *Nucl. Instrum. Methods Phys. Res., Sect. A* **2003,** *505,* 718–728. doi:10.1016/s0168-9002(03)00624-7

License and Terms

BEILSTEIN JOURNAL OF NANOTECHNOLOGY

Towards a quantitative theory for transmission X-ray microscopy

James G. McNally*[1], Christoph Pratsch[1], Stephan Werner[1], Stefan Rehbein[1], Andrew Gibbs[2], Jihao Wang[3], Thomas Lunkenbein[3], Peter Guttmann[1] and Gerd Schneider[1,4]

Full Research Paper

Open Access

Address:
[1]Helmholtz-Zentrum Berlin für Materialien und Energie, Elektronenspeicherring BESSY II, Albert-Einstein-Straße 15, 12489 Berlin, Germany, [2]Department of Mathematics, University College London, London, UK, [3]Department of Inorganic Chemistry, Fritz-Haber-Institut der Max-Planck Gesellschaft, Berlin, Germany and [4]Humboldt Universität zu Berlin, Mathematisch-Naturwissenschaftliche Fakultät, Institut für Physik, Newtonstraße 15, 12489 Berlin, Germany

Email:
James G. McNally* - james.mcnally@helmholtz-berlin.de

* Corresponding author

Keywords:
3D imaging; mathematical model; Mie theory; nanoparticle; transmission X-ray microscope

Beilstein J. Nanotechnol. **2025,** *16,* 1113–1128.
https://doi.org/10.3762/bjnano.16.82

Received: 26 March 2025
Accepted: 13 June 2025
Published: 15 July 2025

This article is part of the thematic issue "Exploring synchrotron radiation and free-electron laser tools for nanostructured materials".

Associate Editor: A. J. Meixner

Abstract

Transmission X-ray microscopes (TXMs) are now increasingly used for quantitative analysis of samples, most notably in the spectral analysis of materials. Validating such measurements requires quantitatively accurate models for these microscopes, but current TXM models have only been tested qualitatively. Here we develop an experimental and theoretical framework for evaluation of TXMs that uses Mie theory to compute the electric field emerging from a nanosphere. We approximate the microscope's condenser illumination by plane waves at the mean illumination angle and the zone plate by a thin lens. We find that this model produces good qualitative agreement with our 3D measurements of 60 nm gold nanospheres, but only if both β and δ for the complex refractive index $n = 1 - \delta + i\beta$ of gold are included in the model. This shows that both absorption and phase properties of the specimen influence the acquired TXM image. The qualitative agreement improves if we incorporate a small tilt into the condenser illumination relative to the optical axis, implying a small misalignment in the microscope. Finally, in quantitative comparisons, we show that the model predicts the nanosphere's expected absorption as determined by Beer's law, whereas the microscope underestimates this absorption by 10–20%. This surprising observation highlights the need for future work to identify the microscope feature(s) that lead to this quantitative discrepancy.

Introduction

Transmission X-ray microscopes (TXMs) operating in the soft and tender X-ray energy range are valuable tools for structural analysis in both biomedical and materials science research [1-4]. These microscopes yield images at a lateral resolution approaching 25 nm, from which quantitative data are often extracted. For example, in materials science applications, nanoscale spectromicroscopy [5-8] is used to examine a sample around its absorption edges, which provides insights into its electronic structure. In biomedical applications [9-12], absorption at selected locations in the sample is used to determine the amount of a material at those sites.

Validation of these quantitative measurements requires a quantitatively accurate TXM model. Such models are also valuable both for the design of new soft TXMs, which relies on a deep understanding of the microscope's image-formation process, and for the improvement of 3D tomographic reconstruction procedures [13-16], which are used to produce 3D volumes from a 2D tilt series of TXM images. Over the past three decades, models for soft TXMs have grown increasingly sophisticated [17-19], with the two most recent both incorporating the 3D nature of the imaging process [20,21]. A 3D model is essential to accurately account for the microscope's large but nevertheless finite depth of focus. Otón et al. [20] developed the first 3D model, making several assumptions to simplify the analysis, including that imaging is incoherent and that only the absorption component β of the sample's refractive index needs to be considered. The latter assumption means that light rays traversing the sample follow Beer's law of absorption, and so we refer to this model as the incoherent Beer's law (inc-BL) model.

Not all the assumptions of the inc-BL model match the TXM we have used in this study at the electron storage ring BESSY II in the Helmholtz-Zentrum Berlin. Specifically, the sample illumination is not incoherent, but rather partially coherent because the sample is illuminated over a narrow angular range of 0.83–1.18° and the numerical aperture (NA) of the condenser is less than the NA of the zone plate objective.

To improve the inc-BL model, Selin et al. [21] developed a more sophisticated 3D model that addressed the microscope's annular illumination by replacing the full annular illumination range by its mean angle. This mean angle is less than the acceptance angle of the objective and so introducing this into the model also accounts for the microscope's partial coherence arising from the mismatch of the condenser and objective NA's. Furthermore, rather than Beer's law, Selin et al. used the parabolic wave equation to propagate light through a sample that was defined by its 3D distribution of complex refractive indices, thereby accounting for both the absorption and phase properties of the sample. We refer to this model as the partially coherent, parabolic-wave-equation (pc-PWE) model.

In the current study, we continue this effort toward further development of 3D models for TXMs. First, we introduce Mie theory as an alternate approach for light propagation through the sample. Mie theory provides an exact solution to Maxwell's equations but limited to spheres of known refractive index [22] and so is well suited to the gold nanospheres that we use as test objects in this study. We therefore name our model the partially coherent Mie (pc-Mie) model. Second, we compare the theory for our model to the preceding two 3D models, providing a deeper understanding of the principles that underlie the different models. Third, we perform detailed qualitative comparisons of the different models' predictions to the measured data from the gold nanosphere. This qualitative analysis demonstrates the importance of accounting for both β and δ in the sample's refractive index, and it also identifies a tilt in the optical train that requires adjustment of the model. Finally, we perform the first quantitative comparisons of a 3D model to real data, revealing that the microscope underestimates the absorption of the 60 nm gold nanospheres.

In sum, our work not only extends the modelling framework for TXMs but also identifies two areas for future work that will improve the quantitative analysis of TXM data. First, our finding that both β and δ play a role in TXM imaging highlights the need to investigate to what extent δ influences quantitative analyses such as those in spectromicroscopy that currently presume a role only for β. Second, our surprising finding that the microscope underestimates absorption underscores the need to understand how this discrepancy arises such that more accurate quantitative TXM measurements are possible.

Results

1 Overview: microscope configuration

To understand the various 3D microscope models and their assumptions, we first describe the key features of the BESSY II soft TXM. The microscope's X-ray source begins at the undulator, which produces largely incoherent light (<2% coherence for the BESSY II third generation synchrotron, p. 32 in [23]). This X-ray light is then propagated through a beamline about 26 m in length [24], which consists of several mirrors and a plane-grating monochromator that yields highly monochromatic light ($E/\Delta E \approx 10000$ for the energy of 510 eV used in the current study).

This monochromator source is then re-focused and demagnified onto the sample plane by a truncated ellipsoidal glass capil-

lary that acts as an ellipsoidal mirror [4,25] positioned at ≈9.7 m from the monochromator exit slit. A central stop is present in front of this ellipsoidal mirror to prevent zero-order light from passing directly through the objective. This combination of the ellipsoidal mirror and central stop produces illumination of the sample (Figure 1a) over an angular range of 0.83–1.18°.

The final size of the ellipsoidal mirror's focused spot (≈2.7 μm × 0.7 μm) is smaller than most samples, and therefore to generate an image of the sample, the focused spot from the ellipsoidal mirror is "scanned" by moving the mirror in a spiral pattern. This light then reaches the microscope's objective, which is a zone plate composed of 900 zones with outermost zone width of dr_n = 25 nm. Finally, images from the objective are acquired with a CCD camera.

2 Models: partially coherent Mie, partially coherent parabolic wave equation, and incoherent Beer's law

We introduce our new model (pc-Mie) and compare it to the other two 3D TXM models (pc-PWE [21] and inc-BL [20]). As in [21], our description of each model is divided into three steps: (1) illumination of the sample by the condenser; (2) light propagation through the sample to the zone plate; and (3) light propagation from the zone plate to the camera. The key features of each model and their assumptions are summarized in Table 1.

2.1 Illumination of the sample by the condenser

Neither of the preceding 3D models considered the spiral scanning of the condenser spot over the sample. This is a reason-

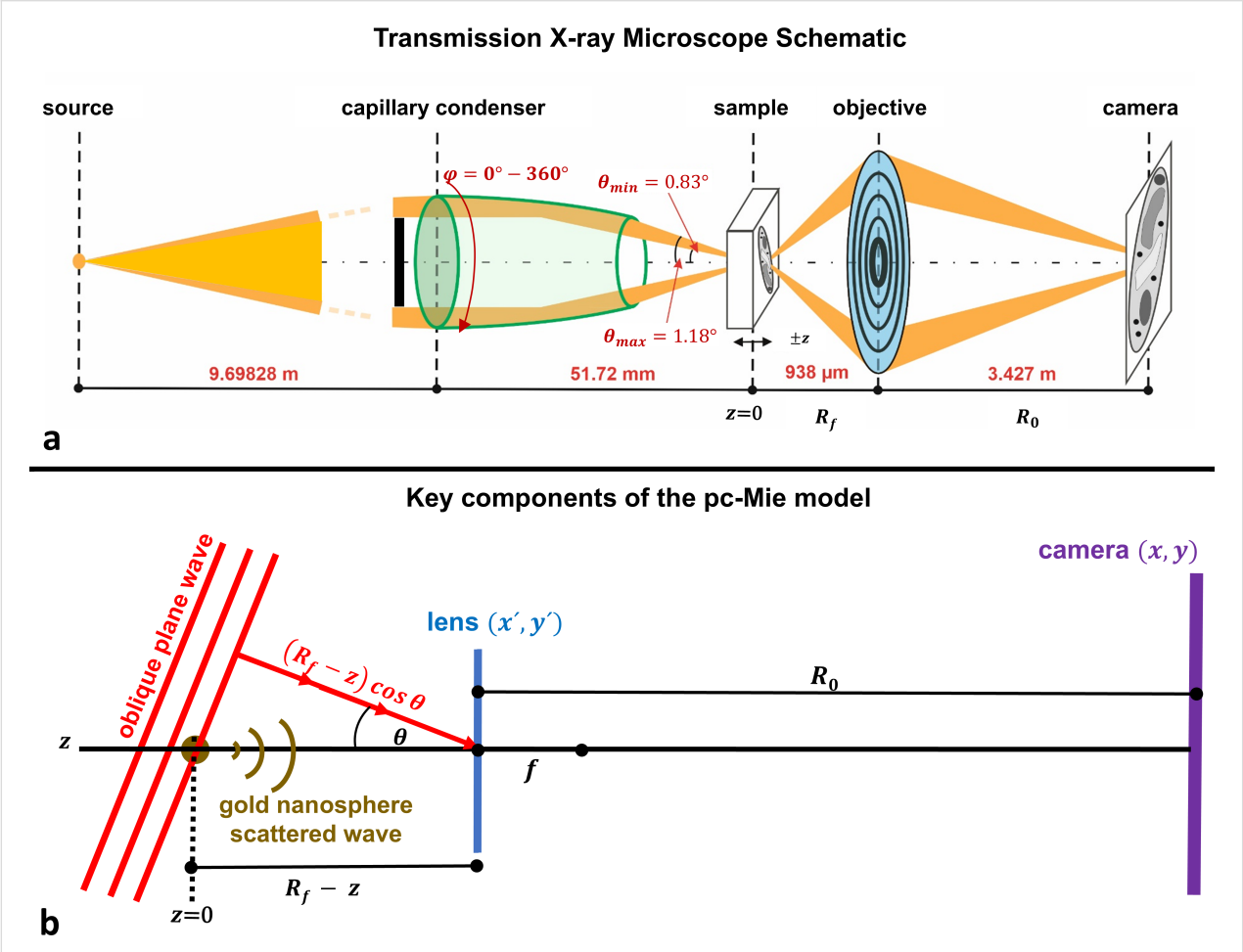

Figure 1: (a) Schematic of the Helmholtz-Zentrum Berlin TXM at the electron storage ring BESSY II. X-ray light from the focal spot produced by the monochromator beamline is demagnified and re-focused by the capillary condenser (which is an ellipsoidal mirror) onto the sample plane and then imaged by a zone-plate objective onto the camera plane. Distances between the different planes for operation at 510 eV are indicated in red. A central stop (black bar) is present in front of the ellipsoidal mirror to prevent zero-order light from reaching the zone plate. The minimum and maximum polar angles (θ) of the condenser illumination are also indicated in red, as is the full circumferential range of azimuthal angle (φ) illumination. (b) The pc-Mie model with key variables shown is based on an oblique plane wave emanating from the condenser that induces a scattered wave in the nanosphere, whose field is calculated using Mie theory. Both the plane and scattered waves are then propagated through the zone plate, which is treated as a lens, and then to the camera (not to scale).

Table 1: Comparison of the existent 3D soft TXM models to the actual Helmholtz-Zentrum Berlin TXM.[a]

	BESSY II Microscope	Model 1: pc-Mie	Model 2: pc-PWE	Model 3: inc-BL
illumination	annular angles (0.83–1.18°)	mean annular angle (1.01°)[b]	mean annular angle (1.01°)[b]	all angles (0–90°)[b]
coherence	partial	partial	partial	incoherent[b]
coherence patch size	unknown	small[b]	small[b]	na[b]
spiral scan pattern	yes	no[b]	no[b]	no[b]
sample *n*	absorption (β) phase (δ)	absorption (β) phase (δ)	absorption (β) phase (δ)	absorption (β) no phase (δ = 0)[b]
light propagation	Maxwell's equations	Mie theory	parabolic wave equation[b]	Beer's law[b]
objective	zone plate	lens[b]	lens[b]	lens[b]

[a]pc = partially coherent; PWE = parabolic wave equation; inc-BL = incoherent Beer's law; na = not applicable; [b]features that are approximations to the actual microscope.

able first approximation since the scanning process can be viewed as producing a patchwork of images that are then added to produce the final acquired image, which should not be significantly different from the image that would be produced from a much larger condenser spot, and so we have also not incorporated the scanning into our model.

The different models make different assumptions about the polar angles at which the sample is illuminated, and this relates to whether the model is incoherent or partially coherent. By assuming incoherent illumination, the inc-BL model implicitly incorporates illumination over all possible azimuthal angles (φ = 0–360°) spanning the ellipsoidal mirror circumference and over all possible polar angles (θ = 0–90°). This model therefore ignores the limited annular polar angle range of the true condenser (0.83–1.18°). In the pc-PWE model, the sample is also illuminated from the complete range of azimuthal angles φ = 0–360°, but at a constant polar angle θ_m that corresponds to the mean angle of the condenser's annular illumination range (θ_m = 1.01° in our case, Supporting Information File 1, Section S1). We adopt the same assumption in our pc-Mie model of a mean polar illumination angle.

Since the different polar angles of illumination are related to the assumptions of either incoherence or partial coherence, these in turn affect whether fields or intensities are added to produce the final image. The inc-BL model assumes incoherence and therefore calculates the intensities arising at each point in the sample. Both the pc-PWE and pc-Mie model are partially coherent because they include the mean polar angle of annular illumination and so intrinsically account for the mismatch of condenser and objective NA. These partially coherent models must therefore also specify the size of a coherence domain over which field amplitudes are added before computing intensities.

The coherence patch size arising from our beamline illumination has not been measured in our TXM. The pc-PWE model assumed that this size was small, and as discussed later, we also find that to match our acquired data, the coherence patch size must be small. Future measurements of the actual coherence patch size of our TXM will be important to determine whether the measured size matches the predictions of a small patch predicted by both our model and the pc-PWE model.

Finally, all three models also assume that the sample illumination can be approximated as plane waves impinging on the sample at the corresponding polar and azimuthal angles (Figure 1b). This is an excellent approximation as demonstrated by modeling the ellipsoidal mirror as an annular lens that produces a converging spherical wave at its focal point in the sample plane. An angular spectrum decomposition of this lens field shows that it is very accurately described as a sum of plane waves spanning the polar angular range (Supporting Information File 1, Section S2).

2.2 Propagation of light through the sample to the zone plate

We first consider light propagation through the sample in our pc-Mie model and then proceed to a discussion of light propagation in the other two 3D models. Mie theory provides an exact solution to Maxwell's equations for a sphere of given diameter and homogeneous refractive index $n = 1 - \delta + i\beta$ [22], an approach well suited to the spherical nanoparticles examined here.

Mie theory is one example of scattering theory in which the time-independent part of the final field is given by the sum of the incident and scattered fields:

$$\mathbf{U}(\mathbf{r}) = \mathbf{U}_{\mathrm{i}}(\mathbf{r}) + \mathbf{U}_{\mathrm{s}}(\mathbf{r}). \quad (1)$$

At a sufficient distance from the scattering object (in our case, the distance between the nanosphere and the zone plate), the scattered field is well approximated by a spherical wave, and can be written as:

$$\mathbf{U}_s(\mathbf{r}) = \frac{\mathbf{S}(\psi)}{(-ik)}\left[\frac{\exp(ik|\mathbf{r}|)}{|\mathbf{r}|}\right], \quad (2)$$

where **S** is the scattering amplitude, ψ the scattering angle from the sphere to a point in the zone plate, and k the wave number. When the incident field $\mathbf{U}_{\mathrm{i}}(\mathbf{r})$ is a plane wave of amplitude one propagating along the optical axis (z_{p} where the subscript "p" indicates this is a propagation distance), then Equation 1 and Equation 2 yield the total field at the zone-plate plane:

$$\mathbf{U}(\mathbf{r}) = \exp(ikz_{\mathrm{p}}) + \frac{\mathbf{S}(\psi)}{(-ik)}\left[\frac{\exp(ik|\mathbf{r}|)}{|\mathbf{r}|}\right], \quad (3)$$

and the problem reduces to determination of the scattering amplitude $\mathbf{S}(\psi)$.

The Mie solution $\mathbf{S}(\psi)$ is given by an infinite series of vector spherical harmonics that for numerical computations is truncated based on the accuracy required. Conventional Mie theory is based on plane waves parallel to the optical axis, and we adapt this by applying a simple geometrical transformation (Supporting Information File 1, Section S3) to account for oblique plane waves emerging from the ellipsoidal-mirror condenser. This yields an expression for the scattered field $\mathbf{S}_\theta(x',y')$ arising due to an oblique plane wave at a polar angle θ to the optical axis and propagating through a sphere to an arbitrary point (x',y') in the zone plate. To compute **S**, we have used Matlab code developed by Mätzler [26].

The scattering amplitude $\mathbf{S}(\psi)$ is a vector with two components, $S_1(\psi)$ and $S_2(\psi)$. For scattering at small angles, the Mie theory reduces to a simplified scalar theory known as the anomalous diffraction approximation (ADA) [27] with $S_1(\psi) = S_2(\psi) = S_{\mathrm{ADA}}(\psi)$ given by:

$$S_{\mathrm{ADA}}(\psi) = k^2\int_0^a\left(1 - e^{2ik(n-1)\sqrt{a^2-\xi^2}}\right)J_0(k\xi\psi)\xi\mathrm{d}\xi, \quad (4)$$

where ξ is the radial coordinate in the sphere and J_0 the Bessel function of the first kind. This equation reflects the sum of the optical path length along different rays parallel to the z-axis passing through the nanosphere relative to rays passing outside the nanosphere [27].

This anomalous diffraction approximation holds under two conditions that should apply in our experiments, namely when the wavelength λ is small relative to the diameter $2a$ of the sphere, and when the magnitude of the complex refractive index n is close to one [27]. These two requirements ensure that light rays pass through the sphere without significant deflection or reflection, subject only to the accumulated phase change. We confirm the validity of the anomalous diffraction approximation for 60 nm gold nanospheres imaged with 2.4 nm light in Supporting Information File 1, Section S4, where we demonstrate that the full Mie solution for either $S_1(\psi)$ or $S_2(\psi)$ is identical to the anomalous diffraction solution $S_{\mathrm{ADA}}(\psi)$.

We then show in Supporting Information File 1, Section S5, how the anomalous diffraction solution of the Mie theory is equivalent to a simplified form of the parabolic wave equation known as the eikonal approximation in light scattering [28]:

$$S_{\mathrm{EA}}(\psi) = k^2\int_0^a\left(1 - e^{ik\left(n^2-1\right)\sqrt{a^2-\xi^2}}\right)J_0(k\xi\psi)\xi\mathrm{d}\xi. \quad (5)$$

The eikonal approximation $S_{\mathrm{EA}}(\psi)$ for the parabolic wave equation holds under the same two conditions required for the Mie theory to reduce to the anomalous diffraction theory, namely when the wavelength is small relative to the size of the object, and when the magnitude of the complex refractive index n is close to one [28]. Note that the only difference between the anomalous diffraction approximation for the Mie theory (Equation 4) and the eikonal approximation for the PWE (Equation 5) is $2(n-1)$ vs n^2-1 in the exponent of the exponential, and this difference is negligible when $n \approx 1$ (Supporting Information File 1, Section S5). We also demonstrate this explicitly in Figure S5 in Supporting Information File 1, Section S4, where we calculate $S_{\mathrm{ADA}}(\psi)$ and $S_{\mathrm{EA}}(\psi)$ and show that the curves overlap for the 60 nm gold nanospheres examined in this study. Thus, for our sample, the Mie theory is equivalent to the parabolic wave equation, and therefore light propagation through the nanosphere is equivalent in the pc-Mie and the pc-PWE models.

Light propagation in the inc-BL model is a simplified version of that in the preceding two models. The simplification arises when the phase term δ in the refractive index is set to zero and

intensities instead of field amplitudes are measured. With δ = 0 then $n = 1 + i\beta$, and the argument in the integral of Equation 4 becomes

$$1 - e^{-2k\beta\sqrt{a^2-\xi^2}}.$$

This reflects the loss in the field amplitude passing through the sphere at a distance ξ from its center, and so the loss in intensity is given by the squared amplitude of the exponential term leading to Beer's law for the absorption $A(t)$ as a function of the distance $t = 2\sqrt{a^2-\xi^2}$ that the ray travels through the sphere:

$$A(t) = 1 - e^{-4k\beta\sqrt{a^2-\xi^2}} = 1 - e^{-2k\beta t}. \quad (6)$$

In sum, we have shown that the Mie theory can be simplified for the experimental case considered here, namely a sphere whose refractive index n is close to one and whose diameter is much larger than the wavelength λ. Then we show that this simplified form of the Mie theory is essentially equivalent to a simplified form of the parabolic wave equation, which applies under precisely the same conditions, that is, a sphere with $n \approx 1$ whose diameter is much larger than λ. Thus, the pc-Mie and pc-PWE models provide equivalent procedures for light propagation through the nanosphere. Finally, we show that light propagation in the inc-BL model, namely via Beer's law, arises from a further simplification of the pc-Mie and pc-PWE procedures in which the phase component of the refractive index is ignored and intensities instead of fields are calculated.

2.3 Propagation of light through the zone plate to the detector plane

Zone plates are diffractive optics with a defined periodic pattern of clear and opaque rings whose transmission function $Z(x',y')$ can be written as a cosine series [17]:

$$Z(x',y') = \begin{cases} \frac{1}{2} + \frac{2}{\pi}\sum_{m=1,3,\ldots}^{\infty}\frac{1}{m}\cos\left[\frac{m\pi\left(x'^2+y'^2\right)}{\lambda f}\right] & x'^2+y'^2 \le r_{zp}^2 \\ 0 & x'^2+y'^2 > r_{zp}^2 \end{cases}, \quad (7)$$

where r_{zp} is the radius of the zone plate, which defines its NA. Expanding the cosine function in Equation 7 in terms of complex exponentials yields:

$$Z(x',y') = \frac{1}{2} + \frac{1}{\pi}\sum_{m=1,3,\ldots}^{\infty}\frac{1}{m}\left(\exp\left[\frac{im\pi\left(x'^2+y'^2\right)}{\lambda f}\right] + \exp\left[\frac{-im\pi\left(x'^2+y'^2\right)}{\lambda f}\right]\right). \quad (8)$$

The odd integers m correspond to the different diffraction orders of the zone plate, each producing a focus with focal length $f_m = f/m$, where f is the focal length of the zone plate's first diffraction order. The intensities of these different foci therefore go as $1/(m\pi)^2$.

Most TXMs operate in first order by using a hollow-cone illumination to remove the zero-order light and by positioning the camera to detect the image produced by the first-order focus. Setting $m = 1$ in Equation 8 yields two exponential terms corresponding, respectively, to the first-order divergent and convergent foci of the zone plate. The convergent term $\exp(-i\pi(x'^2 + y'^2)/\lambda f))$ is exactly the standard quadratic phase shift term $\exp(-ik(x'^2 + y'^2)/2f))$ that arises from a conventional lens, and this is the term we and the other two 3D models have used to approximate the zone plate as a lens.

This is an excellent and widely used approximation [20,21,29] because it has been shown that zone plates with a sufficient number of zones (>200) yield diffraction-limited Airy disk patterns at each focus $f_m = f_1/m$ [30,31]. Indeed, we have shown by numerical computation that the diffraction pattern produced by the zone plate used in this study (900 zones, with outermost zone width dr_n = 25 nm) quantitatively agrees with the expected Airy disk pattern for the lens with the equivalent NA [32].

2.4 pc-Mie model equations

Combining the preceding steps (2.1–2.3) for our model leads to equations for both the plane wave and the scattered wave fields at the camera:

$$U^{cam}(x,y,z) = C\iint_{\mathcal{A}} dx'dy'\left\{U^{zp}(x',y',z)\right\}\left\{\exp\left(-ik\frac{x'^2+y'^2}{2f}\right)\right\}\times \left\{\exp\left(-ik\frac{x'^2+y'^2}{2R_0}\right)\exp\left(-ik\frac{xx'+yy'}{2R_0}\right)\right\}. \quad (9)$$

Note that x and y refer to camera coordinates here, while the variable z refers to the z shifts of the nanosphere along the optical axis relative to the microscope's true focus position R_f

(see Figure 1b for definitions of the variables used). The three bracketed terms in Equation 9 correspond to the three model components: (1) the field $U^{zp}(x',y')$ arriving at the zone plate for either the plane wave or the scattered wave, (2) the approximation of the zone plate as a lens, which yields a quadratic phase shift with its focal length f corresponding to the zone plate's first-order focus, and (3) Fresnel diffraction through the zone-plate aperture, which also gives rise to the constant C in front of the integral. $\mathcal{A}$ is the circular aperture of the zone plate over which the double integration is performed.

As derived in Supporting Information File 1, Section S3, the fields arising at the zone plate $U^{zp}(x',y')$ for the plane and scattered waves are:

$$U_{\mathrm{PW}}^{\mathrm{zp}}\left(x',y',z\right)=\exp\left\{ik\left[\left(R_f-z\right)\cos\theta-y'\sin\theta\right]\right\}, \quad (10)$$

$$U_{\mathrm{SW}}^{\mathrm{zp}}\left(x',y',z\right)=\frac{S_\theta\left(x',y'\right)}{-ik}\left(\frac{\exp\left(ikR_{\mathrm{M}}\left(z\right)\right)}{R_{\mathrm{M}}\left(z\right)}\right), \quad (11)$$

where θ corresponds to the polar angle of illumination and R_{M} is the distance from the nanosphere to a point (x',y') on the zone plate.

Substitution of Equation 10 into Equation 9 leads to the final expression for the plane-wave field at the camera, which depends on the camera coordinates (x, y) and the amount of defocus z of the sample:

$$\begin{aligned}&U_{\theta-\mathrm{PW}}^{\mathrm{cam}}\left(x,y,z\right)=\\&\frac{-i}{\lambda R_0}\exp\left(ik\left[\left(R_f-z\right)\cos\theta+R_0+\frac{\left(x^2+y^2\right)}{2R_0}\right]\right)\times\\&\iint_{\mathcal{A}}\mathrm{d}x'\mathrm{d}y'\left\{\exp\left(-ik\frac{x'^2+y'^2}{2f}\right)\right\}\times\\&\left\{\exp\left(ik\frac{x'^2+y'^2}{2R_0}\right)\exp\left(-ik\frac{xx'+\left(y-R_0\sin\theta\right)y'}{R_0}\right)\right\}.\end{aligned} \quad (12)$$

Similarly, substitution of Equation 11 into Equation 9 leads to the final expression for the scattered-wave field at the camera, but as shown in Supporting Information File 1, Section S6, this expression can be simplified by a paraxial approximation. This leads to a solution that takes a standard form [33], namely the Fourier transform of the lens pupil function (in brackets below) computed over the lens circular aperture $\mathcal{A}$:

$$\begin{aligned}&U_{\theta-\mathrm{SW}}^{\mathrm{cam}}\left(x,y,z\right)=\\&\frac{1}{2\pi R_0R_f}\exp\left(ik\left[\left(R_f-z\right)+R_0+\frac{\left(x^2+y^2\right)}{2R_0}\right]\right)\times\\&\iint_{\mathcal{A}}\mathrm{d}x'\mathrm{d}y'\left\{S_\theta\left(x',y'\right)\exp\left(ik\frac{\left(x'^2+y'^2\right)z}{2{R_f}^2}\right)\right\}\times\\&\exp\left(-ik\frac{xx'+yy'}{R_0}\right).\end{aligned} \quad (13)$$

Note that the pupil function is given by the product of a term accounting for the scattered field in the zone-plate plane, $S_\theta(x',y')$, and a term accounting for the defocus wavefront aberration,

$$\exp(ik\frac{(x'^2+y'^2)z}{2{R_f}^2}).$$

The expressions in Equation 12 and Equation 13 for the plane-wave and scattered-wave fields at the camera are then added to produce the total field at the camera:

$$U_\theta^{\mathrm{cam}}=U_{\theta-\mathrm{PW}}^{\mathrm{cam}}+U_{\theta-\mathrm{SW}}^{\mathrm{cam}}. \quad (14)$$

Note that the constant terms in front of the plane and scattered wave solutions are different in Equation 12 and Equation 13 above, and so these must be incorporated in Equation 14 to account for the proper proportions of each in the sum. As indicated by the subscript θ, the field at the camera U_θ^{cam} depends on the oblique angle of plane wave illumination (the polar angle θ) along the ellipsoidal mirror's long axis.

2.5 inc-BL model equations

The inc-BL model has been previously described [20]. Briefly, the model assumes incoherent illumination such that the amount of light absorption at any point in the nanosphere is convolved with the point-spread function $h(r, z)$ of the objective. As in both our pc-Mie model and the pc-PWE model, the objective zone plate is also approximated by a lens. Given the radial symmetry of the nanosphere, the inc-BL model for the intensity I^{cam} at the camera can be written as:

$$I^{\mathrm{cam}}(Mr)=1-\int_{-a}^{a}\left(\mu\left(r,z\right)\exp\left(-\int_{-a}^{z}\mu\left(r,\xi\right)\mathrm{d}\xi\right)\right)\otimes_r h\left(r,z\right)\mathrm{d}z, \quad (15)$$

where (r, z) are cylindrical coordinates, M the microscope magnification, and μ the linear absorption coefficient defined for a nanosphere of radius a by:

$$\mu(r,\xi)=\begin{cases}2k\beta & r^2+\xi^2\le a^2\\ 0 & r^2+\xi^2>a^2\end{cases}. \quad (16)$$

Note that within the gold nanosphere, the linear absorption coefficient $\mu(r, z)$ is a constant and moves outside of the integral of Equation 15. The remaining exponential term in the integral reflects the accumulated absorption at different depths in the nanosphere defined by Beer's law (Equation 6), which is then convolved with the point-spread function $h(r, z)$ of a lens (whose NA equals that of the zone plate). Supporting Information File 1, Section S7, provides more details about the model and its implementation.

3 Comparisons of the models to each other and to experimental data

3.1 Experimental measurements

To test the models against real data, we collected a series of 2D images of 60 nm gold nanospheres at different amounts of defocus to generate a 3D dataset. Thus z values correspond to the shift of the microscope stage from its true focus location. We used the Helmholtz-Zentrum Berlin TXM operating at 510 eV at the electron storage ring BESSY II. To assess the reproducibility of the image data, we initially collected nine different 3D datasets under similar imaging conditions, but under different adjustments of the beamline due to fluctuations of the beam. The detailed data collection and pre-processing workflow is summarized in the Experimental section, and includes alignment of the focal-plane series to correct for stage jitter using larger 270 nm gold shells that were also included in the sample, plus correction for temporal fluctuations in the X-ray light source occuring during collection of the focal-plane series. Other than these basic corrections for jitter and source flicker, the data were not subjected to any other processing or reconsturction procedures. Three representative final 3D images are shown below in Figure 2.

3.2 Model comparisons: the effects of oblique illumination and the phase component of the refractive index

We compared the experimental data to the model predictions (Figure 2). We used Equations 12–14 above for the pc-Mie model to compute the predicted partially coherent image of the gold nanosphere under the condenser illumination conditions used in the pc-PWE model. Specifically, we assumed that the sample was illuminated by oblique plane waves at the mean polar angle of θ_m = 1.01° and that the coherence patch size around the circumference of the ellipsoidal mirror was small, p_φ = 1°. To do this, we calculated the field $U^{\mathrm{cam}}_{\theta_m,\varphi=0}(x,y,z)$ and then rotated it through 360° by 1° increments. Then we computed intensities at each angle and added them to yield the final image. Note that under these conditions, as described above (Table 1), the pc-Mie and pc-PWE models are equivalent, but in this study we have used our implementation of the pc-Mie model to compute predicted images, and so use this as the label for all images. For the inc-BL model, we used Equation 15 and Equation 16.

We found that the images from the pc-Mie model (Figure 2) were qualitatively similar to the experimental data in many respects: (1) After normalization, the images from both the model and data spanned similar intensity ranges; (2) the complex structure of the xz and yz images were similar showing a central in-focus region with high absorption that gave rise to a double-cone pattern of out-of-focus light above and below focus; (3) a contrast reversal occurred below focus in both experiment and theory, whereas no such reversal occurred above focus, and instead the absorption at the center of the bead slowly decayed; and (4) a contrast reversal also occurred around the nanosphere perimeter in the in-focus image.

As noted before, the pc-Mie model predictions (Figure 2) were calculated using a small azimuthal coherence patch size of 1°. We found that larger coherence patch sizes led to increasing deviations between the model and the experimental data. Specifically, as this azimuthal angular patch size increased, the increased coherence in the model led to more and more ringing in the predicted images (Supporting Information File 1, Section S8). Our observation is consistent with the pc-PWE model, which also used a small azimuthal coherence patch size in comparing their model to a phantom test sample [21].

The inc-BL model showed significantly poorer agreement with the experimental data. While this model (Figure 2) also yielded an absorbing nanosphere image in xy, it did not account for either the axial or in-focus contrast reversals nor the extended axial elongation of the measured image, and also only faintly showed the pronounced double cone pattern of out-of-focus light present in the measured image. Thus, the pc-Mie model with a small coherence patch delivered significantly more accurate predictions than the inc-BL model.

To understand how these different model predictions arose, we evaluated the effect of the differing assumptions made by the models. The inc-BL model presumes incoherent illumination, implying illumination over the full angular range of the zone-plate NA, whereas the pc-Mie model accounts for the mean-angle annular illumination present in the real microscope. To simulate this annular illumination effect in the inc-BL model, we changed the model's microscope PSF to introduce annular collection of light via an apodized objective lens (Supporting Information File 1, Section S7). We found that

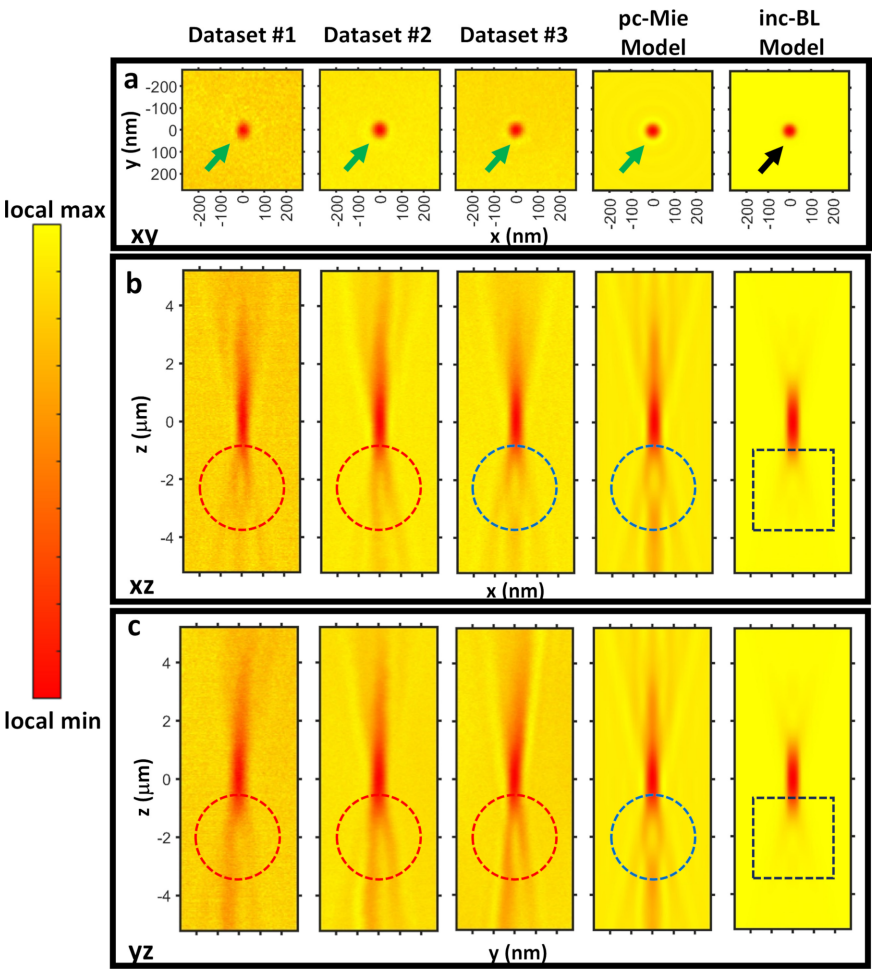

Figure 2: The pc-Mie model is more similar to the experimental data than the inc-BL model. Shown are *xy* (a), *xz* (b) and *yz* (c) views of the experimental data from three different 60 nm gold nanospheres collected months apart (Datasets #1, #2, and #3), and compared to the model predictions for a 63.2 nm nanosphere, which is the diameter of the nanosphere in Dataset #2 as measured by SEM. Exposure times were 2 s (Dataset #1), 8 s (Dataset #3), and an average of 3 × 14 s exposures (Dataset #2). Green arrows point to a contrast reversal around the nanosphere seen in both the data and the pc-Mie model, but absent in the inc-BL model (black arrow). An axial contrast reversal is also present in both the data and the pc-Mie model (dashed circles), but absent in the inc-BL model (dashed square). The red dashed circles highlight the lateral asymmetry in the axial images mostly characteristic of the experimental data, while the blue dashed circles highlight the lateral symmetry characteristic of the axial images from the models.

this led to an axial elongation of the nanosphere image in the inc-BL model (Figure 3), suggesting that oblique, annular illumination contributed to the more elongated images in the pc-Mie model.

Another key difference between the pc-Mie model and the inc-BL model is that the refractive index of the pc-Mie model includes both absorption and phase terms, whereas the inc-BL model neglects the phase term. To simulate this situation, we set $\delta = 0$ in the pc-Mie model and found that this eliminated the axial contrast reversal (Figure 3). This demonstrates that this contrast reversal arises from the phase properties of the sample and underscores the importance of including this term in the model to accurately account for the measured data.

3.3 Introduction of condenser tilt into the pc-Mie model accounts for the lateral asymmetries in the data

While the pc-Mie model accounted reasonably well for many qualitative features of the experimental data, it failed to predict a lateral asymmetry that we consistently observed (highlighted in Figure 2 with the red and blue circles) and that varied from day to day in the data. We found we could eliminate the day-to-day variations by rotating each dataset around the optical axis by an appropriate angle (Supporting Information File 1, Section S9). Following this rotation, the experimental data resembled each other and also the model, except that the data were slightly tilted in *yz* views compared to the model (Figure 4a vs Figure 2).

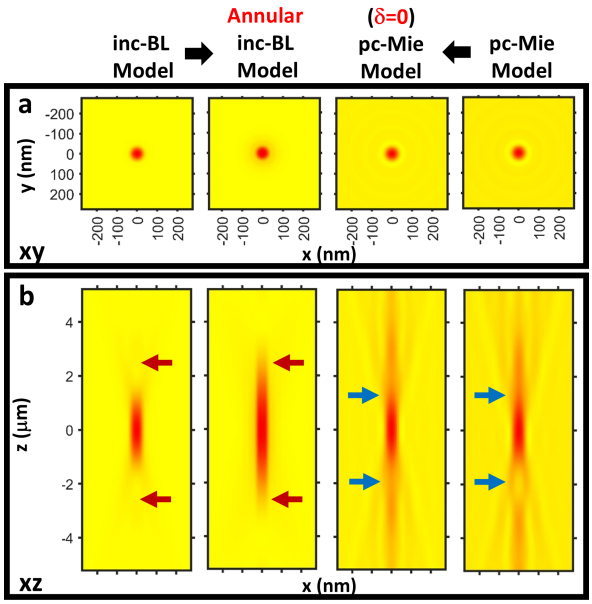

Figure 3: Key differences between the pc-Mie and inc-BL models are the presence or absence of annular illumination and the phase term δ in the refractive index. *xy* (a) and *xz* (b) images of the nanosphere are shown. Simulating annular illumination in the inc-BL model introduces an axial elongation (red arrows, b). Setting δ = 0 in the pc-Mie model eliminates the axial asymmetry (blue arrows). Thus, much of the basic structure of the inc-BL image can be explained by the lack of annular illumination and neglect of the phase term δ in the inc-BL model.

We obtained a rough estimate of this tilt in the data by drawing a line along the apparent tilt axis and measuring its angle with the *z* axis, which we found was 0.26° (Supporting Information File 1, Section S10). This tilt could arise from a misalignment of some optical component, for example, a tilt of the incoming beam relative to the optical axis defined by the zone plate and camera (Figure 4c). In this case, the condenser will be aligned relative to the tilted incoming beam and will lead to polar angles θ of plane wave illumination that vary as a function of the azimuthal angle φ around the ellipsoidal mirror circumference (Figure 4d). This dependence θ = θ(φ) can be calculated based on the tilt angle ω_{tilt} = 0.26° and the geometry of the ellipsoidal mirror (see Supporting Information File 1, Section S11, for the equation and its derivation). We used this dependence θ = θ(φ) for a tilted condenser to calculate the image arising from such a tilt by adding the intensities at 1° increments of the azimuthal angle φ using the field $U^{\text{cam}}_{\theta(\varphi),\varphi}$ for each φ.

We found that such a tilt in the condenser (Figure 4) yielded predicted nanosphere images that were in good qualitative agreement with the lateral asymmetries observed in the experimental images of the nanosphere. This analysis therefore suggests a misalignment of ≈0.26°, which might arise for example from a tilt in the incoming beam relative to the zone plate–camera axis.

3.4 Quantitative comparisons of radial intensity profiles reveal a discrepancy between the pc-Mie model and the data

We next evaluated the quantitative accuracy of the pc-Mie model by computing radial intensity profiles through the center of the nanosphere images. The nanosphere center was defined as the minimum-intensity pixel in the 3D dataset. The focal plane containing this minimum-intensity pixel was defined as best focus. We then computed an average radial intensity in this best focus plane. For this analysis, we used the non-tilted condenser model because its in-focus radial average was the same as that of the tilted condenser model (Supporting Information File 1, Section S12) and the non-tilted condenser model was much easier to compute. To enable a more precise quantitative analysis, we first extensively characterized the gold nanospheres by both scanning and transmission electron microscopy (SEM and TEM, Supporting Information File 1, Section S13) to determine the nanosphere's shape, composition, diameter, and density.

Both SEM and TEM showed that the nanospheres were indeed roughly spherical and of similar size (Supporting Information File 1, Section S13). Specifically, we measured the diameter of 35 nanospheres by SEM and obtained a value of 62.2 ± 2.9 nm. Furthermore, TEM images showed that the nanospheres were solid and had roughly similar densities throughout. By TEM, the interior of the nanospheres did exhibit some lightly shaded stripes, characteristic of a channeling effect expected to arise from a crystalline structure. To investigate this further, we performed selected area electron diffraction on the nanospheres, which revealed the presence of crystalline domains in the nanospheres with the lattice spacing of gold (Supporting Information File 1, Section S13, Figure S12a). Furthermore, a high-resolution TEM image showed the crystalline order extended over the full particle. Fourier transform of a sub-region of this image yielded a lattice spacing for Au(111) of 0.236 nm, close to the nominal value of 0.235 nm (Supporting Information File 1, Section S13, Figure S12b). Finally, an energy-dispersive X-ray spectroscopy analysis revealed that the principal element within the nanosphere was gold with very small contributions from carbon, oxygen, and potassium (Supporting Information File 1, Section S13, Figure S11d). We conclude the nanospheres are solid, nearly spherical and predominantly composed of crystalline gold, which enables us to accurately calculate their expected radial intensity profiles and absorptions.

We then collected 3D TXM images of nine different nanospheres, each of which had been pre-imaged by SEM to deter-

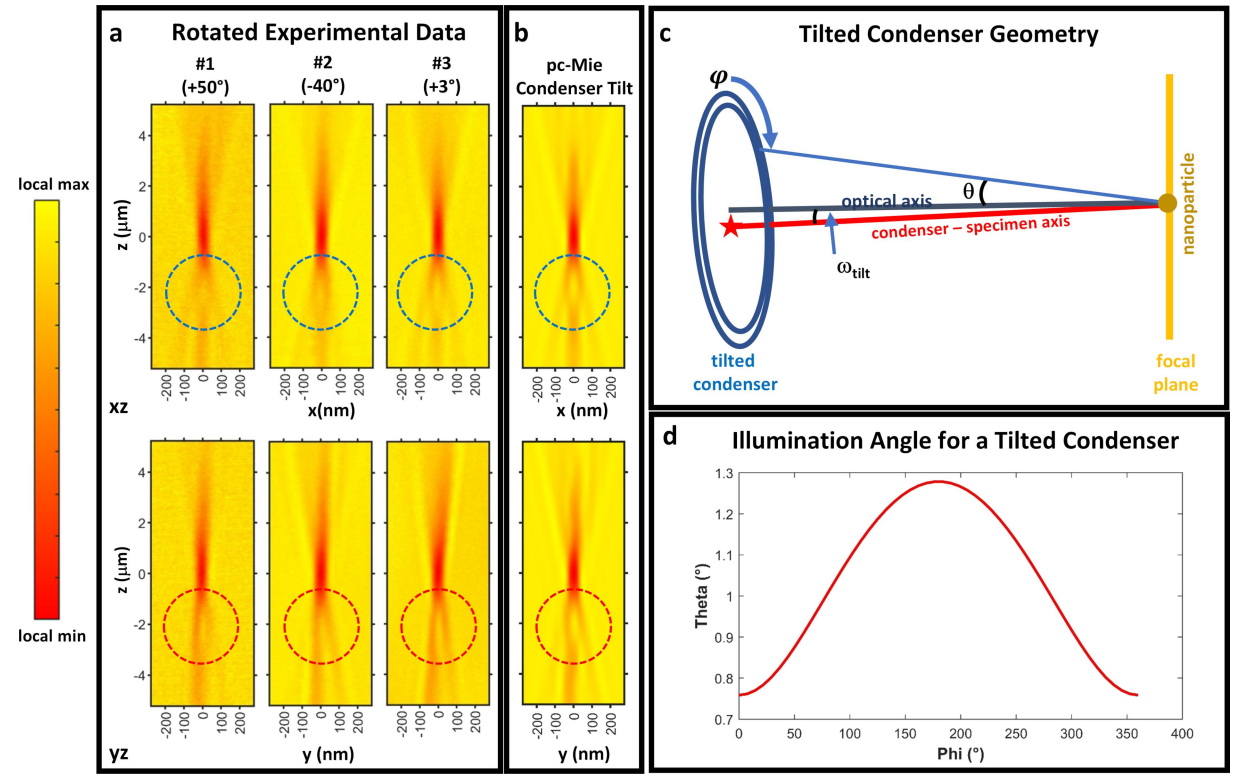

Figure 4: Rotation of the experimental data (a) significantly increased both their similarity to each other and to the predictions of the pc-Mie model (b). Each experimental dataset was rotated around the optical axis by the amount indicated in parentheses (a, see also Figure S7 in Supporting Information File 1, Section S9). Note that rotation of the data eliminated the axial asymmetry in the *xz* views (a, blue dotted circles), and enhanced it in the *yz* views (a, red dotted circles). To account for this *yz* asymmetry, we modified the pc-Mie model by tilting the incoming beam–condenser axis by ω_{tilt} = 0.26° relative to the zone plate–camera axis (c), where ω_{tilt} was determined by estimating the tilt from the *yz* views of the experimental data (Supporting Information File 1, Section S10). This led to a dependence of the polar illumination angle θ on the azimuthal angle φ (d), which was used to produce the predicted images (b), which now more closely resembled the experimental data.

mine its diameter. Based on the SEM images, these nine nanospheres were selected to exclude the outlier sizes and shapes that we had also found by TEM. The 3D TXM images thereby enabled a direct comparison of radial intensity profiles for each nanosphere with those predicted by the model calculated for that specific diameter and the density of crystalline gold. For all nine nanospheres we observed a similar significant undershoot and a slight overshoot of the pc-Mie model compared to the data (Figure 5).

This significant undershoot cannot be explained by errors in estimating the diameters of the slightly oblong nanospheres by SEM, as these estimation errors lead to only small differences in the predicted radial intensity profiles (Supporting Information File 1, Section S14). The same is true for an error in estimation of the gold density, where we found that to match the data the nanosphere would require a nanosphere density of 60% of that for crystalline gold (Supporting Information File 1, Section S14), a result completely inconsistent with the TEM analysis of the nanospheres.

3.5 The microscope underestimates the absorption of the 60 nm gold nanospheres

To understand the consequences of the quantitative discrepancy in the radial profiles between the model and the data, we calculated the absorption of each nanosphere, since this is a commonly measured parameter in samples imaged by TXMs. An exact measurement of experimental absorption is non-trivial because the background around the nanosphere varies slowly with distance from the nanosphere center. Therefore, to achieve a robust estimate of absorption, we integrated the experimental radial intensity profile starting at different points beyond the central inverted peak of the nanosphere. The absorption as a function of the integration endpoint is given by:

$$A(r_{\mathrm{end}}) = \int_0^{2\pi} \mathrm{d}\theta \int_0^{r_{\mathrm{end}}} \left(1 - I(r)\right) r \mathrm{d}r = 2\pi \int_0^{r_{\mathrm{end}}} \left(1 - I(r)\right) r \mathrm{d}r, \quad (17)$$

where $I(r)$ is the radial intensity profile and r_{end} is the endpoint of the integration, which we increased stepwise to include more

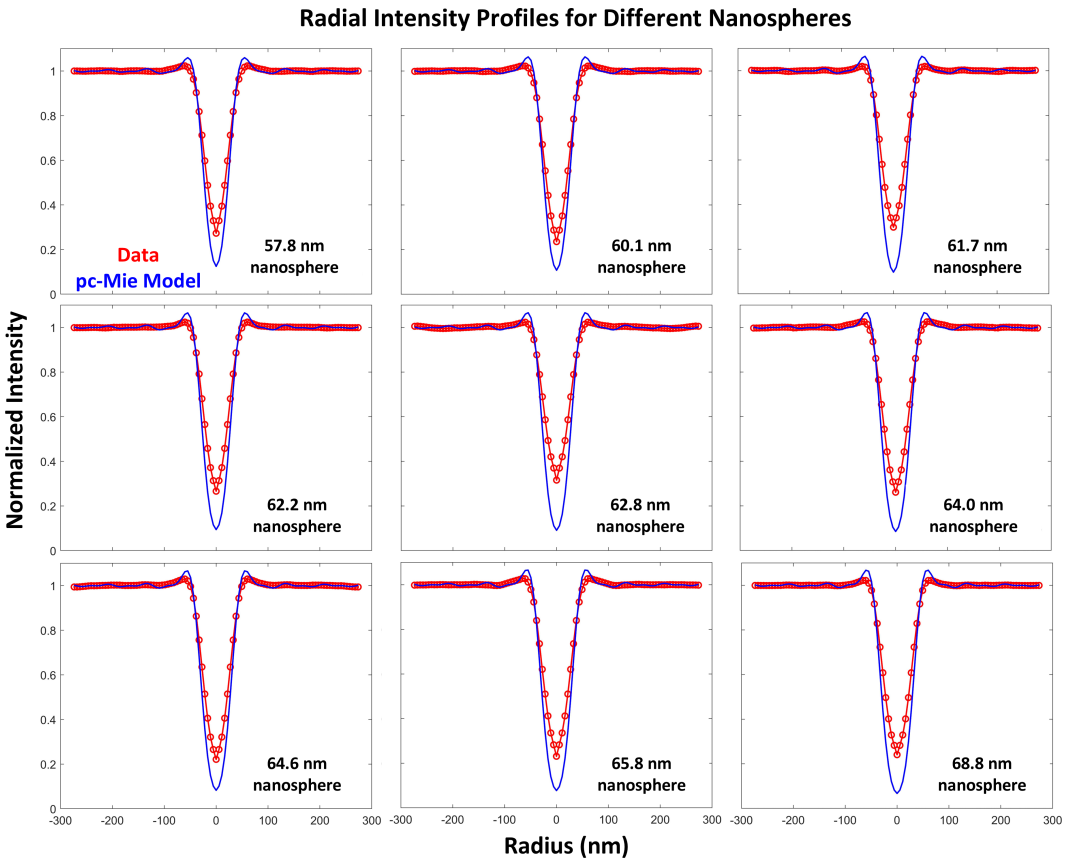

Figure 5: Comparison of measured and predicted radial intensity profiles for nine different nanospheres whose diameters were measured by SEM. An overshoot and undershoot of the pc-Mie model compared to the data are seen in all cases.

and more of the tails of the intensity profile. This yielded multiple absorption estimates from a single nanosphere's best-focus image, enabling an estimate of the mean absorption and its standard deviation.

We performed an analogous measurement of absoprtion from best-focus images produced by the pc-Mie model, and finally we also calculated the absorption predicted by Beer's law:

$$A_{\mathrm{BL}} = 2\pi\int_0^a \left(1-\exp\left(-4k\beta\sqrt{a^2-\xi^2}\right)\right)\xi \mathrm{d}\xi, \qquad (18)$$

where ξ is the radial coordinate in the nanosphere and a is the radius of the nanosphere as measured by SEM.

We found that the predicted absorption from the pc-Mie model was nearly identical to Beer's law (Figure 6). However, consistent with the radial profiles in Figure 5, we found that the measured absorption from each nanosphere was always significantly less than that predicted by either the model or Beer's law. This discrepancy between Beer's law and the measured data was much larger than the standard deviation of the data. As described above, the discrepancy between the model and the data cannot be attributed to uncertainties about the nanosphere geometry. We conclude therefore that the microscope is likely to significantly underestimate the nanosphere's absorption, and so our results suggest that there is some feature of the actual microscope not incorporated into the model that reduces the measured nanosphere absorption.

Discussion

We have developed a 3D soft TXM model and compared it to the two most recent soft TXM models, both of which also incorporated 3D imaging on the microscope (Table 1). We showed that, for the case of the gold nanosphere examined here, the simplest form of our pc-Mie model was essentially identical to the pc-PWE model [21]. This is because we showed that Mie theory and the parabolic wave equation yield virtually identical predictions for soft X-ray light propagation through a 60 nm gold nanosphere.

Our pc-Mie model however yielded predictions very different from the other 3D TXM model, namely the inc-BL model [20].

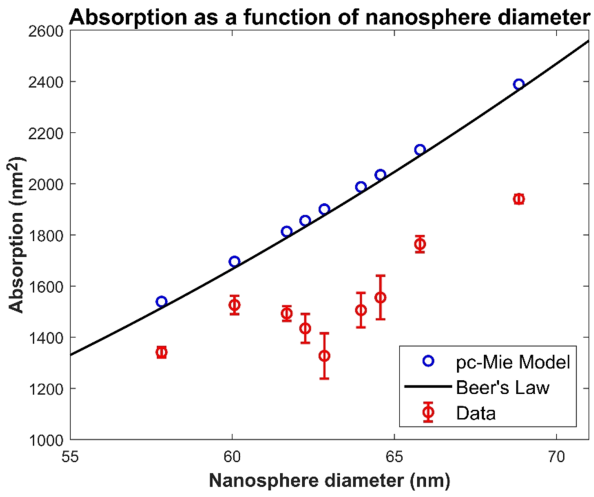

Figure 6: Absorptions from the nine nanosphere images are significantly less than predicted by either the pc-Mie model or Beer's law. This suggests that the microscope may reduce the actual absorption due to some as yet unidentified feature that must ultimately be incorporated into the model.

A key difference was that our model included the phase component δ of the sample's refractive index, and this led to predicted axial images with a marked contrast reversal consistent with the experimental data. By comparison, when we set δ = 0 in our pc-Mie model, the predicted axial images were completely symmetric, as also predicted by the inc-BL model, where the phase component is also not incorporated. This result demonstrates that phase must be included in any soft TXM model for an accurate description of 3D imaging. This is significant because both spectromicroscopy and the most commonly used tomographic reconstruction procedures for TXMs ignore the phase term in the refractive index and presume instead that the image arises solely from absorption, namely Beer's law. Thus, future work should focus on exactly how the phase term δ influences these different imaging applications to enable more accurate measurements.

We identified both qualitative and quantitative discrepancies between our model and the measured data from 60 nm gold nanospheres. Our qualitative comparisons revealed a lateral asymmetry consistently present in the measured data that was absent in the model. We could account for this lateral asymmetry by introducing a small tilt (0.26°) between two axes, the first defined by incoming beam and condenser and the second by zone plate and camera, but other small misalignments in the microscope's optical train could also play a role. In itself, the presence of a small tilt is not surprising given the difficulty in precisely aligning all optical components. Importantly, however, we consistently observed a similar amount of tilt in all datasets collected, and therefore an accurate model for tomographic reconstruction should also incorporate this tilt in order to achieve optimal 3D reconstructions.

Beyond this qualitative difference due to a slight misalignment in the actual microscope, our quantitative comparison of the model's predictions to the measured data also revealed a surprising discrepancy: The model consistently overestimated the amount of absorption in the real data. Strikingly, however, the model's predictions agreed with Beer's law whereas the measured data did not. This discrepancy did not appear to be due to uncertainties in the geometry of the nanospheres examined as both SEM and TEM analysis of the nanospheres indicated a reasonably well-defined spherical geometry composed of crystalline gold. These results suggest that the microscope imaging process itself may introduce some additional component such that measured absorptions are 10–20% lower than predicted by Beer's law.

Our model suggests that this discrepancy might arise because the theoretical data exhibited significantly larger overshoots and undershoots compared to the experimental data. One possible explanation for this is that there is a small background in the microscope images that is currently not accounted for in the model. Such a background would reduce both the over and undershoots in the measured data, but other explanations are also possible. Therefore, it will be important in future work to identify exactly what feature(s) of the actual imaging process introduce this absorption discrepancy, such that it can be corrected.

This goal can be achieved by extending our current pc-Mie model to account more accurately for all of the features in the actual microscope (Table 1). This should include incorporation of (1) the zone plate and its accompanying non-ideal features such as struts [34], rather than the approximation as an ideal lens; (2) partial coherence that is based on future measurements of the microscope's coherence patch size and incorporates the full angular range of illumination rather than just the mean angle; and (3) the spiral scanning of the condenser focal spot rather than a stationary condenser. It is likely that at least one of these three features is responsible for the quantitative discrepancies that we have measured here between the data and the model. Identifying the source of this discrepancy will be important not only for producing an accurate imaging model for improved reconstruction procedures but also for ensuring accurate quantitative measurements with the microscope.

Future work should also explore how our model could be extended from soft to either tender or hard X-rays. At these higher energies, both the Mie theory for light propagation through a sphere and the lens model for the zone plate should still be

valid. However, with increasing energy, the ratio of δ/β progressively increases, indicating that phase effects increasingly dominate. With hard X-rays, phase effects are so dominant that Zernike phase contrast is required, and so our model would have to be extended to account for this imaging modality. With tender X-rays, there is still some absorption if the nanosphere is large enough. However, given a larger object, our simple mean-angle model for the condenser might no longer be valid, and a more general model accounting for the full angular range of condenser illumination is likely to be required. Thus, further comparisons between theory and experiment will be needed to properly extend our model to tender X-rays, and the model itself must be extended to phase contrast imaging for hard X-rays.

Conclusion

We have developed an experimental and theoretical framework to evaluate transmission X-ray microscope models. We find that a relatively simple model of the microscope yields very good qualitative agreement with experimental data, which can be further improved by incorporating a small tilt between microscope components. To achieve this reasonable qualitative agreement with the data, we found that the model must account for both β and δ of the sample's complex refractive index. However, we also showed that this simple model has a deficiency: It does not agree quantitatively with the measured data because the data exhibit less absorption than predicted by Beer's law. Achieving quantitative agreement will require first identifying why the microscope underestimates absorption and then incorporating this feature(s) into the model. This will then enable more quantitatively accurate measurements in both spectromicroscopy and biomedical imaging.

Experimental

The measured data [35] were obtained by allowing both 60 nm gold nanospheres and 270 nm gold shells from a colloidal gold suspension to dry onto holey carbon-coated gold finder grids (Quantifoil). 3D volumes from selected regions of the grid were then collected using the Helmholtz-Zentrum Berlin TXM operating at 510 eV at the electron storage ring BESSY II. A 25 nm zone plate was used with the microscope configured for a magnification of ≈3600×. This led to a pixel size in each 2D image of 5.5 nm. A 3D volume was generated by collecting 301 2D images that were separated from each other in z by 40 nm, thereby yielding a final voxel size for the 3D volume of 5.5 nm × 5.5 nm × 40 nm. Finally, these raw 3D images of the 60 nm nanospheres were processed to reduce stage jitter and flickering of the X-ray light source (Figure 7). Supporting Information File 1 contains additional information for all other experimental procedures and analyses.

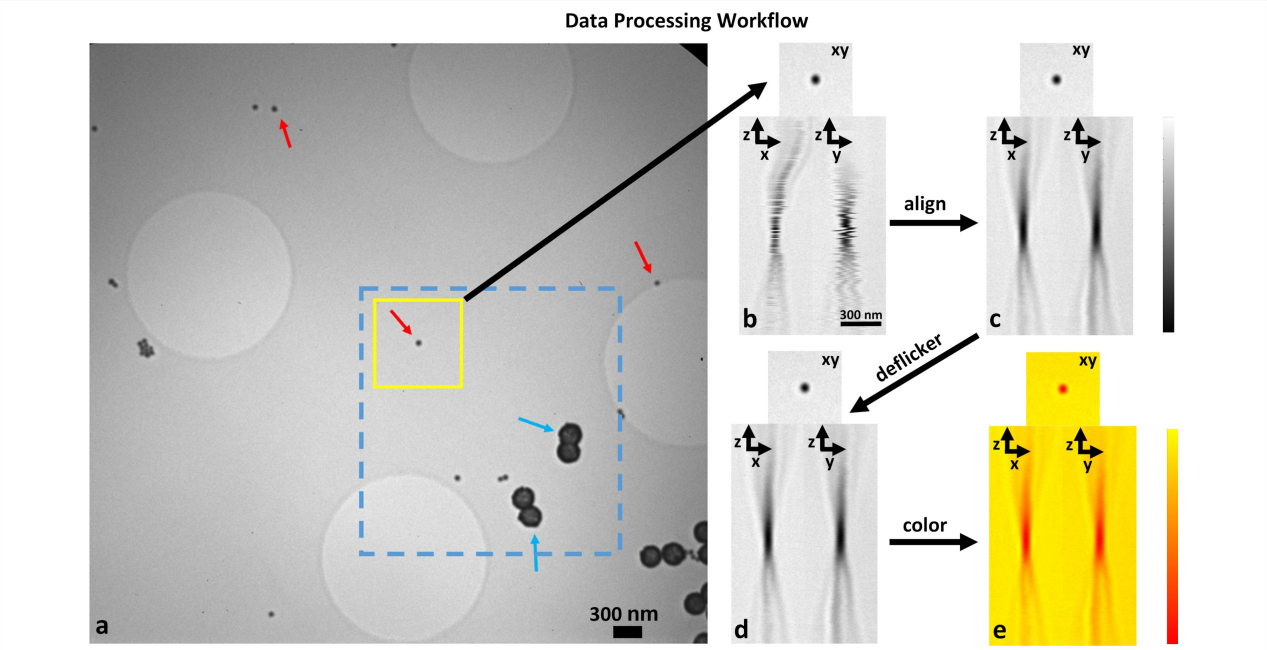

Figure 7: Data processing workflow. A full-field in-focus image is shown from the 3D image stack. Large circles are holes in the carbon foil of the grid. Red arrows point to selected 60 nm gold nanospheres and blue arrows to selected 270 nm gold shells (containing a silicon core). A sub-image (yellow box) around an isolated 60 nm gold nanosphere was extracted to produce a 3D volume, whose *xy*, *xz*, and *yz* cuts are shown (b). Stage jitter and drift were corrected (c) using the StackReg plugin in imagej applied to the 3D stack defined by the dotted blue rectangle in (a), which includes several of the 270 nm gold shells that are essential for good alignment of the stack. Plane-to-plane variation in the X-ray illumination (flicker) was corrected by normalizing the sum of intensities in each plane to a constant (d). A false-color scale ("autumn" in Matlab) was used to better visualize the intensity range, with red corresponding to regions of highest absorption and yellow to regions of highest transmission (e). Scale bar = 300 nm.

Matlab was used to compute all model predictions. Here we summarize the computational approach for calculating the pc-Mie model. Supporting Information File 1 contains detailed descriptions for all other model calculations. We validated the code for computing the fields $U^{\mathrm{cam}}_{\theta-\mathrm{PW}}$ and $U^{\mathrm{cam}}_{\theta-\mathrm{SW}}$ for the pc-Mie model Equations 12 and 13 by comparing results for several approaches including numerical integration by the trapezoidal rule, numerical integration by steepest descent contour deformation designed for highly oscillatory integrals (a custom version of the PathFinder code [36]), and, in the case of the plane-wave field, using a change of variables to convert Equation 12 into Lommel's integral, which can be solved by a sum of Lommel functions [37]. With vectorized Matlab code, these integrals could be computed in less than 5 min using an Intel core i9 processor. All code is available upon request.

Supporting Information

The Supplement is a single document with multiple sections listed according to their order of citation in the main text. The different sections provide (1) detailed explanations of the different models: S1 – Mean angle condenser; S2 – Plane-wave model of the condenser; S3 – Extension of the Mie theory to oblique plane waves; S4 – Simplification of the Mie theory to the anomalous diffraction approximation; S5 – Equivalency of the Mie theory and the parabolic wave equation; S6 – Calculation of the nanosphere's plane-wave and scattered-wave fields at the camera; S7 – Incoherent Beer's law model; S11 – Calculation of polar tilt angle as a function of azimuthal angle in a tilted condenser; (2) calculation of specific model predictions: S8 – Effect of coherence patch size in the mean-angle condenser model; S12 – Radial intensity profiles of the tilted vs. non-tilted theory; S14 – Sensitivity of radial intensity profiles to deviations in nanosphere geometry; and (3) descriptions of experimental procedures and measurements: S9 – Rotation of the experimental data around the optical axis; S10 – Estimation of the axial tilt in the data; S13 – Structural characterization of the 60 nm gold nanospheres by SEM and TEM.

Supporting Information File 1

Supplement.
[https://www.beilstein-journals.org/bjnano/content/supplementary/2190-4286-16-82-S1.pdf]

Acknowledgements

We thank the Helmholtz-Zentrum Berlin für Materialien und Energie for the allocation of synchrotron radiation beamtime.

Funding

T.L. acknowledges the Federal Ministry of Education and Research in the framework of the project Catlab (03EW0015A) for funding.

ORCID® iDs

James G. McNally - https://orcid.org/0000-0002-9032-1988
Stephan Werner - https://orcid.org/0000-0002-9041-1967
Stefan Rehbein - https://orcid.org/0000-0002-1606-1428
Thomas Lunkenbein - https://orcid.org/0000-0002-8957-4216
Peter Guttmann - https://orcid.org/0000-0002-0534-238X

Data Availability Statement

Data generated and analyzed during this study is openly available in HZB Data Service at https://doi.org/10.5442/ND000011.

References

1. Jacobsen, C. *X-Ray Microscopy;* Cambridge University Press: Cambridge, UK, 2019. doi:10.1017/9781139924542
2. Groen, J.; Conesa, J. J.; Valcárcel, R.; Pereiro, E. *Biophys. Rev.* **2019,** *11,* 611–619. doi:10.1007/s12551-019-00567-6
3. Harkiolaki, M.; Darrow, M. C.; Spink, M. C.; Kosior, E.; Dent, K.; Duke, E. *Emerging Top. Life Sci.* **2018,** *2,* 81–92. doi:10.1042/etls20170086
4. Schneider, G.; Guttmann, P.; Rehbein, S.; Werner, S.; Follath, R. *J. Struct. Biol.* **2012,** *177,* 212–223. doi:10.1016/j.jsb.2011.12.023
5. Guttmann, P.; Bittencourt, C.; Werner, S.; Rehbein, S.; Pratsch, C.; Schneider, G. *J. Electron Spectrosc. Relat. Phenom.* **2023,** *266,* 147344. doi:10.1016/j.elspec.2023.147344
6. Liu, Z.; Zeng, Y.; Tan, J.; Wang, H.; Zhu, Y.; Geng, X.; Guttmann, P.; Hou, X.; Yang, Y.; Xu, Y.; Cloetens, P.; Zhou, D.; Wei, Y.; Lu, J.; Li, J.; Liu, B.; Winter, M.; Kostecki, R.; Lin, Y.; He, X. *Nat. Nanotechnol.* **2024,** *19,* 1821–1830. doi:10.1038/s41565-024-01773-4
7. Guttmann, P.; Bittencourt, C.; Rehbein, S.; Umek, P.; Ke, X.; Van Tendeloo, G.; Ewels, C. P.; Schneider, G. *Nat. Photonics* **2012,** *6,* 25–29. doi:10.1038/nphoton.2011.268
8. Yoon, A.; Bai, L.; Yang, F.; Franco, F.; Zhan, C.; Rüscher, M.; Timoshenko, J.; Pratsch, C.; Werner, S.; Jeon, H. S.; Monteiro, M. C. d. O.; Chee, S. W.; Roldan Cuenya, B. *Nat. Mater.* **2025,** *24,* 762–769. doi:10.1038/s41563-024-02084-8
9. Kapishnikov, S.; Weiner, A.; Shimoni, E.; Guttmann, P.; Schneider, G.; Dahan-Pasternak, N.; Dzikowski, R.; Leiserowitz, L.; Elbaum, M. *Proc. Natl. Acad. Sci. U. S. A.* **2012,** *109,* 11188–11193. doi:10.1073/pnas.1118120109
10. Gal, A.; Sorrentino, A.; Kahil, K.; Pereiro, E.; Faivre, D.; Scheffel, A. *Proc. Natl. Acad. Sci. U. S. A.* **2018,** *115,* 11000–11005. doi:10.1073/pnas.1804139115
11. Conesa, J. J.; Otón, J.; Chiappi, M.; Carazo, J. M.; Pereiro, E.; Chichón, F. J.; Carrascosa, J. L. *Sci. Rep.* **2016,** *6,* 22354. doi:10.1038/srep22354
12. Le Gros, M. A.; Clowney, E. J.; Magklara, A.; Yen, A.; Markenscoff-Papadimitriou, E.; Colquitt, B.; Myllys, M.; Kellis, M.; Lomvardas, S.; Larabell, C. A. *Cell Rep.* **2016,** *17,* 2125–2136. doi:10.1016/j.celrep.2016.10.060
13. Selin, M.; Fogelqvist, E.; Werner, S.; Hertz, H. M. *Opt. Lett.* **2015,** *40,* 2201–2204. doi:10.1364/ol.40.002201

14. Otón, J.; Pereiro, E.; Pérez-Berná, A. J.; Millach, L.; Sorzano, C. O. S.; Marabini, R.; Carazo, J. M. *Biomed. Opt. Express* **2016,** *7,* 5092–5103. doi:10.1364/boe.7.005092
15. Otón, J.; Pereiro, E.; Conesa, J. J.; Chichón, F. J.; Luque, D.; Rodríguez, J. M.; Pérez-Berná, A. J.; Sorzano, C. O. S.; Klukowska, J.; Herman, G. T.; Vargas, J.; Marabini, R.; Carrascosa, J. L.; Carazo, J. M. *Sci. Rep.* **2017,** *7,* 45808. doi:10.1038/srep45808
16. Ekman, A.; Weinhardt, V.; Chen, J.-H.; McDermott, G.; Le Gros, M. A.; Larabell, C. *J. Struct. Biol.* **2018,** *204,* 9–18. doi:10.1016/j.jsb.2018.06.003
17. Schneider, G. *Ultramicroscopy* **1998,** *75,* 85–104. doi:10.1016/s0304-3991(98)00054-0
18. von Hofsten, O.; Takman, P. A. C.; Vogt, U. *Ultramicroscopy* **2007,** *107,* 604–609. doi:10.1016/j.ultramic.2006.12.001
19. Bertilson, M.; von Hofsten, O.; Hertz, H. M.; Vogt, U. *Opt. Express* **2011,** *19,* 11578–11583. doi:10.1364/oe.19.011578
20. Otón, J.; Sorzano, C. O. S.; Pereiro, E.; Cuenca-Alba, J.; Navarro, R.; Carazo, J. M.; Marabini, R. *J. Struct. Biol.* **2012,** *178,* 29–37. doi:10.1016/j.jsb.2012.01.006
21. Selin, M.; Fogelqvist, E.; Holmberg, A.; Guttmann, P.; Vogt, U.; Hertz, H. M. *Opt. Express* **2014,** *22,* 30756. doi:10.1364/oe.22.030756
22. Bohren, C. F.; Huffman, D. R. *Absorption and Scattering of Light by Small Particles;* Wiley-VCH: Weinheim, Germany, 1998. doi:10.1002/9783527618156
23. Goslawski, P.; Holldack, K.; Hüsges, Z.; Jankowiak, A.; Kiefer, K.; Meseck, A.; Müller, R.; Sauerborn, M.; Schwarzkopf, O.; Viefhaus, J. BESSY III The Material Discovery Facility, 2022. https://www.helmholtz-berlin.de/media/media/angebote/bibliothek/reports/r0004-bessy-iii-the-materials-discovery-facility.pdf.
24. Guttmann, P.; Werner, S.; Siewert, F.; Sokolov, A.; Schmidt, J.-S.; Mast, M.; Brzhezinskaya, M.; Jung, C.; Follath, R.; Schneider, G. *Microsc. Microanal.* **2018,** *24* (Suppl. 2), 206–207. doi:10.1017/s1431927618013375
25. Guttmann, P.; Zeng, X.; Feser, M.; Heim, S.; Yun, W.; Schneider, G. *J. Phys.: Conf. Ser.* **2009,** *186,* 012064. doi:10.1088/1742-6596/186/1/012064
26. Mätzler, C. *Matlab Functions for Mie Scattering and Absorption. Version 2;* University of Bern: Bern, Switzerland, 2002.
27. van de Hulst, H. C. *Light Scattering by Small Particles;* Dover Publications: New York, NY, USA, 1981.
28. Sharma, S. K.; Somerford, D. J. Scattering of Light in the Eikonal Approximation. *Progress in Optics;* Elsevier: Amsterdam, Netherlands, 1999; Vol. 39, pp 213–290. doi:10.1016/s0079-6638(08)70390-1
29. Weiß, D.; Schneider, G.; Niemann, B.; Guttmann, P.; Rudolph, D.; Schmahl, G. *Ultramicroscopy* **2000,** *84,* 185–197. doi:10.1016/s0304-3991(00)00034-6
30. Boivin, A. *J. Opt. Soc. Am.* **1952,** *42,* 60–64. doi:10.1364/josa.42.000060
31. Arsenault, H. *J. Opt. Soc. Am.* **1968,** *58,* 1536. doi:10.1364/josa.58.001536
32. McNally, J. G.; Rehbein, S.; Pratsch, C.; Werner, S.; Guttmann, P.; Schneider, G. 3D PSF Measurement for a Soft X-Ray Microscope and Comparison to Theory. In *Imaging and Applied Optics 2016,* Computational Optical Sensing and Imaging 2016, Heidelberg, Germany, July 25–28, 2016; Optica Publishing Group: Washington, DC, USA, 2016; CM3D.4. doi:10.1364/cosi.2016.cm3d.4
33. Williams, C. S.; Becklund, O. A. *Introduction to the Optical Transfer Function;* Wiley Series in Pure and Applied Optics; John Wiley & Sons: New York, NY, USA, 1998.
34. Chen, J.; Fan, Q.; Wang, J.; Yuan, D.; Wei, L.; Zhang, Q.; Liao, J.; Xu, M. *Curr. Opt. Photonics* **2020,** *4,* 9–15. doi:10.3807/copp.2020.4.1.009
35. McNally, J. G.; Pratsch, C.; Werner, S.; Guttmann, P. 3D Datasets for 60 nm Gold Nanoparticles. HZB Data Service, 2025; https://data.helmholtz-berlin.de/pub/ND000011. doi:10.5442/nd000011
36. Gibbs, A.; Hewett, D. P.; Huybrechs, D. *J. Comput. Phys.* **2024,** *501,* 112787. doi:10.1016/j.jcp.2024.112787
37. Born, M.; Wolf, E. *Principles of Optics: Electromagnetic Theory of Propagation, Interference and Diffraction of Light,* 7th ed.; Cambridge University Press: Cambridge, UK, 1999.

License and Terms

BEILSTEIN JOURNAL OF NANOTECHNOLOGY

Ambient pressure XPS at MAX IV

Mattia Scardamaglia*[1], Ulrike Küst[2,3], Alexander Klyushin[1], Rosemary Jones[1], Jan Knudsen[1,2,3], Robert Temperton[1], Andrey Shavorskiy[1] and Esko Kokkonen[1]

Review

Open Access

Address:
[1]MAX IV Laboratory, Lund University, Box 118, SE-221 00, Lund, Sweden, [2]Division of Synchrotron Radiation Research, Lund University, Box 118, SE-221 00, Lund, Sweden and [3]NanoLund, Lund University, Box 118, SE-221 00, Lund, Sweden

Email:
Mattia Scardamaglia* - mattia.scardamaglia@maxiv.lu.se

* Corresponding author

Keywords:
2D materials; atomic layer deposition; batteries; catalysis; corrosion

Beilstein J. Nanotechnol. **2025,** *16,* 1677–1694.
https://doi.org/10.3762/bjnano.16.118

Received: 12 June 2025
Accepted: 09 September 2025
Published: 24 September 2025

This article is part of the thematic issue "Exploring synchrotron radiation and free-electron laser tools for nanostructured materials".

Guest Editor: C. Bittencourt

Abstract

Ambient pressure X-ray photoelectron spectroscopy (APXPS) has emerged as an important technique for investigating surface and interface chemistry under realistic conditions, overcoming the limitations of conventional XPS restricted to ultrahigh vacuum. This review highlights the capabilities and scientific impact of APXPS at the MAX IV Laboratory, the world's first fourth-generation synchrotron light source. With the APXPS beamlines SPECIES and HIPPIE, MAX IV offers state-of-the-art instrumentation for in situ and operando studies across a broad pressure range, enabling research in catalysis, corrosion, energy storage, and thin film growth. The high brilliance and small beam size of MAX IV's synchrotron light are essential for pushing the time-resolution boundaries of APXPS, especially in the soft X-ray regime. We discuss representative studies at MAX IV, including investigations of single-atom catalysts, confined catalysis, time-resolved catalysis, atomic layer deposition, and electrochemical interfaces, showcasing the role of APXPS in advancing material and surface science.

Review

Ambient pressure XPS

Electron spectroscopy has significantly contributed to the understanding of chemical and physical processes that govern the complex interactions between a solid surface and its environment. These processes play crucial roles in phenomena such as heterogeneous catalysis, corrosion, and thin film growth. Given that surfaces are heavily influenced by their surroundings, it is essential to study them in situ, while exposed to realistic reaction conditions, or operando, when producing reaction products under realistic conditions. X-ray photoelectron spectroscopy (XPS) is a powerful surface science technique that enables the investigation of modifications in the chemical environment of a sample surface and its electronic states, owing to its exceptional surface sensitivity. However, the requirement for ultrahigh vacuum (UHV) conditions previously limited the use

of XPS in reactive environments. Ambient pressure XPS (APXPS) with soft X-rays addresses this limitation by enabling surface chemical analysis at pressures up to the millibar range, bridging the gap that restricts conventional XPS to UHV. This allows for in situ and operando investigations of material interfaces under more realistic conditions, which is a critical advancement in material research, gaining increasing popularity across various fields. APXPS is crucial for studying dynamic processes in catalysis, environmental science, and energy materials, where reactions typically occur at or near ambient pressure.

Fourth-generation synchrotron light sources, characterized by their unprecedented photon flux, provide a key advantage for APXPS, enabling rapid data acquisition with low signal-to-noise ratio and facilitating the study of transient phenomena. This capability is essential for tracking surface chemical processes in real time.

Due to the scattering of the photoelectrons in a gas environment at millibar pressures, APXPS is intrinsically a photon-hungry technique. Although pioneering work on gases and liquids performed by Kai and Hans Siegbahn date back to the 1970s [1], it was only at the turn of the century that APXPS instruments were developed, thanks to the high flux of the third and then, particularly, fourth generation of synchrotron radiation light sources. At the same time, the development of differentially pumped electron energy analyzers (EEA) with higher transmission also played a crucial role [2]. The technical development of APXPS was driven forward in particular by groups at BESSY II (Berlin, Germany) and ALS (Berkeley, US) [3,4]. Today, APXPS is a consolidated technique, and instruments are widely available both in synchrotron radiation facilities and in university laboratories [5].

MAX IV Laboratory in Lund is a Swedish national laboratory inaugurated in 2016; it was the first fourth-generation synchrotron light source worldwide [6,7]. The accelerator complex comprises a linear accelerator as well as a 1.5 GeV and a 3 GeV storage ring for electrons. MAX IV offers access to 16 beamlines, soon 17; among them, SPECIES and HIPPIE are dedicated to APXPS and are located on the two rings, respectively. Both beamlines offer a portfolio of experimental setups that allow one to explore different aspects of scientific research dedicated to the investigation of solid–gas, solid–liquid, and liquid–gas interfaces in situ and under operando conditions.

In this review, we highlight exemplary APXPS experiments conducted in different environments to study solid–gas and solid–liquid interfaces. APXPS at MAX IV is making a considerable contribution in various scientific fields including catalysis, energy materials, and corrosion, to name a few. As an example in catalysis research, we will discuss experiments on solid–gas interfaces about single-atom catalysts, catalysis in confined space, time-resolved catalysis, and photocatalysis. Remaining in the solid–gas environment, atomic layer deposition (ALD) is another field particularly developed at MAX IV. Also, the ultrahigh brightness of MAX IV ring, joined with in-house developments, make feasible in the soft X-ray regime, experiments accessing liquid layers and their interfaces with solids, opening up to completely new research fields with respect to traditional surface science, such as corrosion and battery research, with specifically designed electrochemical cells suitable for APXPS measurements [8].

The SPECIES & HIPPIE beamlines

SPECIES is a soft X-ray beamline on the 1.5 GeV ring. It covers a wide photon energy range of 30–1500 eV with variable polarization and high photon flux in the low photon energy range [9]. The optics provide a moderately focused beam (~100 µm). The beamline covers an energy resolution typical for soft X-ray beamlines of resolving power values of the order of 5000–10000 over nearly the entire photon energy range. The main instrument of the APXPS endstation is the Phoibos 150 NAP electron energy analyzer from SPECS GmbH, equipped with a delay line detector (DLD). The APXPS endstation is used to study solid–gas interfaces and has sample environments allowing for experiments in the fields of, among others, catalysis research, material characterization, and thin film deposition, utilizing dedicated cells.

HIPPIE, on the 3 GeV ring, covers a wider photon energy range than SPECIES (250 to 2500 eV), also with variable polarization [10]. It has two branches, each with its own permanently installed endstation dedicated to APXPS, that is, one for solid–gas experiments (SGE) and one primarily, but not limited to, for solid–liquid studies (SLE). The optics provide a spot size of 65 µm × 25 µm on the SGE and 60 µm × 50 µm on the SLE and a resolving power up to 35000. The SGE branch features a Scienta Omicron HiPP-3 analyzer with microchannel plate detector and camera up to 120 Hz frame rate (soon to be upgraded to a DLD). The SLE branch employs a SPECS Phoibos-NAP spectrometer equipped with a 2D DLD. Both the SGE endstation at HIPPIE and the APXPS endstation at SPECIES, use the so-called “cell in cell” method, whereby a small ambient pressure cell is inserted into the UHV chamber where it makes a seal-tight connection to the lenses of the electron analyzer, from which is separated via a small aperture cone [11]. This allows for the creation of the ambient pressure environment inside the cell while still maintaining UHV conditions on the outside, which enables the connection to the synchrotron beamline. The synchrotron radiation enters the cell through a

thin membrane, which can hold the necessary pressure in the millibar range inside the cell. The endstations are also equipped with complementary instruments (e.g., mass spectrometers) mainly allowing researchers to probe gas phase products and connect this information easily to the XPS data acquired from the surface. Common in-vacuum surface preparation tools (e.g., Ar ion sputtering and sample annealing) are additionally available, which allows for preparing sample surfaces before commencing the APXPS experiments. Both beamlines have other external light sources (e.g., to provide solar radiation or UV light) available to all users in order to perform photocatalysis experiments. HIPPIE offers also a catalytic reactor to expose samples up to 1 bar gas atmosphere and 900 °C connected to the main UHV system. In addition, a polarization modulation infrared reflection absorption spectroscope (PM-IRRAS) is also available, enabling simultaneous APXPS and IRRAS measurements.

The SLE at HIPPIE is designed as a large back-filled vacuum chamber with two manipulators and base pressure in the 10^{-6} mbar range. Access to the chamber is realized via a large front door. This offers a versatile and flexible system where various custom setups and sample environments can be installed. The primary setup used at the SLE is an electrochemical (EC) cell; a liquid microjet is also used to a smaller extent. In the EC setup, a three-electrode setup is immersed and retracted from a beaker of liquid electrolyte, forming a thin, electrochemically active meniscus on the working electrode that can be probed using APXPS or XAS, see Figure 1. Electrochemistry is controlled via a Biologic SP200 potentiostat.

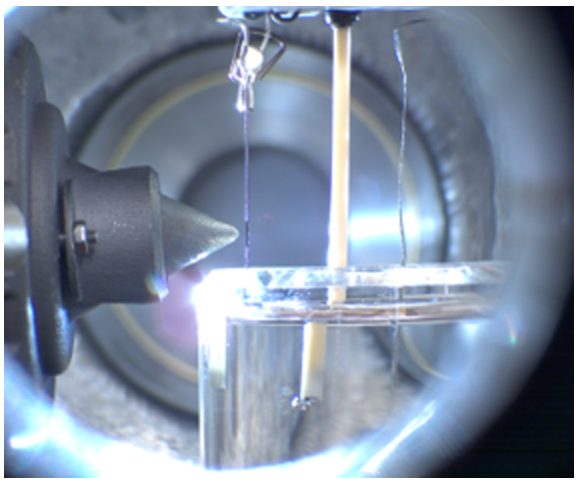

Figure 1: Picture of the electrochemical APXPS setup at HIPPIE. The EEA on the left is facing the working electrode. The three-electrode cell is then further composed of reference and counter electrodes. The electrodes are immersed in a beaker with a liquid electrolyte. The system is at equilibrium at the vapor pressure of the liquid. The picture was taken by Robert Temperton. This content is not subject to CC BY 4.0.

Catalysis

Heterogeneous catalysis is one of the most prominent and long-standing applications of APXPS and one of the primary drivers of its development [4,5,12]. APXPS extends the tradition of UHV-XPS surface science by enabling direct, operando observation of catalytic surfaces under reaction conditions. This allows for full life cycle characterization of catalysts, offering insights into surface structure, composition, and dynamic behavior during catalysis. Thanks to its intrinsic surface sensitivity, APXPS is uniquely positioned to probe the active sites on catalytic materials. These surface sites, often structurally undercoordinated and electronically distinct from the bulk material, drive the transformation of reactants into products. While catalysts regenerate at the end of each cycle, their surfaces can be highly sensitive and unstable under ambient conditions, necessitating time- and environment-resolved measurements to capture their true reactive state.

Particularly important is the combination of APXPS with complementary techniques that could simultaneously explore the sample. At HIPPIE, PM-IRRAS can be performed in situ and operando. With IRRAS, vibrational information is available, which greatly complements the electronic information obtained by photoelectron spectroscopy. This combination enables a more complete picture of surface reaction mechanisms. The examples discussed here focus on “model catalysts”, that is, systems where the active phase is well defined and often prepared on single crystals. While studies on industrial catalysts are limited by charging effects (insulating oxide-supported samples) and higher pressure requirements, model systems remain invaluable for fundamental insights.

We now turn to specific case studies from MAX IV’s APXPS beamlines. We will not concentrate on the typical reactions (e.g., CO oxidation, ethylene epoxidation, and methanol oxidation) already deeply reviewed elsewhere [5,12,13]. We will instead discuss a few catalysis niche cases dealing with complex catalytic reactions and instrumentation development which highlight better the use of advanced light sources in probing the structure and dynamics of nanostructured materials and instrumental developments that enable novel investigations of materials under operando conditions. We will therefore discuss scientific examples about single-atom catalysts and progressing to confined catalysis, time-resolved measurements, photocatalysis, and atomic layer deposition.

Single-atom catalysts

Single-atom catalysts (SACs) have emerged as a frontier in (electro)catalysis, combining exceptional catalytic activity with optimal utilization of precious metals such as Rh, Pd, and Pt [14,15]. Their atom-level dispersion maximizes surface expo-

sure and minimizes metal consumption, which is critical for both economic and environmental sustainability. However, their inherently low site density and metastability under reaction conditions present significant challenges for both synthesis and in operando characterization. In particular, photon-hungry techniques like APXPS require the high brilliance provided by fourth-generation synchrotron sources to probe such dilute systems.

From a synthetic perspective, stabilizing isolated metal atoms against agglomeration, especially at elevated temperatures, requires advanced strategies. Accordingly, diverse approaches have been developed to realize stable SACs across a wide range of metals and supports. Among these, site-selective atomic layer deposition [16], supported catalytically active liquid metal solutions (SCALMS) [17,18], and cluster encapsulation via strong metal–support interaction (SMSI) [19] have shown promise. While these methods have been successfully characterized using APXPS, the systems themselves were not investigated under catalytic turnover conditions and are therefore not discussed further here.

Instead, we focus on a study by Vesselli and co-workers that directly addresses catalytic activity in a biomimetic SAC system [20,21]. In their work, a cobalt single-atom biomimetic model catalyst is based on a self-assembled monolayer of Co-porphyrins grown on an almost free-standing graphene sheet. This well-defined platform mimics the structure of metal–nitrogen–carbon catalysts used in oxygen reduction reactions (ORRs).

Using a combination of results obtained from APXPS at HIPPIE and pump–probe infrared–visible sum-frequency generation (SFG) in a dedicated setup at the Department of Physics of the University of Trieste [22], and supported by DFT, the authors demonstrated that the Co-porphyrin SAC stabilizes a hydroperoxyl–water (O_2H-H_2O) cluster in O_2+H_2O atmosphere at room temperature [21]. This is considered the fundamental reaction intermediate in the ORR. In particular, the configuration of the O_2H radical could drive the selectivity for $2e^-$ vs $4e^-$ pathway ORR. The APXPS measurements revealed distinct changes in the Co 2p and O 1s core levels consistent with the formation of this reactive intermediate. Figure 2 shows spectroscopic evidence for the O_2H–H_2O/Co complex, highlighting the power of operando APXPS to capture chemically relevant intermediates on SACs under realistic reaction environments. This example highlights the unique ability of APXPS, particularly when combined with complementary vibrational spectroscopies, to provide molecular-level insight into active sites and mechanisms in single-atom catalysis.

2D confined catalysis

Confined catalysis is an emerging field that investigates how spatial constraints can influence the efficiency, selectivity, and performance of catalytic reactions. This approach leverages the principles of confinement within various nanostructures (pores, cavities, or interlayer regions of materials) to create unique reaction environments that can significantly alter the behavior of catalytic processes. The confined environment can affect how reactants approach each other, stabilize reaction intermediates, and influence transition states, often lowering activation energies and altering reaction pathways [23-25].

A particularly interesting case is “undercover catalysis”, where the void space between a 2D material and a catalytic surface is exploited. Materials such as graphene [26-28], hexagonal boron nitride (hBN) [29], and transition metal dichalcogenides [30] are widely studied for this purpose. Boix, Knudsen and collaborators combined APXPS with gas pulsing with varied composition to repeatedly form and remove undercover reaction products. Specifically, they studied CO and H_2 oxidation below oxygen-intercalated graphene flakes partially covering an Ir(111) surface, as illustrated in Figure 3 [28].

Although the reaction products (H_2O and CO_2) were below the APXPS detection limit, the C 1s signal proved sensitive enough to monitor the dynamics of undercover catalysis during gas pulsing (see Figure 4). Their results revealed that H_2 promotes the formation of a dense OH–H_2O phase below the graphene. In contrast, CO alone showed minimal intercalation and instead scavenged oxygen. When CO and H_2 were pulsed together, hydrogen modified the undercover chemistry: the formation of the OH-H_2O phase lifts the graphene flake and allows the CO to intercalate and then oxidize.

Rather than studying the reaction below 2D materials, Scardamaglia et al. investigated graphene and hBN as protective layers for copper metal surfaces in a reactive environment [31]. In operando experiments with a linear temperature ramp in 2 mbar O_2, bare copper rapidly oxidized to Cu_2O at room temperature and further to CuO at ~200 °C. However, with hBN or graphene layers, oxidation was significantly delayed. Both 2D materials retard the oxidation of Cu by more than 120 °C, but with different kinetics. The behavior of hBN/Cu is relatively simple: the hot copper surface is well shielded from oxygen, and even if some oxygen penetrates through wrinkles or boundary areas, the insulating nature of hBN prevents rapid copper oxidation. This protection remains effective until the coating layer is fully and quickly etched away (up to 300 °C). Beyond this point, the exposed hot copper surface undergoes rapid oxidation, transforming from metallic Cu to Cu_2O, and, eventually, to CuO within a small temperature range. In contrast, with

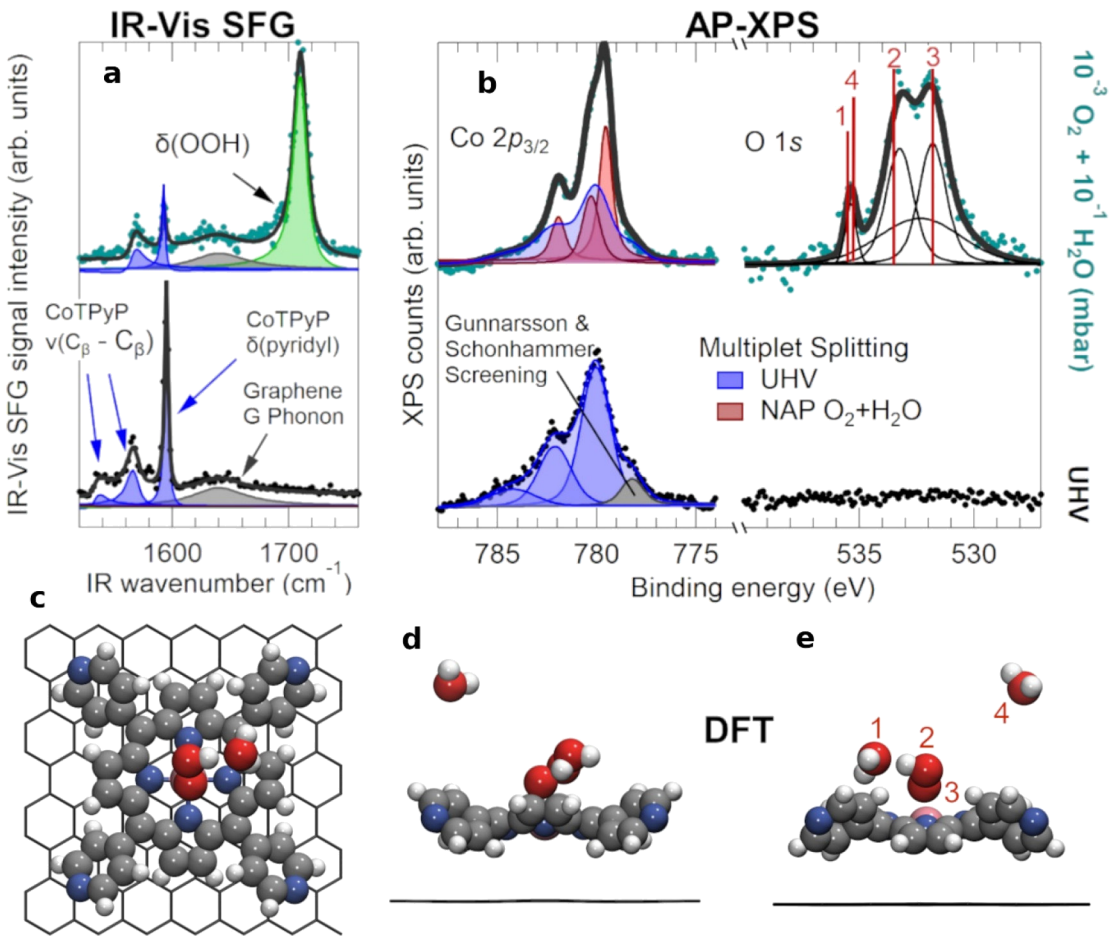

Figure 2: Spectroscopic and geometric characterization of the hydroperoxyl–water complex. (a) IR–vis SFG spectra of the pristine CoTPyP/GR layer in UHV (bottom) and in 10^{-3} mbar O_2 +10^{-1} mbar H_2O at room temperature (top); experimental data (markers) are reported together with the best fit (continuous lines) and deconvolution envelopes (filled profiles). (b) NAP-XPS spectra of the Co $2p_{3/2}$ (left, *hv* = 910 eV) and O 1s (right, *hv* = 660 eV) core levels corresponding to the same conditions as in (a); red vertical lines indicate the binding energies obtained for the optimized O_2H–H_2O complex on CoTPyP/GR from ab initio DFT calculations for different O 1s core levels, as labeled in (e): 1 – physisorbed/ wetting water, 2 – OOH, 3 – OOH, 4 – gas phase water. (c) Top view of the DFT-optimized model of the O_2H–H_2O/Co/TPyP/GR system. (d,e) Side views of the same system with an additional water molecule in the gas phase from two different points of view, to show the order-2 rotational symmetry of the CoTPyP, with a saddle shape macrocycle and peripheral pyridyl groups alternatively rotated by +39° and –39° with respect to GR. Figure 2 was reproduced from [21] (© 2022 F. Armillotta, et al., published by American Chemical Society, distributed under the terms of the Creative Commons Attribution 4.0 International License, https://creativecommons.org/licenses/by/4.0).

graphene/Cu, although the protective layer degrades at a slightly higher temperature than hBN, oxygen begins to intercalate beneath graphene at around 220 °C, initiating a slower, undercover oxidation of copper to Cu_2O. This process is a galvanic reaction facilitated by graphene's high conductivity, enabling electron transfer from copper to oxygen atoms. However, the graphene/Cu_2O hybrid structure slows further oxidation to CuO due to limited oxygen availability, as the reaction occurs beneath the surface. This is significant because it offers a method to stabilize the Cu_2O phase at high temperatures, preventing its conversion to CuO. As the temperature increases further, CuO formation and graphene etching occur simultaneously. This is summarized in Figure 5 where the 2D intensity plot vs temperature of O 1s and N 1s or C 1s, for hBN or graphene, respectively, are reported.

Time-resolved catalysis

Catalysts are inherently dynamic systems. The optimal catalyst should have a nanostructure that enhances activation kinetics, contain active sites that are dynamically stabilized, and be in a state of deviation from chemical equilibrium under reaction conditions. Therefore, fully describing a functional catalyst requires addressing a range of dynamics across multiple temporal scales. To examine such a dynamic at the atomic level, we must ensure a well-controlled environment that is relevant to catalytic conditions. This includes enhancing the temporal reso-

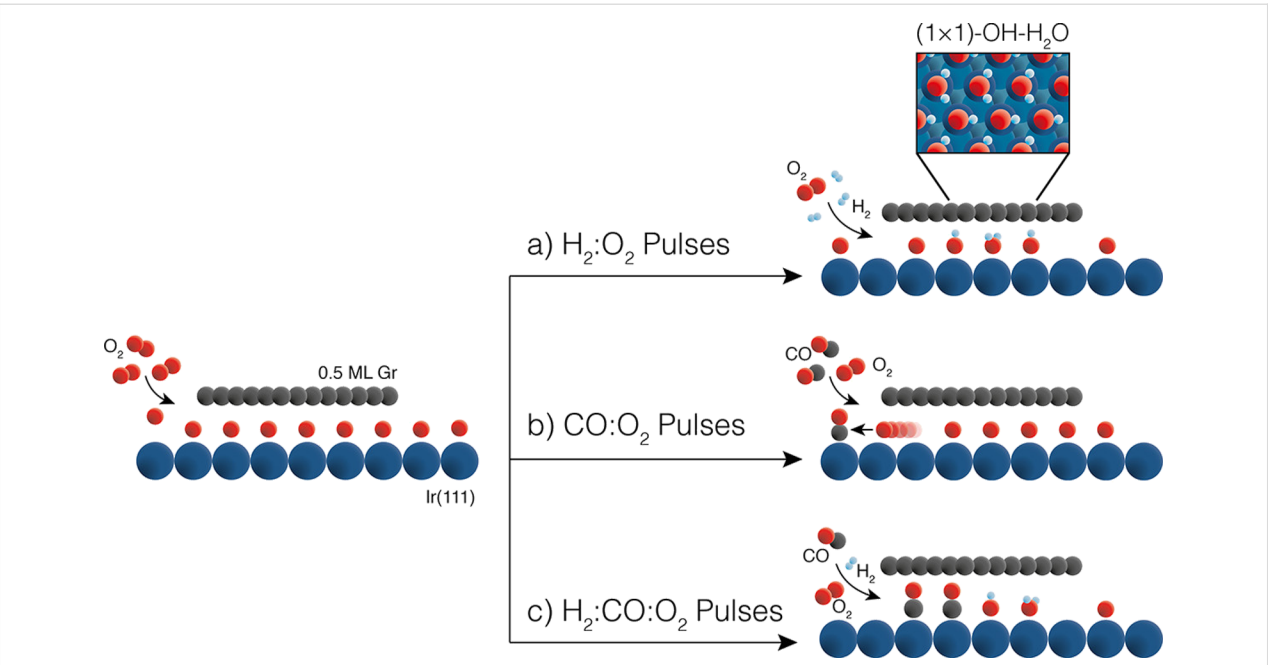

Figure 3: Schematic representation of the three undercover reactions studied. Starting from oxygen-intercalated Gr/Ir(111) (left), we expose the system to 50 s pulses of (a) a hydrogen-rich mixture resulting in the formation of OH–H_2O under graphene (inset: ball model of the (1 × 1)- OH–H_2O undercover structure), (b) a CO-rich mixture resulting in the removal of intercalated oxygen, and (c) a combined H_2:CO-rich mixture resulting in the hydrogen-assisted intercalation of CO. Figure 3 was reproduced from [28] (© 2022 V. Boix et al., published by American Chemical Society, distributed under the terms of the Creative Commons Attribution 4.0 International License, https://creativecommons.org/licenses/by/4.0).

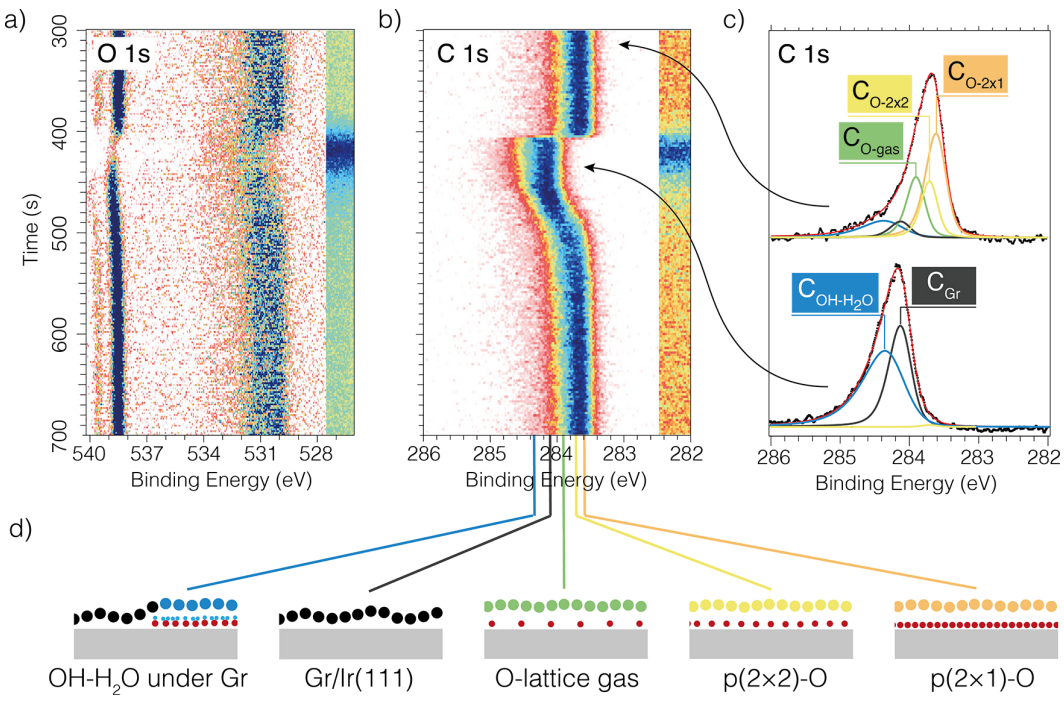

Figure 4: Hydrogen oxidation reaction under ~0.5 ML Gr on Ir(111) at 370 K and 1 mbar total pressure. (a, b) 2D image plots of (a) O 1s and (b) C 1s during one hydrogen-rich pulse (50 s of a hydrogen-rich mixture H_2/O_2 9:1 sccm). (c) Average spectrum of 10 individual C 1s spectra recorded before and during the pulse. (d) Schematic representation of the five Gr/Ir(111) intercalation structures that define the five components used to fit the data. The position of each C 1s component is indicated with a line to the binding energy axis in panel (b). See main text for exact values. Figure 4 was reproduced from [28] (© 2022 V. Boix et al., published by American Chemical Society, distributed under the terms of the Creative Commons Attribution 4.0 International License, https://creativecommons.org/licenses/by/4.0).

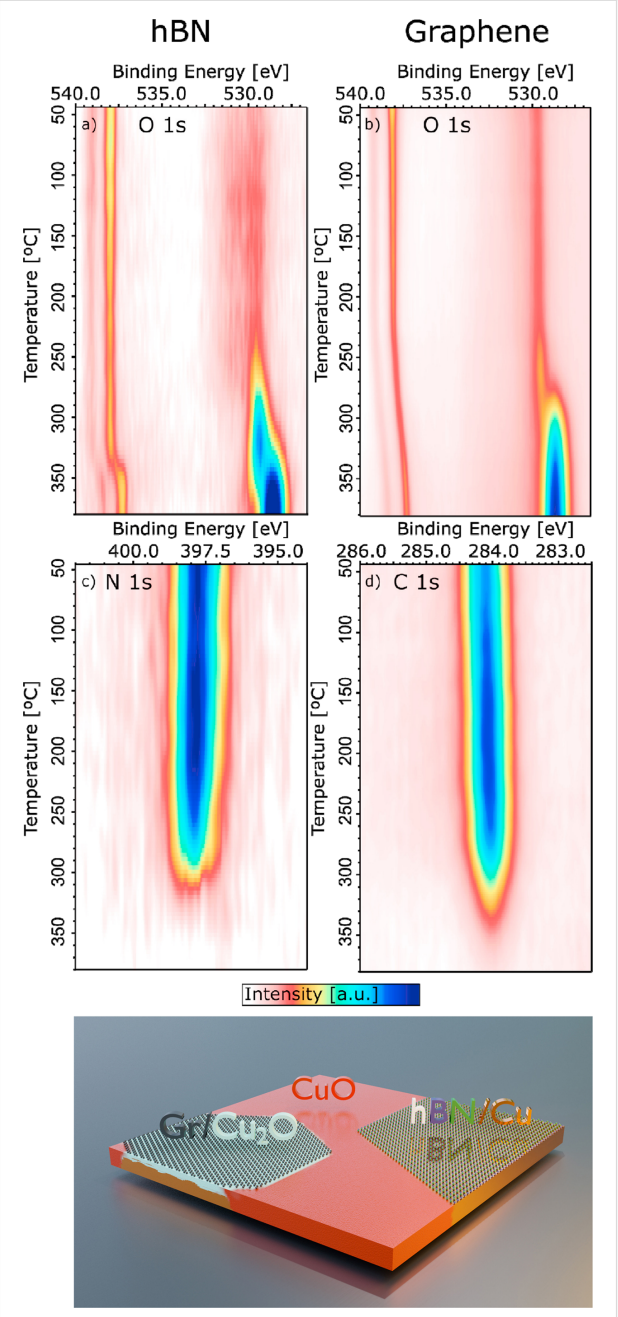

Figure 5: (Top) hBN and graphene protected Cu foils. (a, b) O 1s and (c, d) N 1s and C 1s 2D intensity plots as a function of temperature for hBN/Cu (a, c) and graphene/Cu (b, d). The spectra are recorded in 2 mbar O_2, with a photon energy of 1070 eV. The intensity is normalized to the background at lower binding energy with respect to the peak. The fingerprint of Cu_2O is the O 1s peak at about 530 eV, while CuO is at 529 eV. (Bottom) Sketch of the surface at 250 °C. Figure 5 was reproduced from [31] (© 2021 M. Scardamaglia et al., published by American Chemical Society, distributed under the terms of the Creative Commons Attribution 4.0 International License, https://creativecommons.org/licenses/by/4.0).

lution of APXPS measurements. Ultimately, the goal is to understand the heterogeneity of a catalytic system with greater specificity regarding site, time, chemistry, and environment.

Recent years have seen growing interest in time-resolved APXPS studies, particularly those enabled by DLDs [32-37]. These detectors offer microsecond-scale time resolution, unlocking the ability to track fast chemical transformations. In this section, we focus on ultrafast measurements that are possible with the new DLDs at the HIPPIE and the SPECIES beamlines. These DLDs are built like a very tight check pattern of electrical wires. Every impinging electron sends an electrical signal along two orthogonal wires and its location is determined by the readout electronics based on the time of flight. This architecture allows for high-speed acquisition (only limited by the speed of the readout electronics), either as continuous time-resolved data or in pump–probe mode. In continuous mode, spectra are recorded in sequence without scanning the analyzer's retardation voltage. To observe quick, periodic changes in the APXP spectra, we apply fast gas pulses to the catalyst surface [38-40]. During continuous acquisition, APXP spectra are measured one after the other with a high time resolution and for many gas pulses. This enables ultrafast capture but results in the measured signal being convoluted with the analyzer's transmission function.

During pump–probe acquisition, a synchronization signal triggers spectral acquisition with each external perturbation (e.g., gas pulse). This makes it possible to assign a time difference between gas pulse and spectrum acquisition to every measurement. Thus, scanning of the retardation voltage becomes possible, that is, the analyzer transmission is accounted for. Since event averaging over many gas pulses is done in the analyzer, the measurement can be run very fast. A significant difference in the direct analysis can immediately be observed when comparing the data measured with the two acquisition techniques in Figure 6. The spectroscopic changes induced by the modulation can often be directly seen in pump–probe data, while post-processing is necessary for continuous measurements to obtain similar information. Examples of the two different measurement schemes are presented below. The data are taken from two experiments performed at the SLE of the HIPPIE beamline, while exposing a catalyst to gas pulses.

Ammonia oxidation (microsecond time-resolution, pump–probe mode): This experiment used 150 µs wide 170 V voltage pulses with a repetition rate of 5 Hz to control O_2 gas injection (piezoelectric valve) in a background of NH_3 (15 sccm) and O_2 (10 sccm) achieving 3.8 mbar (the local pressure at the sample surface is much higher) total pressure at 460 °C on a PtRh(100) catalyst. Spectra were acquired at 200 kHz (5 µs time resolution), averaging over 720,000 pulses. One measured spectrum is sorted into the 2D image shown in Figure 7 by using the time difference between the pump signal

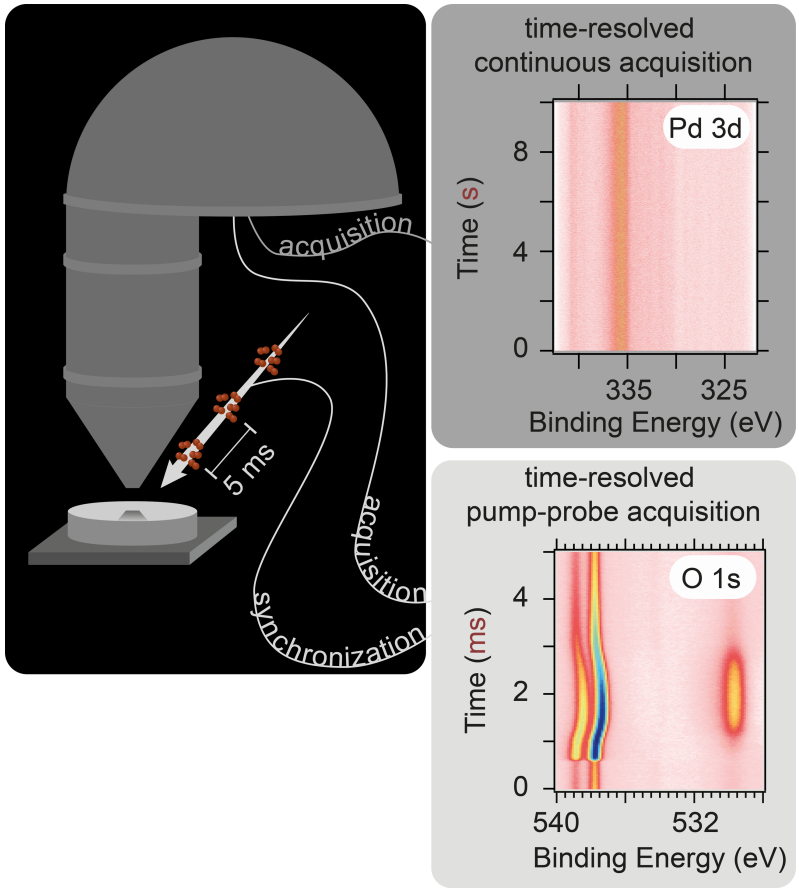

Figure 6: Sketch of the two different measurement mechanisms possible at the DLD at HIPPIE.

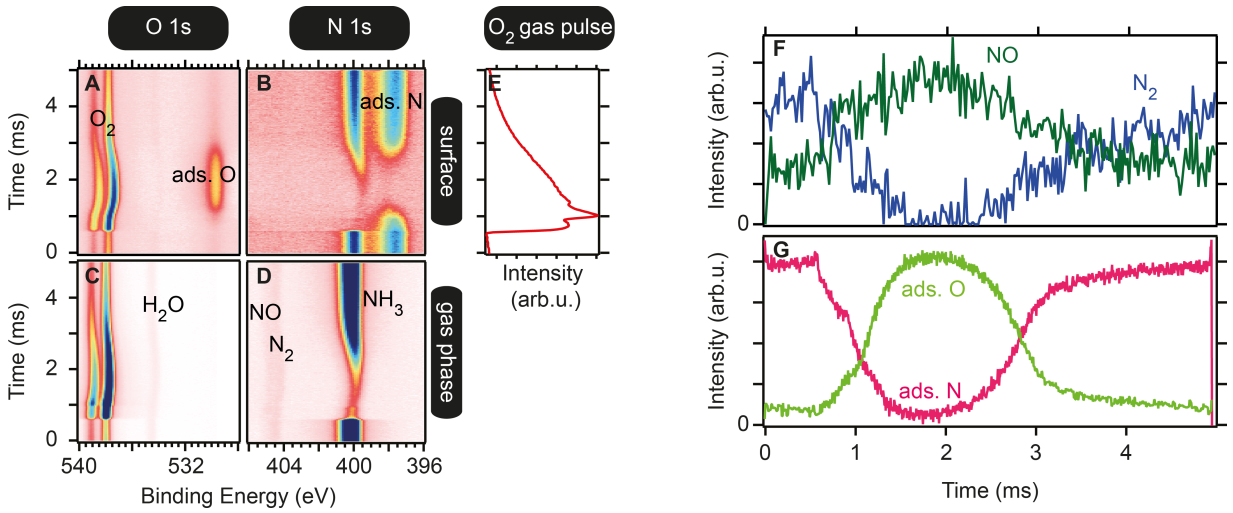

Figure 7: (A–D) O 1s and N 1s core level spectra in surface- and gas phase-sensitive positions measured in pump–probe mode during experiment 1. (E) Profile of the injected gas pulse over time. (F) Time evolution of the nitrogen-containing products of NH_3 oxidation. (G) Time evolution of the surface adsorbates.

and the probing signal. The 2D image averages over 720,000 gas pulses.

Using the O 1s and N 1s core levels (Figure 7A–D), it is possible to follow both the surface composition and the catalyst selectivity by observing the gas phase (with a slightly retracted sample). The time evolution of NO and N_2 taken from curve fits of the N 1s gas phase spectra (Figure 7D) is shown in (Figure 7F) while the evolution of the dominant surface adsorbate taken from curve fits in the O 1s (Figure 7A) and N 1s (Figure 7B) spectra is shown in Panel (Figure 7G). The main conclusion here is that the selectivity of the catalyst towards NO formation increases, similar to the increase in coverage of the surface with oxygen. Likewise, an increasing coverage of adsorbed nitrogen leads to an increased selectivity towards N_2.

Previously, Resta et al. [41] could correlate the production of NO with the formation of surface RhO_2 for four different NH_3-to-O_2 ratios. In the presented example, studying the reaction in a time-resolved manner, it was possible to study a continuous range of different reactant ratios and their effect on the product composition within one experiment, which makes them inherently comparable. Thus, this pump–probe acquisition mode enables structure–activity correlations with high time resolution.

Ethylene oxidation (millisecond time-resolution, continuous mode): In a second experiment, 200 µs pulses of C_2H_4 were introduced into a 10 sccm O_2 flow over a polycrystalline Pd catalyst at 365 °C with a repetition rate of 10 Hz and a total pressure of 3.7×10^{-3} mbar (the local pressure at the sample surface is much higher). The resulting APXP spectra shown in Figure 8 were measured continuously in time-resolved snapshot mode with an acquisition frequency of 1 kHz (1 ms time resolution). One measured spectrum covers approximately 100 pulses.

While the raw data showed no visible modulation (Figure 8A), Fourier analysis of the spectra as described in detail elsewhere [42,43] revealed an oscillatory response as highlighted by the black arrows in (Figure 8B) at the driving frequency of the gas pulses and higher harmonics. If the magnitude and phase of the Fourier transform at the fundamental frequency (i.e., 10 Hz) are extracted and plotted (Figure 8C), a clear footprint of oscillating components can be seen in the blue phase signal at 335–337 eV. Magnification of the oscillation magnitude even reveals three different oscillating components within the broad Pd $3d_{5/2}$ peak seen in the time average in (Figure 8C). Here, the phase signal shows that the middle component (2) oscillates in antiphase with the other two (1,3); when 2 increases, 1 and 3 decrease and vice versa. Thus, even though the oscillating signal picked up during the measurement is small in comparison to the time average of the spectra, Fourier analysis can reveal the periodic spectroscopic answer.

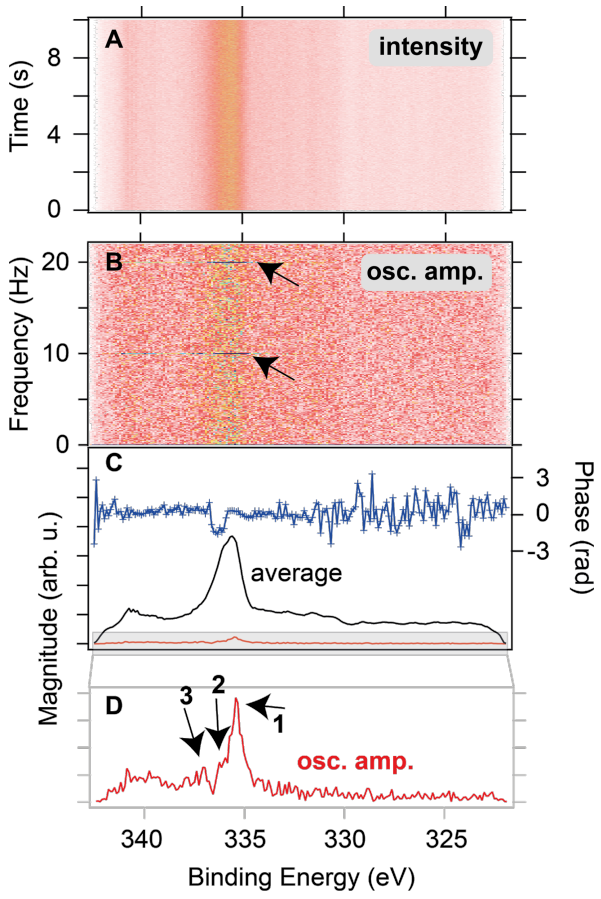

Figure 8: (A) Pd 3d core level spectra measured in continuous mode during experiment 2 in surface sensitive position. (B) Magnitude of the Fourier transform as a function of frequency and binding energy. (C) Oscillation amplitude and phase at the fundamental frequency (10 Hz), together with the time average of the spectra. (D) Magnified oscillation amplitude.

Comparing continuous and pump–probe acquisition: Pump–probe mode offers higher sensitivity to transient signals and smaller datasets but requires precise periodic modulation. It is ideal for fast, repeatable processes. Continuous acquisition, in contrast, is suitable for systems with self-sustained or aperiodic oscillations. Fourier analysis allows for selective extraction of oscillating signals, removing static background contributions. Both modes have proven indispensable in revealing the real-time dynamics of catalytic reactions, and they have only become possible with the recent advances in detector development. Their availability at HIPPIE and SPECIES is a major asset for APXPS studies.

Photocatalysis

Utilizing solar energy to drive chemical reactions is a central focus of sustainable energy research. Replacing fossil fuels with clean and renewable energy sources is one of the most important challenges for modern human civilization. Reactions such as water splitting, CO_2 reduction, and pollutant degradation rely on photocatalysts that absorb light, generate electron–hole pairs, and drive redox reactions at interfaces. For the rational and methodical design of a more sophisticated photocatalyst, it is essential to combine the photocatalyst's performance with mechanistic knowledge under operando reaction conditions.

APXPS is uniquely suited to investigate such systems. Its surface sensitivity enables the detection of charge transfer processes, reaction intermediates, and active sites under operando conditions. Additionally, the kinetics of charge transfer and the role of specific chemical species or components functioning as charge donors or acceptors during photocatalytic reactions can be clarified using APXPS. At MAX IV, external light sources (e.g., UV lamps or solar simulators) are coupled to the HIPPIE and SPECIES endstations to allow for photoirradiation in both UHV and ambient pressure environments (Figure 9) [44].

The most environmentally friendly alternative to fossil fuels is green hydrogen; however, producing it at a reasonable price remains challenging. A prominent application is photocatalytic water splitting for green hydrogen production. Urpelainen and colleagues clarified the mechanisms of photocatalytic hydrogen evolution reaction (HER) in a new prospective model system, the Ni@NiO/$NiCO_3$ photocatalyst, under dark and illuminated conditions at 1 mbar of H_2O [45]. Figure 10a illustrates how the complex Ni 2p spectrum is caused by multiplet splitting, shake-up, and plasmon loss structures. When the catalyst surface is dark, the Ni $2p_{3/2}$ structure can be well matched with three main components assigned to Ni^0, NiO, and $NiCO_3$. Upon illumination, the Ni^0 peak vanishes, and the main Ni 2p peak broadens due to the emergence of an additional peak at 857.4 eV attributed to NiOOH. This indicates that photoexcitation triggers oxidation and structural changes, consistent with plasmon-driven electron excitation at the Ni/NiO interface. The authors propose a mechanism where photoexcited holes migrate to NiO and are trapped, facilitating water oxidation via an intermediate NiOOH species (Figure 10b).

APXPS thereby provides mechanistic insight into photoinduced surface chemistry, enabling rational catalyst design. Similar approaches can be extended to CO_2 reduction, pollutant remediation, and other light-driven processes.

Atomic layer deposition

Atomic layer deposition (ALD) is a critical thin-film technology widely used in semiconductors, nanoelectronics, energy storage, catalysis, and advanced coatings. It enables atomically precise control over film thickness and composition, even on topologically complex surfaces, making it essential for the fabrication of next-generation devices [46-48]. In the semiconductor industry, ALD enables the creation of nanoscale transistors and high-*k* dielectric materials, essential for shrinking transistor dimensions and enhancing performance in integrated circuits. Its precision, scalability, and ability to produce conformal films on intricate surfaces make ALD a cornerstone in the pursuit of miniaturization and enhanced performance in technology.

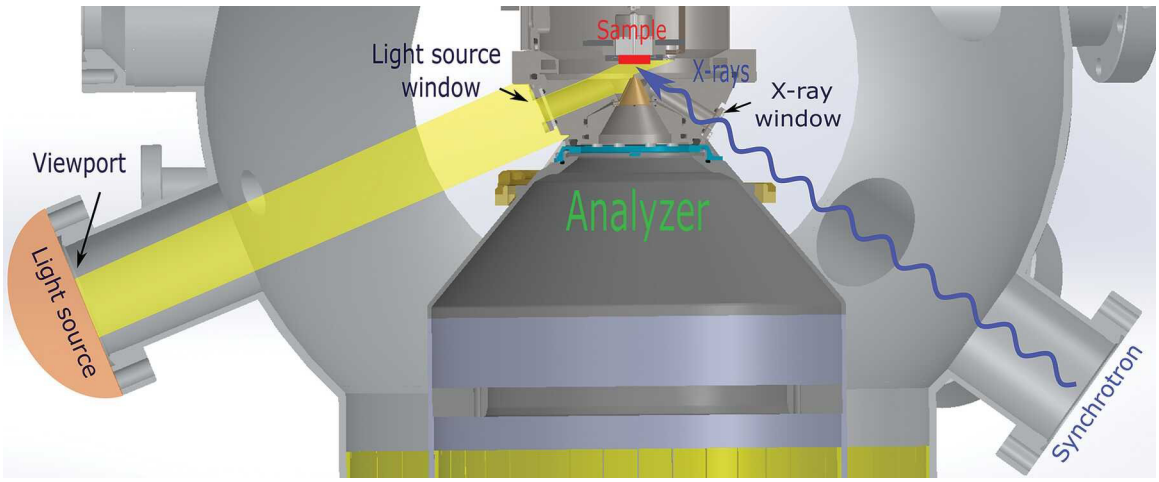

Figure 9: Schematic layout showing the alignment between external light sources, beamline, and analyzer nozzle in the analysis chamber with AP cell at the SPECIES beamline at MAX IV Laboratory. Figure 9 was reproduced from [44] (© 2023 A. Klyushin et al., published by the International Union of Crystallography distributed under the terms of the Creative Commons Attribution 4.0 International License, https://creativecommons.org/licenses/by/4.0).

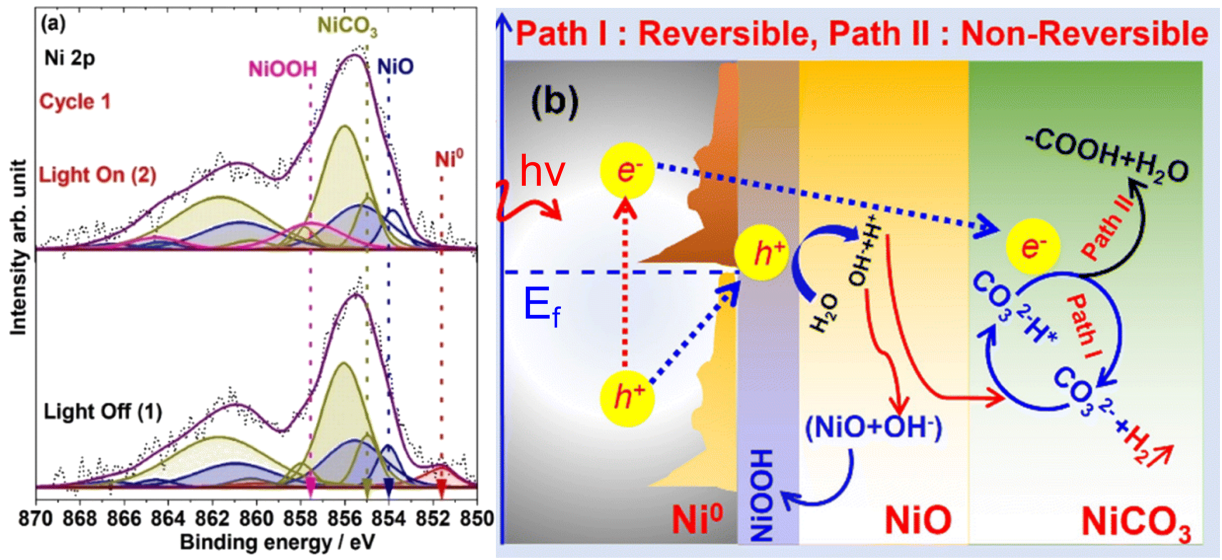

Figure 10: (a) Ni 2p XP spectra recorded at 1 mbar H_2O pressure under dark (bottom spectra) and light illumination (top spectra) conditions. (b) Photocatalytic HER mechanism under light illumination 1 mbar H_2O pressure. Figure 10 was reproduced from [45] ("Solar light driven atomic and electronic transformations in a plasmonic Ni@NiO/NiCO3 photocatalyst revealed by ambient pressure X-ray photoelectron spectroscopy", © 2024 M. K. Ghosalya et al., published by The Royal Society of Chemistry, distributed under the terms of the Creative Commons Attribution 3.0 Unported Licence, https://creativecommons.org/licenses/by/3.0).

ALD achieves such high levels of growth control by a well-separated alternating exposure of a surface to precursors and co-reactants. Each reaction with the surface should be saturated and self-limiting, thus allowing the deposition of one monolayer to progress in a highly conformal layer-by-layer way, even on nanostructured materials of high aspect ratios. Traditional insights into ALD surface chemistry have come from ex situ or in vacuo XPS, often complemented by other surface characterization tools, used to characterize the resulting film [49-51], as well as to investigate chemical mechanisms cycle-to-cycle [51,52]; the latter procedure is often termed in situ XPS. However, such approaches are blind to the time-dependent dynamics that govern film nucleation and early growth. Operando APXPS overcomes this limitation, enabling direct observation of surface reactions cycle-by-cycle in real time [53].

ALD typically operates in the 10^{-3} to 1 mbar pressure range, ideally matched to the working range of APXPS. Time-resolved APXPS has proven especially powerful for studying the initial ALD cycles, where the chemical interactions at the surface are most critical [54-60]. At MAX IV, the SPECIES beamline has led the development of ALD studies using APXPS. A dedicated reaction cell was designed to replicate commercial ALD conditions, including independent pulsing of precursor gases, laminar flow across the sample, and substrate heating. The setup allows for independent control of precursor and co-reactant exposure and supports a variety of chemistries [60].

ALD is a key technology for the future development of smaller and more power-efficient devices. One step in this development is the replacement of silicon, which cannot reach the development goals set by international technological roadmaps [61]. A potential replacement for silicon oxide is a high-*k* oxide material such as HfO_2, which allows for the creation of much smaller gate sizes. Another suggested change is to substitute the silicon channels with a III–V semiconductor material such as InAs, which, among other properties, has a narrower band gap [62]. However, one challenge to overcome with the InAs/HfO_2 material is to obtain a clean interface between the materials, which is critical for the proper function of the potential devices. In situ and operando APXPS has been utilized in many works to study the deposition of HfO_2 on InAs to elucidate the chemical reactions that occur as those layers are grown in order to better understand how to create sharp interfaces between the materials [55,57,58,63].

In one study by D'Acunto et al., the surface composition and thickness of the initial growth of HfO_2 on InAs was investigated using tetrakis(dimethylamido)hafnium(IV) (TDMAHf) as the hafnium precursor [63]. Four InAs samples with varying native (samples A, B, and C) or thermal oxide (sample G) layers were exposed to TDMAHf at ~200 °C under ~10^{-3} mbar pressure. Results showed that TDMAHf interacts with the surface oxide to produce HfO_2 already in the first half-cycle, a "self-cleaning" effect that removes native oxides from InAs and transfers oxygen to Hf. The resulting interface contained an

In–O–Hf layer limited to approximately one monolayer. The second half-cycle is often done using water as the co-reactant and is the principal source of oxygen for the creation of HfO_2 in the later ALD cycles. Figure 11 shows high-resolution photoelectron spectra of As 3d, In 4d, and Hf 4f core levels before and after the first TDMAHf half-cycle on the four samples. The oxide peaks of As and In disappear for all the thermal oxide (samples A–C), and HfO_x peaks emerge consistently across samples with differing initial oxide thicknesses. The only exception was the native oxide sample (G); it showed stronger Hf 4f intensity, but still the formed HfO_x thickness was estimated to be limited to one monolayer of approximately 5.6 Å.

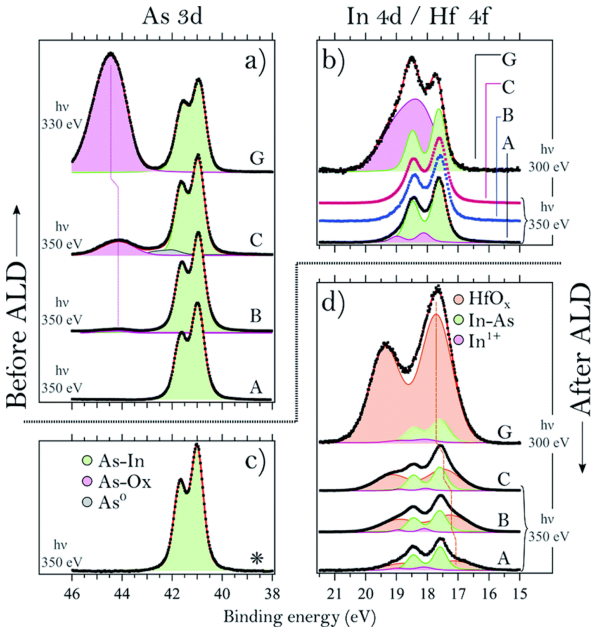

Figure 11: Sample A was initially cleaned by bombarding it with elemental hydrogen, thus removing all of the oxide components. Samples B and C were characterized to have 0.05 L, and 6.0 L of O_2 exposure, respectively; sample G was treated with a water bath and is referred to as having a native oxide. (a) As 3d core level spectra of four different InAs samples with varying As oxide thickness measured before TDMAHf deposition. (b) In 3d spectra of the same samples showing the In oxide. (c) As 3d spectrum of sample C after the first TDMAHf half-cycle. (d) In 4d and Hf 4f spectra (which overlap in energy) acquired after the first TDMAHf half-cycle. Figure 11 was reproduced from [63] ("Oxygen relocation during HfO_2 ALD on InAs ", © 2022 G. D'Acunto et al., published by The Royal Society of Chemistry, distributed under the terms of the Creative Commons Attribution 3.0 Unported Licence, https://creativecommons.org/licenses/by/3.0).

Time-resolved APXPS (Figure 12) confirmed that the removal of surface oxides and the formation of HfO_x occur simultaneously during precursor exposure. These results suggest that HfO_2 can form even without an external oxygen source during the first half-cycle, using the available oxygen content on the surface, challenging traditional ligand-exchange descriptions of ALD chemistry.

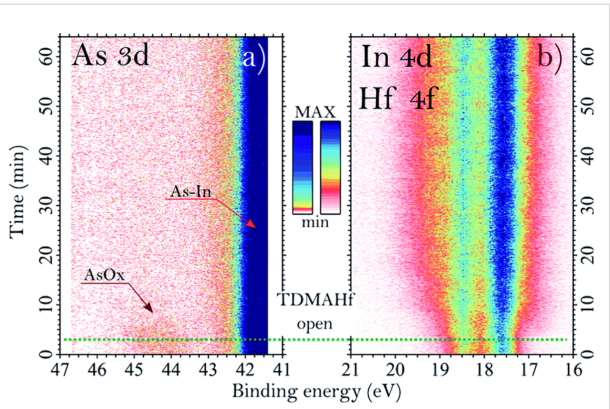

Figure 12: Time-resolved XP spectra acquired during the TDMAHf deposition on InAs showing (a) the As 3d core level and (b) the combined In 4d and Hf 4f region. The green dotted line indicates the time when the TDMAHf valve was opened. Figure 12 was reproduced from [63] ("Oxygen relocation during HfO_2 ALD on InAs ", © 2022 G. D'Acunto et al., published by The Royal Society of Chemistry, distributed under the terms of the Creative Commons Attribution 3.0 Unported Licence, https://creativecommons.org/licenses/by/3.0).

Electrochemical APXPS

Another field where APXPS has opened entirely new experimental possibilities is the study of electrochemical interfaces. Traditional XPS, limited to ultrahigh vacuum environments, has historically been unable to access solid–liquid interfaces, crucial for understanding electrochemical reactions in batteries, fuel cells, corrosion, and electrocatalysis. With the advent of ambient pressure setups and specially designed sample environments, APXPS now allows for direct probing of the chemical and electronic structure at solid–liquid interfaces under realistic conditions. This capability provides unique insight into surface reactions, charge transfer, and interface stability, which are central to the performance and degradation mechanisms of electrochemical systems. Electrochemical interfaces can be studied by APXPS using two primary cell types, namely, membrane-based flow cells and "dip-and-pull" systems. While flow cells are ideal for large currents and gas evolution, dip-and-pull cells, whilst more compromised from an electrochemical cell perspective, are more flexible and compatible with well-defined materials such as single crystals or layered structures [64]. Here, we outline some case-studies that use the dip-and-pull method available at HIPPIE.

The measurements can be performed in situ or operando. In the first, easier, case, the electrochemical reaction is performed with the sample immersed in the electrolyte, then all potentials are dropped, and the sample is pulled for APXPS measurements at the vapor pressure of the electrolyte. This method is used mostly for corrosion studies. In the second case, the potential is held during the XPS analysis, and a thin electrolyte film (meniscus) is maintained at the interface of the working elec-

trode (WE) during measurement. This meniscus must be thin enough to allow photoelectrons to escape, yet thick enough to maintain electrical contact. The meniscus thickness depends on factors such as the wetting properties of the WE, liquid viscosity, surface tension, and pulling speed. This geometry enables true operando studies of solid–liquid interfaces and is particularly relevant for battery research.

Corrosion

Nanometer-thin and spontaneously formed oxide layers, also known as passive films, play a crucial role in the corrosion resistance of many advanced alloys. The current knowledge of the passive films' structure and composition is largely derived from ex situ surface analysis using XPS and scanning tunneling microscopy. However, the findings of UHV-XPS do not accurately represent the genuine passive film/electrolyte interface. APXPS is essential to observe the onset and progression of corrosion and to gain a fundamental understanding of corrosion mechanisms.

Lundgren's and Pan's groups studied in situ, in 17 mbar of water vapor, the electrochemical oxide growth and breakdown on Ni-Cr-Mo industrial alloys in a NaCl solution at different pH values, by following the anodic growth of the oxide film at potentials up to 700 mV vs Ag/AgCl [65,66]. The oxide, natively rich in Cr^{3+}, undergoes a dynamic change and becomes enriched in Mo^{6+}, with a chemical environment similar to that of pure MoO_3. The accumulation of Mo in the passivated oxide film is believed to result from the depletion of Cr and the concurrent enrichment of Mo just beneath the native oxide layer, as reported in Figure 13.

The Ni-Cr-Mo alloy exhibited activity towards the oxygen evolution reaction (OER), which is responsible for initiating passivity breakdown due to the dissolution of Mo in its Mo^{6+} state. This mechanism contrasts with the typical transpassive breakdown behavior observed in Cr-containing alloys, where Cr^{6+} dissolution occurs at high anodic potentials, compromising the integrity of the passive layer. However, in this case, Cr^{6+} dissolution was not observed. Furthermore, at high current densities, the OER contributes to the localized acidification near the alloy's surface, exacerbating metal dissolution. The passive film breakdown has been studied for different acidities of the electrolyte solution, as reported in Figure 14. A parallel study extended these findings to martensitic stainless steel, offering further insights into the chemical evolution of passive films under electrochemical stress [67,68].

Batteries

The dip-and-pull method allows for surface-sensitive XPS measurements of interfaces that are typically hidden inside batteries. Whilst the cell geometry obviously differs dramatically from that of any conventional cell, the approach can provide a valuable model system to study fundamental chemical processes. Experiments can take two forms. First, dip-and-pull can be used to measure a "thick" film (greater than the ~10 nm information depth of XPS) of electrolyte solution. Kallquist et al. have shown that measurements of these thick liquid films can be used to infer charge transfer processes, since the emitted kinetic energy of a photoelectron is dependent on the potential of the probed liquid relative to the grounded working electrode [69,70]. Specifically, the interfaces of gold, copper oxide, and $LiNi_{1/3}Mn_{1/3}Co_{1/3}O_2$ with 1 M $LiClO_4$ in propylene carbonate

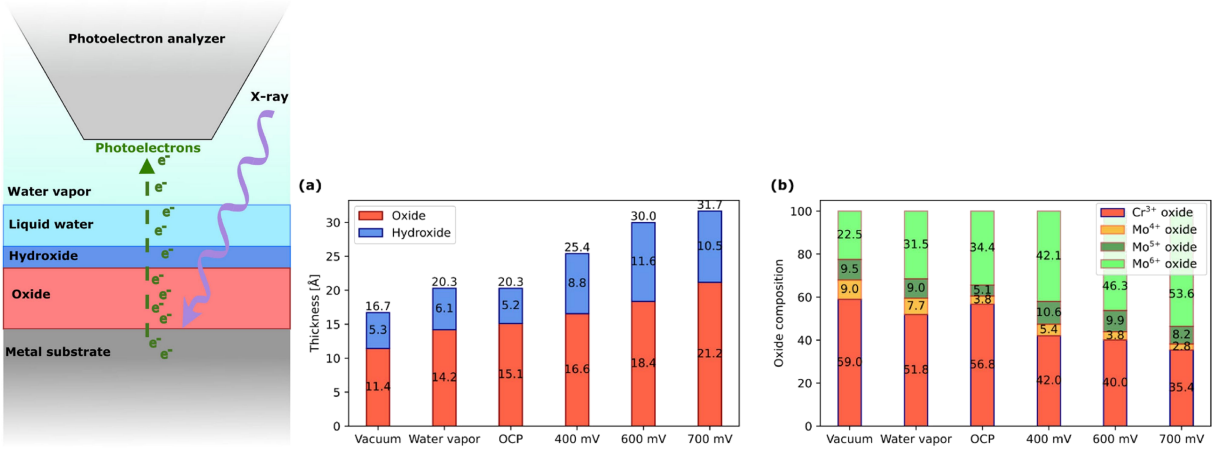

Figure 13: (Left) Layered model of surface region illustrating the metal substrate, oxide layer, hydroxide layer, liquid water layer, and the surrounding water vapor. Quantitative analysis. (a) Oxide and hydroxide thickness for different exposure conditions. (b) Total oxide composition for different exposure conditions. All potentials are reported against Ag/AgCl reference electrode. Figure 13 was reproduced from [66] (© 2023 A. Larsson et al., published by Elsevier, distributed under the terms of the Creative Commons Attribution 4.0 International License, https://creativecommons.org/licenses/by/4.0).

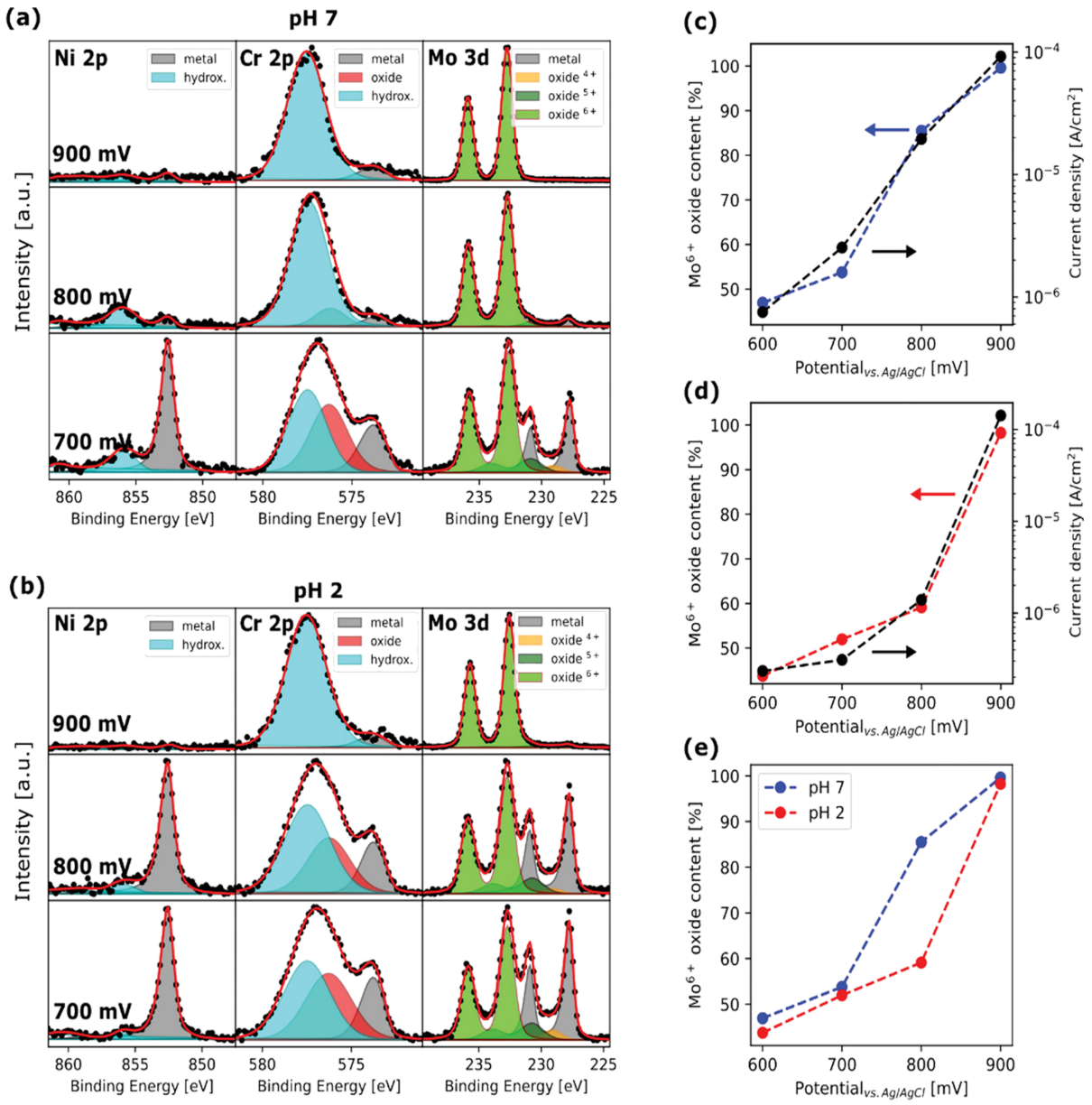

Figure 14: Passive film breakdown. (a) In situ APXPS spectra of Ni $2p_{3/2}$, Cr $2p_{3/2}$, and Mo 3d measured at pH 7 for the potential range of 700–900 mV. (b) In situ APXPS spectra of Ni $2p_{3/2}$, Cr $2p_{3/2}$, and Mo 3d measured at pH 2 for the potential range of 700–900 mV. (c) Mo^{6+} oxide content and current density after 10 min vs potential at pH 7. (d) Mo^{6+} oxide content and current density after 10 min vs potential at pH 2. Arrows indicate the axis corresponding to the data. (e) Comparison of Mo^{6+} oxide content at pH 7 and pH 2 vs potential. Figure 14 was reproduced from [65] (© 2023 A. Larsson et al., published by Wiley, distributed under the terms of the Creative Commons Attribution 4.0 International License, https://creativecommons.org/licenses/by/4.0).

have been studied. When there is no lithiation/delithiation, the expected 1:1 ratio of changes in photoelectron kinetic energy and applied potential are observed. However, when high enough potentials are reached to induce lithiation/delithiation, a deviation from this ratio is observed. These measurements demonstrate how APXPS, through its sensitivity to potential changes, can be used to probe interfacial chemistry without direct access to the interface.

The second form of experiment studies the solid–liquid interface directly, which, in the case of batteries, is where solid–electrolyte interphases (SEIs) form. Having stable SEIs formation is critical for the performance of a battery. A stable SEI stops the electrode from degrading, but uncontrolled growth can, in the extreme case, lead to short-circuit conditions inside the cell. Dip-and-pull XPS has been used to study the growth of SEIs at the interface between a 1 M $LiPF_6$ in propy-

lene carbonate electrolyte solution and a glassy carbon working electrode in a two-electrode cell with a Li metal counter electrode [71]. Here, XPS of the electrode–solution interface was measured at series of voltage steps. First, the electrodes were dipped into the solution, and the cell voltage was swept to the desired voltage. Then the electrode was pulled up under a potential hold for XPS measurements, and, due to the favorable wetting properties of this choice in materials, it was possible to find an area at the top of the liquid meniscus that was thin enough for photoelectrons generated at the electrode surface to escape and be measured. By repeating this dip-and-pull process at different potentials, the evolution of the carbonate and hydrocarbon SEI components could be observed (Figure 15). Similar studies have been performed on sputtered $LiCoO_2$ cathodes, demonstrating the broader applicability of this technique to conventional battery materials [10].

Conclusion and Perspectives

Ambient pressure X-ray photoelectron spectroscopy has emerged as a powerful and versatile technique for probing surface and interface phenomena under realistic environmental conditions. At MAX IV, the synergy between fourth-generation synchrotron source brightness and beamline-specific developments, such as advanced electron analyzers, tailored AP cells, and time-resolved detection schemes, has enabled operando and in situ investigations with unparalleled time resolution. These capabilities have pushed the boundaries of surface science, allowing for direct insights into reaction mechanisms in catalysis, electrochemistry, thin film growth, and corrosion.

The examples presented throughout this review, ranging from single-atom catalyst stabilization and confined 2D reactivity, to time-resolved studies of gas–solid reactions, photocatalytic water splitting, atomic layer deposition, and electrochemical interfaces, demonstrate the breadth of scientific questions that APXPS can now address. MAX IV's SPECIES and HIPPIE beamlines have contributed to this development, not only by offering high-performance instrumentation but also by fostering integrated experimental strategies and user-driven innovation.

Looking ahead, one of the most significant challenges for the APXPS community is the transition from simplified model systems to realistic, complex materials operating under industrially relevant conditions. Achieving this shift will require further innovations in sample environments, pressure compatibility, and surface sensitivity, especially for systems that exhibit spatial or chemical heterogeneity at the micro- and the nanoscale.

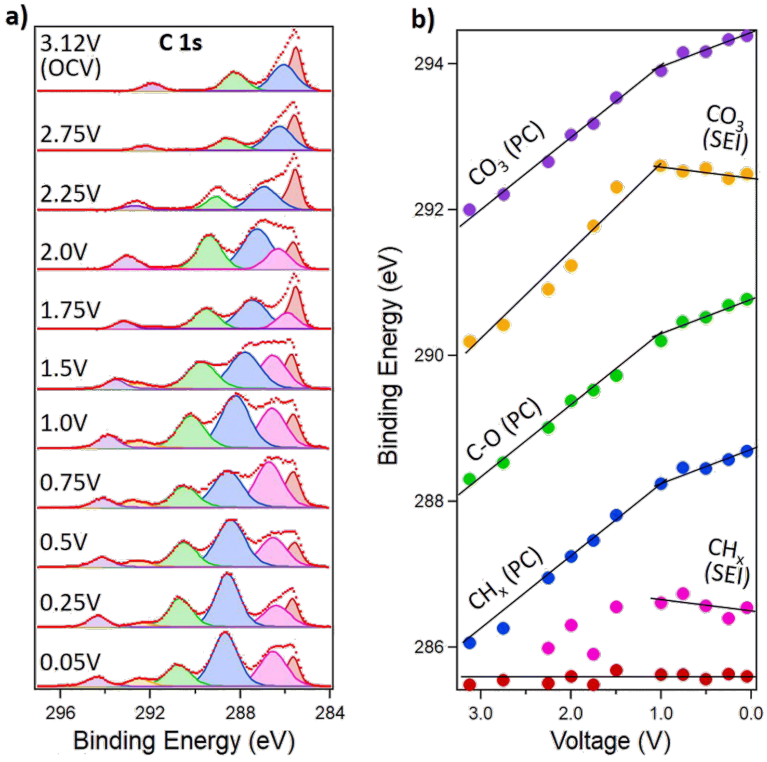

Figure 15: (a) C 1s spectra of the interface between glassy carbon and a 1 M $LiPF_6$/propylene carbonate electrolyte as a function of cell potential. (b) Trends of the binding energies of the various spectral components. Figure 15 was reproduced from [71] with permission of the Royal Society of Chemistry. This content is not subject to CC BY 4.0.

A key direction for the future lies in the multimodal integration of APXPS with complementary surface-sensitive and bulk-sensitive techniques. Combining APXPS with vibrational spectroscopies (such as IRRAS and Raman), structural probes (such as X-ray absorption spectroscopy or X-ray diffraction), and mass spectrometry will enable a more holistic understanding of structure–function relationships at working interfaces. Additionally, the development of correlated, spatially resolved measurements, potentially via photoemission electron microscopy (PEEM) or scanning probe methods, could further bridge the gap between fundamental surface studies and application-relevant complexity.

Another promising frontier is the coupling of APXPS with advanced data acquisition and analysis, such as machine learning for spectral interpretation, real-time kinetic modeling, and high-throughput experimentation. These approaches will be instrumental in interpreting the large, multidimensional datasets produced by time-resolved and pressure-dependent measurements, especially in dynamic systems with multiple reaction pathways.

Ultimately, the goal is to move beyond the use of APXPS as a purely observational tool and to establish it as a quantitative, mechanistic probe that directly informs materials design and process optimization. By continuing to refine its resolution, sensitivity, and integration with complementary modalities, APXPS is positioned to contribute to pressing societal challenges, including clean energy conversion, sustainable catalysis, environmental remediation, and next-generation electronic and electrochemical devices.

Through its unique ability to reveal buried, reactive, and dynamic interfaces under realistic conditions, APXPS will not only remain a cornerstone of modern surface science, but increasingly, a bridge between fundamental understanding and functional performance.

Acknowledgements

For the time-resolved experiments, we acknowledge MAX IV Laboratory for time on the beamline HIPPIE under proposal 20231730 and 20230723. The right panel of the Graphical Abstract was reproduced from [60] (© 2022 E. Kokkonen et al., published by the American Institute of Physics, distributed under the terms of the Creative Commons Attribution 4.0 International License, https://creativecommons.org/licenses/by/4.0). The picture in the left panel of the Graphical Abstract was taken by Robert Temperton. This content is not subject to CC BY 4.0.

Funding

Research conducted at MAX IV, a Swedish national user facility, is supported by the Swedish Research council under contract 2018-07152, the Swedish Governmental Agency for Innovation Systems under contract 2018-04969, and Formas under contract 2019-02496. This work was supported by Swedish Research Council (U.K. 2022-04363, J.K. 2017-04840, 2022-04363). U.K. and J.K. also acknowledge financial support for this work from the Crafoord foundation.

Author Contributions

Mattia Scardamaglia: conceptualization; investigation; visualization; writing – original draft; writing – review & editing. Ulrike Küst: data curation; formal analysis; investigation; visualization; writing – original draft; writing – review & editing. Alexander Klyushin: conceptualization; investigation; writing – original draft; writing – review & editing. Rosemary Jones: investigation; writing – original draft; writing – review & editing. Jan Knudsen: conceptualization; investigation; supervision; writing – original draft; writing – review & editing. Robert Temperton: conceptualization; investigation; writing – original draft; writing – review & editing. Andrey Shavorskiy: conceptualization; investigation; writing – original draft; writing – review & editing. Esko Kokkonen: conceptualization; investigation; writing – original draft; writing – review & editing.

ORCID® iDs

Mattia Scardamaglia - https://orcid.org/0000-0002-1128-7524
Ulrike Küst - https://orcid.org/0009-0009-0056-3165
Rosemary Jones - https://orcid.org/0000-0001-6273-4243
Esko Kokkonen - https://orcid.org/0000-0002-3674-7486

Data Availability Statement

Data reported in Figures 6, 7 and 8 are new and never published.

References

1. Siegbahn, H.; Siegbahn, K. *J. Electron Spectrosc. Relat. Phenom.* **1973,** *2,* 319–325. doi:10.1016/0368-2048(73)80023-4
2. Ogletree, D. F.; Bluhm, H.; Lebedev, G.; Fadley, C. S.; Hussain, Z.; Salmeron, M. *Rev. Sci. Instrum.* **2002,** *73,* 3872–3877. doi:10.1063/1.1512336
3. Salmeron, M.; Schlögl, R. *Surf. Sci. Rep.* **2008,** *63,* 169–199. doi:10.1016/j.surfrep.2008.01.001
4. Starr, D. E.; Liu, Z.; Hävecker, M.; Knop-Gericke, A.; Bluhm, H. *Chem. Soc. Rev.* **2013,** *42,* 5833–5857. doi:10.1039/c3cs60057b
5. Schnadt, J.; Knudsen, J.; Johansson, N. *J. Phys.: Condens. Matter* **2020,** *32,* 413003. doi:10.1088/1361-648x/ab9565
6. Tavares, P. F.; Leemann, S. C.; Sjöström, M.; Andersson, Å. *J. Synchrotron Radiat.* **2014,** *21,* 862–877. doi:10.1107/s1600577514011503
7. Robert, A.; Cerenius, Y.; Tavares, P. F.; Hultin Stigenberg, A.; Karis, O.; Lloyd Whelan, A.-C.; Runéus, C.; Thunnissen, M. *Eur. Phys. J. Plus* **2023,** *138,* 495. doi:10.1140/epjp/s13360-023-04018-w
8. Stoerzinger, K. A.; Hong, W. T.; Crumlin, E. J.; Bluhm, H.; Shao-Horn, Y. *Acc. Chem. Res.* **2015,** *48,* 2976–2983. doi:10.1021/acs.accounts.5b00275

9. Kokkonen, E.; Lopes da Silva, F.; Mikkelä, M.-H.; Johansson, N.; Huang, S.-W.; Lee, J.-M.; Andersson, M.; Bartalesi, A.; Reinecke, B. N.; Handrup, K.; Tarawneh, H.; Sankari, R.; Knudsen, J.; Schnadt, J.; Såthe, C.; Urpelainen, S. *J. Synchrotron Radiat.* **2021,** *28,* 588–601. doi:10.1107/s1600577521000564
10. Zhu, S.; Scardamaglia, M.; Kundsen, J.; Sankari, R.; Tarawneh, H.; Temperton, R.; Pickworth, L.; Cavalca, F.; Wang, C.; Tissot, H.; Weissenrieder, J.; Hagman, B.; Gustafson, J.; Kaya, S.; Lindgren, F.; Källquist, I.; Maibach, J.; Hahlin, M.; Boix, V.; Gallo, T.; Rehman, F.; D'Acunto, G.; Schnadt, J.; Shavorskiy, A. *J. Synchrotron Radiat.* **2021,** *28,* 624–636. doi:10.1107/s160057752100103x
11. Knudsen, J.; Andersen, J. N.; Schnadt, J. *Surf. Sci.* **2016,** *646,* 160–169. doi:10.1016/j.susc.2015.10.038
12. Han, Y.; Zhang, H.; Yu, Y.; Liu, Z. *ACS Catal.* **2021,** *11,* 1464–1484. doi:10.1021/acscatal.0c04251
13. Nguyen, L.; Tao, F. F.; Tang, Y.; Dou, J.; Bao, X.-J. *Chem. Rev.* **2019,** *119,* 6822–6905. doi:10.1021/acs.chemrev.8b00114
14. Kraushofer, F.; Parkinson, G. S. *Chem. Rev.* **2022,** *122,* 14911–14939. doi:10.1021/acs.chemrev.2c00259
15. Wang, Y.; Su, H.; He, Y.; Li, L.; Zhu, S.; Shen, H.; Xie, P.; Fu, X.; Zhou, G.; Feng, C.; Zhao, D.; Xiao, F.; Zhu, X.; Zeng, Y.; Shao, M.; Chen, S.; Wu, G.; Zeng, J.; Wang, C. *Chem. Rev.* **2020,** *120,* 12217–12314. doi:10.1021/acs.chemrev.0c00594
16. Wang, C.; Tissot, H.; Escudero, C.; Pérez-Dieste, V.; Stacchiola, D.; Weissenrieder, J. *J. Phys. Chem. C* **2018,** *122,* 28684–28691. doi:10.1021/acs.jpcc.8b08494
17. Taccardi, N.; Grabau, M.; Debuschewitz, J.; Distaso, M.; Brandl, M.; Hock, R.; Maier, F.; Papp, C.; Erhard, J.; Neiss, C.; Peukert, W.; Görling, A.; Steinrück, H.-P.; Wasserscheid, P. *Nat. Chem.* **2017,** *9,* 862–867. doi:10.1038/nchem.2822
18. Hohner, C.; Kettner, M.; Stumm, C.; Blaumeiser, D.; Wittkämper, H.; Grabau, M.; Schwarz, M.; Schuschke, C.; Lykhach, Y.; Papp, C.; Steinrück, H.-P.; Libuda, J. *J. Phys. Chem. C* **2020,** *124,* 2562–2573. doi:10.1021/acs.jpcc.9b10944
19. Kaiser, S.; Plansky, J.; Krinninger, M.; Shavorskiy, A.; Zhu, S.; Heiz, U.; Esch, F.; Lechner, B. A. J. *ACS Catal.* **2023,** *13,* 6203–6213. doi:10.1021/acscatal.3c00448
20. Vesselli, E. *JPhys Mater.* **2020,** *3,* 022002. doi:10.1088/2515-7639/ab7ab2
21. Armillotta, F.; Bidoggia, D.; Baronio, S.; Biasin, P.; Annese, A.; Scardamaglia, M.; Zhu, S.; Bozzini, B.; Modesti, S.; Peressi, M.; Vesselli, E. *ACS Catal.* **2022,** *12,* 7950–7959. doi:10.1021/acscatal.2c02029
22. Corva, M.; Vesselli, E. *J. Phys. Chem. C* **2016,** *120,* 22298–22303. doi:10.1021/acs.jpcc.6b05356
23. Li, H.; Xiao, J.; Fu, Q.; Bao, X. *Proc. Natl. Acad. Sci. U. S. A.* **2017,** *114,* 5930–5934. doi:10.1073/pnas.1701280114
24. Fu, Q.; Bao, X. *Chem. Soc. Rev.* **2017,** *46,* 1842–1874. doi:10.1039/c6cs00424e
25. Deng, D.; Novoselov, K. S.; Fu, Q.; Zheng, N.; Tian, Z.; Bao, X. *Nat. Nanotechnol.* **2016,** *11,* 218–230. doi:10.1038/nnano.2015.340
26. Mu, R.; Fu, Q.; Jin, L.; Yu, L.; Fang, G.; Tan, D.; Bao, X. *Angew. Chem., Int. Ed.* **2012,** *51,* 4856–4859. doi:10.1002/anie.201200413
27. Jin, L.; Fu, Q.; Dong, A.; Ning, Y.; Wang, Z.; Bluhm, H.; Bao, X. *J. Phys. Chem. C* **2014,** *118,* 12391–12398. doi:10.1021/jp5034855
28. Boix, V.; Scardamaglia, M.; Gallo, T.; D'Acunto, G.; Strømsheim, M. D.; Cavalca, F.; Zhu, S.; Shavorskiy, A.; Schnadt, J.; Knudsen, J. *ACS Catal.* **2022,** *12,* 9897–9907. doi:10.1021/acscatal.2c00803
29. Diulus, J. T.; Novotny, Z.; Dongfang, N.; Beckord, J.; Al-Hamdani, Y.; Comini, N.; Muntwiler, M.; Hengsberger, M.; Iannuzzi, M.; Osterwalder, J. *J. Phys. Chem. C* **2024,** *128,* 5156–5167. doi:10.1021/acs.jpcc.3c07828
30. Ryu, Y.; Kim, W.; Koo, S.; Kang, H.; Watanabe, K.; Taniguchi, T.; Ryu, S. *Nano Lett.* **2017,** *17,* 7267–7273. doi:10.1021/acs.nanolett.7b02621
31. Scardamaglia, M.; Boix, V.; D'Acunto, G.; Struzzi, C.; Reckinger, N.; Chen, X.; Shivayogimath, A.; Booth, T.; Knudsen, J. *Carbon* **2021,** *171,* 610–617. doi:10.1016/j.carbon.2020.09.021
32. Shavorskiy, A.; Kokkonen, E.; Redekop, E.; D'Acunto, G.; Schnadt, J.; Knudsen, J. *Synchrotron Radiat. News* **2022,** *35,* 4–10. doi:10.1080/08940886.2022.2082166
33. Shavorskiy, A.; Schnadt, J.; Knudsen, J. *ACS Symp. Ser.* **2021,** *1396,* 219–248. doi:10.1021/bk-2021-1396.ch009
34. Chavez, S.; Werghi, B.; Sanroman Gutierrez, K. M.; Chen, R.; Lall, S.; Cargnello, M. *J. Phys. Chem. C* **2023,** *127,* 2127–2146. doi:10.1021/acs.jpcc.2c06519
35. Redekop, E. A.; Yablonsky, G. S.; Gleaves, J. T. *Catal. Today* **2023,** *417,* 113761. doi:10.1016/j.cattod.2022.05.026
36. Tusini, E.; Casapu, M.; Zimina, A.; Doronkin, D. E.; Störmer, H.; Barthe, L.; Belin, S.; Grunwaldt, J.-D. *ACS Catal.* **2024,** *14,* 7463–7477. doi:10.1021/acscatal.3c05847
37. Hartfelder, U.; Singh, J.; Haase, J.; Nachtegaal, M.; Grolimund, D.; van Bokhoven, J. A. *Sci. Rep.* **2016,** *6,* 37597. doi:10.1038/srep37597
38. Roger, M.; Artiglia, L.; Boucly, A.; Buttignol, F.; Agote-Arán, M.; van Bokhoven, J. A.; Kröcher, O.; Ferri, D. *Chem. Sci.* **2023,** *14,* 7482–7491. doi:10.1039/d3sc01274c
39. Buttignol, F.; Maggiulli, L.; Kochetygov, I.; Alxneit, I.; Ferri, D. *Chimia* **2024,** *78,* 313–319. doi:10.2533/chimia.2024.313
40. Baurecht, D.; Fringeli, U. P. *Rev. Sci. Instrum.* **2001,** *72,* 3782–3792. doi:10.1063/1.1400152
41. Resta, A.; Hejral, U.; Blomberg, S.; Albertin, S.; Vlad, A.; Garreau, Y.; Chatelier, C.; Venturini, F.; Ferrer, P.; Held, G.; Grinter, D.; Lundgren, E.; Coati, A. *J. Phys. Chem. C* **2020,** *124,* 22192–22199. doi:10.1021/acs.jpcc.0c07128
42. Knudsen, J.; Eads, C.; Klyushin, A.; Temperton, R.; Küst, U.; Boix, V.; Kraina, A.; Scardamaglia, M.; Shavorskiy, A.; Kokkonen, E.; Schnadt, J. *ACS Catal.* **2025,** *15,* 1655–1662. doi:10.1021/acscatal.4c06355
43. Küst, U.; Prumbs, J.; Eads, C.; Wang, W.; Boix, V.; Klyushin, A.; Scardamaglia, M.; Temperton, R.; Shavorskiy, A.; Knudsen, J. *Surf. Sci.* **2025,** *751,* 122612. doi:10.1016/j.susc.2024.122612
44. Klyushin, A.; Ghosalya, M.; Kokkonen, E.; Eads, C.; Jones, R.; Nalajala, N.; Gopinath, C. S.; Urpelainen, S. *J. Synchrotron Radiat.* **2023,** *30,* 613–619. doi:10.1107/s1600577523002801
45. Ghosalya, M. K.; Talebi, P.; Singh, H.; Klyushin, A.; Kokkonen, E.; Alaoui Mansouri, M.; Huttula, M.; Cao, W.; Urpelainen, S. *Catal. Sci. Technol.* **2024,** *14,* 3029–3040. doi:10.1039/d4cy00204k
46. Johnson, R. W.; Hultqvist, A.; Bent, S. F. *Mater. Today* **2014,** *17,* 236–246. doi:10.1016/j.mattod.2014.04.026
47. Macco, B.; Kessels, W. M. M. (Erwin). *Appl. Phys. Rev.* **2022,** *9,* 041313. doi:10.1063/5.0116732
48. Miikkulainen, V.; Leskelä, M.; Ritala, M.; Puurunen, R. L. *J. Appl. Phys.* **2013,** *113,* 021301. doi:10.1063/1.4757907
49. Pore, V.; Heikkilä, M.; Ritala, M.; Leskelä, M.; Areva, S. *J. Photochem. Photobiol., A* **2006,** *177,* 68–75. doi:10.1016/j.jphotochem.2005.05.013

50. Cho, D.-Y.; Jung, H. S.; Yu, I.-H.; Yoon, J. H.; Kim, H. K.; Lee, S. Y.; Jeon, S. H.; Han, S.; Kim, J. H.; Park, T. J.; Park, B.-G.; Hwang, C. S. *Chem. Mater.* **2012,** *24,* 3534–3543. doi:10.1021/cm3001199
51. Nieminen, H.-E.; Putkonen, M.; Ritala, M. *Appl. Surf. Sci.* **2024,** *648,* 159015. doi:10.1016/j.apsusc.2023.159015
52. Methaapanon, R.; Bent, S. F. *J. Phys. Chem. C* **2010,** *114,* 10498–10504. doi:10.1021/jp1013303
53. Leskelä, M.; Ritala, M. *Thin Solid Films* **2002,** *409,* 138–146. doi:10.1016/s0040-6090(02)00117-7
54. Head, A. R.; Johansson, N.; Niu, Y.; Snezhkova, O.; Chaudhary, S.; Schnadt, J.; Bluhm, H.; Chen, C.; Avila, J.; Asensio, M. *J. Vac. Sci. Technol., A* **2018,** *36,* 02D405. doi:10.1116/1.5005533
55. D'Acunto, G.; Troian, A.; Kokkonen, E.; Rehman, F.; Liu, Y.-P.; Yngman, S.; Yong, Z.; McKibbin, S. R.; Gallo, T.; Lind, E.; Schnadt, J.; Timm, R. *ACS Appl. Electron. Mater.* **2020,** *2,* 3915–3922. doi:10.1021/acsaelm.0c00775
56. Jones, R.; D'Acunto, G.; Shayesteh, P.; Pinsard, I.; Rochet, F.; Bournel, F.; Gallet, J.-J.; Head, A.; Schnadt, J. *J. Vac. Sci. Technol., A* **2024,** *42,* 022404. doi:10.1116/6.0003349
57. D'Acunto, G.; Jones, R.; Pérez Ramírez, L.; Shayesteh, P.; Kokkonen, E.; Rehman, F.; Lim, F.; Bournel, F.; Gallet, J.-J.; Timm, R.; Schnadt, J. *J. Phys. Chem. C* **2022,** *126,* 12210–12221. doi:10.1021/acs.jpcc.2c02683
58. D'Acunto, G.; Shayesteh, P.; Kokkonen, E.; Boix de la Cruz, V.; Rehman, F.; Mosahebfard, Z.; Lind, E.; Schnadt, J.; Timm, R. *Surf. Interfaces* **2023,** *39,* 102927. doi:10.1016/j.surfin.2023.102927
59. Temperton, R. H.; Gibson, A.; O'Shea, J. N. *Phys. Chem. Chem. Phys.* **2019,** *21,* 1393–1398. doi:10.1039/c8cp06912c
60. Kokkonen, E.; Kaipio, M.; Nieminen, H.-E.; Rehman, F.; Miikkulainen, V.; Putkonen, M.; Ritala, M.; Huotari, S.; Schnadt, J.; Urpelainen, S. *Rev. Sci. Instrum.* **2022,** *93,* 013905. doi:10.1063/5.0076993
61. International Roadmap for Devices and Systems (IRDS™) 2024 Edition - IEEE IRDS™. https://irds.ieee.org/editions/2024 (accessed Sept 9, 2025).
62. Sze, S. M.; Ng, K. K. Appendix F Properties of Important Semiconductors. *Physics of Semiconductor Devices;* John Wiley & Sons: Hoboken, NJ, USA, 2006; p 789. doi:10.1002/9780470068328.app6
63. D'Acunto, G.; Kokkonen, E.; Shayesteh, P.; Boix, V.; Rehman, F.; Mosahebfard, Z.; Lind, E.; Schnadt, J.; Timm, R. *Faraday Discuss.* **2022,** *236,* 71–85. doi:10.1039/d1fd00116g
64. Velasco-Vélez, J.-J.; Falling, L. J.; Bernsmeier, D.; Sear, M. J.; Clark, P. C. J.; Chan, T.-S.; Stotz, E.; Hävecker, M.; Kraehnert, R.; Knop-Gericke, A.; Chuang, C.-H.; Starr, D. E.; Favaro, M.; Mom, R. V. *J. Phys. D: Appl. Phys.* **2021,** *54,* 124003. doi:10.1088/1361-6463/abd2ed
65. Larsson, A.; Grespi, A.; Abbondanza, G.; Eidhagen, J.; Gajdek, D.; Simonov, K.; Yue, X.; Lienert, U.; Hegedüs, Z.; Jeromin, A.; Keller, T. F.; Scardamaglia, M.; Shavorskiy, A.; Merte, L. R.; Pan, J.; Lundgren, E. *Adv. Mater. (Weinheim, Ger.)* **2023,** *35,* 2304621. doi:10.1002/adma.202304621
66. Larsson, A.; Simonov, K.; Eidhagen, J.; Grespi, A.; Yue, X.; Tang, H.; Delblanc, A.; Scardamaglia, M.; Shavorskiy, A.; Pan, J.; Lundgren, E. *Appl. Surf. Sci.* **2023,** *611,* 155714. doi:10.1016/j.apsusc.2022.155714
67. Yue, X.; Larsson, A.; Tang, H.; Grespi, A.; Scardamaglia, M.; Shavorskiy, A.; Krishnan, A.; Lundgren, E.; Pan, J. *Corros. Sci.* **2023,** *214,* 111018. doi:10.1016/j.corsci.2023.111018
68. Yue, X.; Chen, D.; Krishnan, A.; Tidesten, M.; Larsson, A.; Tong, H.; Gloskovskii, A.; Schlueter, C.; Scardamaglia, M.; Shavorskiy, A.; Pan, J. *Corros. Sci.* **2024,** *234,* 112133. doi:10.1016/j.corsci.2024.112133
69. Källquist, I.; Lindgren, F.; Lee, M.-T.; Shavorskiy, A.; Edström, K.; Rensmo, H.; Nyholm, L.; Maibach, J.; Hahlin, M. *ACS Appl. Mater. Interfaces* **2021,** *13,* 32989–32996. doi:10.1021/acsami.1c07424
70. Källquist, I.; Ericson, T.; Lindgren, F.; Chen, H.; Shavorskiy, A.; Maibach, J.; Hahlin, M. *ACS Appl. Mater. Interfaces* **2022,** *14,* 6465–6475. doi:10.1021/acsami.1c12465
71. Capone, F. G.; Sottmann, J.; Meunier, V.; Pérez Ramírez, L.; Grimaud, A.; Iadecola, A.; Scardamaglia, M.; Rueff, J.-P.; Dedryvère, R. *Energy Environ. Sci.* **2024,** *17,* 1509–1519. doi:10.1039/d3ee03228k

License and Terms